Doctoral Thesis

Numerical simulations in multimode fibres for astronomical spectroscopy

Author:
Eloy HERNANDEZ

Submitted to:
Institute of Physics and Astronomy
Faculty of Science
University of Potsdam

Supervisors:
Prof. Dr. Martin M. ROTH[ab]
Prof. Dr. Klaus PETERMANN[c]
Dr. Andreas KELZ[a]

[a]Leibniz-Institut für Astrophysik Potsdam
[b]Universität Potsdam
[c]Technische Universität Berlin

Potsdam
September 4,2019

Date of final exam: 27 May 2020

To Nitxia Anguizola and Eloy Hernandez Sr.

Ehrenwörtliche Erklärung

Vor- und Nachname: **Eloy Hernandez**
Geburtsdatum: **17.02.1985**
Wohnadresse: **Ueckermünder Str. 16, 10439 Berlin**
Geburtsort: **Panama**

Die vorliegende Arbeit wurde von Oktober 2014 bis September 2019 am Leibniz Institut für Astrophysik Potsdam unter der Betreuung von Prof. Dr. Martin M. Roth angefertig.

Hiermit versichere ich, dass die vorliegende Arbeit an keiner anderen Hochschule eingereicht sowie selbständig von mir und nur mit den angegebenen Mitteln angefertigt wurde. Alle Stellen, die wörtlich oder sinngemäß aus veröffentlichten oder nicht veröffentlichten Arbeiten anderer entnommen sind, habe ich kenntlich gemacht.

Potsdam, 4. September 2019

_____
Eloy Hernandez

Acknowledgments

Abstract

The goal of this thesis was to thoroughly investigate the behavior of multimode fibres to aid the development of modern and forthcoming fibre-fed spectrograph systems. Based on the Eigenmode Expansion Method, a field propagation model was created that can emulate effects in fibres relevant for astronomical spectroscopy, such as modal noise, scrambling, and focal ratio degradation. These effects are of major concern for any fibre-coupled spectrograph used in astronomical research. Changes in the focal ratio, modal distribution of light or non-perfect scrambling limit the accuracy of measurements, e.g. the flux determination of the astronomical object, the sky-background subtraction and detection limit for faint galaxies, or the spectral line position accuracy used for the detection of extra-solar planets.

Usually, fibres used for astronomical instrumentation are characterized empirically through tests. The results of this work allow to predict the fibre behaviour under various conditions using sophisticated software tools to simulate the waveguide behaviour and mode transport of fibres.

The simulation environment works with two software interfaces. The first is the mode solver module FemSIM from Rsoft. It is used to calculate all the propagation modes and effective refractive indexes of a given system. The second interface consists of Python scripts which enable the simulation of the near- and far-field outputs of a given fibre. The characteristics of the input field can be manipulated to emulate real conditions. Focus variations, spatial translation, angular fluctuations, and disturbances through the mode coupling factor can also be simulated.

To date, complete coherent propagation or complete incoherent propagation can be simulated. Partial coherence was not addressed in this work. Another limitation of the simulations is that they work exclusively for the monochromatic case and that the loss coefficient of the fibres is not considered. Nevertheless, the simulations were able to match the results of realistic measurements.

To test the validity of the simulations, real fibre measurements were used for comparison. Two fibres with different cross-sections were characterized. The first fibre had a circular cross-section, and the second one had an octagonal cross-section. The utilized test-bench was originally developed for the prototype fibres of the 4MOST fibre feed characterization. It allowed for parallel laser beam measurements, light cone measurements, and scrambling measurements. Through the appropriate configuration, the acquisition of the near- and/or far-field was feasible.

By means of modal noise analysis, it was possible to compare the near-field speckle patterns of simulations and measurements as a function of the input angle. The spatial frequencies that originate from the modal interference could be analyzed by using the power spectral density analysis. Measurements and simulations yielded similar results. Measurements with induced modal scrambling were compared to simulations using incoherent propagation and once again similar results were achieved. Through both measurements and simulations, the enlargement of the near-field distribution could be observed and analyzed. The simulations made it possible to explain incoherent intensity fluctuations that appear in real measurements due to the field distribution of the active propagation modes.

By using the Voigt analysis in the far-field distribution, it was possible to separate the modal diffusion component in order to compare it with the simulations. Through an appropriate assessment, the modal diffusion component as a function of the input angle could be translated into angular divergence. The simulations gave the minimal angular divergence of the system. Through the mean of the difference between simulations and measurements, a figure of merit is given which can be used to characterize the angular divergence of real fibres using the simulations. Furthermore, it was possible to simulate light cone measurements. Due to the overall consistent results, it can be stated that the simulations represent a good tool to assist the fibre characterization process for fibre-fed spectrograph systems.

This work was possible through the BMBF Grant 05A14BA1 which was part of the phase A study of the fibre system for MOSAIC, a multi-object spectrograph for the Extremely Large Telescope (ELT-MOS).

x

Zusammenfassung

Vorrangiges Ziel der Arbeit war eine ausführliche Untersuchung von Eigenschaften multimodaler Glasfasern mittels Simulationen und experimenteller Tests, welche die Charakterisierung fasergekoppelter astronomischer Spektrographen unterstützt. Die simulierten Effekte sind von großer Bedeutung für alle fasergekoppelten Spektrographen, die in der astronomischen Forschung verwendet werden. Jede Änderung des Öffnungsverhältnisses (durch Focal-Ratio-Degradation), der Modenanregung in der Glasfaser (modal noise) oder einer variablen Ausleuchtung (durch unzureichendes scrambling) schränkt die Genauigkeit der Messungen ein. Dies hat Auswirkungen auf die Intensitätsbestimmung des astronomischen Objekts, die Subtraktion des Himmelshintergrundes und damit die Detektion von lichtschwachen Galaxien, oder die spektrale Stabilität, die für den Nachweis von extra-solaren Planeten benötigt wird.

Zwei Softwareprogramme wurden für die Simulationsumgebung verwendet. Zunächst wurde ein Modenrechner benötigt, um die ausbreitungsfähigen Moden des simulierten Systems zu berechnen. Dafür wurde das FemSIM-Modul von RSOFT eingesetzt. Anschließend wurden durch selbst geschriebene Python-Skripte die Nah- und Fernfelder am Faserausgang berechnet. Die Funktionen beinhalten die Berechnungen des Eingangsfeldes, der räumlichen Verschiebung, der Winkelabweichung des Eingangsfeldes, sowie der Störungseffekte durch Modenkopplung.

Bisher konnte die Propagation der Felder kohärent oder inkohärent simuliert werden. Das umfangreiche Themenfeld der partiellen Kohärenz wurde in dieser Arbeit nicht behandelt. Außerdem sind die von der Wellenlänge abhängigen Verlustkoeffizienten nicht berücksichtig worden und die Simulationen beschränken sich auf den monochromatischen Fall. Dennoch war es möglich, eine gute Übereinstimmung von realen Messwerten und Simulationsergebnissen zu erlangen.

Um die Gültigkeit der Simulationen zu überprüfen, wurden optische Fasern vermessen und die Ergebnisse zwischen Simulationen und Messungen verglichen. Hierfür wurden zwei Fasern mit unterschiedlichem Querschnitt verwendet: eine zirkulare Faser und eine oktagonale Faser. Der verwendete Prüfstand wurde für die Charakterisierung der 4MOST Faserprototypen entwickelt. Verschiedene Konfigurationen zur Charakterisierung optischer Fasern waren durch den Prüfstand möglich, z.B. die Aufnahmen von Nah- und Fernfeldern.

Durch die Analyse des Modenrauschens war es möglich, die Abhängigkeit der Interferenzmuster als Funktion des Eingangswinkels zu vergleichen. Mittels der spektralen Leistungsdichte konnten die räumlichen Frequenzen der Interferenzmuster untersucht und eine gute Übereinstimmung zwischen Theorie und Experiment bestätigt werden. Messungen mit induzierter Durchmischung wurden mit Simulationen veglichen, die den inkohärenten Ausbreitungsfall benutzen. Die Vergrößerung des Nahfeldes auf Grund schnellerer Blendenzahlen wurde in Messungen und Simulationen beobachtet und nachgewiesen. Durch die Simulationen ist es gelungen, inkohärente Intensitätsfluktuationen zu erklären.

Mittels der Voigt Analyse der Fernfelder war es möglich, die modale Diffusionskomponente zwischen Messungen und Simulationen zu vergleichen. Durch eine geeignete Auswertung konnten die Diffusionskomponenten als Funktion des Eingangswinkels ermittelt werden und die Winkeldivergenz der Fernfelder berechnet werden. Das Minimum der Winkeldivergenz eines Systems konnte durch Simulationen berechnet werden. Als Leistungszahl wurde die Mittelung der Differenz zwischen der minimalen und der gemessenen Winkeldivergenz ermittelt. Obwohl die Simulationen durch einige Faktoren begrenzt sind, ist es gelungen, die Ergebnisse der Lichtkegel Messungen zu emulieren. Auf Grund der insgesamt guten Übereinstimmung zwischen Simulationen und Messungen ist es damit möglich, die Charakterisierung von fasergekoppelten Spektrographen im Vorfeld realistisch zu simulieren.

List of Abbreviations and Acronyms

4MOST 4-meter Multi-Object Spectroscopic Telescope

AAO Australian Astronomical Observatory

AAT Anglo-Australian Telescope

ADU Analog-to-Digital Unit

AESOP Australian European Southern Observatory Positioner

AIP Leibniz-Institut für Astrophysik Potsdam

APOGEE The Apache Point Observatory Galactic Evolution Experiment

AO Adaptive Optics

BOSS Baryon Oscillation Spectroscopic Survey

CALIFA Calar Alto Legacy Integral Field Area

CCD Charge-Coupled Device

DESI Dark Energy Spectroscopic Instrument

ELT Extremely Large Telescope

EE Encircled Energy

EEM Eigenmode Expansion Method

ESO European Southern Observatory

f-number focal number

FBG Fibre Bragg Grating

FEM Finite Element Method

FF Far-Field

FFT Fast Fourier Transform

FOV Field-Of-View

FRD Focal Ratio Degradation

FWHM Full Width at Half-Maximum

HeNe Helium-Neon

HETDEX Hobby-Eberly Telescope Dark Energy Experiment

IFS Integral Field Spectroscopy

IFU Integral Field Unit

JWST James Webb Space Telescope

IR Infrared

KPNO Kitt Peak National Observatory

LAMOST Large Sky Area Multi-Object Fiber Spectroscopic Telescope

LWD Long Working Distance

MARVELS Multi-object APO Radial Velocity Exoplanet Large-area Survey

MaNGA Mapping Nearby Galaxies at Apache Point Observatory

MMF Multimode Fibre

MOONS Multi-Object Optical and Near-infrared Spectrograp

MOS Multi-Object Spectrograph

MOSAIC Multi-Object Spectrograph for the ELT

MPD Modal Power Distribution

NA Numerical Aperture

NF Near-Field

NIR Near-Infrared

ODE Ordinary Differential Equation

PEPSI Potsdam Echelle Polarimetric and Spectroscopic Instrument

PMAS Potsdam Multi-Aperture Spectrophotometer

PSD Power Spectral Density

PFS the Subaru Prime Focus Spectrograph

PSF Point Spread Function

SDSS Sloan Digital Sky Survey

SMF Single-Mode Fibre

SNR Signal-to-Noise Ratio

STELLA STELLar Activity

TME Transverse Electromagnetic

UV Ultraviolet

VIS Visible

VIRUS Visible Integral-Field Replicable Unit Spectrograph

VISTA Visible and Infrared Survey Telescope for Astronomy

VLT Very Large Telescope

WEAVE WHT Enhanced Area Velocity Explorer

WHT William Herschel Telescope

Contents

Chapter 1

Fibre-Fed Astronomical Instrumentation

Introduction

The use of optical fibres in astronomical instrumentation has come a long way up to their current applications in many state-of-the-art research projects. One of the first approaches of a fibre-fed instrument for Astronomy can be found in the work of Angel et al. (1977), "A Very Large Optical Telescope Array Linked with Fused Silica Fibers" [1], in which it was suggested to link many telescopes together to obtain the same gathering power as a 100 square meter telescope. The first light actually accomplished by a fibre based spectrograph was by Hill et al. (1980) [2] at the Steward observatory by the means of the Medusa spectrograph. Short length fused silica fibres of 300 microns in diameter were used to acquire multiple targets at the Cassegrain focus of the 2.29 meter telescope. Although significant losses were registered, the multiplex of the system provided a sixfold reduction in the required telescope time per galaxy [2]. Nowadays, fibre-fed instruments can be found in many applications such as wide-field spectroscopy to address cosmological issues, including studies of dark matter and stellar archeology to map the history of the galaxy assembly. Additional applications are in high precision spectroscopy which is required for extra-solar planet studies to achieve radial velocity accuracies of a few cm/s [3].

The Sloan Digital Sky Survey (SDSS), arguable one of the most important sky surveys in astronomy during the past decades, has been carried out with a moderately-sized telescope of 2.5 metre, but with a large field-of-view of 3 degrees and spectrographs that are fed with 640 fibres from the focal plane. The survey was originally aimed to cover approximately one-quarter of the celestial sphere, collect a photometrically and astrometrically calibrated digital imaging, and collect spectra of $\approx 10^6$ galaxies; $100,000$ quasars; $30,000$ stars; and $30,000$ serendipity targets [4] [5]. The publication of the technical summary by York et al. (2000) [4] has over 6500 citations with over 5900 refereed citations. The original SDSS redshift surveys, as well as the scientific successor projects using the MARVELS [6], BOSS [7] and APOGEE[8] spectrographs and the MaNGA Fiber Feed [9], they all benefited from the large multiplex factor that only a deployable fibre system could offer.

An almost equal scientific impact, in particular in the area of near-field-cosmology, can be attributed to the 2df galaxy redshift survey [10], obtained at the Anglo-Australian telescope (AAT). The 2dF-instrument features a pick-and-place robot that can position 2×400 fibres to their target locations at the focal plane of the telescope. With this automated multi-fibre positioning system, the 2dF Galaxy Redshift Survey was the first to observe more than 100,000 redshifts of galaxies.

In the advent of extremely large telescopes, optical fibres are the best and most flexible option to connect large and heavy instrumentation that can be placed remotely to the telescope. The Extremely Large

Telescope (ELT) will be the largest ground-based telescope with a primary mirror having a diameter of 39m, located at Cerro Armazones in Chile. Amongst others, the ELT instrumentation plan foresees a Multi-Object-Spectrograph (ELT-MOS [11]) and a High-resolution Spectrograph (ELT-HiRes [12]). The conceptional planning for both these instruments foresee fibre-systems to feed the light from the Adaptive-Optics (AO) corrected focal plane to various spectrographs operating on the visible and infrared wavelength regimes.

The MOSAIC concept has been selected by ESO as the fibre-fed multi-object spectrograph for the ELT. Science cases that will be addressed range from spectroscopy of the most distant galaxies, mass assembly, and evolution of galaxies via resolved stellar populations, galactic archeology, and planet formation studies. Additionally, the instrument is planned to be used for follow up observations from targets discovered by the James Webb Space Telescope (JWST) [13]. The instrument should cover the wavelength range from $460nm$ up to $1800nm$, with modular spectrograph subsystems, observing in the visible and the near-infrared spectral range at moderate resolving power ($R \sim 5000$) and with higher resolution ($R \sim 15000$) at selected spectral bands. The aim is to observe 80-100 sources in a high-multiplex mode, or to obtain spectroscopy of 8-10 spatially-extended fields through deployable integral field units (IFUs) [14].

As the light-collecting power and sensitivity of an ELT-MOS will be unprecedented, the instrumental stability, throughput, and calibration will be crucial. In particular, the complex optical fibre-link between the AO-assisted input feed at the telescope and the output into the (cryostatic) NIR-spectrographs need to be understood well in advance for a proper design and development. For these purposes, the work presented in this thesis was undertaken as a part of the ELT-MOS research and development project but is of application to fibre-coupled spectrographs in general.

1.1 Benefits of Fibre-Based Systems

The use of fibres as an optical link between telescope and spectrographs offers various benefits which are listed below and supported by examples of instruments that were developed at AIP.

Optical fibres offer the possibility to decouple the instrument from the focal plane of the telescopes and place it in a more stable environment, such as a bench-mounted spectrograph in a temperature and humidity controlled room. While this facilitates the spectrograph optical alignment, reduces its sensibility on movement and vibration, and eases the detector maintenance and operation, special care is needed to minimize any effects that result from the fibre routing and possible fibre movements. The benefits of remote fibre-coupled instruments are most obvious for high-resolution spectrographs that require uttermost opto-mechanical stability and benefit from a de-coupling of any direct seeing-effects due to the scrambling properties of the fibres. Often, bench-mounted spectrographs are simply too large for a direct mounting on the telescope. AIP-built examples are the STELLA-Echelle Spectrograph [15] and the Potsdam Echelle Polarimetric and Spectroscopic Instrument (PEPSI) [16]. In extreme cases, an instrument could be fibre-coupled to a different telescope located at a separate dome; e.g. the linking of PEPSI to the Vatican Advanced Technology Telescope using a 450m long fibre [17].

Additionally, optical fibres enable the simultaneous recording of multiple targets in the field-of-view and allow for multi-object spectroscopy (MOS). State-of-the-art instrumentation that feature several hundred to thousands of fibres include WEAVE [18] at the William Herschel Telescope, DESI for the KPNO 4m telescope [19], the Subaru Prime Focus Spectrograph (PFS) [20], the LAMOST spectrograph [21], MOONS for the VLT [22] and 4MOST.

The 4-meter Multi-Object Spectroscopic Telescope (4MOST) is a multi-object spectrograph with 2436 fibres and a 4 square degree field-of-view for the ESO-VISTA telescope [23]. The fibres feed two low-resolution spectrographs (with 1624 fibers) and one high-resolution spectrograph (with 812 fibers). The system also includes guide fibre bundles, metrology fiducial fibres, and calibration fibres as well as cable wraps and de-rotators to route the fibres from the Cassegrain focal plane to the spectrographs under the Azimuth floor of the telescope [24]. A tip-tilt based fibre positioning system (AESOP), developed by the

Australian Astronomical Observatory (AAO) should reposition the 2436 science fibres simultaneously to an accuracy of $10\mu m$ within one minute. The scientific surveys should run for five years+, delivering over 7 million spectra and mapping $10,000$ to $20,000$ square degrees. This represents an order of magnitude larger than the SDSS spectroscopic survey. Through the highly multiplex manner and high spectral resolution, the instrument should be able to detect chemical and kinematic substructure in the stellar halo, as well as bulge and thin and thick discs of the Milky Way. Due to the large wavelength coverage ($\sim 400nm$ up to $\sim 900nm$), the measurement of velocities from extra galactic objects over a large range of redshift should be possible. The science cases include spectroscopic follow-ups of space-based observatories, such as Gaia and eROSITA [23].

Finally, if the fibres are positioned densely in the telescope field-of-view, they can sample spatially extended objects and be re-arranged in a linear-slit configuration to feed a spectrograph. Through the usage of these integral field units (IFUs), the spatial information in the field-of-view can be recorded as a data cube of $I(\alpha, \delta, \lambda)$, a technique that is refered to as either Integral Field Spectroscopy (IFS) or as 3D-Spectroscopy. In both MOS and IFS cases, the fibres are rearranged along the slit of the spectrograph, and the spectra are dispersed in the second dimension of the detector array.

As an example, the Hobby-Eberly Telescope Dark Energy Experiment (HETDEX) uses 75 units of so-called Visible Integral-Field Replicable Unit Spectrographs (VIRUS). Each fibre bundle consist of 448 optical fibers, with the entire system having around 34,000 individual fibers [25]. This large numbers of fibres allows a (sparsley-sampled) field-of-view of 20 arcminutes on the sky. Figure 1.1 shows one of the VIRUS integral field units (left), how the fibres are rearranged as a slit (centre) and calibration spectra dispersed on a detector array (right). Illustrated are two raw frames obtained with an Hg-arc exposure (top part) and halogen white light (lower part). The x-axis shows the wavelength dispersion, and the y-axis shows the different fibres. These images are from Kelz et al. (2014) [26].
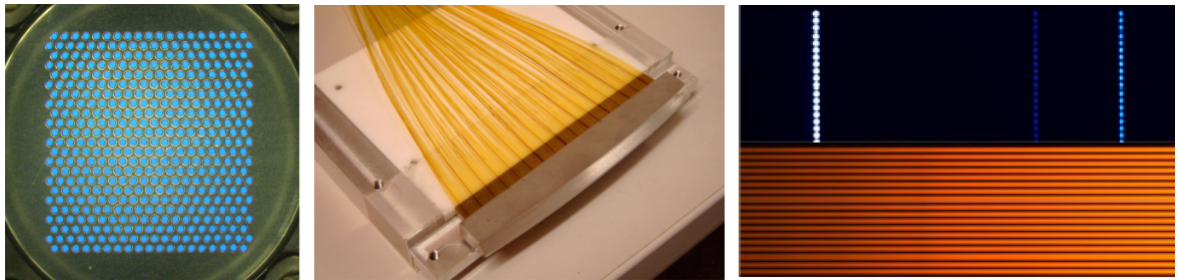
Figure 1.1: From left to right: • Fibre bundle from the instrument Visible Integral-Field Replicable Unit Spectrograph (VIRUS) • Fibres rearranged as a slit • Calibration spectra dispersed on a detector array. Illustrated are two raw frames obtained with an Hg-arc exposure (top part) and halogen white light (lower part). The x-axis shows the wavelength dispersion, and the y-axis shows the different fibres. These images are from Kelz et al. (2014) [26]

In general, there is always a trade-off between spatial resolution and the field-of-view (FOV) that can be sampled. As an example, the Potsdam Multi-Aperture Spectrophotometer (PMAS) installed at the Calar Alto 3.5m telescope possesses a 16×16 element IFU. Depending on the fore-optics magnification, it can either provide seeing limited sampling 0.5" per spatial element (called spaxel), resulting in a field-of-view of 8" × 8". PMAS can observe a field-of-view of up to 16" × 16" but with a decreased spatial resolutiona sampling of 1"/spaxel [27]. In addition, PMAS features a second IFU, called PPak with a larger FOV of 74" × 65". It uses 331 fibres providing a resolution of 2.7"/spaxel [28]. Using the PPak-IFU of PMAS, the Calar Alto Legacy Integral Field Area (CALIFA) survey yielded the resolved spectroscopic information in the optical wavelengths from $370nm$ to $700nm$ of ~ 600 galaxies in the local Universe. This information was used to study fundamental issues of galaxy evolution through statistical significant samples [29].

In nearly all instruments, some fibres are used for monitoring the sky background, while others are used for calibration lamps and for telescope tracking purposes. If individual fibres need to be re-arranged at the focal plane of the telescope, complex positioning systems may be required. In summary, fibre add a

large flexibility in the design of spectrograph-telescope systems and enable a large multiplex as well as the re-formatting of the integral fields.

1.2   Motivation

There are many benefits that fibre-fed instruments have. However, fibres are not perfect optical components and do incorporate losses and unwanted effects that lower the efficiency and the overall throughput of the systems. Fibres do not conserve the etendue, a figure that expresses how much a beam of light spreads in area and solid angle [30]. The focal ratio at the output of the fibre tends to decrease, manifesting as a spread in the solid angle. This effect is known as Focal Ratio Degradation (FRD) and translates directly into losses of fibre-fed instruments.

Another relevant effect for fibre-based spectroscopy is known as modal noise and arises from modal interference. Modal noise is a phenomenon that was already identified in the late '70s in fibre optical communication links. Richard Epworth (1978) [31] explained the phenomenon of unwanted amplitude modulation of a received signal and how this modulation is extremely sensitive to slight mechanical distortions of the fibre, joints, and source. The effect of modal noise in astronomical spectroscopy was observed by Baudrand et al. (1998) [32] during the characterization of the high-resolution multi-aperture fibre-fed spectrograph FUEGOS for the Very Large Telescope (VLT). When the fibres where perfectly still, the signal-to-noise ratio followed the expected photon statistics, in which the noise increases with the square root of photons detected as $\sqrt{N}$ [33]. But when the fibre bundle was in stress or motion, significant degradation of the photometric performance was measured, deviating strongly from the limit set by photon noise [32].

Induced modal scrambling tends to help mitigate modal noise but usually increases FRD. Scrambling describes the process in which the output distribution becomes independent of the input distribution of the fibre. Since input conditions may fluctuate, it is beneficial that the output field of the optical fibre remains stable. This can guarantee a spectrograph response isolated from sources of systematic wavelength errors [34]. Errors are minimized for precision spectroscopy since the barycenter of light at the entrance of the spectrograph slit becomes independent from any details that may happen at the telescope focal plane and zonal error levels can be reduced by orders of magnitude [34].

When fibres started being used in astronomy, authors such as Ramsey [35], Barden [36], and Heacox [37] did relevant groundwork through the '80s on FRD and scrambling. Mechanical deformations and irregularities in the cylindrical shape through the fibre (microbendings) were said to be one of the causes of FRD [35]. It was also acknowledged that the treatment of the fibre when e.g. polishing or cleaving, can cause a tremendous amount of FRD if not done correctly. Avila (1998) [38] pointed out the fact that FRD measurements are sensitive to various factors, but the most relevant are: micro- & macrobendings, alignment, perpendicularity between the fibre surface and fibre axis, polishing errors, and stability of the light source and movable mechanical parts. The sensitivity of FRD on so many factors indicates why many authors do not obtain reproducible results.

To aid with the characterization of multimode fibres for fibre-fed spectrograph systems, a simulation tool was created in the work presented in this thesis that addresses specifically the effects of FRD, modal noise and scrambling in fibre-fed spectrographs. Simulations of optical components are usually conducted by ray tracing or wave analysis. Although it is possible through both methods to simulate the field propagation in optical fibres, commercially available software do not tend to address effects like FRD, modal noise or scrambling in multimode fibres [39]. In the work of Allington-Smith et al. 2012 [39] FRD was simulated using ray tracing implemented in MathCad. It was based on Gloge's model and represents a portion of the fibre with scattering centers to account for the deformations and irregularities a fibre may be subjected to. The scrambling effects of fibres and modal noise (to an extent) could be analyzed with the model. In the simulations presented in this thesis, wave theory is used to describe and simulate the effects of FRD, scrambling and modal interference in multimode fibres. The Eigenmode Expansion Method is used as the basis to calculate the field propagation in multimode fibres. It creates the possibility

to analyze the different modal effects as a function of the input focal ratio, spatial and angular translation, focus variations, different wavelengths, and fibre geometries. The simulations are compared to typical experimental measurements applied for fibre characterization [40]. As will be explained and illustrated in the following chapters, the simulations were able to match the results of realistic measurements, confirming the simulations as a good tool to aid with the fibre characterization for fibre-fed spectrograph systems.

1.3 Overview

In Chapter 2, the characteristics of astronomical fibres are explained. Using geometrical and wave optics, relevant quantities for the simulation environment are presented. Furthermore, this chapter explains the effects, former work and characterization methods of focal ratio degradation, modal noise, and scrambling that are of relevance for this thesis. Chapter 3 presents how the simulation environment is constructed. First, the mode solver package used in RSoft is explained. Afterwards, the different functions written in python are illustrated. The functions include mode selection, input field variations, analyzing modal amplitudes, analyzing output fields, and incoherent phase propagation, among other topics. Examples of simulations are presented at the end of this chapter. If not stated otherwise, all Rsoft calculations, and all python scripts were conducted and written by the author of this thesis. Chapter 4 illustrates the measured fibres and explains the test-bench used for the different experimental measurements. All of the equipment is specified, and each of the possible fibre characterization configurations is described.

Chapter 5 presents the results of the measurements and how the simulations can emulate each of the characterization methods. The chapter starts with the modal interference of the near-field analyzed through the power spectral density method. Afterwards, induced modal scrambling is compared to the incoherent propagation of the simulations. The enlargement of the near-field as a function of the input angle and focal ratio is illustrated. Afterwards, the far-field of the parallel laser beam method is analyzed via the Voigt-fit, giving the possibility of separating the modal diffusion component. Through an appropriate assessment, the modal diffusion component as a function of the input angle is translated into the angular divergence. Through the mean of the difference between simulations and measurements, a figure of merit is given which can be used to characterize the angular divergence of real fibres. In addition, the light cone method is compared to the simulations. Through an appropriate method, it was possible to emulate the FRD characteristics of the measured fibres, demonstrating the simulations as a good supplement for fibre characterization purposes. A final section of this chapter gives a summary of the results.

The conclusion and outlook of this work are presented in Chapter 6. It gives insight into the relevant findings that were achieved by comparing the simulations and the measurements. Furthermore, remaining open points are presented, and an outlook for future work is explained.

Chapter 2

Characteristics of Astronomical Fibres

Introduction

Fibres used for astronomical instrumentation are mostly of step-index profile with multimode characteristics. The core diameter ranges from $\sim 50\mu m$ up to $\sim 300\mu m$ with a typical numerical aperture (NA) of NA ≈ 0.21 [41]. The large core diameters and NA allows for simple and efficient coupling to the input end of the fibres. The spectral windows targeted in ground-based applications are in the visible (VIS) and near-infrared (NIR) wavelengths, making conventional fused silica fibres the best solution [30]. A high number of propagation modes are supported, ranging from 1700 up to 70000 in the visible wavelengths [41]. Authors like Avila et al. (2010) [42] and Allington-Smith et al. (2011) [39], among others, have found different polygonal cross-sections to improve optical scrambling, which is why non-circular multimode step-index fibres are of interest for astronomical instrumentation.

Graded-index multimode fibres are vastly known in telecommunication since the structure provides an effective way of minimizing modal dispersion. Typically, any kind of dispersion minimizes the amount of data that can be sent through an optical link [43]. This is not the case in astronomical instrumentation, where the main concern is that the optical fibre delivers the radiant flux from the focal plane of the telescope to the spectrograph/detector without any or minimal flux losses. Higher modal dispersion lowers the coherence among modes, a situation that helps mitigate modal noise [31] and raises the signal-to-noise ratio in a high-resolution spectrograph [32]. In addition, efficient coupling mechanisms tend to be more complicated and fewer propagation modes are allowed [44], a condition that tends to diminish optical scrambling. For these reasons, graded-index fibres are less suitable for astronomical applications than the basic multimode step-index fibres .

Although single-mode fibres (SMF) present more of a challenge for efficient coupling than any other type of fibre [45], they can be found in special cases of astronomical instrumentation. Such cases include interference based techniques [36], fibre Bragg gratings (FBGs) for filtering of parasitic atmospheric light [46] [47] and photonic lanterns to join multimode with single-mode fibres [48]. These topics are beyond the scope of this work; more information can be found in the references. Single-mode fibres do not experience complex modal effects since only the fundamental mode in its two polarization states propagates through the fibre. Although it is possible to model single-mode fibres in the simulation environment, there would be no insights nor information on the topics of FRD, scrambling and modal noise. All the simulations and measurements in this thesis are based on step-index multimode fibres (MMF).

This chapter explains the properties of step-index multimode fibres that are relevant to astronomical spectroscopy. The first section explains the light propagation in optical fibres through geometrical optics and

wave optics. Wave optics allow the description of modal interference and the appropriate transformations for obtaining the far-field angular distribution. The second section addresses optical throughput calculations of a fibre-based system through the use of the optical etendue and the first and second law of thermodynamics. In section three, the transmission characteristics in optical fibres are illustrated, explaining why fused silica is the best material to cover the wavelength ranges of astronomical interest and why different conditions and materials are used when going to NIR wavelengths. Section four explains the effects, characterization methods, and previous work done on the topics of FRD, modal noise, and scrambling.

2.1 Light Propagation in Optical Fibres

2.1.1 Geometrical optics

In geometrical optics, light can be portrayed as straight lines (rays) when traveling in a homogeneous medium. Light rays can be reflected or refracted when going through a boundary that separates two mediums with different refractive index n. A typical step-index optical fibre has an area with higher refractive index material, n_{core} or n_1, known as the core; and an area with lower refractive index material, n_{clad} or n_2, around the core known as the cladding. The difference between the refractive indexes is usually small, so that [45]

$$\Delta = \frac{n_1^2 - n_2^2}{2n_1^2} \approx \frac{n_1 - n_2}{n_1} \ll 1. \tag{2.1}$$

Light rays propagate through the core of the optical fibre due to total internal reflection. This happens when a ray hits the boundary to a medium with a lower refractive medium in a suitable incident angle α and gets completely reflected. If the ray has an incident angle that surpasses the critical angle α_{max}, it will not be guided in the fibre and leaves the high index medium. Rays propagating on a single plane intersecting the axis of the fibre are denominated as meridional. Rays that tend to follow a helical path avoiding the axis are denominated as skew rays [39]. The projection of skew rays on the transverse plane is a polygon that is not necessarily closed [45]. Figure 2.1 illustrates the process of total internal reflection of a ray inside an optical fibre and shows both meridional and skew ray propagation.
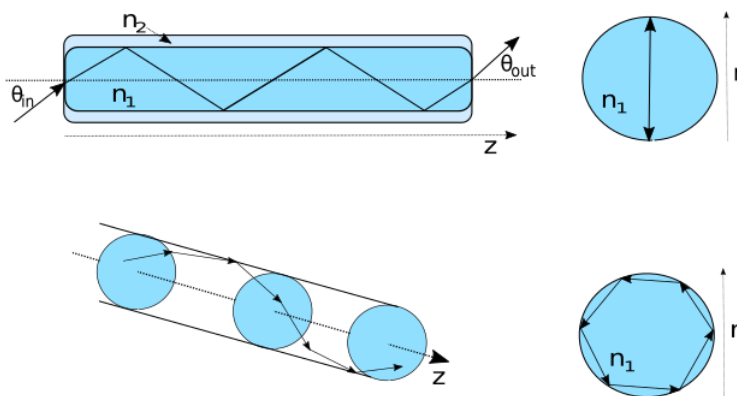
Figure 2.1: Rays propagating through an optical fibre. The upper part illustrates meridional rays traveling along the z-axis of the fibre. At the fibre end face (transverse plane), meridional rays tend to follow the same path. The lower illustration shows the path of a skew ray. The projection at the fibre end face (transverse plane) resembles a polygon.

The critical angle is derived from the Snell's law of refraction and dictates the maximum input angle an

incoming ray can have. It is set by the refractive index of the core and the cladding as

$$\alpha_{max} = \arcsin\left(\sqrt{n_1^2 - n_2^2}\right). \tag{2.2}$$

The argument in Eq.2.2 gives the numerical aperture (NA) of a step-index fibre. It gives a measure of the index difference between the core and cladding and together with α_{max} characterizes the cone of external rays that can be guided by the fibre,

$$\mathrm{NA} = \sqrt{n_1^2 - n_2^2}. \tag{2.3}$$

The focal ratio (also known as f-number or $f\#$) is the ratio between the beam length and diameter of the optical element. It is an important quantity for calculating the efficiency and optical throughput of a (fibre-based) system. High value f-numbers are denominated as slow, e.g. $f\# > 8$; and low value f-numbers are denominated as fast, e.g. $f\# < 5$. It is connected to the NA through

$$f\# = \frac{1}{2\mathrm{NA}}, \tag{2.4}$$

and gives the fastest acceptance beam the fibre can handle. To couple light efficiently into a multimode fibre, the incoming beam should be slower than the fastest acceptance beam. To couple light efficiently into a single-mode fibre, the fundamental mode needs to be matched, a situation that can be described only through wave optics. Figure 2.2 shows the focal ratio as a function of numerical aperture. The typical NA values with the corresponding $f\#$ of single-mode and multimode fibres are marked. Rays belonging to a beam under the NA of the multimode fibre will be efficiently coupled and propagated. The values for typical SMF and MMF were taken from Thorlabs, Inc. The blue shaded area marks the values for effective coupling into a multimode fibre with an NA = 0.21.
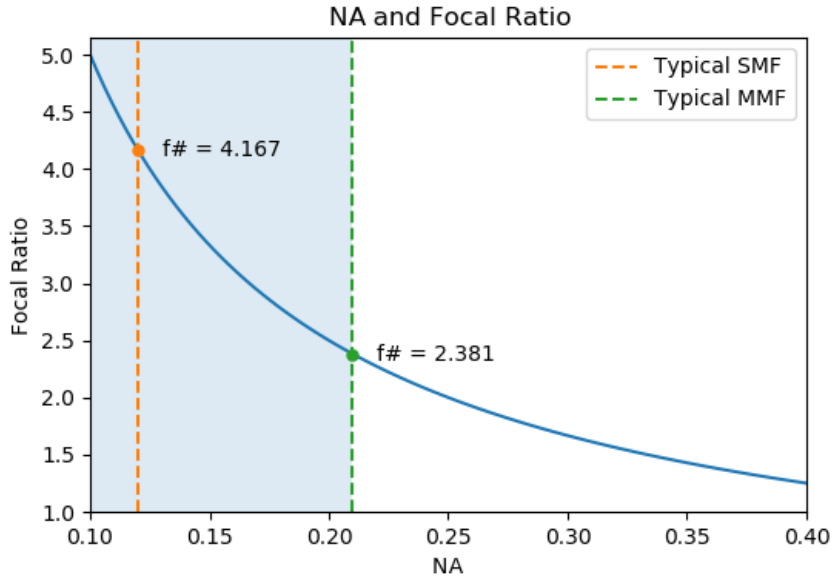
Figure 2.2: Focal ratio as a function of the numerical aperture. The NA equals 0.12 for a typical SMF and 0.21 for a typical MMF. The blue shaded area marks the values for effective coupling into a multimode fibre with an NA = 0.21

2.1.2   Wave optics

As described in Eq. 2.1, most fibres have a small index difference with $n_1 \approx n_2$. Because of this characteristic, the longitudinal components of the electric and magnetic fields are far weaker than the transverse components, which makes the guided wave approximately transverse electromagnetic (TEM) [45]. The

field for a given frequency ν can be described with an amplitude $\psi(\mathbf{r})$ and a phase $\phi(\mathbf{r})$ through the complex wave function

$$\Psi(\mathbf{r}, t) = \psi(\mathbf{r}) \exp\left[j\phi(\mathbf{r})\right] \exp\left(-j2\pi\nu t\right), \tag{2.5}$$

having the complex amplitude $\Psi(\mathbf{r}) = \psi(\mathbf{r}) \exp\left[j\phi(\mathbf{r})\right]$ with $\mathbf{r}$ describing a real function of position $\mathbf{r} = (x, y, z)$. Any complex wave must satisfy the wave equation

$$\nabla^2 \Psi(\mathbf{r}, t) - \frac{1}{c^2} \frac{\partial^2 \Psi(\mathbf{r}, t)}{\partial t^2} = 0. \tag{2.6}$$

By separating $\Psi(\mathbf{r}, t)$ into $\Psi(\mathbf{r}) \exp(j2\pi\nu t)$ and using Eq. 2.6, the Helmholtz equation is obtained as

$$\nabla^2 \Psi(\mathbf{r}) + n^2(\mathbf{r}) k_0^2 \Psi(\mathbf{r}) = 0 \tag{2.7}$$

with

$$k_0 = \frac{2\pi}{\lambda_0} \tag{2.8}$$

describing the vacuum wavenumber. The Helmholtz equation describes the electric and magnetic field, which are joined through the Maxwell Equations and must be obeyed by the two regions of the optical fibre. The solutions give a discrete set of modes that can propagate through the optical fibre, each of which has a propagation constant β_m, a characteristic field distribution $\psi_m(x, y)$ and two independent linear polarized states with the same propagation constant and the same spatial distribution. Each mode possesses an effective refractive index, $n_{eff,m}$, which is attached to the propagation constant through

$$\beta_m = \frac{2\pi}{\lambda} n_{eff,m}. \tag{2.9}$$

Each propagation constant obeys the relation $n_2 k_0 < \beta_m < n_1 k_0$. For the effective refractive index of the individual propagation modes it means $n_2 < n_{eff,m} < n_1$. Using this information, it is possible to describe a propagation mode as

$$\Psi_m = \psi_m(x, y) e^{j\beta_m z}. \tag{2.10}$$

Propagation modes are orthogonal to each other. This implies that the scalar product of two different propagation modes equals zero

$$\langle \Psi_m, \Psi_n \rangle = \int \int \psi_m \psi_n^* \exp\left(j(\beta_m - \beta_n)z\right) \partial x \partial y = 0, \text{ for } m \neq n. \tag{2.11}$$

At any distance z in the optical fibre, it is possible to use the propagation modes as a basis for linear expansion as

$$\Psi(x, y, z) = \sum_{m=0}^{M} c_m \psi_m(x, y) \exp\left(j\beta_m z\right), \tag{2.12}$$

thus calculating the spatial distribution of the optical field as a function of z. Equation 2.12 represents the **Eigenmode Expansion Method** (EEM). The factor c_m refers to the modal amplitude. The square of the absolute value of the modal amplitude, $|c_m|^2$, represents the amount of power each specific mode propagates. Due to the power conservation law, the sum of the square of each amplitude is equal to the (normalized) power of the system,

$$\sum_{m=0}^{M} |c_m|^2 = 1. \tag{2.13}$$

The optical intensity I at the end of the fibre is equivalent to the intensity of the near-field distribution. It can be calculated through the absolute square of the field $\Psi(x, y, z = L)$ and takes the form

$$I = |\Psi(x, y, L)|^2 = \left| \sum_{m=0}^{M} c_m \psi_m(x, y) \exp\left(j\beta_m L\right) \right|^2. \tag{2.14}$$

To approximate the number of modes in a step-index fibre, it is useful to use the dimensionless normalized frequency parameter

$$V = 2\pi \frac{r}{\lambda} \sqrt{n_1^2 - n_2^2}, \tag{2.15}$$

also known as the V-Number. The parameter r is for the radius of the fibre, $n_{1,2}$ the different refractive indexes and λ the free-space wavelength. The approximation for the number of modes in fibres is done through

$$M \approx \frac{V^2}{2}, \tag{2.16}$$

with M being the number of modes a fibre can hold. When $V < 2.405$, only the fundamental mode in its two polarization states propagates through the optical fibre; in this case, the fibre is called a single-mode fibre (SMF). One way of creating a SMF is to make the core sufficiently small. For example, if the propagation wavelength is between $1.2\mu m$ and $1.6\mu m$ and the fibre has a NA $= 0.12$, the core needs a diameter of $\approx 9\mu m$ for the fibre to have the single-mode condition. Fibres that carry higher-order modes are known as multimode fibres (MMF). As Eq. 2.15 shows, the V-Number depends on the geometry and refractive index of the fibres, as well as the free-space wavelength. Typical MMF fibres for astronomy vary from $\sim 50\mu m$ up to $300\mu m$ [41]. Figure 2.3 shows the number of modes a specific fibre can hold as a function of the wavelength λ. The calculation is done for a fibre having diameter of $50\mu m$ and a difference in refractive index $\Delta = 0.0102$ (see Eq. 2.1), which translates to the NA $= 0.21$. The number of modes is calculated for the wavelength range from $350nm$ to $2000nm$.
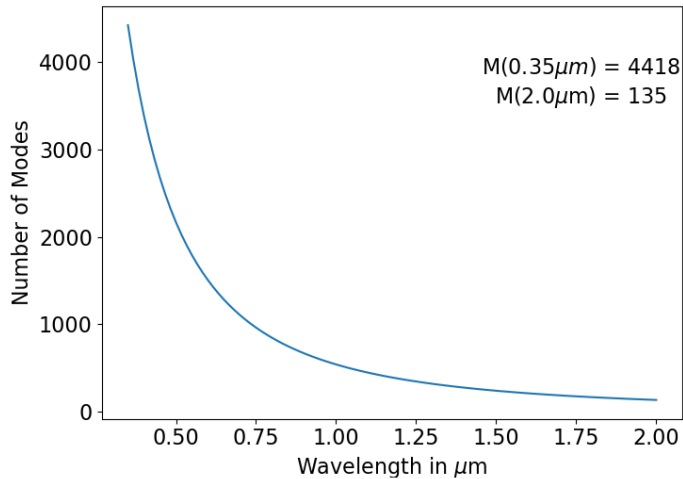
Figure 2.3: The number of supported modes as a function of increasing wavelength. The x-axis ranges from $0.35\mu m$ to $2.0\mu m$. The simulated fibre has a $50\mu m$ core diameter and a difference in refractive index $\Delta = 0.0102$ (see Eq. 2.1), which translates to the NA $= 0.21$.

2.1.3 Modal interference

From the linear characteristic of the wave equation (see Eq. 2.6) follows the superposition of two or more optical waves. It states that the total wave function is the sum of all individual wave functions [45]. The superposition principle for monochromatic waves carries over to the complex amplitude due to the linearity of the Helmholtz Equation (see Eq. 2.7). The superposition of propagation modes follows the same principle. Having two propagation modes ψ_1 and ψ_2 with respective intensities $I_1 = |\psi_1|^2$ and $I_2 = |\psi_2|^2$, the result would be

$$I = |\psi|^2 = |\psi_1 + \psi_2|^2 = |\psi_1|^2 + |\psi_2|^2 + \psi_1^*\psi_2 + \psi_1\psi_2^*. \tag{2.17}$$

Expressing the modal field as a function of the intensity, $\psi = \sqrt{I}\exp(j\varphi)$, allows to rewrite Eq. 2.17 as

$$I = I_1 + I_2 + 2\sqrt{I_1 I_2}\cos\varphi, \tag{2.18}$$

with the term that describes the phase difference $\varphi = \varphi_2 - \varphi_1$. Equation 2.18 is called the interference equation, and it is accompanied by a spatial redistribution of the optical intensity without a violation of

power conservation [45]. If the values of the phase difference φ are distributed equally between 0 and 2π, the term $\cos \varphi$ gets averaged to 0. This would be the case for random fluctuations of the terms φ_1 and φ_2.

A stationary interference pattern is possible through coherent light. Coherent light is said to be deterministic, meaning the dependence of the wave function on time and position is perfectly periodic and predictable. On the other hand, completely random light can be described best through statistical methods [45]. To get the intensity of a random function of time and position, the average intensity is used,

$$I(\mathbf{r}, t) = \langle |\Psi(\mathbf{r}, t)|^2 \rangle. \tag{2.19}$$

The average intensity can be time independent, which makes the wave statistically stationary. Applied to Eq. 2.19 it means

$$I(\mathbf{r}) = \lim_{T \to \infty} \frac{1}{2T} \int_{-T}^{T} |\Psi(\mathbf{r}, t)|^2 \partial t. \tag{2.20}$$

The temporal coherence function of a stationary complex random function can be obtained with the autocorrelation function

$$G(\tau) = \langle \Psi^*(t) \Psi(t + \tau) \rangle. \tag{2.21}$$

For $\tau = 0$, Eq. 2.21 equals Eq. 2.20. The normalized autocorrelation function is described as

$$g(\tau) = \frac{G(\tau)}{G(0)} = \frac{\langle \Psi^*(t) \Psi(t + \tau) \rangle}{\langle \Psi^*(t) \Psi(t) \rangle}, \tag{2.22}$$

and it is the complex degree of temporal coherence. The coherence time τ_c describes the period of time in which fluctuations of a random wave are strongly correlated. It can be calculated through

$$\tau_c = \int_{-\infty}^{\infty} |g(\tau)|^2 \, d\tau. \tag{2.23}$$

If $|g(\tau)| = 1$, which is the case for monochromatic light, the coherence time is infinite. The coherence length is defined by

$$l_c = c\tau_c, \tag{2.24}$$

with c being the speed of light. The mutual intensity is the mutual coherence function at $\tau = 0$ and can be described as

$$G(\mathbf{r}_1, \mathbf{r}_2) = \langle \Psi^*(\mathbf{r}_1, t), \Psi(\mathbf{r}_2, t) \rangle. \tag{2.25}$$

Using the mutual intensity, Equation 2.22 turns into the normalized mutual intensity

$$g(\mathbf{r}_1, \mathbf{r}_2) = \frac{G(\mathbf{r}_1, \mathbf{r}_2)}{\sqrt{I(\mathbf{r}_1) I(\mathbf{r}_2)}}. \tag{2.26}$$

Equation 2.26 measures the degree of spatial coherence. If $g(\mathbf{r}_1, \mathbf{r}_2) \approx 0$, the light is said to be incoherent [45]. It is possible to write the interference equation (see Eq. 2.18) as

$$I = I_1 + I_2 + 2\sqrt{I_1 I_2} |g_{12}| \cos \varphi \tag{2.27}$$

and thus describing the case of complete correlation with $|g_{12}| = 1$ allowing interference; and the case of two uncorrelated waves with $|g_{12}| = 0$ describing the incoherent case $I = I_1 + I_2$.

2.1.4   Far field description

In this work, the far-field description is done using the Fraunhofer approximation, which comes from Fourier optics and uses harmonic analysis to describe the propagation of light. If the complex amplitude $f(x, y)$ at $z = 0$ plane is at sufficient distance $z = d$ from $g(x, y)$ at the output plane, only the wave possessing the angles $\theta \approx x/d$ and $\theta \approx y/d$ with the optical axis contribute to the complex amplitude

$F(\nu_x, \nu_y)$ with $\nu_x = x/\lambda d$ and $\nu_y = y/\lambda d$ [45]. The free-space propagation can be seen as a Fourier transform using

$$g(x,y) \approx h_0 F\left(\frac{x}{\lambda d}, \frac{y}{\lambda d}\right) \tag{2.28}$$

with $\mathcal{F}\{f(x,y)\} = F(\nu_x, \nu_y)$ and $h_0 = (j/\lambda d)\exp(-jkd)$. Contributions of all other waves cancel out as a result of destructive interference. The angular distribution at the output plane can be obtained by using the approximations of $\theta_x \approx x/d \approx \lambda \nu_x$ and $\theta_y \approx y/d \approx \lambda \nu_y$. Figure 2.4 illustrates the situation. For the Fraunhofer approximation to be valid, $f(x,y)$ at the input plane must be confined to a circle of radius b with $b^2/\lambda d \ll 1$ and at points in the output plane within a circle of radius a with $a^2/\lambda d \ll 1$.
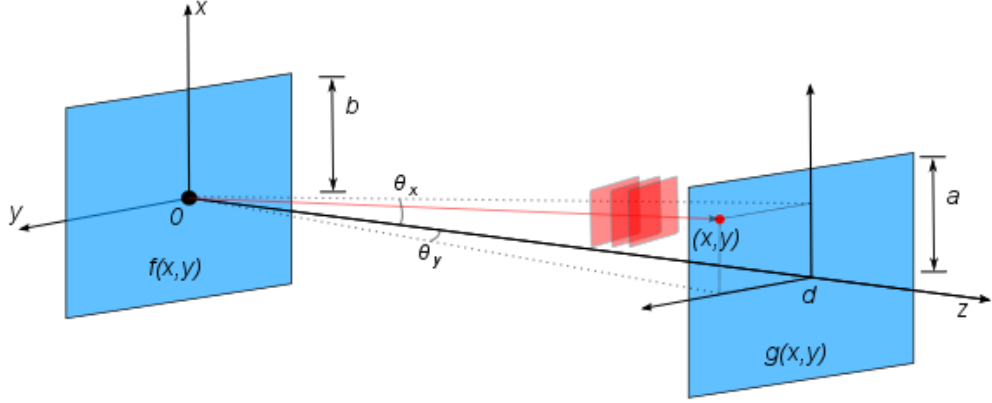
Figure 2.4: When distance d is sufficiently long, the complex amplitude at point $g(x,y)$ is proportional to the Fourier transform of $f(x,y)$ [45].

2.2   Optical Throughput

The optical throughput or etendue E expresses how much a beam of light spreads out in an area S and solid angle Ω [30] [49]. Using the refractive index n, the etendue can be expressed as

$$E = n^2 S\Omega. \tag{2.29}$$

For a light cone having a half angle α orthogonal to the surface S, Eq. 2.29 can be rewritten as

$$E = n^2 S \int_0^\alpha \cos\theta \partial\Omega = n^2 \pi S \sin^2\alpha. \tag{2.30}$$

The radiant flux Φ carried by a beam is described as $\Phi = LS\Omega$, were L represents the radiance in $[W \cdot sr^{-1} \cdot m^{-2}]$. As a beam propagates through an optical system, the etendue never decreases. This is called the $S\Omega$ conservation [30]. If there is no loss in the optical path, the total flux emitted by the source $\Phi = LS\Omega$ equals the total flux collected at the output $\Phi' = L'S'\Omega'$. Figure 2.5 shows the schematic representation of the $S\Omega$ conservation.

Figure 2.5: Illustration of etendue conservation. $S\Omega = S'\Omega'$ for any optical system [30].

The flux conservation, which is the first principal of thermodynamics, states

$$LS\Omega = L'S'\Omega'. \tag{2.31}$$

The second principle of thermodynamics states non-decreasing entropy, which means that the radiance of an optical system obeys $L'/n'^2 < L/n^2$. The etendue of a fibre can be calculated using the acceptance solid angle $\Omega = \pi \sin^2 \theta_{max}$ and acceptance area $S = \pi d^2/4$, with $d = 2r$. Taking into account Eq. 2.2 and Eq. 2.3, it means
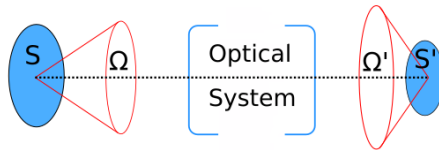
$$E_{fibre} = \pi^2 r^2 \mathrm{NA}^2. \tag{2.32}$$

For the means of characterizing the focal ratio degradation, it helps to express the etendue as a function of the focal ratio as

$$E_{fibre} = \pi^2 r^2 \frac{1}{(2f\#)^2}. \tag{2.33}$$

2.3 Transmission Characteristics in Optical Fibres

Most fibres are made of fused silica glass (SiO_2) of high chemical purity since it has good transmission from the visible spectrum up to the NIR wavelengths. Usually, the refractive index ranges from 1.44 to 1.46 and can be altered by adding low concentrations of doping materials like germanium and phosphorus for increasing, or fluorine for decreasing it [44]. The index difference Δn typically has values between 0.001 and 0.02 [45].

Absorption and scattering make up the intrinsic attenuation and losses in fused silica optical fibres. Rayleigh scattering affects strongly shorter wavelengths and arises from density and composition fluctuations in the fibre. The λ^{-4} behavior can be seen in the increased attenuation for the blue and near UV region [34]. Trace impurities are the cause of absorption. The Hydroxyl ion (OH) is a well-known impurity with a vibration absorption at $2.73\mu m$ and significant overtones at $1.37\mu m$, $0.95\mu m$ and $0.72\mu m$ [36]. The manipulation of the OH percentage in the fibre allows tuning the transmission window. High purity fibres with substantial OH contamination, usually denominated as wet fibres, are the best choice to use in UV and blue light. In the red and near IR, a trade-off in hydroxyl content is required to limit the strength of the absorption bands. The hydroxyl content becomes a function of the wavelength of interest [34]. Besides impurities, fused silica possesses intrinsic absorption originating from charge transfer bands in the UV and vibration bands in the IR. Atomic defect absorption may arise if intense radiation, large temperature variation, or hydrogen permeation occurs. Nevertheless, this plays a minor role in optical fibres used in astronomy [34]. Figures 2.6 and 2.7 show typical transmission plots for high OH and low OH fibres. The information for the transmission plots was taken from Polymicro, now part of Molex, LLC in the United States of America.

Fibres used for NIR wavelengths

Due to atmospheric filtering, three bands of near-infrared (NIR) signals can be obtained in ground telescopes. These are denominated as the J ($1.1\mu m$–$1.4\mu m$), H ($1.5\mu m$–$1.8\mu m$) and K ($2.0\mu m$–$2.4\mu m$) bands. As can be observed from Fig. 2.7, fused silica exhibits high intrinsic losses above $2.0\mu m$ and it is why other solutions besides silica are used for longer wavelengths.

Infrared fibres are fibres that transmit radiation with a wavelength greater than $2.0\mu m$ [50]. Since the market for IR fibers is limited primarily to non-telecommunication applications, there has been a slow development compared to silica fibers [51]. Poor mechanical stability and higher cost are associated with these fibres. This may imply why the end-user might desist using IR fibres and conform to not working at longer wavelengths. Not only the fibre system tends to be a challenge, but also factors involving increasing thermal background, cooling at cryogenic temperatures, and NIR equipment cost tend to complicate the design of instruments going beyond $2.0\mu m$.
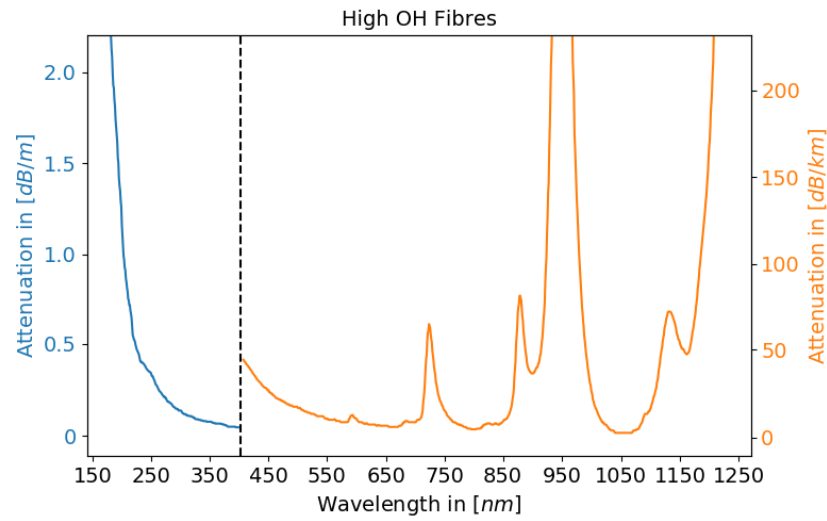
Figure 2.6: Transmition plot of Molex-Polymicro high OH fibres.
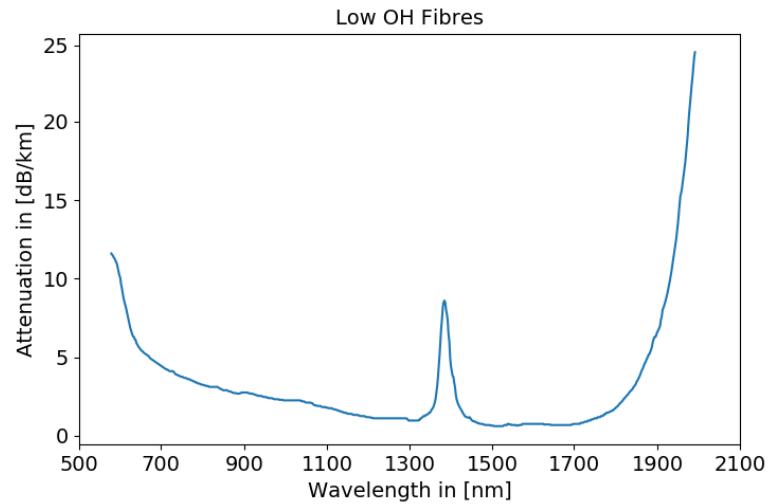
Figure 2.7: Transmition plot of Molex-Polymicro low OH fibres.

Table 2.1 shows the three main categories of IR fibres and the corresponding subcategories. Figure 2.8 shows examples of transmission plots for three different IR fibres as can be found in Harrington (2001) [50].

Main	Subcategory	Example
Glas	Heavy metal fluoride	ZBLAN
	Germanate	GeO_2-PbO
	Chalcogenide	As_2S_3 and AsGeTeSe
Crystal	Polycrystalline	AgBrCl
	Single crystal	Sapphire
Hollow waveguide	Metal/dielectric film	Hollow glass waveguide

Table 2.1: Categories of IR fibres with examples [50]
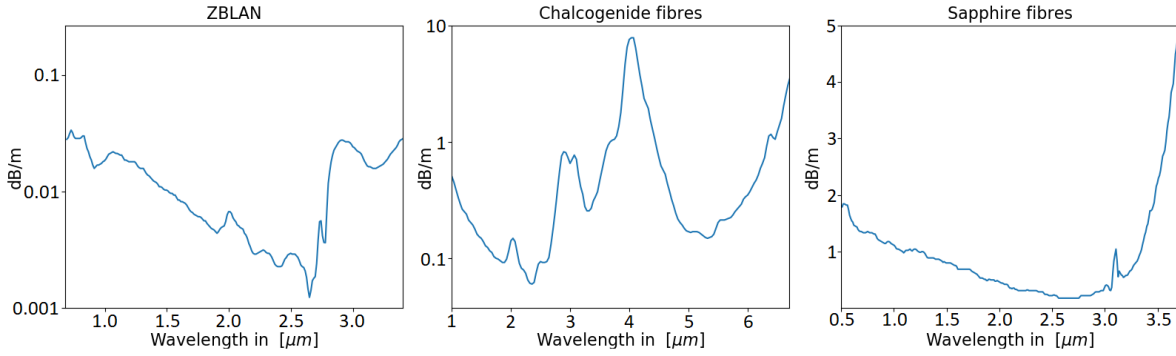
Figure 2.8: Example of transmission plots for different IR fibres [50].

2.4 Multimode Effects Relevant for Astronomical Spectroscopy

2.4.1 Focal ratio degradation

As explained in Sec. 2.2, the etendue of a beam traveling through an optical system never decreases, it can only increase and translates into the loss of throughput. Fibres, unfortunately, do not conserve the etendue. The focal ratio at the output of the fibre tends to be smaller than at the input, indicating a spread in the solid angle. This effect is known as focal ratio degradation (FRD) and translates directly into losses in a fibre-fed instrument. Figure 2.9 shows the basic principle of FRD with an illustration of an optical fibre undergoing a spread in solid angle with $\phi_{in} < \phi_{out}$ and a typical FRD plot with the output focal ratio as a function of the input focal ratio.
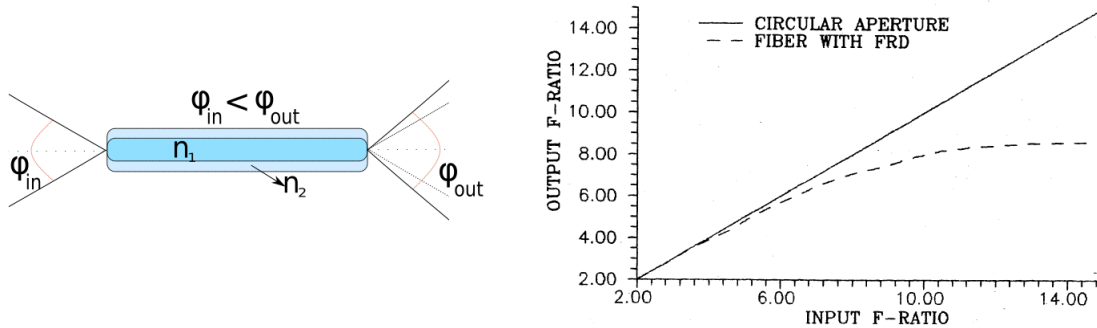
Figure 2.9: Basic principle of FRD. The focal ratio is smaller at the output than at the input, meaning a spread in solid angle. The illustration shows a fibre having $\phi_{in} < \phi_{out}$, and the plot shows a typical FRD plot with $f\#_{in}$ as the x-axis and $f\#_{out}$ as the y-axis. This plot was taken from Ramsey (1988) [35].

Gloge (1972) [52] described the broadening of the angular distribution at the output of the fibre through one differential equation that accounts for the exchange of energy between the modes caused by random irregularities in the fibre. When energy is transferred to higher-order modes, beam broadening follows from $\theta_{m+1} > \theta_m$, with θ_m being the angular distribution of mode m. Using a simplified model that assumes coupling between the neighboring modes only and transitioning from discrete modes to a continuum, the variation of power ∂P along a guide increment ∂z can be described as

$$\frac{\partial P}{\partial z} = -\alpha(\theta)P + (\Delta\theta)^2 \frac{\partial}{\partial \theta}\left[d(\theta)\frac{\partial P}{\partial \theta}\right], \tag{2.34}$$

expressing a functional dependence of θ. The factor $\alpha(\theta)$ comprises loss and can be expanded into

$$\alpha(\theta) = \alpha_o + A\theta^2 + ... \tag{2.35}$$

with α_o being a common loss to all modes that can be accounted for by multiplying the final solution by $\exp(-\alpha_o z)$. The factor $A\theta^2$ represents the loss caused at the core-cladding interface and shows that the power density at the interface increases quadratically with θ. The other higher-order terms are not taken into account. The factor $d(\theta)$ is the coupling coefficient and can be expanded with the corresponding zero-order term being essential for describing coupling as a diffusion process. It can be described as $d(\theta) = d_o$ or $D = (\Delta\theta)^2 d_o$. Solving for D in Eq. 2.34 and having $P = Qe^{-\gamma z}$, delivers the equation for the diffusion parameter in an optical fibre as

$$\frac{D}{\theta}\frac{\partial}{\partial\theta}\left(\theta\frac{\partial Q}{\partial\theta}\right) = (A\theta^2 - \gamma)Q. \tag{2.36}$$

Geometric defects (irregularities) on a scale comparable to the fibre core diameter are denominated as microbends. In the early '70s, there was a substantial amount of defects when creating optical fibres, making the fibres differ greatly from perfectly cylindrical waveguides and strengthening modal diffusion as a function of the length of the fibre. Gloge stated that the coupling process was, among other factors, a function of the length of the fibre. Nowadays, fibre manufacturing techniques allow for very few intrinsic defects over very long lengths of fibre [53], making the dependence on length on the order of magnitudes fewer than before.

The term FRD was introduced in the late '70s when fibres started being used in Astronomy [30]. Ramsey (1988) [35] demonstrated that the microbendings are crucial causes of FRD adding that the treatment of the fibre when e.g. polishing or cleaving, can cause a tremendous amount of FRD if not done correctly. He also found that the best f-ratios to feed a typical step-index fibre were from f/3.0 to about f/7.0, depending on the fibre diameter.

As stated in Heacox (1992) [34], macrobendings also induce FRD. Since fibres have a relatively small core, a substantial amount of curvature is allowed, but the stress induced in the curvatures may produce microbendings. He also points out the importance of fibre mounts since excess stress induces substantial amounts of FRD. Avila (1998) [38] points out the fact that FRD measurements are sensitive to various factors, but the most relevant are: micro- & macrobendings, alignment, perpendicularity between the fibre surface and fibre axis, polishing errors, and stability of the light source and movable mechanical parts. The sensitivity of FRD on so many factors indicates why many authors do not obtain reproducible results.

In the work of Schmoll et al.(2003) [54] a large statistical sample of individual fibres was measured concerning FRD properties. It was found that immersion coupling on average improves FRD, augmenting the reproducibility of results. It was observed that the surface perturbations introduced e.g. by the fibre termination process were healed out under immersion. There was no wavelength dependency found between the 400nm and 700nm range. There was also no wavelength dependency found by Crause et al. (2008) [55] in the same range and the correlation of termination and polishing to the increase of FRD was demonstrated once again.

In Haynes et al. (2011) [53], three main phenomena were attributed to originating FRD: scattering, diffraction, and modal diffusion. Scattering is caused by procedures that introduce subsurface damage and surface roughness, such as cleaving, lapping, and polishing. Contributing to modal diffusion are Rayleigh scattering, Mie scattering, and micro-& macrobending. The far-field pattern of the parallel laser beam method (see Sec. 2.4.2) was used to demonstrate that a Lorentz profile could be fitted best to the scattering characteristic of the fibre end having different surface roughness and that diffraction and modal diffusion are characterized by a Gaussian component. Together the outcome represents a Voigt profile, in which the FWHM of the profile can be used as a tool for characterizing FRD (see Sec. 2.4.2).

Commercially available software do not tend to address effects like FRD in multimode fibres. In the work of Allington-Smith et al. (2012) [39], FRD was simulated using a phase-tracking ray-tracing method implemented in MathCad. It is based on Gloge's model (see Eq. 2.34) and represents a portion of the fibre with scattering centers to account for the deformations and irregularities a fibre may be subjected to. The scattering centers introduce perturbations in the ray path, which scatter the light into higher and lower order modes. In the context of the ray model, into larger or smaller propagation angles. Although it is possible to reproduce FRD, there was no natural link between Gloge's diffusion parameter d_o and the

parameter $\Delta\Theta_F$ that introduces perturbations to the ray path. The model was subsequently calibrated using actual measurements to obtain realistic amounts of FRD. Since the total path length of each ray is recorded, the effects of coherence could be simulated to some extent, but not completely, reducing the accuracy for thin fibres or fibres where the amount of supported modes is small.

Simulating FRD for its better understanding remains an issue for fibre-based astronomical systems. Since so many external parameters influence in degrading the focal ratio, it is crucial to understand its intrinsic origin through the multimode propagation of light in optical fibres. Chapter 3 explains the model created in this work and how it helps improve the understanding of FRD for modern and future instruments.

In the following section, both of the typical characterization methods of FRD will be explained: the parallel laser beam method and the light cone method.

2.4.2   Characterization methods of FRD

Parallel laser beam method

When collimated light is introduced to a fibre under a specific input angle α_{in}, with $\alpha_{in} < \alpha_{max}$ (see Eq. 2.2), the far-field at the end of the optical fibre creates a ring of finite width $\Delta\theta$ that spreads under the angle $\alpha_{out} = \alpha_{in}$ [39] [53] [52] [37] [56]. As described in Gloge (1972) [52], each input angle α_{in} can relate to a specific set of propagation modes, meaning that the far-field angular distribution directly represents the modal power distribution. If perturbations occur to a specific modal power distribution, $\Delta\theta$ experiences broadening equivalent to an increase of FRD in the system. Figure 2.10 shows a simplified sketch of the ring formation in the far-field as a function of the input angle α_{in}.
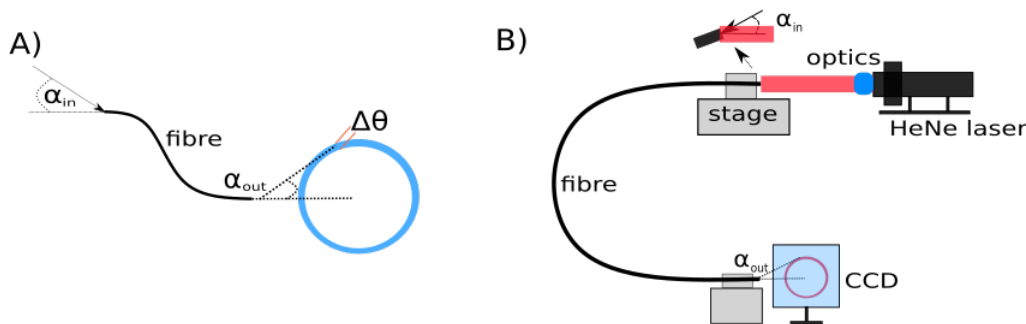
Figure 2.10: A) Simplified sketch of ring formation in the far-field as a function of the input angle α_{in}. B) Possible experimental setup for using the parallel laser beam method [53].

In practice, the broadening of $\Delta\theta$ is highly sensitive to small changes in the system and therefore can be used as a rapid diagnostic technique [53]. A possibility to implement this technique is using a laser (typically a HeNe laser) as the light source. The laser beam can be expanded and collimated with appropriate optics if there is the need for it. Through a x-y-z-θ stage the input in the fibre can be manipulated, obtaining any intended input angle. At the fibre end, the far-field distribution can be re-imaged or recorded directly to a CCD camera for proper evaluation. Figure 2.10 shows a possible experimental setup. In this setup, the far-field is recorded directly to a CCD.

The Voigt function

Through measurements on different fibre end-face surface roughness structures, it was acknowledged in Haynes et al. (2011) [53] that the scattering profiles were fitted best using a Lorentzian profile. As thor-

oughly explained in Gloge (1972) [52], modal diffusion follows a Gaussian distribution. Similarly, circular aperture diffraction can be approximated using a Gaussian distribution. Since the three phenomena attributed to originating FRD can be described through a Gauss or a Lorentz profile, the Voigt function seems like a perfect tool for examining the FRD a fibre might exhibit. This comes from the fact that the Voigt function is a convolution of a Gauss profile and a Lorentz profile and therefore can be used to measure the amount of scattering and the amount of modal diffusion that is involved in the broadening of $\Delta\theta$.

To apply the Voigt function, the measured ring needs to be collapsed to a 1D function. A pseudo-Voigt function $\mathcal{V}(r)$ can be used for ease of calculations, which represents a linear approximation that provides an analytical integrable combination of Gaussian and Lorentzian functions [53]. The validity of the pseudo-Voigt function has been proven and used by many authors such as Whiting (1968) [57], Peyre and Principi (1972) [58], Kielkopf (1973) [59], Wertheim et al. (1974) [60], Titov and Haus (1997) [61], Ida et al. (2000) [62] and Liu et al. (2001) [63]. The approximation used in this Thesis is the one described in Ida et al. (2000) [62] and used in Haynes et al. (2011) [53],

$$\mathcal{V}(r) = (1 - \eta)\frac{1}{\sigma\sqrt{\pi}}\exp\left(-(r^2)/\sigma^2\right) + \eta\frac{1}{\pi}\left(\frac{\gamma}{r^2 + \gamma^2}\right). \tag{2.37}$$

The parameter η acts as a weight factor. The calculation of η is done through

$$\eta = 1.36603\left(\frac{\Gamma_L}{\Gamma_\mathcal{V}}\right) - 0.47719\left(\frac{\Gamma_L}{\Gamma_\mathcal{V}}\right)^2 + 0.11116\left(\frac{\Gamma_L}{\Gamma_\mathcal{V}}\right)^3 \tag{2.38}$$

with Γ_V = pseudo-Voigt FWHM, Γ_L = Lorentzian component, Γ_G = Gaussian component. These parameters are joined through the equation [62]

$$\Gamma_\mathcal{V} = \left(\Gamma_G^5 + 2.69269\Gamma_G^4\Gamma_L + 2.42843\Gamma_G^3\Gamma_L^2 + 4.47163\Gamma_G^2\Gamma_L^3 + 0.07842\Gamma_G\Gamma_L^4 + \Gamma_\mathcal{V}^5\right)^{1/5} \tag{2.39}$$

with $\Gamma_G = 2\sigma\sqrt{\ln 2}$ and $\Gamma_L = 2\gamma$ respectively. To obtain Γ_G of the Gaussian component, it is possible to use the sum of the standard deviation of two uncorrelated normal distributions $\sigma_z = \sqrt{\sigma_x^2 + \sigma_y^2}$. Since FWHM $= 2 \cdot \sigma_{Gauss}\sqrt{\ln 2}$, using the modal diffusion component D_{FWHM} and diffraction component A_{FWHM}, it provides

$$\Gamma_G = \sqrt{A_{FWHM}^2 + D_{FWHM}^2}. \tag{2.40}$$

Figure 2.11 shows an example of a parallel laser beam measurement using a similar experimental setup described in Fig. 2.10 and the respective Voigt fit after integrating the 2D image to a 1D distribution as a function of the radius from the center of the ring. The measured fibre had a $50\mu m$ circular core diameter with a $N.A. = 0.21$. The input angle was set to 10° using the HeNe laser wavelength of $633nm$.

The y-axis in the plot of Fig. 2.11 is logarithmic. There is a clear asymmetry in the distribution. This comes from the fact that light scattered inside the ring is in a smaller area, and after the 2π integration leads to a higher intensity. To compensate for this, a function $y(x)$ can be added to $V(r)$. A possible function $y(x)$ was found empirically by the author of this thesis and takes the form

$$y(x) = \begin{cases} \dfrac{-1}{1 - \sin(x)} \cdot C_1 + D_1, \text{ with } \dfrac{\pi}{4} < x < \dfrac{\pi}{2} & \textbf{case 1} \quad (2.41) \\[3mm] \dfrac{1}{1 - \sin(|x|)} \cdot C_2 - D_2, \text{ with } -\dfrac{\pi}{2} < x < -\dfrac{\pi}{4} & \textbf{case 2} \quad (2.42) \end{cases}$$

It is divided into **case 1**, which is used for the data points before the maximum value of the Voigt profile; and **case 2**, which is used for the data points after the maximum value of the Voigt profile. The 1D averaged data that goes from $r \in \{0, .., N\}$, with N being the total number of pixels in the 1D array,
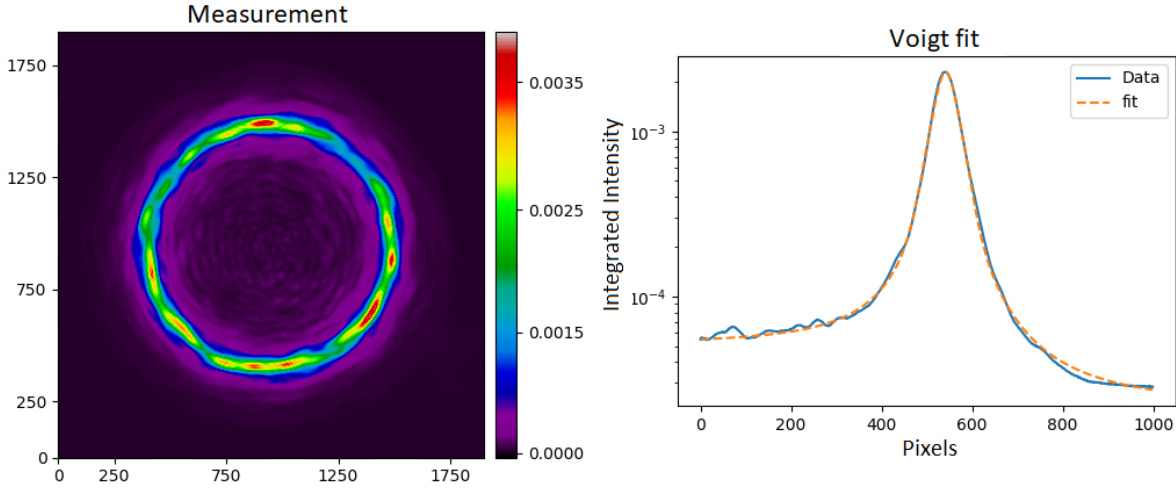
Figure 2.11: Example of a parallel laser beam measurement and the respective Voigt fit after the 2D image is integrated to a 1D distribution.

can be defined as $F(r)$. With the Voigt function defined as $\mathcal{V}(r)$ and using **case 1**, C_1 and D_1 are found through the conditions

$$
\lim_{x \to \pi/4} y(x) \stackrel{!}{=} F(0) - \mathcal{V}(0)
$$
$$
\lim_{x \to \pi/2} y(x) \stackrel{!}{=} 0
$$

(2.43)

The same procedure is applied with **case 2** and for finding C_2 and D_2. The conditions are

$$
\lim_{x \to -\pi/2} y(x) \stackrel{!}{=} 0
$$
$$
\lim_{x \to -\pi/4} y(x) \stackrel{!}{=} F(N) - \mathcal{V}(N)
$$

(2.44)

Light cone method

The light cone method consists of injecting a cone of light with a fixed focal ratio at the fibre input and afterwards recording the output cone. It is then possible to compare $f_{in}\#$ to $f_{out}\#$ and give a direct estimate on the total light loss that might be expected. In the works of Ramsey (1988) [35], Avila (1998) [38], Schmoll et al. (2003) [54], Crause et al. (2008) [55], as well as in many others, there has been an adaptation of this basic principle. Figure 2.12 shows a possible experimental setup to inject a specific f-number and record the output f-number from a tested fibre.

The source can be an LED that goes through a diffuser D to provide a homogeneous distribution for an input pinhole P. The light from P goes afterwards through the collimator C, then goes through an aperture A that sets the input f-number. The light is injected into the test fibre through the objective lens O. The output field can be recorded afterwards , e.g. with a CCD, in multiple sampling steps with a fixed step distance Δx. In the case of Fig. 2.12, $m = 7$ sampling steps are referenced but any m number of sampling steps needed can be used. The output f-number becomes a linear function of the step size Δx and the difference in spot size radius r_{spot} recorded in every step $f\#(\Delta x, r_{spot})$.

The encircled energy (EE) is used to determine the recorded spot size radius and thus the output f-number. A possible way of doing this is by first averaging the 2D image to a 1D distribution as a function of the radius $F(r)$. The 1D function is weighted by the circumference at distance r as in $F_w(r) = F(r) * 2\pi r$.
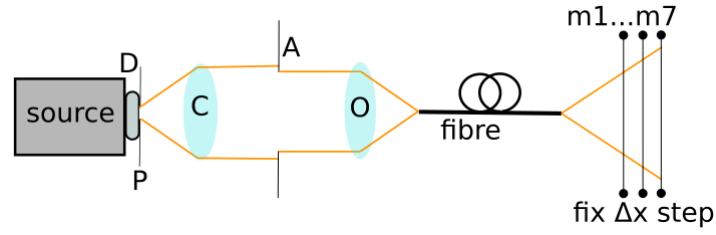
Figure 2.12: Example of experimental adaptation of the light cone method. The light source can be followed by a diffuser D, before it passes through a pinhole P. The light coming out of the pinhole is collimated by the collimator C and passes through the aperture A, where a specific $f\#$ is set. The $f\#$ is injected to the test fibre through an objective lens O. The output is recorded by a camera in steps $m1$ to $m7$ having uniform distance Δx for the calculation of the output $f\#$.

Afterwards, the 1D distribution $F_w(r)$ is normalized to the condition $\sum_{r=0}^{n} F_w(r) = 1$. Since the images are taken with a CCD, it is convenient that r is in the unit of one pixel element and at the end multiplied by the actual pixel size of the camera d_{pix}. The sum of the normalized function $F_w(r)$ gives the desired encircled energy through the condition

$$\sum_{r=0}^{n} F_w(r) \overset{!}{=} EE, \tag{2.45}$$

with $n \cdot d_{pix}$ giving the spot size recorded. Figure 2.13 shows as CCD image recorded using a similar experimental set up as shown in 2.12 and the 1D distribution $F(r)$ with different values of encircled energy. The output $f\#$ depends completely on the required EE of the system.
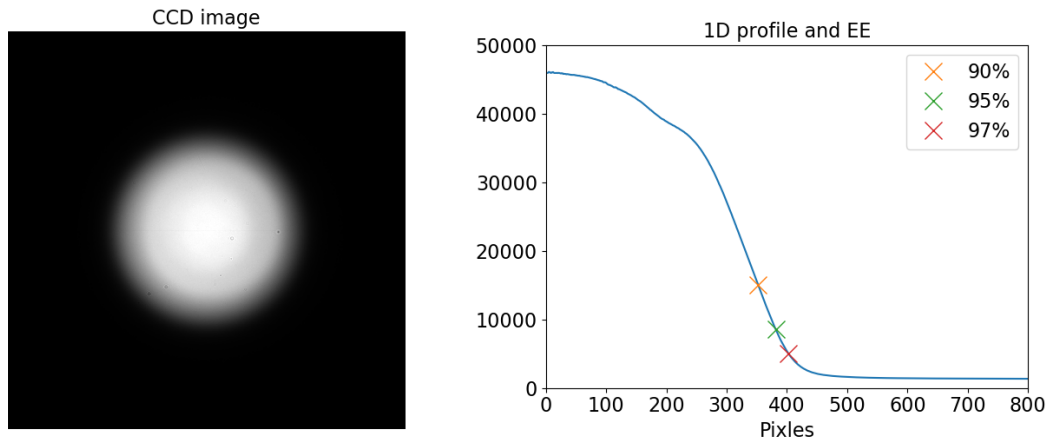
Figure 2.13: Recorded CCD image with 1D distribution and different values of encircled energy.

2.4.3 Modal noise

The broadening of a pulse inserted in an optical fibre is the result of dispersion, which can manifest itself as modal dispersion, material dispersion, waveguide dispersion, polarization-mode dispersion, and nonlinear dispersion. Relevant for this work is modal dispersion. It is the result of the difference in group velocities of the various modes [45]. The group velocity is the derivative of the angular frequency with respect to the propagation constant, $v_q = d\omega/d\beta_q$ with $q = 1, 2, ..., M$. The solution for a step-index fibre can be approximated to

$$v_q = c_1 \left(1 - \frac{q}{M}\Delta\right) \tag{2.46}$$

with $c_1 = \omega/(n_1 k_o)$ and $\Delta \approx (n_1 - n_2)/n_1$ [45]. For v_{min} and v_{max} being the smallest and largest group velocities, the pulse will spread over the distance $z = L$ to

$$\sigma_\tau = \frac{L}{2}\left(\frac{1}{v_{min}} - \frac{1}{v_{max}}\right). \tag{2.47}$$

This gives an estimate of the overall pulse duration and is denominated as the modal dispersion response. If a fibre has M modes, the pulse spreads into M pulses with a differential delay as a function of z. Due to uncontrollable imperfections, strains, and temperature fluctuations, random phase shifts occur to every mode. If a coherent source is being used, the superposition of all modes at the end of the fibre results in a speckle pattern due to modal interference (see Sec. 2.1.3). The number of speckles is proportional to the number of modes propagating in the fibre [31]. Figure 2.14 shows the example of a pulse spreading along the distance z of the fibre and the example of a speckle pattern due to interference.
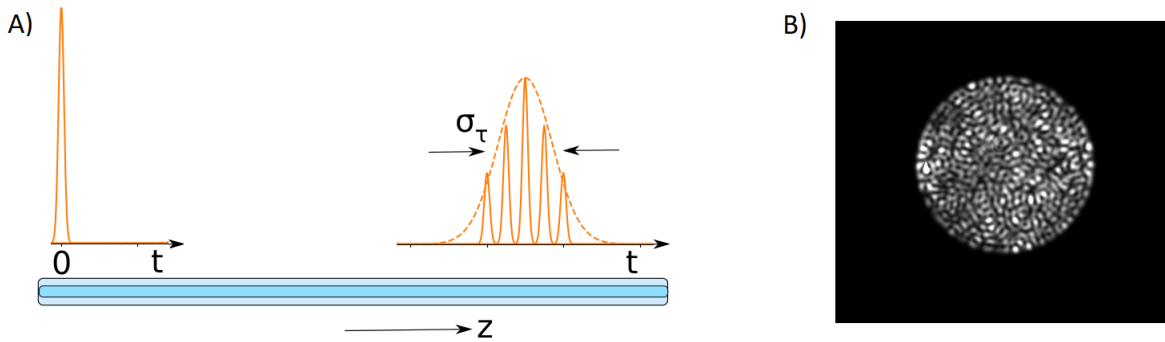

Figure 2.14: A) Pulse spreading due to modal dispersion [45]. B) Speckle pattern at the fibre end face (near-field distribution) due to modal interference.

When a changing speckle pattern exits the fibre and spatial filtering occurs (e.g. misaligned connector), the optical signal power fluctuates. Such fluctuations are called modal noise [64]. Modal noise is a phenomenon that was already identified in the late '70s in fibre optical communication links. Richard Epworth (1978) [31] explained the phenomenon of unwanted amplitude modulation of a received signal and how this modulation is extremely sensitive to slight mechanical distortions of the fibre, joints, and source. In digital transmission the sampling scheme (e.g. NRZ) may get distorted, incrementing the difficulty in reconstructing the signal at the receiver. Analog transmissions are more affected since intensity variations create heavy distortions in the transmitted signal.

Misaligned connectors play a crucial role in the creation of modal noise. Since the position of the individual speckles is extremely sensitive to small fibre distortion, slight different bendings produce variations in both near- and far-field. If there is an axial misalignment, only a portion of the speckles of the near-field will couple into the next fibre. In a longitudinal misalignment, there may be a combination of both near- and far-field effects. Longitudinal misalignments tend to produce more modal noise than axial misalignments [31]. The coupled power is highly sensitive to any changes in the speckle pattern, in other words, to anything that introduces random phase shifts to the propagation modes. Figure 2.15 illustrates axial and longitudinal misalignment.

Figure 2.15: Example of axial and longitudinal misalignment.

The coherence of the source plays an important role in the formation of modal noise. If two modes are launched and both the path length and dispersion create enough differential delay greater than the

coherence time τ_c (see Eq. 2.23), no interference between the two modes would take place. Petermann (1980) [65] did a rigorous evaluation involving mode coupling analysis to determine noise and distortions that fibre connectors introduce to optical links with graded-index optical fibres. For decreased coherence of the source, there will be fewer fluctuations in the coupling efficiency and less sensitivity to misalignments. Additionally, fibres with a greater $V-$number (see Eq. 2.15) should have less variance in the coupling efficiency. He concluded that for analog modulations, no coherent source with a multimode fibre should be used since higher-order harmonic distortions become unacceptably high [65].

Rawson and Goodmann (1983) [64] applied speckle theory to describe modal noise in step-index optical fibres. Through applying a gamma probability density function to the integrated intensity measured at a detector as a function of M and the ratio of the detector area to the fibre core area, $\rho^2 = A_d/A_f$, they were able to calculate signal-to-noise ratio (SNR) of a system with

$$SNR = \rho\sqrt{\frac{M+1}{1-\rho^2}}. \tag{2.48}$$

The modal power distribution (MPD) is a way of graphically showing how much power carries an excited mode. It is equivalent to the representation of the modal amplitude square in Eq. 2.12 for all propagation modes in a system. Wood (1984) [66] analyzed the MPD to check the preceding assumption that power was distributed equally among all modes after coupling to a laser source. He was able to find out that the coupling conditions dictate which modes will be excited. If coupling without any tilt or axial displacement, mostly all power travels in a few guided modes. As will be shown in Chapter 3.3, by introducing tilt and/or offset, it is possible to increase the number of excited modes in a multimode fibre. Through the use of the formulas found in Petermann (1980), the SNR was calculated by Wood (1984) for cases assuming an equally distributed MPD compared to realistic highly nonuniform MPD. The results demonstrated that the nonuniform MPD cases showed better SNR compared to equally distributed MPD. It follows that the magnitude of speckle selective loss should be greater if every mode is equally excited. The results also showed that a simple increase in the number of excited modes does not lead to an increased SNR [66]. An explanation was that higher-order modes are more modal noise sensitive. The dependence of modal noise on mode excitation is more complex than previously thought.

It is possible to summarize the conditions for modal noise into: 1) a sufficiently narrow source spectrum; 2) spatial or angular filtering; 3) time variation of either modal or spatial filtering [31]. These conditions are given in high-resolution fibre-fed spectroscopy since: 1) the recorded spectral width may be very narrow (a resolving power $R = \lambda/\Delta\lambda_{spec} = 150000$ posses a spectral bandwidth $\Delta\lambda_{spec}$ comparable to that of a HeNe laser with $\Delta\lambda_{HeNe} \approx 0.002nm \sim \Delta\lambda_{spec}$); 2) usually angular limitation occurs for the light injection and vignetting-obscuration may take place in the spectrograph; 3) the fibre link moves with the telescope [32]. The effect of modal noise in astronomical spectroscopy was observed by Baudrand et al. (1998) [32] during the characterization of the high-resolution multi-aperture fibre-fed spectrograph FUEGOS for the Very Large Telescope (VLT). When the fibres where perfectly still, the signal-to-noise ratio followed the expected photon statistics, in which the noise increases with the square root of photons detected as $\sqrt{N}$ [33]. But when the fibre bundle was in stress or motion, a significant degradation of the photometric performance was measured, deviating strongly from the limit set by photon noise [32]. The modal noise element was described as $S/\sqrt{n}$, with S representing the signal and n the number of propagation modes. Figure 2.16 shows the SNR degradation observed by Baudrand et al. (1998). Both the expected photon statistic SNR and the degraded SNR are illustrated.

Baudrand and Walker (2001) [67] analyzed the effects of injection perturbation, spatial filtering, fibre length, focal ratio, and wavelength on modal noise for high-resolution spectra experimentally and proposed a solution for mitigating modal noise. Any change in the position or light injection of the fibre induces noise. When comparing modal noise in a $7m$ and a $70m$ fibre, no difference was found. For the focal ratios of $F/4$ and $F/2.8$ no influence was recorded. A direct correlation between increasing wavelength and decreasing of the SNR was measured in the range of $500nm$ to $900nm$, reaffirming the influence of wavelength on modal noise. The authors also found that a continuous agitation of the fibre smooths out the modal pattern. After several trials, the best results were achieved with relatively high frequency
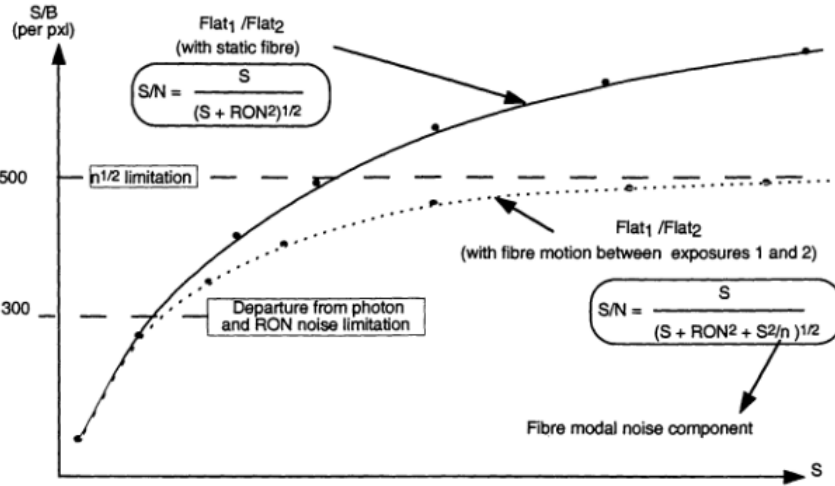
Figure 2.16: SNR degradation observed by Baudrand et al. (1998). SNR versus signal of a series of flat spectra (Flat1) divided by another flat spectrum of very high SNR (Flat 2) [32]. The expected photon statistic SNR with the static fibre and the degraded SNR due to fibre motion are illustrated.

(30Hz), low amplitude (1mm), and agitation applied near the fibre exit [67].

Corbett and Allington-Smith (2006) [68] verified the fact that Eq. 2.48 given by Rawson et al. [64] delivers better results to actual SNR in modal noise measurements. Investigation on the changes in MPD concluded that the power distributed among the modes depends on the characteristics of the input field, and a good match between ray optical theory and MPD was proven. No further assessment on the dependence of the SNR as a function of the MPD could be made. There is the possibility that modal noise could decrease significantly if only specific modes are excited. The question, how a differing slit width reacts to arbitrary MPD, could not be answered.

Lemke et al. (2010) [69] adds the visibility factor v to Eq. 2.48. The visibility factor accounts for partial incoherence of the source. The visibility factor was originally derived by Kanada and Aoyama (1983) [70] as a function of the fibre bandwidth and the optical source linewidth. The parameter is defined between 0 and 1 ($0 \leq v \leq 1$), and it is calculated through the autocorrelation function at the fibre output. The v part is considered coherent and the $v - 1$ part incoherent. It can be described as

$$v = \left[1 + \left(\frac{f_s}{f_c}\right)^2\right]^{-1/2}, \qquad (2.49)$$

with f_c representing the $6dB$ bandwidth of the Gaussian applied to describe the ratio of the number of modes having a transmission delay t to the total number of supported modes, and f_s representing the FWHM of the Gaussian describing the autocorrelation function of the optical source [70]. To estimate f_c, the difference in the propagations constant between on-axis rays β_o and rays coupled with the maximum angle θ_{max} is calculated as [69]

$$\Delta\beta = \beta_o - \beta_o\sqrt{1 - \frac{\theta_{max}^2}{n_{core}^2}} \approx \frac{1}{2}\frac{\theta_{max}^2}{n_{core}^2}\beta_o. \qquad (2.50)$$

The time needed by a mode to travel the whole fibre length L is determined by the group velocity $v_g = (\partial k/\partial\omega)^{-1}$, and produces a time delay between the two marginal rays can be given by $\Delta t = \Delta\beta L/2\pi\nu$, which results in

$$f_c = \frac{2\pi\nu}{\Delta\beta L} = \frac{2n_{core}c}{L\theta_{max}^2}. \qquad (2.51)$$

The approximation of f_s is possible using the parameters of the spectrograph

$$f_s = \nu_1 - \nu_2 \approx \frac{\nu_c}{R} = \frac{c}{R\lambda_c}, \tag{2.52}$$

with λ_c being the central wavelength. Equation 2.49 becomes

$$v = \left[1 + \left(\frac{L\theta_{max}^2}{2n_{core}R\lambda}\right)^2\right]^{1/2}, \tag{2.53}$$

and the signal-to-noise equation of Rawson et al. (1983) [64] can be expressed as

$$SNR = \frac{\rho^2}{v}\sqrt{\frac{M+1}{1-\rho^2}}. \tag{2.54}$$

The visibility is a measure of the coherence and contrast of speckle pattern. As described in Eq. 2.54, if the visibility increases, the SNR decreases. Experimental measurements were conducted on circular and square fibres to assert the equations and test the agitation method to mitigate modal noise. In this case, a frequency of 100Hz was used for the best results. Opposite to what Eq. 2.53 suggests, modal noise did not show a dependence on length. This result was previously demonstrated by Baudrand et al. (2001) [67]. There was no significant difference measured in the SNR between the square fibre and conventional circular fibre, and results deviated greatly from the theoretical prediction for $\rho \approx 1$.

2.4.4 Characterizing modal noise

As described above, it can be fairly complicated to calculate correctly the theoretical SNR and compare it to experimental measurements. Since no spectrograph was used in this work, it was not possible to test Equations 2.48 to 2.54 experimentally (no values for ρ nor for v). To characterize mechanical scramblers, McCoy et al. (2012) [71] measured the far-field output intensity distribution of fibres and applied the power spectral density method. Since the method only needs the output intensity field, the PSD approach seemed more appropriate for this work.

The power spectral density (PSD) of a field is a mathematical tool that disaggregates the intensity of the field into the individual contributions from the different spatial frequencies. Mathematically, it is the Fourier transform of the autocorrelation function of the field, which contains power across a range of wavevectors [72]. It is typically used for characterizing rough surfaces. An increase in spatial frequency means smaller elements in the measured intensity field. It applies to a higher number of speckles and a greater rate of intensity fluctuations inside the field.

A way to obtain a PSD is by first calculating the Fast Fourier Transform (FFT) of the field. Afterwards, the power spectral density equals the square of the absolute value. This is valid since the correlation of two complex functions is defined as [45]

$$f(t) = \int_{-\infty}^{\infty} f^*(\tau)f_2(t+\tau)d\tau. \tag{2.55}$$

If $F(\nu) = \mathcal{F}(f(t))$, Equation 2.55 can be described in Fourier space as

$$F(\nu) = F_1^*(\nu)F_2(\nu) \tag{2.56}$$

In the case of $f_2(t) = f_1(t)$, Equation 2.55 is called autocorrelation [45], with $F(\nu) = |F_1(\nu)|^2$. It can be applied to two dimensional functions. If $I(x,y)$ represents the intensity of a given field $\Psi(x,y)$, the power spectral density is given through the autocorrelation of the intensity, which means

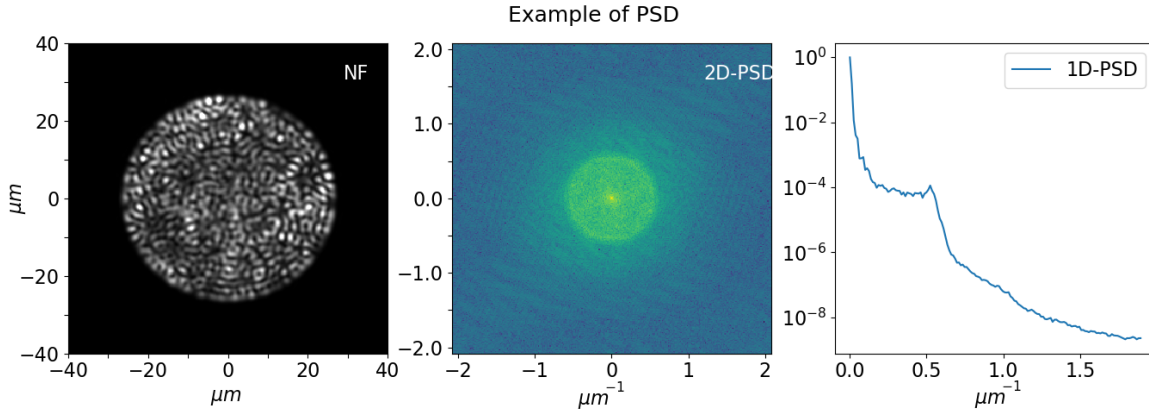$$PSD = |\mathcal{F}(I(x,y))|^2 = |I(\nu_x, \nu_y)|^2, \tag{2.57}$$

Figure 2.17: Example of the PSD of a given intensity field. The NF represents a measured near-field distribution. The 2D-PSD represents the autocorrelation of the field in the Fourier plane. The 1D-PSD is the rotationally averaged and normalized 2D-PSD.

with $I(\nu_x, \nu_y)$ representing the image after the FFT in the spatial frequency plane (ν_x, ν_y). The spatial frequency image $I(\nu_x, \nu_y)$ is rotationally averaged to produce the normalized power over spatial frequency 1D-plot. Figure 2.17 illustrates first an intensity field, then the 2D autocorrelation, and lastly the $\mathcal{I}(\nu)$ 1D-PSD of the field.

The intensity field distribution in Fig. 2.17 was measured using the parallel laser beam method, as can be seen in Fig. 2.10. The near-field was measured through an objective lens (see Sec. 4.2). The fibre had a diameter of $50\mu m$ with an N.A. of 0.21. The input angle was $\phi_{in} = 10^o$.

2.4.5   Scrambling

Step-index fibres only partially retain spatial and angular information of images that are inserted at the input end of the fibre. The characteristic that the output distribution becomes independent of the details of illumination at the input of the fibre is denominated as scrambling [73]. Since input conditions may fluctuate, it is beneficial that the output field of the optical fibre remains stable. This can guarantee a spectrograph response isolated from sources of systematic wavelength errors [34]. Slit zonal errors are a main source of systematic errors [74] that occur when there is a shift of the slit photo center due to guide fluctuations, seeing variations and optical misalignments [37]. With optimal scrambling, spectrographs can achieve the highest level of precision in radial velocity measurements [75]. This is needed for planetary detection around other stars, as well as stellar seismology [74].

The input image experiences both azimuthal scrambling and radial scrambling. The former is nearly perfect in step-index multimode fibres. The pseudo helical path of skew rays results in an intensity pattern that is always circularly symmetric [76]. Radial scrambling is not always perfect nor complete [77]. For input spot sizes substantially smaller than the fibre, the output field might experience an inhomogeneous intensity distribution that depends on the position of the input spot [73]. As described by Heacox (1986) [37], the output flux of a perfectly centered input spot will follow a 1/r distribution, with r being the radial coordinate. If the spot is off-centered, skew rays dominate, improving radial scrambling. Figure 2.18 shows an example of two near-field measurements. In both cases, the input spot was $d_i/d_f = 0.4$, with $d_i = 20\mu m$ being the diameter of the input spot and $d_f = 50\mu m$ being the diameter of the fibre. The source was a halogen lamp inserted with an $f\# = 2.5$. A complete explanation of the setup is in Sec. 4.2. In the first case, the input spot was located in the center of the fibre, while in the second case the input spot was located at the edge of the fibre. The color scale was chosen for better display of the intensity distribution.
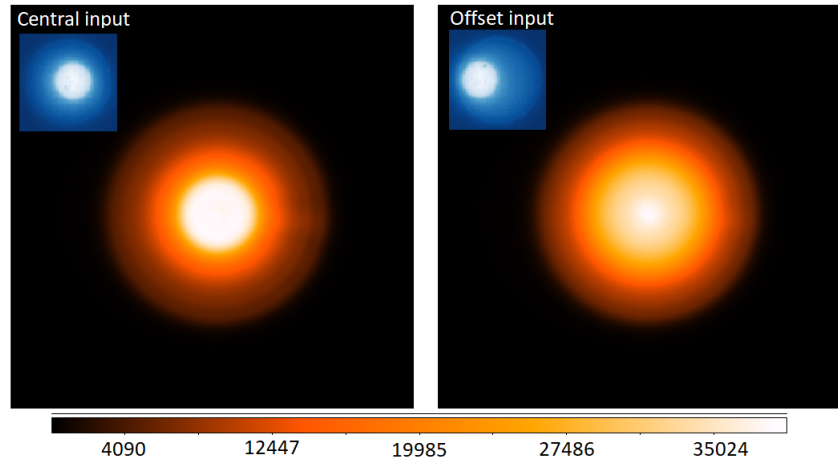
Figure 2.18: Example of incomplete scrambling when using a input spot size $d_i/d_f = 0.4$. *(left)* Near-field measurement when using a central input. *(right)* Near-field measurement when using an offset input, e.g. at the edge of the fibre.

Different techniques have been developed to improve scrambling in fibre-fed spectrographs. In the work of Hunter and Ramsey (1992) [74] a double scrambler was introduced. The idea consisted in attaching a lens to the output of the fibre guiding the light from the telescope. The lens consequently reimages the output of the first fibre into a second fibre-lens system, mixing all outgoing rays and thus increasing radial scrambling. The results showed that the angular and position sensitivity of the input field decreased substantially, thus increasing the scrambling for both near-field and far-field. A drawback of the double scrambler was the low throughput. High Fresnel losses resulted due to the high angles of incidence of rays on the scrambler lenses. Avila (1998) [38] used a similar technique to improve radial scrambling. It consisted in cutting the fibre in two and inserting a single relay lens with the fibre ends in the focal plane of the lens. Throughput losses or additional drawbacks were not specified.

Avila and Singh (2008) [78] defined the quantity of scrambling gain, G, to characterize the amount of scrambling a given system provides. As an example, the measurement of radial velocities with the highest accuracy need scrambling gains superior to 5000. It is defined as

$$G = \frac{d/D}{f/F},$$ (2.58)

with d determining the displacement of the input field in the fibre, D the diameter of the fibre, f the shift of the point spread function (PSF) on the detector (after the spectrograph), and F the FWHM of the PSF on the detector. The scrambling gain of an optical scrambler as in Hunter and Ramsey (1992) [74] was measured. Although the gain increased, angular fluctuations of the first fibre were transformed to spatial fluctuations on the second fibre. The devices showed relatively low optical efficiency. Avila, Singh, and Chazelas (2010) [42] tested different fibre geometries with different scrambling methods. Beam homogenizers and field rotators were discarded because of their low efficiencies. Mechanical fibre squeezers showed the best values between scrambling gain and losses, although squeezing the fibres translates to FRD. Circular fibres with high NA and large diameter showed great results. An increment in both NA and fibre diameter increases the number of propagation modes, a situation that should lead to better scrambling performance. Non-circular fibres showed the best results when used in combination with mechanical fibre squeezers. Similarly, in the simulations of Allington-Smith et al. (2012) [39], the results showed improvement in scrambling for fibres with polygonal cross-sections.

The fibre agitation technique for improving scrambling was mentioned in Sec. 2.4.3. A number of authors such as Baudrand et al. (1998)(2001) [32][67], Lemke et al. (2010)(2011)[69][73], McCoy et al. [71] have tested the this technique successfully. Temporary varying stress applied to the fibre causes phase scrambling among the propagation modes [73]. Since energy among modes will also be reformatted, FRD

is expected to increase with this technique. An example is presented in Fig. 2.19. The parallel laser beam technique was used for these measurements. The near-field of an octagonal fibre can be seen. The experimental set up is fully explained in Sec. 4.2. Since the HeNe source is being used, the output is highly coherent. When applying fibre agitation, the phases of the modes get scrambled. The propagation modes add incoherently at the output, thus eliminating the speckle pattern.
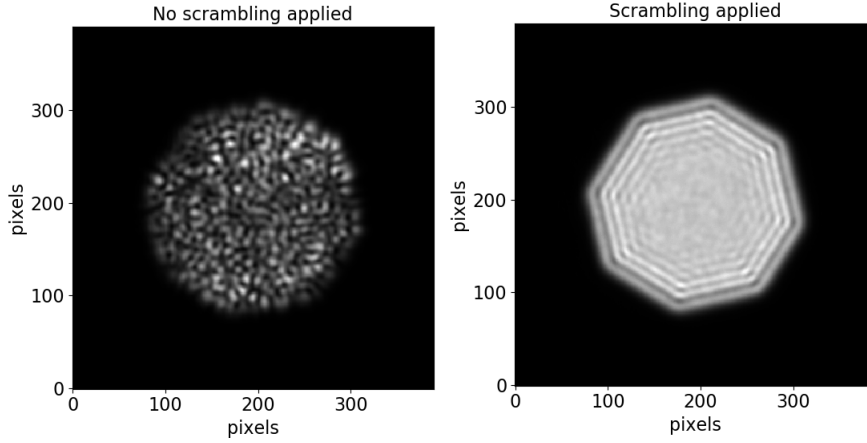

Figure 2.19: Experimental near-field measurement of a $50\mu m$ (NA = 0.21) octagonal fibre without agitation and with agitation. The incident angle of the input field is $\phi_{in} = 8^o$. When agitation is applied the speckle pattern is eradicated.

Scrambling is not only important for precision spectroscopy, but also for highly multiplexed spectroscopy. For accurate throughput calculations, each interface should be adequately assessed. This depends on any change in the near-field and far-field distributions [39].

2.4.6 Characterizing scrambling

In this work, the ratio of images is used to characterize the scrambling performance of a fibre. This method was introduced and applied in Hunter (1992) [74], Avila et al. (2010) [42], Olaya et al. (2012) [48], among others. It consists in moving the input field across the input fibre end and for each position acquiring the resulting near-field or far-field. When the position of the input field is at the center of the fibre, the resulting output field is denominated as I_o. The output fields I_n resulting from the translation of the input field are divided by I_o to obtain the residual image as in $I_{res} = I_n/I_o$. The process is illustrated in Figure 2.20. First, three different input fields are shown. In the mid part of the image, the resulting near-fields intensities are displayed. The ratio image I_n/I_o is shown at the bottom. In this example, a $50\mu m$ circular fibre is being used. The input spot has a $20\mu m$ diameter. A complete explanation of the setup is in Sec. 4.2.

A good way of analyzing the ratio distributions is by statistically quantifying the amount of change in the distribution [48]. If the region of interest is the fibre core, the corresponding SNR is equivalent to

$$SNR = \frac{\mu_{\mathrm{s}}}{\sigma_{\mathrm{s}}}, \tag{2.59}$$

with μ_s being the mean of the intensity distribution and σ_s being the standard deviation. Furthermore, it is possible to calculate the azimuthal and radial scrambling parameters. As can be seen in Fig. 2.21, four regions of interest are defined symmetrically across the reduced image, with each region having identical height and width. The radial parameter R_s and the azimuthal parameter A_s can then be calculated through

$$R_s = 100 \cdot \left| 1 - \frac{W_1 + W_4}{W_2 + W_3} \right|, \tag{2.60}$$
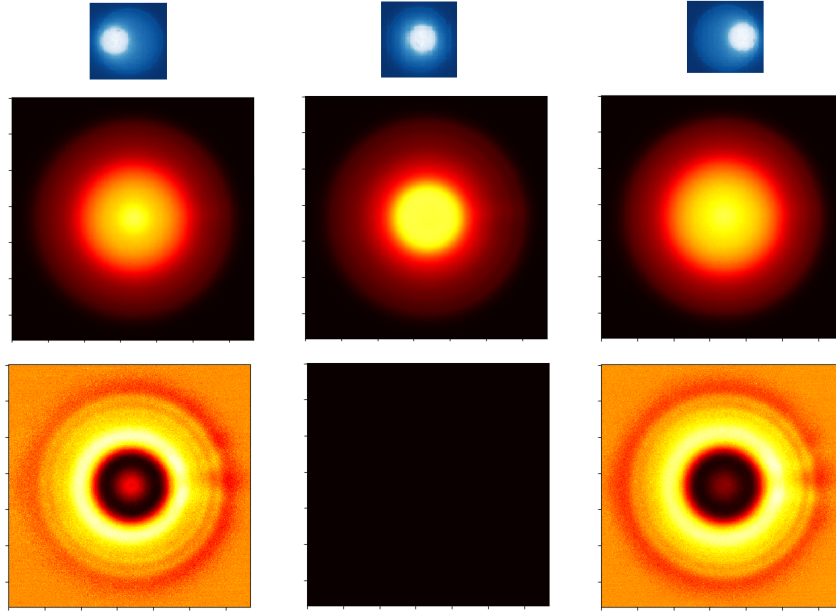
Figure 2.20: A $50\mu m$ circular fibre with an input spot of $20\mu m$ is being displayed. Top: Displacement of input field across the fibre input end. Mid: Near-field distribution as a function of the input field translation. Bottom: Image ratio I_n/I_o with respect to the central image.

$$A_s = 100 \cdot \left| 1 - \frac{W_1 - W_2}{W_3 - W_4} \right|. \tag{2.61}$$

The closer R_s and A_s are to zero, the better the scrambling performance of the measured fibre [48].

Figure 2.21: Four regions of interest defined symmetrically across the reduced image with each region having identical height and width.

Chapter 3

Simulations

Introduction

As described in Section 2.4, modal effects like FRD, scrambling and modal noise have a substantial impact on the results of fibre-based spectrograph systems. Gloge (1972) [52] stated that the exchange of energy between the modes during propagation causes the angular distribution (far-field) to diverge. Th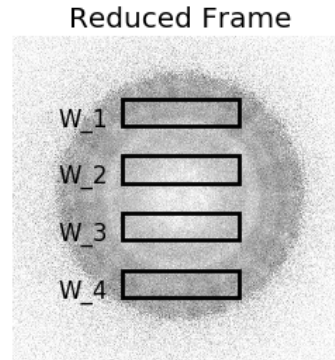e optical etendue increases, causing focal ratio degradation and translating into the loss of throughput. Through the simulations, it is possible to analyze the modal power distribution based on the injection parameters. The possibility of looking into the modal power distribution (MPD) should give insights into the process of beam divergence. Analyzing the far-field distribution created through different input conditions should illustrate how much FRD is to be expected if, e.g. focal variations, spatial or angular translation occur. Furthermore, the simulations allow the analysis of coherent and incoherent propagation for both the near-field and the far-field. These are relevant issues for modal effects in multimode fibres since modal noise can be seen as a direct function of the coherence of the propagation modes and scrambling depends on the number of modes propagating through the system.

Based on the Eigenmode Expansion Method (see Eq. 2.12), a simulation environment has been developed that allows analyzing the modal power distribution (MPD), near-field distribution, and far-field distribution in simulated multimode step-index fibres of any length, geometry and with any kind of index difference Δ (see Eq. 2.1). This allows for simulations of systems with multiple degrees of freedom and normalized frequency numbers (see Eq. 2.15). With this theoretical framework, it is possible to compare the results of the mode excitation for different input parameters such as different wavelengths, spatial translations, angular translations, or focus variations. Additionally, it is possible to see if different fibre geometries have any influence on the MPD and thus in the near- and far-field distributions.

The simulations are created using two software interfaces. The first software interface is the finite element method module FemSIM of the commercially available software Rsoft, which is used as the mode solver. Since multimode fibres with a large number of propagation modes are simulated, a numerical tool for the calculation of the individual mode fields is required. Furthermore, circular fibres are compared to non-circular fibres, for which only numerical solutions exist for calculating the individual fields of the propagation modes. Python (Version 2.7) is the second software interface, and it is used to compute the input field distribution, the propagation of the modes along the z-axis, the superposition of modes at the fibre end $z = L$, and the near- and far-field distributions. All analysis functions are self-written scripts developed for this work. A block diagram is shown in Fig. 3.1.

The best advantage of using the EEM is that the propagation can be calculated in a simple and fast way compared with other simulation methods, for example, the beam propagation method. This is explained in Sec. 3.1. This section describes also how the FemSIM module is used as a mode solver and how the
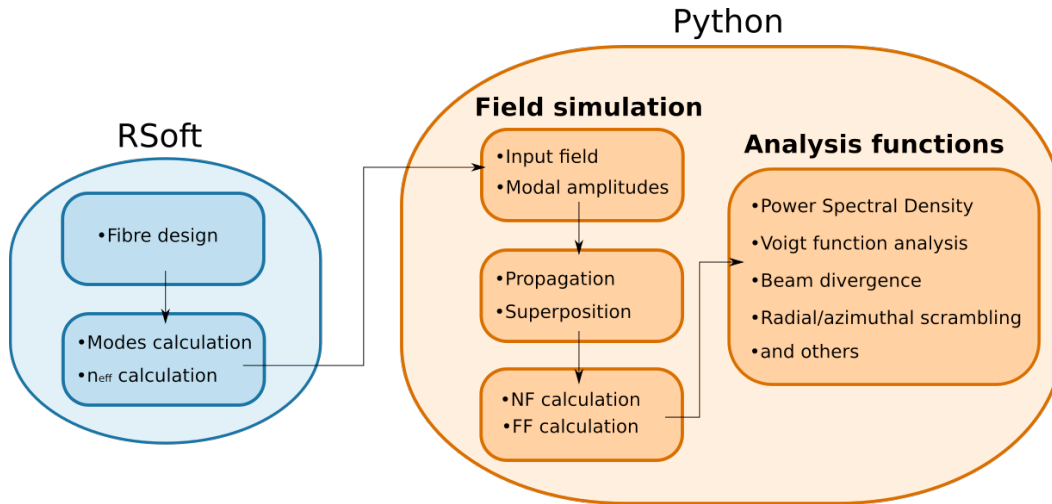
Figure 3.1: Basic block diagram of the simulation environment

results are used for the rest of the computations. Section 3.2 explains the different functions that are used to create appropriate input field distributions for the simulated systems. Section 3.3 is dedicated to the modal amplitudes of the propagation modes, which play a key role in determining the modal power distribution, the near-field spatial distribution, and far-field angular distribution. Section 3.4 deals with the coherent and incoherent superposition of the different propagation modes to create the output field distributions. Section 3.5 explains how mode coupling is simulated. Section 3.6 demonstrates simulations in which characteristics of different fibres are compared. Results presented in the SPIE 2018 will be explained, and the newest results on the divergence of the far-field as a function of the input field FWHM will be illustrated.

3.1   Numerical Methods

Benefits of the Eigenmode Expansion Method

One way of calculating the field propagation in a multimode fibre is through the Beam Propagation Method (BPM). Many commercially available softwares apply BPM. As an example, it is offered as the BeamPROP module in Rsoft. It uses finite difference methods to solve the parabolic or paraxial approximation of the Helmholtz equation [79]. The refractive index distribution $n(x, y, z)$ and the input wave $\Phi_{in}(x, y, z = 0)$ dictate the wave field propagation in the simulated device. The solution algorithm requires numerical simulation parameters such as: a finite computational domain for x, y, z ranges, transverse grid sizes Δx and Δy, and the longitudinal step size Δz. The calculation time scales with the size of the device.

The EEM described in Eq. 2.12 shows that modes have a very simple harmonic z-dependence $(e^{j\beta_m z})$, which is the key to enabling the Eigenmode Expansion Method to solve for long structures quickly and efficiently [80]. This allows to calculate fibres having lengths of $100\mu m$ or $100km$ at the same speed. The factor that affects the time of the calculation is the number of modes a structure can handle. Before creating this simulation system, the author of this thesis attempted to simulate MMF with $\sim 50\mu m$ diameter and having a couple of cm in length using BeamProp. The time it took to conduct a simulation was in the order of days. After creating the simulation environment and using the EEM to calculate the output fields, the time it takes for the same simulation is in the order of minutes.

The BPM method is very effective for certain structures. Nevertheless, for simulating MMF having core sizes and length that resemble the real fibres used in astronomy, the simulation times were not optimum

for conducting the studies in this thesis. The quickness and efficiency of the EEM was a deciding factor in creating the simulation environment for understanding the different modal effects in MMF that are relevant for astronomical spectroscopy.

FemSIM - Mode solver

Rsoft is a commercially available software used in the design and simulation of photonic devices. It was acquired by the company Synopsys in the year 2013. Different modules can be purchased depending on the specific need. For this thesis, the FemSIM module is of relevance. It is based on the Finite Element Method (FEM) [81] and is used to calculate any number of transverse modes for 2D or 3D structures.

To calculate the field distribution $\psi_m(x, y)$ of the individual propagation modes, the elemental parameters of the fibre need to be correctly defined. These are the refractive indexes (n_1, n_2), wavelength λ, diameter and geometry. The parameters can be entered through the graphical user interface (GUI) of FemSIM module. An approximation on the number of propagation modes is done by using Eq. 2.15 together with the elemental parameters. After the parameters of the fibre have been set and the amount of propagation modes has been found, the mode solver calculates the spatial distributions $\psi_m(x, y)$ and effective refractive index $n_{eff,m}$ of all modes via the finite element method. If one of the elemental parameters changes, Eq. 2.15 is applied again and a new set of propagation modes is calculated.

FemSIM does not completely separates the Maxwell equations into TE or TM versions. Results must be filtered out by the user. The easiest way is by examining the normalized peak values of each field component as described in the Rsoft manual [82]. This is done by a self-written python script. The end result is a set of modes in one linear polarized state (lp-state). This means that the actual amount of calculated modes used in the simulation environment equals M/2 since only one lp-state is taken into account. As an example Fig. 3.2 shows 12 modes calculated by FemSIM and filtered into one lp-state for a $24\mu m$ fibre with a NA = 0.121 using a $1300nm$ wavelength. Using Eq. 2.15, $M \approx 24$, which results in the total number of 12 modes in one lp-state.

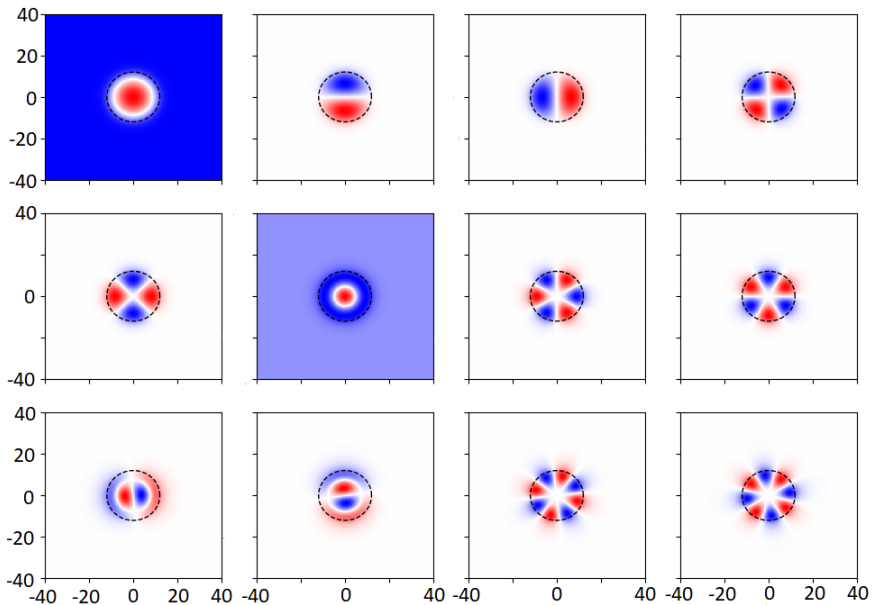Figure 3.2: Modes filtered into one lp-state of a simulated fibre. The dashed black line marks the outline of the $24\mu m$ optical fibre with a NA = 0.121. The modes were calculated using $\lambda = 1300nm$. The x- and y-axis of the plots are in μm. For displaying purposes only some of the axis are marked

The effective refractive indexes of the modes are compared to the core and cladding refractive indexes of

the optical fibre. All the $n_{eff,m}$ should be between n_1 and n_2. Figure 3.3 shows the effective refractive indexes of the modes in Fig.3.2.
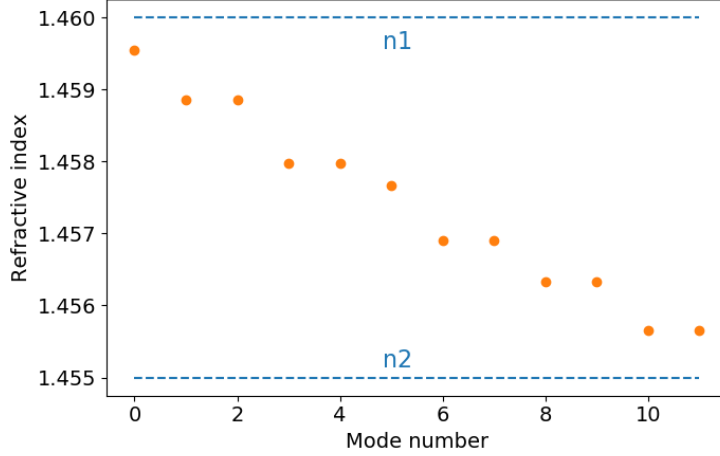

Figure 3.3: Effective refractive index of the calculated modes marked as dots between the refractive index of the core n_1 and the refractive index of the cladding n_2.

The mode fields are afterwards normalized to unity and hold $\int \int |\psi_m(x,y)|^2 \partial x \partial y = 1$. To date, up to 2292 modes have been successfully calculated via FemSIM and filtered into 1146 *lp*-modes. This was achieved simulating a $50\mu m$ square fibre with an N.A. of 0.21 using a $500nm$ wavelength. Besides the spatial distribution $\psi_m(x,y)$ and the effective refractive index $n_{eff,m}$ of all individual modes, the files also contain the span and grid points needed for the simulations. This information translates into the width of the individual simulation fields in μm. The simulated input field uses the same grid information for compatibility, and thus the analysis functions for the near-field and far-field.

3.2 Creating the Input Field

The characteristics of the input field have a direct impact on the modes that are excited in a multimode fibre. Depending on its size, angle, and position, different modes will propagate. This will consequently produce different modal power distributions, near-field distributions and far-field distributions. As a basic input field, a 2-D Gaussian distribution can be simulated using [45]

$$\Psi_{Gauss}(x,y) = A_o \cdot \exp\left[-\frac{\sqrt{x^2+y2}}{2\sigma_o^2}\right] \tag{3.1}$$

The factor A_o is the amplitude and is set as a constant. The input field Ψ_{Gauss} is normalized to unity with the condition $\int \int |\Psi_{Gauss}(x,y)|^2 \partial x \partial y = 1$. The FWHM is used as a measure of the input field size. For a Gaussian distribution, the FWHM can be calculated through the standard deviation σ_o with

$$\text{FWHM} = 2\sigma_o\sqrt{\ln 2}. \tag{3.2}$$

The FWHM is consequently used as the input parameter for determining the spot size in μm. A variation in focus is simulated by changing the spot size of the input field. If needed, the field radius w_o of the distribution can be calculated through

$$w_o = 2 \cdot \sigma_o. \tag{3.3}$$

Spatial displacements in the input field may occur when fibres are being moved to position in the focal plane of the telescope, or when fibres are moving with the telescope [75]. This produces a shift to the barycenter

of light to the edges of the optical fibre, a situation that produces different modal power distributions and may lead to photometric fluctuations in the detector. Simulations of spatial translation are applied with $\bar{x} = x - x_o$, $\bar{y} = y - y_o$ in Eq. 3.1 as $\Psi_{Gauss}(\bar{x}, \bar{y})$.

A perfectly collimated optical beam with a flat wavefront and a specific beam size resembles a top hat function. Two steps are used to produce a distribution that resembles a 2-D top hat function. First, an over dimensioned Gauss is created. The FWHM is chosen to be factor 100 of the spot radius to be simulated. Subsequently, a threshold function is applied to set the values outside the spot radius to zero [83]. Figure 3.4 shows the example of an input field with spatial displacement $(x_o, y_o \neq 0)$ and an example of a 1D cut of a top hat input field. In both cases, the simulated optical fibre has a diameter of $24\mu m$. The FWHM of the Gaussian for the displacement example was of $5\mu m$. The spot diameter of the top hat function was simulated to have the size of the optical fibre, $d_{\mathrm{spot}} = 24\mu m$.
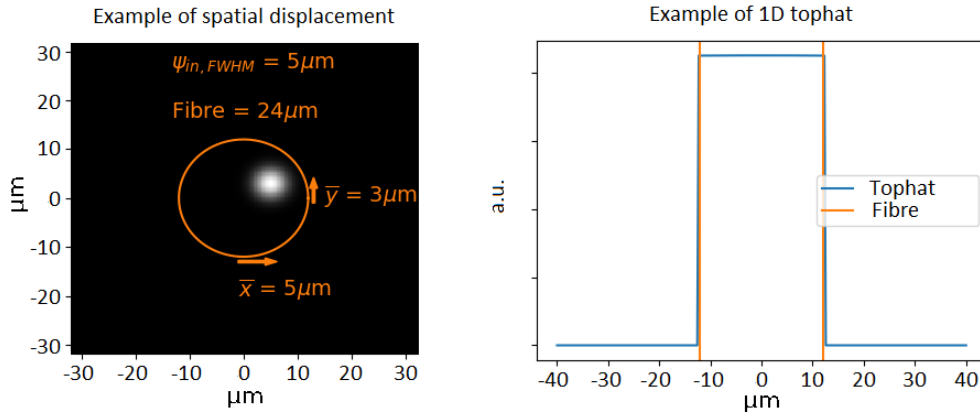

Figure 3.4: Example of ψ_{in} with spatial displacement and example of a 1D top hat function. The FWHM of the input Gaussian for the displacement example was of $5\mu m$. The spot diameter of the 1D top hat distribution was simulated to have the size of the fibre $d_{\mathrm{spot}} = 24\mu m$.

A similar situation happens with angular displacements due to fibre movement and positioning. Depending on the system, different f-numbers might be used. To simulate an angular displacement and specific f-numbers, an incident angle needs to be introduced to $\Psi_{Gauss}(\bar{x}, \bar{y})$. This is achieved by multiplying

$$\psi_\varphi = \exp(j\varphi_n k_o n), \ n \in \{x, y\} \tag{3.4}$$

to Eq. 3.1, with φ_n representing the desired incident angle to be simulated. The parameter k_o represent the wavenumber, and can be calculated through $k_o = 2\pi/\lambda_o$, with λ_o being the wavelength used in the simulation (see Eq. 2.8).

In some cases the pupil of the telescope is injected into the optical fibre via a lenslet array [30]. Since the pupil of the telescope represents the first mirror, it possesses often central obscuration. To see the effects on the modal power distribution, fields with central obscuration are also simulated. A field with central obscuration can be achieved by multiplying Eq. 3.1 with

$$R = (x - x_o)\cos(\phi) + \jmath(y - y_o)\sin(\phi), \ \text{with } \phi = \pi/4 \tag{3.5}$$

The function R was found by trying different methods to produce a 2D function with central obscuration. It follows the scheme of a rotation matrix with a fixed phase [45]. After the multiplication with the Gaussian function, the absolute square value produces a real input field with central obscuration,

$$\Psi_{CO} = |\Psi_{Gauss} \cdot R|^2. \tag{3.6}$$

Figure 3.5 shows an input field with central obscuration Ψ_{CO} that has the spot size diameter of a $50\mu m$ simulated fibre. In a nutshell, the simulated input field can take three forms: simple Gauss distribution, 2D top hat function, and field with central obscuration. For all three forms, spatial translation and incident angle can be applied by using $\bar{x} = x - x_o$, $\bar{y} = y - y_o$ and Eq. 3.4.
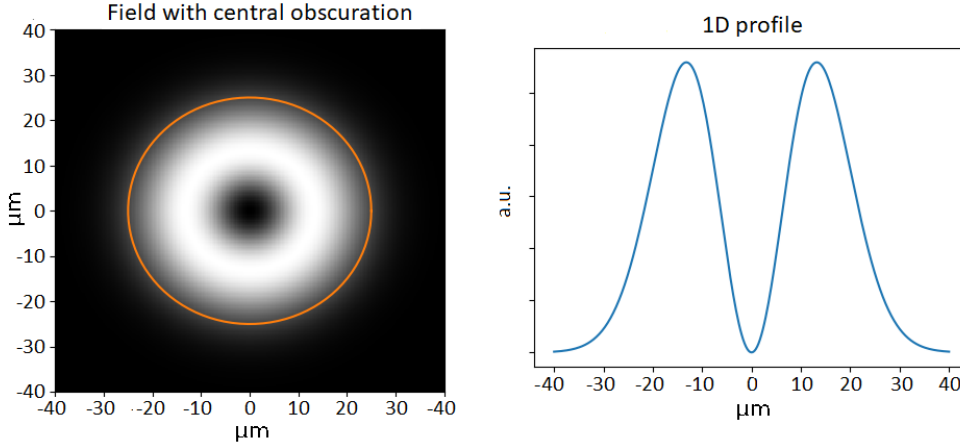
Figure 3.5: Input field with central obscuration as 2D function and 1D profile

3.3 Modal Amplitudes

As described in Eq. 2.12, the modal amplitudes are represented with the parameter c_m. If Ψ_{in} contains the power P going into the fibre, this power is divided into all the active modal amplitudes as in Eq. 2.13 with $\sum_{m=0}^{M}|c_m|^2 = P$, thus obeying power conservation. This means that the modal amplitude c_m dictates how much portion of power a specific mode propagates. If $z = 0$ in Eq. 2.12, it results in

$$\Psi_{x,y,z=0} = \sum_{m=0}^{M} c_m \psi_m e^{j\beta_m 0}, \tag{3.7}$$

thus

$$\Psi_{in}(x,y) = \sum_{m=0}^{M} c_m \psi_m. \tag{3.8}$$

If the input field is known, it is possible to calculate the modal amplitudes using an overlap integral between the input field and each of the propagation modes as in

$$c_m = \int\int \Psi_{in}\psi_m^* \partial x \partial y, \tag{3.9}$$

with

$$c = [c_0, c_1, c_2, \cdots, c_M]. \tag{3.10}$$

After applying Eq. 3.9, the modal amplitude array c contains all the modal amplitudes contributing to the propagation in the system, thus containing the modal power distribution (MPD) as in Corbett et al. (2007) [84]. Figure 3.6 shows the MPD of a system with 180 modes. The simulated fibre has a circular geometry with a diameter of $50\mu m$ and NA $\approx$ 0.121. Using a wavelength of $1\mu m$ with Eq. 2.15 and 2.16, the number of propagation modes equals $M \approx 180$ and the normalized frequency parameter equals $V = 18.963$. The simulated input field is a Gaussian beam having a FWHM of $25\mu m$ with an incident angle of $\phi_{in} = 5^o$.

The modal amplitude array is normalized to unity under the condition $\sum_{m=0}^{M}|c_m|^2 = 1$. By looking into Fig. 3.6, it is possible to visualize, how much percentage of the complete power goes to the individual modes. As described in Wood (1984) [66], it is clear that the active propagation modes in the system are a function of the input angle ϕ_{in} and not all modes are excited equally. The mode that will propagate with the most power, c_{max}, is marked. For this example, the output angle of that mode is $\phi_{cmax} = 5^o$. It is equivalent to the input angle that was used for the input field, which indicates $\phi_{cmax} = \phi_{in}$. Through the bar plot of the MPD, it is also clear that modes with higher order than c_{max} are also excited. All of
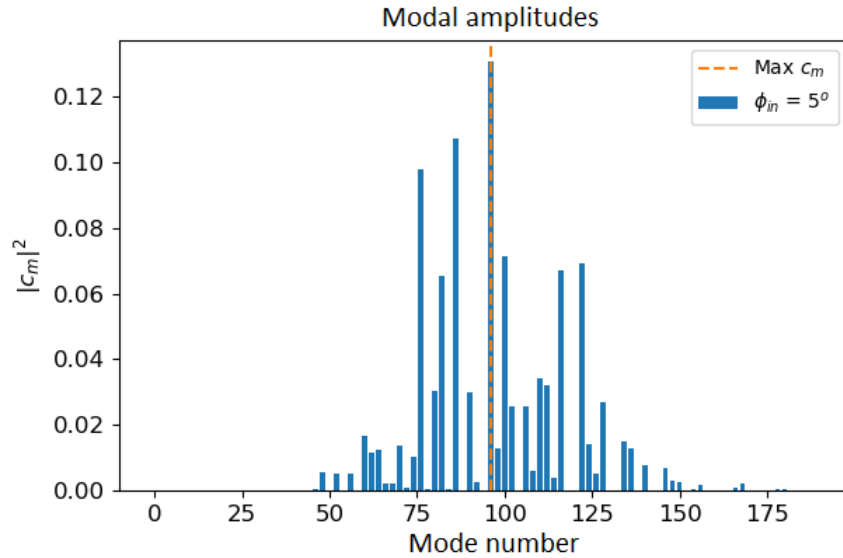
Figure 3.6: Modal Power Distribution of a system with 180 modes: Circular $50\mu m$ fibre with NA ≈ 0.121 using a wavelength of $1\mu m$.

those higher order modes possess a more divergent output angle than the mode with c_{max}. Although no perturbations of the system have been taken into account, this indicates the possibility that the output beam will have a more divergent beam than the input, signifying focal ratio degradation. Due to the superposition of the different modes, the exact exit angle of the output beam can be calculated only after a complete simulation.

3.3.1 Analyzing the divergence of the output beam through the active modes

Even though a complete assessment on the divergence of the output beam can be done only after a complete simulation, the knowledge of the active modes in a system already gives insights into the output fields of the fibre. For the ease of illustrating the output divergence, the NA of a specific output beam will be calculated. The NA is a value attached to the refractive index difference of the fibre (see Eq. 2.3). Since each mode has a specific exit angle [52] and possesses an effective index $n_{eff,m}$, each mode could be given a effective NA as a function of the propagation mode as in $NA_{eff}(m)$. The value $NA_{eff}(m)$ will be used to asses the divergence of the output angle depending on the active propagation modes. Three different methods were studied to approximate the output $NA_{eff}(m)$: using the number of excited modes m, using the effective refractive index $n_{eff,m}$ of the modes, and using the angular distribution obtained from the Fraunhofer approximation. Through each method the same description of the divergence is to be expected.

Provided the spatial distribution of the input field fills the core of the fibre, it is possible to use the underfilled NA of the fibre to estimate the number of excited modes *(private communication Prof. Tim Birks and Dionne Haynes)*. This means that for each input angle $\phi_{in} < \phi_{max}$, the number of modes can be calculated as a function of the input angle, $M(\phi_{in})$. As there is only a discrete set of possible distributions of the electrical field in the fibre cross section, there is going to be a discrete set of possible output angles. The calculation of the number of propagation modes $M(\phi_{in})$ in a fibre is a function of the normalized frequency parameter V. As described in Eq. 2.15, the NA sets the maximal input/output angle possible for the fibre [83]. If the $NA_{eff}(m)$ is expressed as a function of the number of propagation modes, Eq. 2.15 can be expressed as

$$NA_{eff}(m) = \frac{\lambda\sqrt{2m}}{2\pi r}. \tag{3.11}$$

Equation 3.11 describes the increment in divergence with increasing active modes in the fibre. Furthermore, using directly the effective refractive index of each mode, $NA_{eff}(m)$ can be calculated with Eq. 2.3. If the effective refractive index is used instead of n_2, it is possible to get an approximation of the output NA as a function of $n_{eff,m}$ via

$$NA_{eff}(n_{eff,m}) = \sqrt{n_1^2 - n_{eff,m}^2} \tag{3.12}$$

As already shown in Fig. 3.3, the fundamental mode has the smallest index difference with respect to $n1$, meaning it should possess the shallowest angle. The highest order mode will have the most divergent beam. Another way of calculating the angular distribution is by the means of the Fourier transform and the Fraunhofer approximation described in Sec. 2.1. The approximation allows to use the transform of a mode $\psi_m(x, y)$ to obtain the angular distribution in the far-field $\Psi_m(\theta_x, \theta_y)$, thus allowing for the approximation of the output NA as a function of θ_x, θ_y [83]. This method is analog to Snyder and Love (1983) who showed that for $M \gg 1$, each mode can be associated with a unique characteristic ray angle $\theta_{in,out}$ [84].

Ray optics simplifies the field propagation as light rays confined in the fibre core. In wave optics, each propagation mode has a portion in the fibre core and a portion that decays in the cladding. When the modes are analyzed in the far-field, the situation is the same. An intensity field does not possesses a sharp boundary that marks a specific output angle. After the Fourier transform was a applied to a specific mode, the angular intensity field was averaged to a 1D intensity distribution. The maximum of the averaged 1D distribution was used to mark the output angle of the field. Figure 3.7 illustrates the process of obtaining the angular output of a high order mode from the simulated circular fibre.
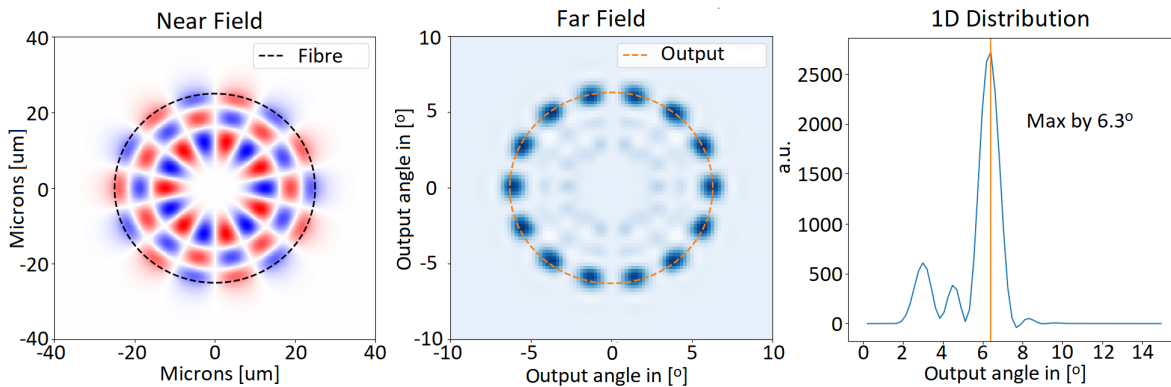

Figure 3.7: Allocating an output angle to a specific modal field. The Fourier transform is applied to the near-field distribution and averaged into a 1D intensity function. The maximum of the 1D function is used to mark the output angle of the specific mode. The illustration shows a high order mode of the simulated circular fibre [83].

Figure 3.8 shows the results of the three different methods for the system of 180 modes presented in Fig. 3.6. The simulated fibre has a circular geometry with a diameter of $50\mu m$ and a NA ≈ 0.121. If $\lambda = 1\mu m$, then $M = 180$ and $V = 18.963$. If an incoming beam would have an incident angle of 5°, the mode with the highest c_m would be $m = 96$. The modal amplitude carrying the most power with the corresponding ϕ_{out} is marked.

As can be seen in Fig. 3.8, the three different methods correlate with the prediction that increasing modes will increment $NA_{eff}(m)$ and produce more divergence at the output end of the fibre. It is analog to the description in Lemke et al. (2011) [73] that the number of propagation modes rises with an increment in ϕ_{in}. Since the number of propagation modes is a function of the input angle, $M(\phi_{in})$, and the divergence of the output beam depends on the number of propagation modes, Fig. 3.8 shows how input angular fluctuations could translate directly into far-field angular fluctuations, a situation that can result in photometric errors of the fibre-fed spectrograph system.
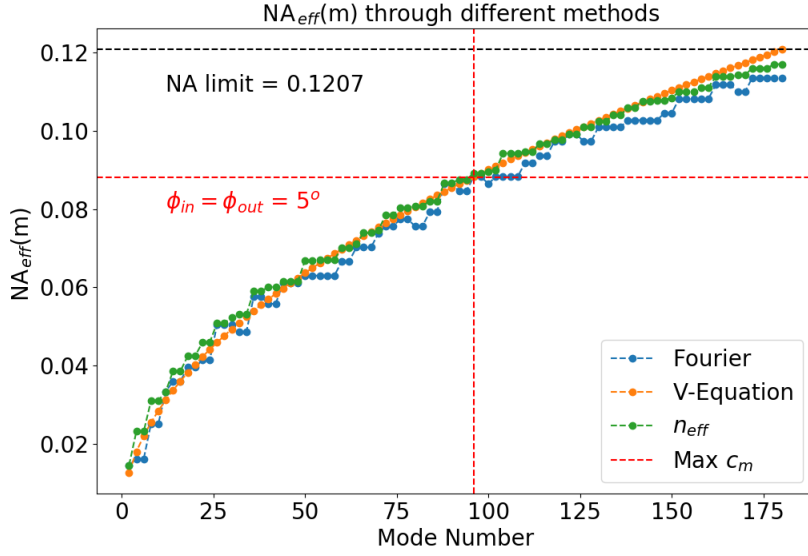
Figure 3.8: Calculation of $NA_{eff}(m)$ as a function of the propagation modes using three different methods: Fraunhofer approximation, V-Equation and $n_{eff,m}$. $NA_{eff}(m)$ can be used as a measure for the output beam divergence. The mode carrying the maximum power in Fig. 3.6 with the respective output angle ϕ_{out} is marked.

3.4 Generating the Output Fields

3.4.1 Superposition of the modes

After the modal amplitudes are calculated, the summation of all propagation modes at the distance $z = L$ provides the resulting field. As described in Sec. 2.1.3, the superposition between the modes can be coherent, partially coherent, or incoherent. A study on how partial coherence occurs in multimode fibres was not part of this work. For the time being, the case of complete coherence and the case of complete incoherence are taken into account. As will be demonstrated, complete coherence resembles cases where speckles patterns can be observed, while complete incoherence resembles cases were the phases of the propagation modes are completely scrambled.

In the case of coherent propagation, the near-field output intensity is calculated as

$$I_{out}(x, y, L) = |\Psi_{out}(x, y, L)|^2 = \left| \sum_{m=0}^{M} c_m \psi_m(x, y) \exp(j\beta_m L) \right|^2, \tag{3.13}$$

with $z = L$ denominating the length of the simulated optical fibre. In the case of incoherence, the phases of the modes contributing to the intensity $|\Psi_{out}|^2$ are assumed as random over time, and the average intensity is calculated (see Sec. 2.1.3) [45]. This means

$$I_{out} = \langle |\Psi_{out}(x, y, t)|^2 \rangle_t = \lim_{T \to \infty} \frac{1}{2T} \int_{-T}^{T} |\Psi_{out}(x, y, t)|^2 \, \partial t. \tag{3.14}$$

In Eq. 3.14, $\langle \cdot \rangle_t$ means averaging over time. To solve Eq. 3.14 lets take into account two functions $f(t)$ and $g(t)$ with $|f(t)|^2 = A$ and $|g(t)|^2 = B$. The absolute square of both functions would be

$$|f(t) + g(t)|^2 = |f(t)|^2 + |g(t)|^2 + 2\sqrt{|g(t)|^2 |f(t)|^2} \cdot \cos\left(\phi_g(t) - \phi_f(t)\right) \tag{3.15}$$

Equation 3.15 resembles the interference equation described in Sec. 2.1.3. Using the average intensity of Eq. 3.15 results in

$$\langle |f(t) + g(t)|^2 \rangle_t = \langle |f(t)|^2 \rangle_t + \langle |g(t)|^2 \rangle_t + \langle 2\sqrt{|g(t)|^2 |f(t)|^2} \cdot \cos\left(\phi_g(t) - \phi_f(t)\right) \rangle_t, \qquad (3.16)$$

with the term $\langle |g(t)|^2 \cdot |f(t)|^2 \cdot \cos\left(\phi_g(t) - \phi_f(t)\right) \rangle_t$ being equal to [45]

$$\lim_{T \to \infty} \frac{1}{2T} AB \int_{-T}^{T} \cos\left(\phi_g(t) - \phi_f(t)\right) \partial t = 0, \qquad (3.17)$$

in the case that $\phi_g(t)$ and $\phi_f(t)$ are completely random. Equation 3.17 allows to write Eq. 3.15 as

$$\langle |f(t) + g(t)|^2 \rangle_t = \langle |f(t)|^2 \rangle_t + \langle |g(t)|^2 \rangle_t = |f(t)|^2 + |g(t)|^2 \qquad (3.18)$$

Equation 3.18 states that the intensity of the active propagation modes can be added to obtain the near-field output intensity in the incoherent case, resulting in

$$I_{out} = \sum_{m}^{M} I_m = |c_0 \psi_0|^2 + |c_1 \psi_1|^2 + |c_2 \psi_2|^2 + ... + |c_M \psi_M|^2. \qquad (3.19)$$

At the moment, only monochromatic propagation can be simulated. For the coherence case, monochromatic propagation means that a speckle pattern is expected as the near-field intensity distribution. For the incoherent case, an intensity distribution showing the modal patterns of the individual active modes is expected. As an example, a comparison between simulations and actual near-field measurements of a fibre is shown in Fig. 3.9. The measured fibre was an octagonal fibre with a diameter $d = 50\mu m$, NA ≈ 0.21 and length $l = 2m$. The parallel laser beam method was used with the HeNe source wavelength of $\lambda = 633nm$. An incident angle of $\phi = 8^o$ was introduced. To induce scrambling, the measured fibre was attached to a probe shaker. More details of the experimental setup can be found in Sec. 4.2. The simulated fibre used the same characteristics. A total number of $m \approx 1200$ modes were calculated with the FemSIM module, giving ≈ 600 modes in one $lp-$state. The upper part of the image shows the case for coherence propagation in both simulation and measurement. The lower part of the image shows the case for incoherence propagation. For the incoherent simulation to resemble a real measurement, mode coupling needed to be applied. This is explained in Sec. 3.5.

3.4.2 Obtaining the angular distribution (far-field)

The superposition of modes in the far-field follows the same rules as for the near-field. As described in the former section (Sec. 3.4.1), only the cases of complete coherence and complete incoherence are taken into account. The Fraunhofer approximation described in Sec. 2.1.2 is used for calculating the angular far-field distribution. Through the Fourier transform of the near-field, $\Psi(\nu_x, \nu_y) = \mathcal{F}\{\Psi_{out}(x, y)\}$, and applying $\theta_{x,y} \approx \lambda \nu_{x,y}$, the angular distribution is obtained as $\Psi(\theta_x, \theta_y)$. The intensity of the angular distribution is equivalent to $I(\theta_x, \theta_y) = |\Psi(\theta_x, \theta_y)|^2$.

For computing the coherent case, a 2D-FFT can be applied directly to the near-field distribution. Another way of computing the coherent angular distribution is by transforming each mode individually and applying the coherent superposition in the angular plane. Since the transform of a mode can be expressed as

$$\mathcal{F}\left\{c_m \psi_m e^{j\beta_m z}\right\} = c_m e^{j\beta_m z} \int\int_{-\infty}^{\infty} \psi_m(x, y) e^{-j2\pi(\nu_x x + \nu_y y)} \partial x \partial y, \qquad (3.20)$$

a single mode in the far-field angular plane can be expressed $c_m e^{j\beta_m z} \mathcal{F}\{\psi_m\}$. The **linearity** characteristic of the Fourier Transform allows for [45]

$$\mathcal{F}\{ax(t) + by(t)\} = a\mathcal{F}\{x(t)\} + b\mathcal{F}\{y(t)\}. \qquad (3.21)$$
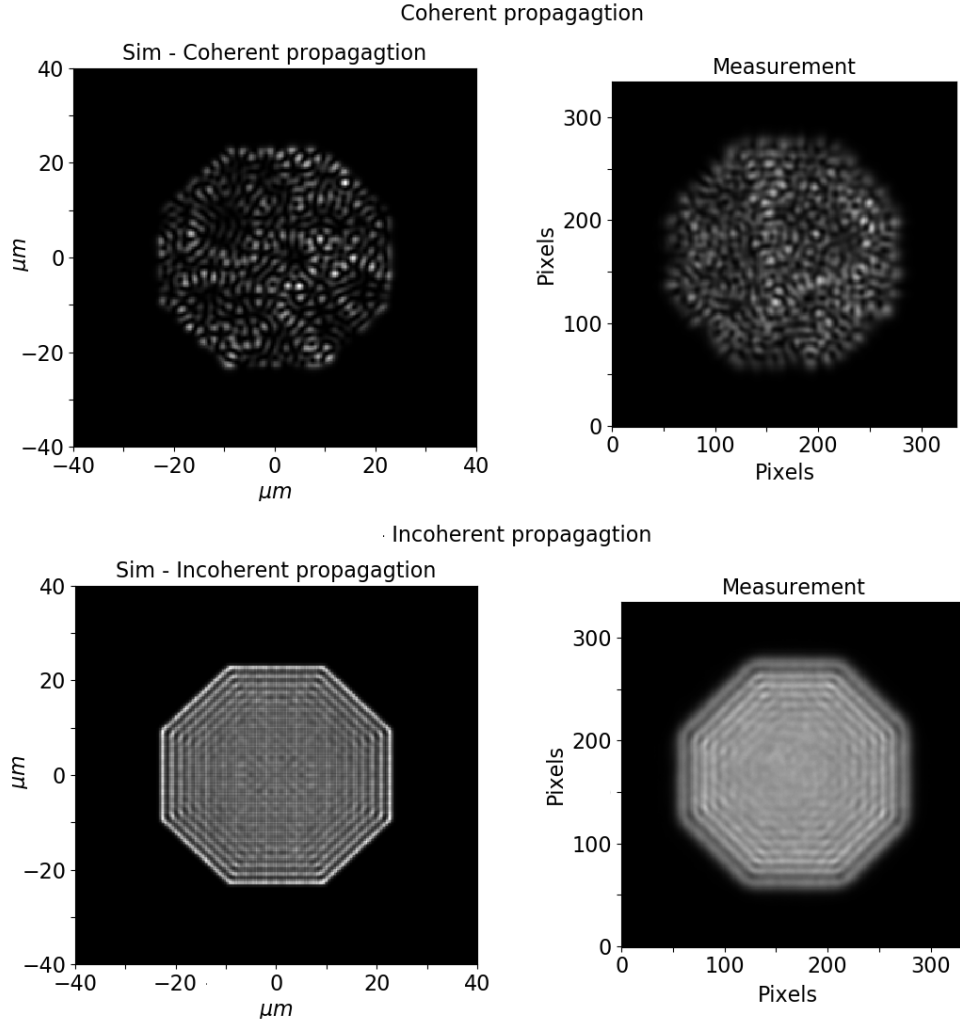
Figure 3.9: The near-field of an octagonal fibre with coherent and incoherent propagation. The fibre was a $50\mu m$ octagonal fibre with an NA $= 0.21$ and length of $2m$, using a propagation wavelength of $\lambda = 633nm$ with an incident angle $\phi = 8^o$. Due to the coherence, interference patterns (speckles) appear in $I_{out,coh}$ (see Sec. 2.4.3). The incoherent addition of the active modes appears in $I_{out,incoh}$.

If applied to the EEM, it results in

$$\mathcal{F}\{\Psi_{out}\} = \mathcal{F}\left\{\sum_{m=0}^{M} c_m \psi_m e^{j\beta_m z}\right\} = c_0 e^{j\beta_0 z}\mathcal{F}\{\psi_0\} + ... + c_M e^{j\beta_M z}\mathcal{F}\{\psi_M\}. \tag{3.22}$$

$\Psi_{out}(x,y)$ and $\psi_m(x,y)$ were written without the argument (x,y) for ease of displaying the equation. Equation 3.22 is used for simulating coherence propagation in the angular plane, since it facilitates the computation of multiple simulations. All the propagation modes of a fibre are transformed and saved in a different file, meaning that an FFT is run on every mode only once. This allows easy access to the information of each individual mode in the far-field if needed. Since the modal amplitudes are already calculated for the near-field, no additional complicated calculation steps need to be done, thus simplifying computations for each far-field calculation. Accordingly, each simulation has a file containing the modes in spatial coordinates for the near-field distribution and a file containing the transformed modes in angular coordinates for the far-field distribution.

Parseval's Theorem states that the field's energy, which is the integral of the field's power $|f(x)|^2$, equals the integral of the energy spectral density $|F(\nu)|^2$ [45]

$$\int_{-\infty}^{\infty} |f(x)|^2 \, \partial x = \int_{-\infty}^{\infty} |F(\nu)|^2 \, \partial \nu = \int_{-\infty}^{\infty} S_F(\nu) \partial \nu, \tag{3.23}$$

with the energy spectral density equivalent to

$$S_F(\nu) = |F(\nu)|^2 = |\mathcal{F}\{f(x)\}|^2. \tag{3.24}$$

Using Eq. 3.22 in 3.24 results in

$$S_{\Psi_{out}}(\nu_x, \nu_y) = |\mathcal{F}\{\Psi_{out}\}|^2 = \left|\mathcal{F}\left\{c_0\psi_0 e^{j\beta_0 z}\right\} + ... + \mathcal{F}\left\{c_M\psi_M e^{j\beta_M z}\right\}\right|^2. \tag{3.25}$$

Equation 3.25 comes in handy when calculating the far-field distribution of incoherent propagation. With the use of Eq. 3.18 it can be written as

$$|\mathcal{F}\{\Psi_{out,incoh}\}|^2 = |\mathcal{F}\{c_0\psi_0\}|^2 + ... + |\mathcal{F}\{c_M\psi_M\}|^2. \tag{3.26}$$

As an example, Fig. 3.10 shows the comparison between simulations and actual far-field measurements. The measured fibre was a $50\mu m$ circular fibre with an NA of ≈ 0.21 and $l \approx 2m$. The parallel laser beam method was used for the measurement with an incident angle of $\phi_{in} = 9^o$. The source wavelength was $\lambda = 633nm$, resulting in $M \approx 1200$ propagation modes with 600 modes in one $lp-$state. To induce scrambling, the measured fibre was attached to a probe shaker. More details of the experimental setup can be found in Sec. 4.2. As describe in Gloge (1972) [52], Haynes et al. (2011) [53], and Allington-Smith et al. (2012) [39], the angular distribution of such an input field results in an annulus spread with the input's incident angle. The upper part of the image shows coherent superposition. The lower part of the image shows incoherent superposition for the simulation and the measurement. For the incoherent simulation to resemble a real measurement, mode coupling needed to used be applied. This is explained in Sec. 3.5. The different color map is to highlight the speckle pattern and intensity fluctuations. The x-axis and y-axis are in angular coordinates, meaning θ_x and θ_y. For clarity, only the values of the axes are illustrated.

3.4.3   Creating a 1D intensity distribution

For better analysis of both the near-field and the far-field, the 2D distribution is often mapped into a 1D function of the radius $F(r)$. This gives the opportunity of using fit functions, e.g. to analyze the FWHM of the distribution and obtain detailed information regarding the output angular divergence in the far-field. It requires that the intensity is averaged over the 2π azimuthal angle as a function of the radius.

First, the center of mass of the 2D image needs to be found. For a simulation, this is fairly simple, but measurements do not tend to be in the center of an image. The resulting CCD-fits file needs to be scanned for the center of mass. To obtain reliable and reproduceable results, this process was automated through a script based on the analysis of binary images [85]. The measured intensity distribution is converted to a black and white image. The centroid is found through the moments of the image. The different moments of a binary image are calculated using

$$\mu_{m,n} = \sum_{x=0}^{N} \sum_{y=0}^{N} x^m y^n f(x,y), \tag{3.27}$$

with N being the total number of pixels in one dimension, x and y the pixel number in the respective dimension , and $f(x,y)$ the pixel value that takes 1 or 0 for a binary image. The area of the binary image can be described with $\mu_{0,0}$, while $\mu_{1,0}$ and $\mu_{0,1}$ account for the first moments of the image in x-axis and y-axis. The centroid can be found through

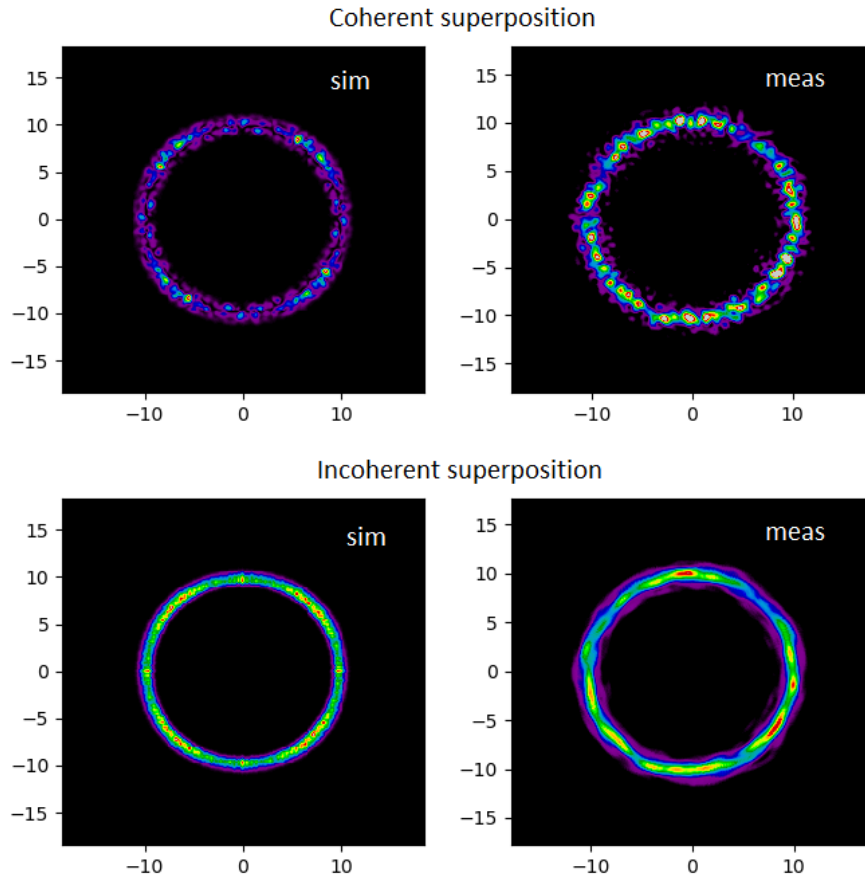$$C_{x,y} = \left(\frac{\mu_{1,0}}{\mu_{0,0}}, \frac{\mu_{0,1}}{\mu_{0,0}}\right). \tag{3.28}$$

Figure 3.10: Simulations and measurements of the far-field of a circular fibre using the parallel laser beam method with $\phi_{in} = 9^o$. The fibre had a diameter of $50\mu m$ with an NA of ≈ 0.21 and $l = 2m$. The upper figures show the coherent case, in which speckles are clearly visible. The lower figures show the incoherent case. The different color map is used to highlight the speckles and intensity fluctuations. The x-axis and y-axis are in angular coordinates, meaning θ_x and θ_y. For clarity, only the values of the axes are illustrated.

For each azimuthal angle $\phi \in \{0 \text{ to } 2\pi\}$, there is a 1D function $f_n(x, y)$ that can be used to describe the energy distribution along the azimuthal axis ϕ as a function of the radius r. The pixel values of the function $f_n(x, y)$ are obtained through $x = r \cdot \cos(\phi) + C_x$ and $y = r \cdot \sin(\phi) + C_y$. The average of all $f_n(x, y)$ is used to produce $F(r)$. Figure 3.11 shows an example of obtaining the 1D intensity distribution. The original image is a CCD-fits file from a measurement using the parallel laser beam method with a $50\mu m$ circular fibre and an input angle of $\phi_{in} = 10^o$. As can be seen, it is not in the center of the frame. It is transformed to a binary image, so that the centroid can be found. The 1D-distribution is the average of all the $f_n(x, y)$ functions.

3.5 Mode coupling

Equation 3.9 states how the modal amplitudes are calculated. If the input field and the modal distributions of a system are known, the modal power distribution (MPD) of a system can be obtained. In a real fibre, the MPD is not static throughout the propagation of the field. Due to perturbations in the refractive index, the MPD changes through the propagation length. The modal power distribution at the end of the fibre will be different than at the beginning, meaning MPD(z=0) $\neq$ MPD(z=L). The modal amplitudes interchange power as they propagate along the waveguide, making the modal amplitude array a function
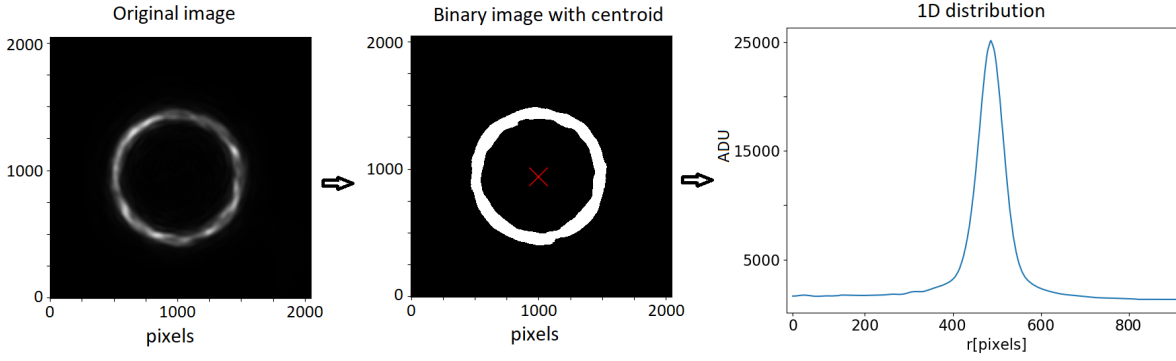
Figure 3.11: Example of finding the center of an image and averaging the radial profile over 2π. The original image is a CCD-fits file from a parallel laser beam measurement of a $50\mu m$ circular fibre. The input angle was $\phi_{in} = 10^o$. The transformed binary image shows the centroid found through Eq. 3.28. The 1D intensity distribution is the average of all $f_n(x, y)$, with $x = r \cdot \cos(\phi) + C_x$ and $y = r \cdot \sin(\phi) + C_y$.

of the propagation distance $c(z)$. The power exchange between propagation modes is known as mode coupling. The modal amplitudes are no longer constant and Eq. 2.12 can be rewritten as

$$\Psi_{out}(z) = \sum_{m=0}^{M} c_m(z)\psi_m e^{j\beta_m z} \tag{3.29}$$

Equation 3.29 makes the modal amplitudes a function of the propagation length z. To solve for the modal amplitudes, it is helpful to use the simplified ordinary differential equation (ODE) [86]

$$\frac{\partial c_\nu}{\partial z} = \sum_\nu j\kappa_{\nu\mu}c_\nu e^{j(\beta_\mu - \beta_\nu)z}, \tag{3.30}$$

and describing the coupling coefficients as

$$\kappa_{\nu\mu} = \omega \int \int \psi_\nu^* \Delta n^2 \psi_\mu \partial x \partial y. \tag{3.31}$$

The factor Δn^2 is a function that describes the perturbations in the refractive index. For a numerical calculation of $\kappa_{\nu\mu}$, an appropriate Δn^2 function needs to be found. This is fairly difficult since it would be based on perturbation theory and should depend on many input parameters that go beyond the scope of this work. Besides the complications of Δn^2, the actual solving of 3.30 is not possible. An attempt was made but it seemed appropriate to go with a phenomenological approach as in Allington-Smith et al. (2012) [39]. In Sec. 3.5.1 the actual implementation of mode coupling in the simulations will be explained. The rest of this section describes the attempt of solving Eq. 3.30.

The ODE can be written as

$$\frac{\partial c}{\partial z} = M_{\nu\mu}\vec{c}. \tag{3.32}$$

Using a non-vectorial approach, it is possible to solve for Eq. 3.32 as

$$\frac{\partial y}{\partial x} = f(x) \cdot y(x) \text{ with } F'(x) = f(x) \tag{3.33}$$

$$\frac{\partial y}{\partial x} - f(x) \cdot y(x) = 0 \mid \cdot e^{-F(x)} \tag{3.34}$$

$$e^{-F(x)}\frac{\partial y}{\partial x} - e^{-F(x)}f(x) \cdot y(x) = 0 \tag{3.35}$$

$$\frac{\partial(e^{-F(x)} \cdot y(x))}{\partial x} = 0 \text{ (Product rule)} \tag{3.36}$$

$$e^{-F(x)} \cdot y(x) = C \text{ (Derivation of a constant).} \tag{3.37}$$

This gives the solution

$$y(x) = y_o \cdot \exp\left(\int_0^x f(x)dx\right). \tag{3.38}$$

Applying Eq. 3.38 to Eq. 3.30 gives

$$c(z) = c_o \cdot \exp\left(\int_0^z M_{\nu\mu}(z)dz\right). \tag{3.39}$$

The c_o in Eq. 3.39 can be calculated as in Eq. 3.9 with $c_o = \langle \Psi_{in}, \psi_m \rangle$. The matrix M takes the form

$$M_{\nu\mu} = j \cdot \begin{bmatrix} \kappa_{11} \cdot e^{j(\beta_1 - \beta_1)z} & \kappa_{12} \cdot e^{j(\beta_2 - \beta_1)z} & \dots & \kappa_{1\mu} \cdot e^{j(\beta_\mu - \beta_1)z} \\ \kappa_{21} \cdot e^{j(\beta_1 - \beta_2)z} & \kappa_{22} \cdot e^{j(\beta_2 - \beta_2)z} & \dots & \kappa_{2\mu} \cdot e^{j(\beta_\mu - \beta_2)z} \\ \vdots & \vdots & \ddots & \vdots \\ \kappa_{\nu 1} \cdot e^{j(\beta_1 - \beta_\nu)z} & \kappa_{\nu 2} \cdot e^{j(\beta_2 - \beta_\nu)z} & \dots & \kappa_{\nu\mu} \cdot e^{j(\beta_\mu - \beta_\nu)z} \end{bmatrix}. \tag{3.40}$$

For $M_{\nu\mu}$, the commutivity of the exponential function does not apply since $\exp(A) \cdot \exp(B) = \exp(A + B)$ only holds for $A \cdot B = B \cdot A$. In this case $M_{\nu\mu}(z1) \cdot M_{\nu\mu}(z2) \neq M_{\nu\mu}(z2) \cdot M_{\nu\mu}(z1)$ in $z[0, L]$ with L representing the length of the fibre. This means that solving the integral in Eq. 3.39 is not possible.

To get an approximation of the exponential integral, it is possible to use the **Magnus expansion**, which expresses the solution by means of the exponential of a certain $n \times n$ matrix function $\Omega(t, t_o)$, also known as *Time Dependent Exponential Perturbation Theory* in Quantum Mechanics. This could be a study for future work.

3.5.1 Simplification of mode coupling for the simulations

In a regular multimode fibre, mode coupling occurs mostly between neighboring modes and the coupling strength decreases with the mode spacing. This has been tested experimentally and describe theoretically by D. Gloge in "Optical Power Flow in Multimode Fibers" (1972) [52]. Through the power flow equation (see Eq. 2.34) and coupling parameter D (see Eq. 2.36), Gloge analyzed the modes of a multimode fibre as a continuum and described coupling as a diffusion process.

In "Simulation of complex phenomena in optical fibres" by Allington-Smith et al. (2012) [39], it was stated that the effects describe by Gloge postulate the existence of scattering sites distributed within the fibre, which scatter light into higher- and lower-order modes. As explained by Allington-Smith et al. (2012) [39] and by Haynes et al. (2011) [53], the scattering is concentrated in the termination points of the fibre. Mechanical and thermal stress caused by the finishing processes (e.g. polishing, grinding and/or cleaving) is believed to introduce micro-ruptures into the core and cladding causing abrupt refractive index changes Δn that are the source of mode coupling. The factor Δn can be seen in Eq. 3.31 and is needed to define the coupling coefficient between two propagation modes. In the ray-tracing model of Allington-Smith et al. (2012), the coupling parameter D was introduced as $\Delta\theta_F$ to represent the amplitude of angular perturbations along a length L_F which was used to sum termination defects of both ends of the fibre.

To reproduce a similar procedure, the modal amplitude array $c = \{c_0, c_1, ..., c_M\}$ is convolved with a 1-D Gaussian function $\Gamma_\sigma = \exp(-x^2/2\sigma^2)$. The number of elements in c is the same as for Γ_σ. Having a FWHM $= 2 \cdot \sqrt{2\ln 2} \cdot \sigma$, the factor σ in Γ_σ indicates how strong the mode coupling is used in the simulation. The values for σ are normalized to 1. It results in $c_\sigma = c \circledast \Gamma_\sigma$, with c_σ still holding the power conservation to unity $\sum_{m=0}^{M} |c_\sigma|^2 = 1$.

As in Allington-Smith et al. (2012) [39], the calibration of σ and thus the amount of FRD is done by using actual measurements and finding the appropriate values for the simulations. Figure 3.12 shows the modal power distribution c_σ for different σ values. The simulated fibre is an octagonal fibre with a diameter of $50\mu m$ and NA ≈ 0.21. The propagation wavelength $\lambda = 633nm$ is used. A total mode number of $m \approx 1200$ modes can propagate, resulting in ≈ 600 modes in one $lp-$state. A Gaussian with an incident
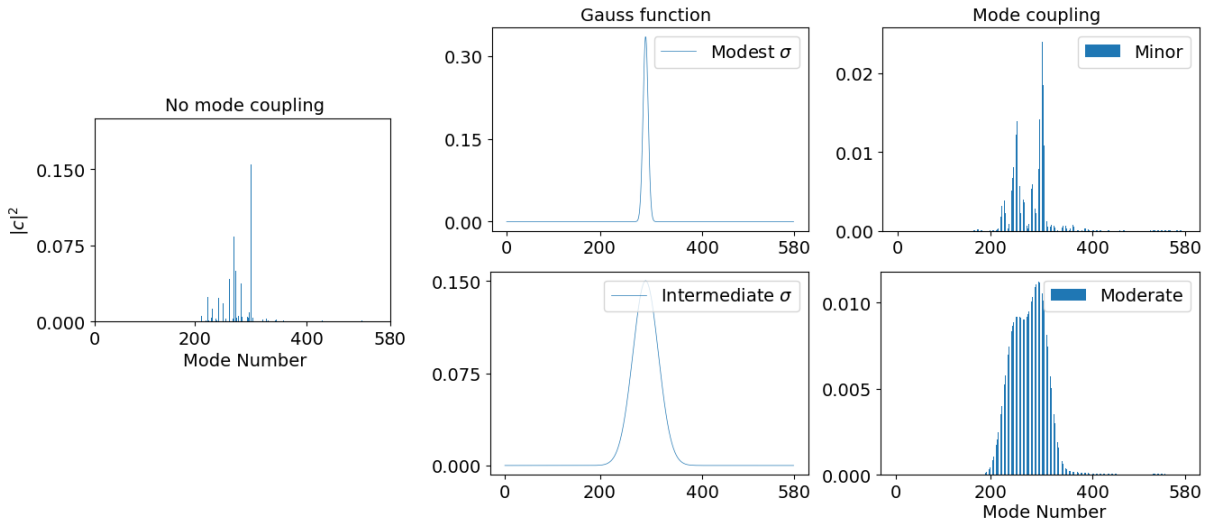
Figure 3.12: Example of mode coupling using different σ values. Minor and moderate mode coupling are illustrated. The simulated fibre is an octagonal fibre with a diameter of $50\mu m$ and NA ≈ 0.21. The propagation wavelength $\lambda = 633nm$ is used. A total number of $m \approx 1200$ modes can propagate, giving ≈ 600 modes in one $lp-$state. A Gaussian with $\phi_{in} = 8^o$ and a FWHM $= 25\mu m$ is the input field.

angle of $\phi_{in} = 8^o$ and a FWHM $= 25\mu m$ is the input field. Two different values of σ are used, creating two different modal power distributions.

To test this method, the measured near-field of an octagonal fibre was reproduced by simulations with the simplified mode coupling technique. The measured octagonal fibre had the same characteristics as the simulated fibre. The parallel laser beam method was used for the experimental measurements with $\lambda_{in} = 633nm$. An input angle $\phi_{in} = 8^o$ was used. Scrambling was induced by attaching the fibres to a probe shaker. For the near-field measurement, the end face of the fibre was re-imaged on a $1k \times 1k$ CCD Apogee Andor using a $\times 50$ objective. To simulate the induced scrambling, incoherent propagation was used. Figure 3.13 shows the results of the simulation compared to the result of the measurement. There is a good match in the measured near-field and the simulated near-field with mode coupling. Since it is not possible to get rid of mode coupling in the measurements, there is no way in testing the reality of the simulation without mode coupling.
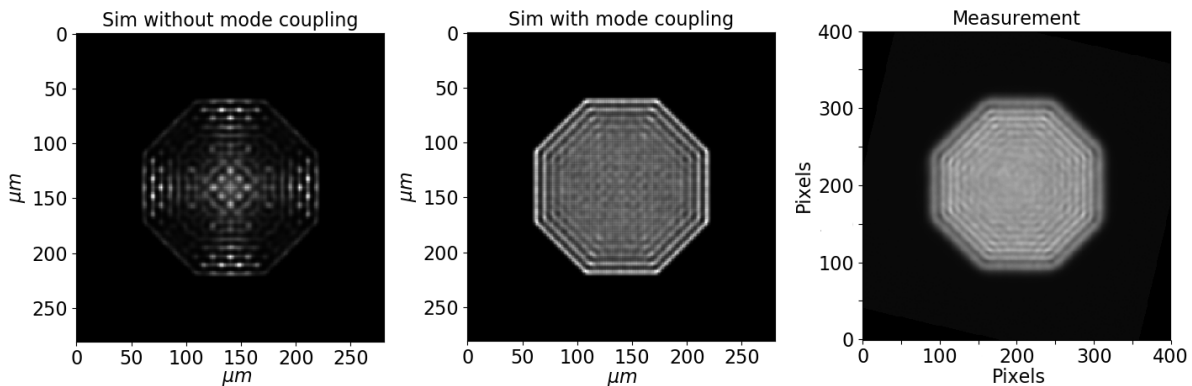

Figure 3.13: Comparison of experimental measurement and simulation with/without applying mode coupling. The mode coupling was induced using $\Gamma_{\sigma=25}$. The probe fibre was the $50\mu m$ octagonal fibre, using a propagation wavelength of $\lambda = 633nm$ with an incident angle of $\phi = 8^o$.

3.6 Simulations

3.6.1 Analysis of mode excitation on fibres with different cross-sections

In recent years, fibres with different cross-sections have become of interest for astronomical instrumentation. Authors such as Allington-Smith et al. (2012) [39], Spronck et al. (2012) [87], Avila (2012) [88], and Stürmer et al. (2016) [89] have achieved better scrambling results using non-circular fibres than conventional circular fibres. Since FRD depends on so many factors, there is no specific conclusion that non-ciruclar fibres could have better FRD properties than circular fibres.

Since the field propagation model gives the opportunity of simulating fibres with different cross-sections, a study was conducted on how the input field modifies the MPD and output fields from circular and non circular fibres. The results give a direct estimate on the beam divergence for each fibre. These results were presented on the conference paper "Analysis of mode excitation on different geometries of optical fibres for astronomical spectroscopy" by Hernandez et al. (2018) [83] at the SPIE 2018 in Austin, Texas.

To obtain the far-field angular distribution, the parallel laser beam method was simulated with the different fibre geometries. The angular distribution can be seen a function of the specific input angle ϕ_{in}. As already described in Sec. 3.3.1, there is no sharp boundary in the angular intensity field. To determine a boundary, different methods were approached. The first method consisted in finding out through the MPD, which mode transports the most amount of power. Consequently, the output angle of that mode would be used as the output angular distribution. The second method consisted in analyzing the MPD with a specific power threshold, e.g. 95%. The last method was through the Fourier transform of the complete system and determining the angular distribution with an specific beam size. The 2D far-field intensity distribution is averaged into a 1D function, and different definitions for acquiring the beam size can be applied, e.g. $1/e^2$ [45]. Figure 3.14 illustrates the different methods. The simulated fibre was a $50\mu m$ circular fibre with an NA = 0.1207. The propagation wavelength was $\lambda = 1.00\mu m$, which results in a total of $m = 180$ modes and $V = 18.96$. The critical angle is $\theta_{out} = 6.9^o$ with a corresponding f-number = 4.14. The simulated incident angle was $\phi_{in} = 5^o$.
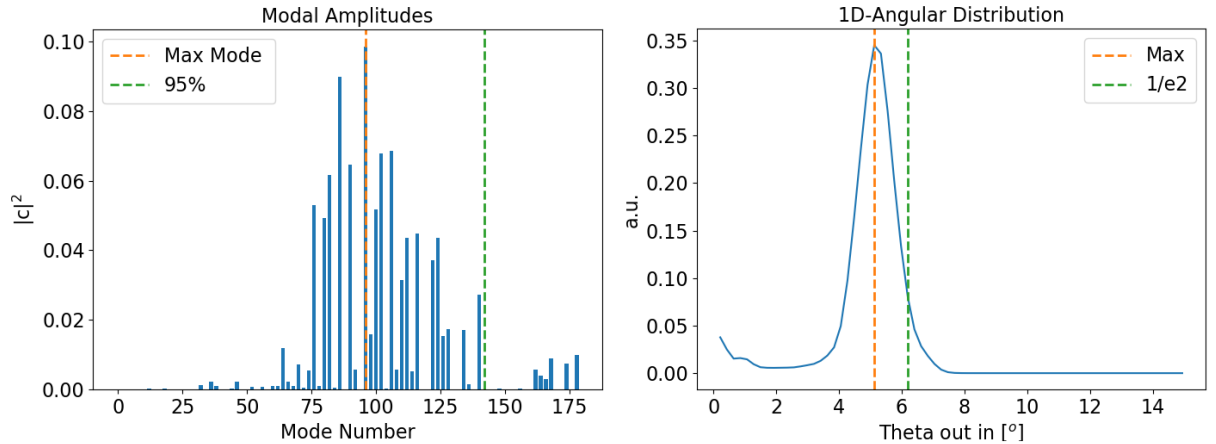

Figure 3.14: Different methods for finding out the output angular distribution of the simulations. *(left)* The bar plot shows modal amplitudes $|c|^2$. It marks the mode transporting the most power, and a threshold that reaches 95% of the power. *(right)* The plot shows the avarged 1D function of the 2D angular far-field distribution. Different methods can be applied for obtaining the beam size, e.g. $1/e^2$ [45].

To compare the methods, different input angles were used and the resulting angular distributions were converted to an output f-number through $f\#_{out} = 1/(2\sin(\phi_{out}))$. Since the input angle is known, it is possible to plot the results of $f\#_{out}$ as a function of $f\#_{in}$. The simulated $50\mu m$ circular fibre with the NA = 0.1207 was used once more. The input angle was incremented in steps of $\Delta\phi_{in} = 0.5^o$ until the

$\phi_{max} = 7^o$, which is the maximum angle corresponding to the NA of fibre. Figure 3.15 shows the results.
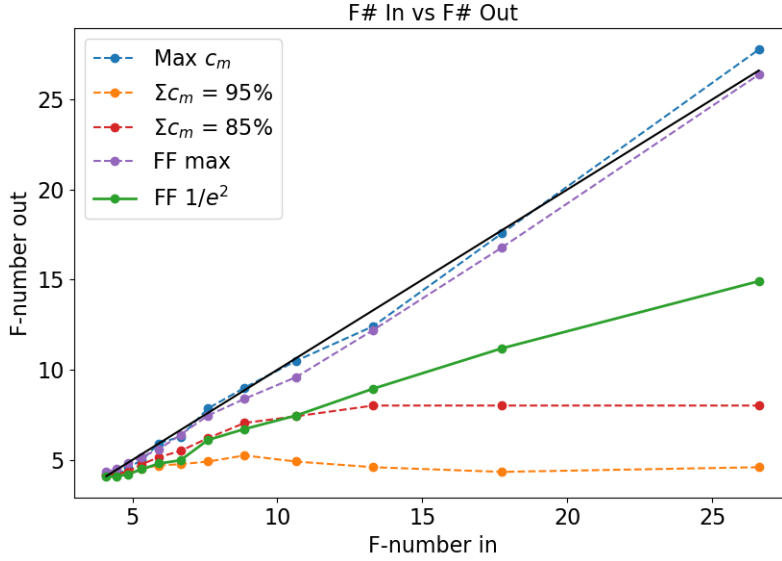

Figure 3.15: Example of the different methods used to determine the output focal ratio as a function of the input focal ratio for simulations using the $50\mu m$ circular fibre with NA $= 0.1207$ and using a propagation wavelength of $\lambda = 1\mu m$.

When mapping the output f-number as a function of the mode that carries the most power, the output focal number appears to match the input focal ratio, diverging at certain points. The results are similar if the output f-number is calculated as a function of the maximum averaged 1D far-field intensity distribution. The results change drastically if a certain energy threshold in the modal power distribution is used to determine the output f-number. The 95% power threshold shows very high FRD characteristics. If the beam is determined through the $1/e^2$ criterion [45] or using the 85% power threshold, the FRD characteristics start showing a more realistic approach. Interestingly, the $1/e^2$ method delivers a $\approx 86\%$ threshold for determining the angular distribution in the far-field intensity. In a simple manner can be demonstrated, how FRD occurs when trying to apply a geometrical optics term to wave optics. In a system without perturbations, defining a beam size translates already into FRD.

Comparison of fibres with different NA and different cross-sections

Further calculations were done using the $1/e^2$ criterion [45] for determining the beam size in the far-field angular distribution. First, an additional circular fibre was simulated that had an augmented NA value of 0.209. For the $\lambda = 1\mu m$ propagation wavelength, the number of propagation modes rises from ≈ 200 up to ≈ 600 modes. The maximum input angle is $\phi_{max} = 12^o$ with an equivalent f-number $f\# = 2.38$. The input array of f-numbers for the simulations with the low NA fibre starts with $f\# = 4.1$ and slows down to $f\# \approx 28$. For the high NA fibre, it start with $f\# = 2.38$ and slows down to $f\# \approx 28$. Figure 3.16 shows the results. The blue box is illustrated in the lower part of the figure and shows a linear fit function for the area until $f\# \approx 14$, which is equivalent to f-numbers that could be used by telescope optics [30].

Both fibres have a fairly similar behavior. The difference in NA produces minor variations in the FRD plot. As can be seen from the lower part of Fig. 3.16, there is a difference in the slope of the linear fit of Δslope $= 0.655 - 0.596 = 0.059$. The simulated low NA fibre shows a slightly worst FRD characteristic. The simulated fibre with lower NA had a normalized frequency number of $V_{low} = 18.9$. It can be expected that fibres with a normalized frequency number above V_{low} will have a similar or better FRD characteristic. It is possible that fibres with V-numbers below V_{low} could show worst results, since fewer propagation modes
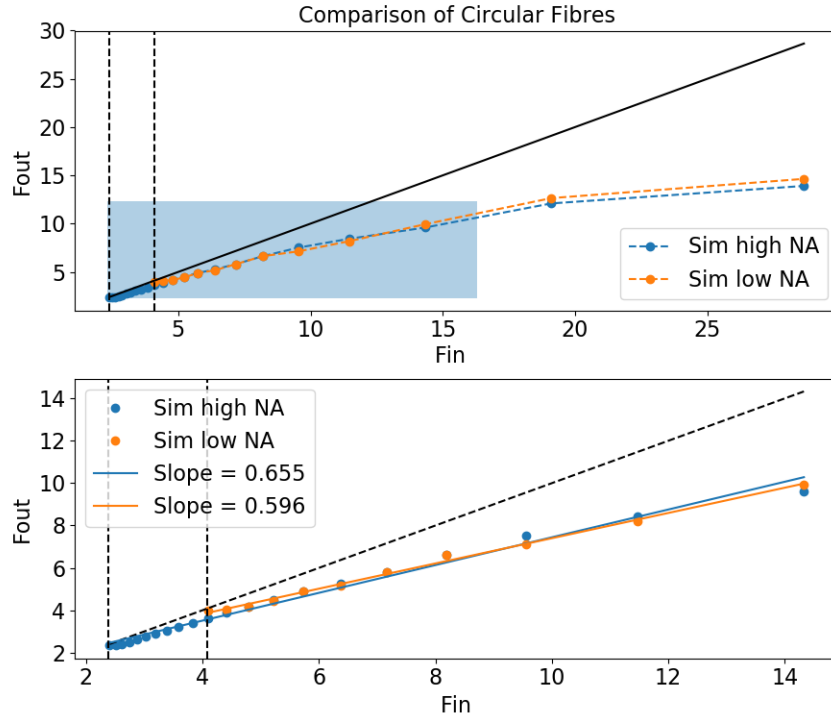
Figure 3.16: Comparison of two ciruclar fibres with different NA values. The lower plot shows a linear fit until $f\# \approx 14$, which represents the blue rectangle in the upper plot.

means that the output angular distribution possesses a diminished amount of possible output angles.

Both circular fibres were compared to octagonal and square fibres. The same characteristics were used: $50\mu m$ diameter or $50\mu m \times 50\mu m$ size; the propagation wavelength $\lambda = 1\mu m$; and the NA values equal to 0.1207 and 0.209. With these properties, the normalized frequency numbers are equivalent to $V_{low} = 18.9$ and $V_{high} = 32.9$. For clarity, the fibres with a higher NA were compared separately from the lower NA fibres. Once more, a linear fit was made for the f-numbers that could be realistically used in telescopes. Figure 3.17 shows the results.

A very similar behavior is observed in all fibres. The square fibre showed minimally better results for the higher NA fibres, having a difference $\Delta s_{s-c} = 0.042$ with the circular fibre and a difference $\Delta s_{s-o} = 0.029$ with the octagonal fibre. There was almost no difference for the lower NA fibres. The circular and the square fibres produced the same results, and the octagonal had a difference $\Delta s = 0.008$. Once more the higher NA fibres had an overall better FRD characteristic than the lower NA fibres.

Fibres in astronomical instruments are usually not used with an input f-number slower than $f\# = 7$ [30]. To examine if any changes would occur in the obtained values, all the fibres were simulated until $f\# = 7$. In this configuration, the fibres with higher NA had an improvement in the FRD characteristics. The results are in good agreement with the known FRD theory (see Sec. 2.4.1). The slopes of the linear fits had a mean value of 0.773, which was 1.15 times better than before. The lower NA fibres showed a similar result, with a slope median value of 0.609. Almost no improvement could be observed. In the simulated range of input f-numbers, the fibres with higher NA do show a better performance than the lower NA fibres. Figure 3.18 shows the results.
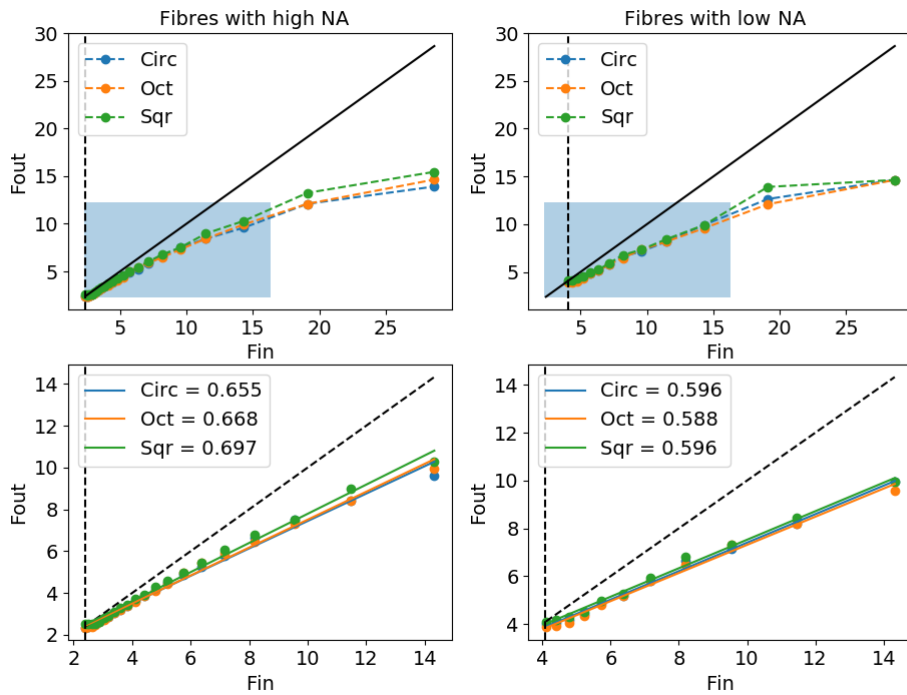
Figure 3.17: Comparison between the circular, octagonal and square fibres. The fibres with a higher NA were compared separately from the lower NA fibres.
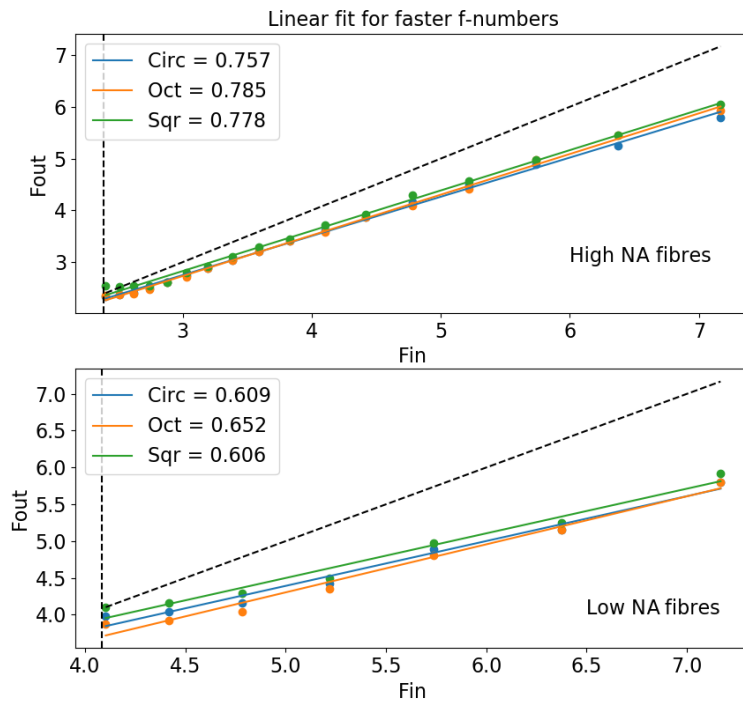

Figure 3.18: Linear fit for faster f-numbers. All the fibres were simulated until the $f\# = 7$ to resemble applications of astronomical instrumentation [30].

To observe the effects of input beam translation and defocus on the FRD characteristics, spatial displacement and change of FWHM of the input Gaussian beam were simulated. The output f-number was calculated as a function of both the spatial displacement and change in FWHM. In both cases, a steady input focal number $f\# = 5.74$ ($\varphi_{in} = 5^o$) was used. The fibres had the same characteristics as before. For the simulations of spatial translation, the FWHM of the input beam was of $10\mu m$. The input field was moved across the fibre input face in $x_o = [-15, -12, -10, -7, -5, -3, 0]\mu m$ steps, with x_o representing the location of the beam center. The change in FWHM was done in steps of FWHM $= [1, 5, 10, 20, 50, 200, 500]\mu m$. In both cases, the lower NA fibres had better FRD characteristics. This is accounted to the fact that the input f-number ($f\#_{in} = 5.74$) was closer to the limit f-number of the lower NA fibres ($f\#_{low} = 4.1$) than the higher NA fibres ($f\#_{high} = 2.38$). Fibres with higher NA did show a strong sensibility to changes in the FWHM of the input field. If working closer to limit $f\#_{high}$ of the fibre, the sensibility should be substantially diminished. This implies that if the working f-number is slower than the limit fibre f-number, $f\#_{in} > f\#_{\phi_{max}}$, the FRD characteristics will be more sensitive to changes in FWHM of the input field. As an example, seeing variations could manifest in such an effect. Changes in the FRD characteristics due to spatial translation were minimal. This could change if the working f-number is much slower than the limit f-number of the fibre. In both spatial translation and change in FWHM simulations, the different cross-section fibres had fairly similar results. Figure 3.19 shows the results of the simulations.
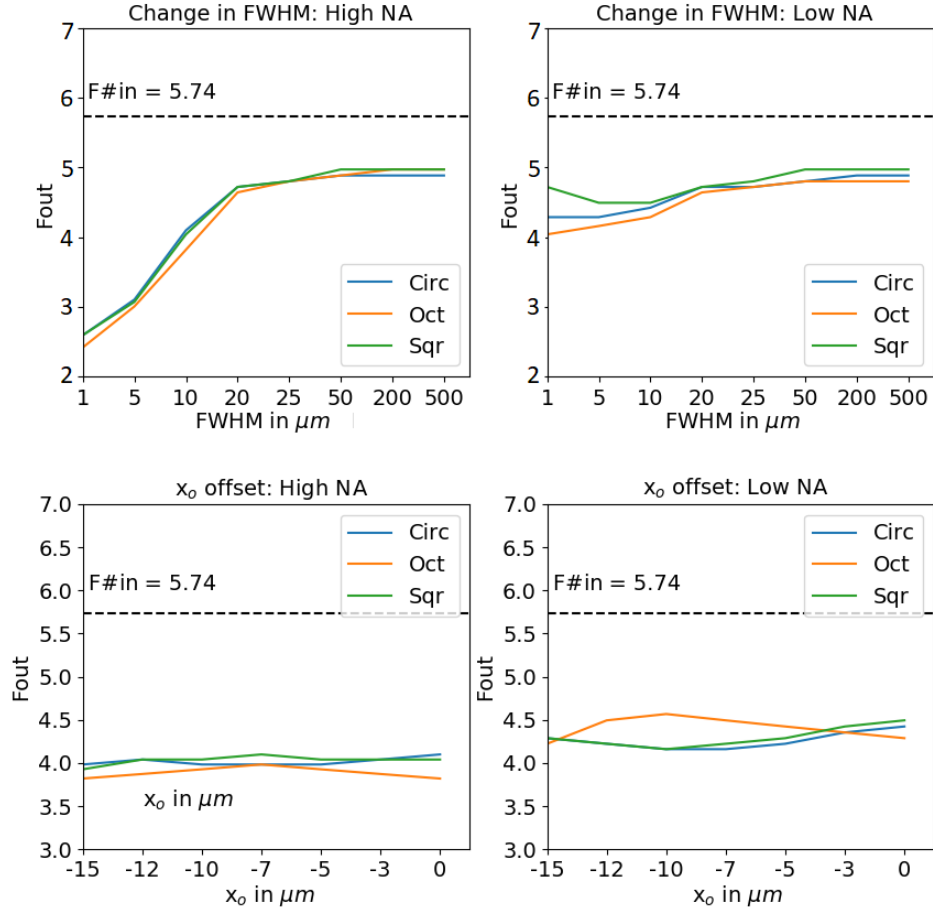

Figure 3.19: Simulation results of spatial translation and changes FWHM. Fibres with different NA and different cross-sections were compared. The FRD performance between the fibres with different cross-sections were similar. Changes in the FWHM of the input affected substantially fibres with higher NA Spatial translation did not produce much differences in the FRD characteristics.

3.6.2   Angular divergence as a function of the input field diameter

The influence of the input FWHM on the resulting far-field angular distribution of a fibre was examined into detail. Since augmented divergence in the angular distribution translates into FRD, fluctuations in the input spot diameter need to be avoided. This situation may occur not only through seeing variations, but also through mechanical misalignment of the fibres in the telescope focal plane. For slower beams (higher f-numbers), the broadening of the angular distribution due to changes in the spot size is expected to be more severe. For a complete analysis, both the normalized mutual intensity and the angular distribution are needed. The former will be explained first.

The normalized mutual intensity $g_{1,2}$ is a measure of the degree of spatial correlation between two fields (ψ_1, ψ_2) at a specified fixed time delay τ. For the case of $\tau = 0$, the mutual intensity can be defined as

$$G_{1,2} = \langle \psi_1^*, \psi_2 \rangle, \tag{3.41}$$

with the normalized mutual intensity (NMI) as

$$g_{1,2} = \frac{G_{1,2}}{\sqrt{I_1 I_2}}. \tag{3.42}$$

Analog as in describing the coherence between two fields (see Sec. 2.1.3), the absolute value of $g_{1,2}$ is bounded between zero and unity, $0 \leq |g_{1,2}| \leq 1$. If $|g_{1,2}| = 1$, both fields are identical ($\psi_1 = \psi_2$). As described in Eq. 3.7, the input field can be calculated for $z = 0$ as in

$$\Psi_{in} = \sum_{m=0}^{M} c_m \psi_m = \psi_o. \tag{3.43}$$

Since only a finite number of propagation modes are available, Equation 3.43 can be described best with $\Psi_{in} \approx \psi_o$. If the normalized mutual intensity is applied to both Ψ_{in} and ψ_o, then $|g_{in,o}|$ gives a reliable statement in the similarity between both fields. The difference $1 - |g_{in,o}|$ translates into coupling loss. This can be used to analyze the input beam coupling as a function of the input FWHM, displacement or angle. For fibres with low normalized spatial frequency values V, the normalized mutual intensity is expected to be lower. To test this method, two few-mode fibre systems were simulated and compared. Both systems used the same fibre, both with different propagation wavelength, which results in different normalized frequency numbers. The simulated fibre had a diameter of $24\mu m$ and NA = 0.121, which corresponds to $\phi_{max} = 7^o$ and translate to $f\# = 4.1$. The two different propagation wavelengths were $\lambda_1 = 1.3\mu m$ and $\lambda_2 = 2.0\mu m$. The corresponding V-values were $V_1 = 7.0$ and $V_2 = 4.55$. The input field diameter was changed as a function of the size of the fibre $d_f = 24\mu m$ as in: $1d_f$, $0.5d_f$ and $0.1d_f$. Figure 3.20 shows the results. Systems with lower V are expected to show more losses as a function of the coupling angle. With decreasing input spot diameter, angle dependent losses should increases.
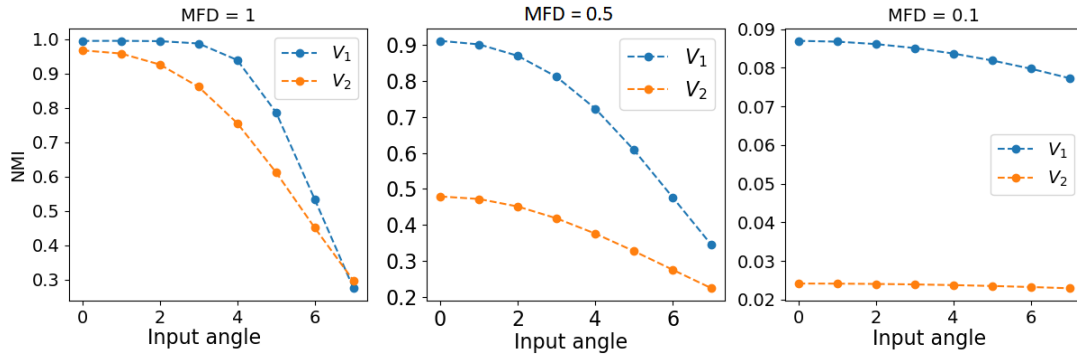

Figure 3.20: Normalized mutual intensity as a function of the input angle. Two different systems with $V_1 > V_2$ were tested.

As can be observed from Fig. 3.20, low normalized mutual intensity values can be achieved when the input spot is relatively small compared to the fibre diameter. Fibres with higher normalized frequency values are less sensitive to angle dependent coupling loss. Due to the high number of propagation modes in real fibres used for astronomical instrumentation, the angle dependent loss is minimal, as long as the input field is within the NA of the fibre.

Simulations of the beam parallel method were used to obtain the far-field angular distribution. Similar to the analysis presented in the previous section, (Sec. 3.6.1), the 2D ring distribution was averaged into a 1D function. For these tests, a Gaussian function was fitted on top of the 1D distribution. It is based on the same process described in Sec. 2.4.2. Since no perturbations and other effects are taken into account, only modal distribution accounts for the width of the ring produced in the angular distribution. As originally presented in Gloge (1972)[52], the modal far-field distribution can be approximated best with a Gaussian function. The standard deviation of the Gaussian fit function can be used as a measure of the divergence. Figure 3.21 shows the example of a simulated far-field distribution and its corresponding 1D averaged distribution. The Gaussian fit is also illustrated in the 1D plot. The simulated fibre was the $50\mu m$ circular fibre with NA $= 0.209$ and $\lambda = 633nm$. The input angle was $\phi = 7^o$.
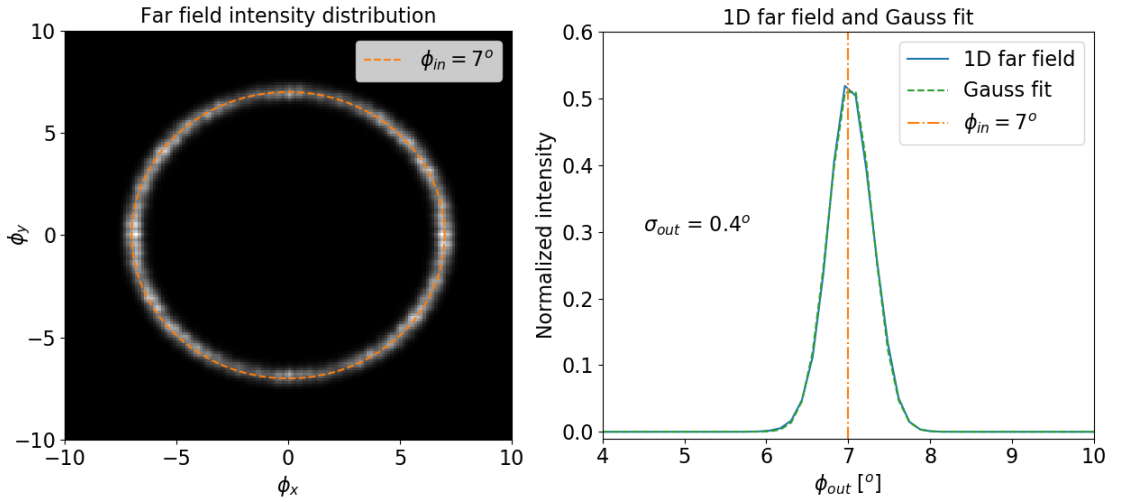

Figure 3.21: Example of a simulated far-field distribution and its corresponding 1D averaged distribution.

The standard deviation equals 0.4^o in the example presented in Fig. 3.21. The input angle ϕ_{in} is marked in both the 2D and 1D intensity distributions. The error between the Gauss fit and the 1D distribution was calculated as $err = |F(\phi) - Fit(\phi)|^2$, with both functions normalized to unity as in $\sum_0^n |F(\phi_n)|^2 \overset{!}{=} 1$. The obtained value was of 5.86×10^{-4}, which indicates $err \approx 0$. Since only the modal far-field distribution is taken into account, such a low error value was expected [52].

To run a simulation, the input angle ϕ_{in} is set to a specific value, e.g. $\phi_{in} = 7^o$, and afterwards the input field diameter is incremented from $0.1d_f$ up to $5d_f$. As in the previous simulations, df indicates the diameter of the simulated fibre. The output is expressed in the angular divergence of the standard deviation. Figure 3.22 shows the example for the input angle $\phi_{in} = 7^o$. As before, the simulated fibre was the $50\mu m$ circular fibre with NA $= 0.209$. The propagation wavelength was $\lambda = 633nm$, which results in $m \approx 1200$ modes and a normalized frequency $V = 51.98$.

As can be observed in Fig. 3.22, the output angular divergence increases with decreasing input field diameter. The minimal value is marked in the plot with $\sigma_{out,min} = 0.39^o$. If the input field diameter equals the diameter of the optical fibre, the corresponding output divergence equals $\sigma_{df} = 0.48^o$. This is a ratio of $\sigma_{df}/\sigma_{min} = 1.28$, which is quite substantial. For obtaining the minimum output divergence, a beam larger than the fibre needs to be used. Coupling a beam larger than the diameter of the fibre results in coupling losses. It means, there needs to be a trade-off between output beam divergence and coupling
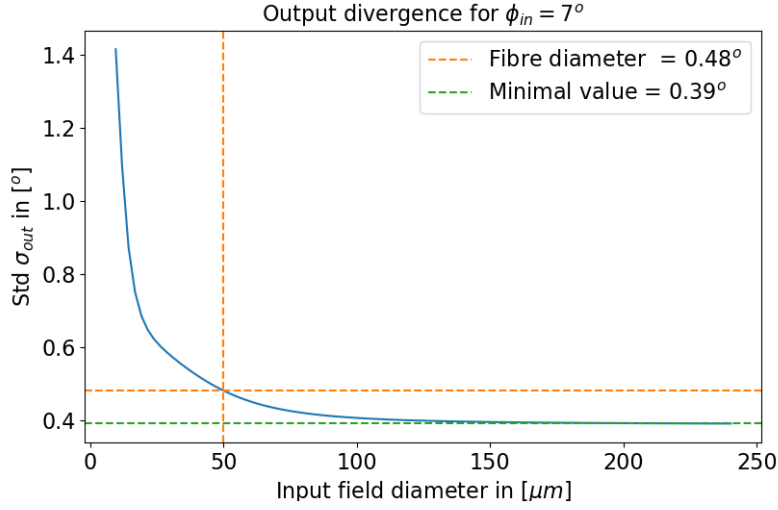
Figure 3.22: Example of the far-field divergence as a function of the input field diameter. The divergence is expressed as the standard deviation of the Gaussian function needed to fit the 1D averaged far-field intensity. When the input field is the size of the fibre diameter, the result diverges from the minimal achievable value.

losses, if the minimum divergence wants to be achieved. Furthermore, the input spot diameter is always equal to or smaller than the fibre diameter. When the spot diameter is of a similar size to the fibre core diameter ($d_{input} \sim d_{fibre}$), minimal fluctuations can create substantial changes in the output divergence.

The behavior shown in Fig. 3.22 was noticed for all tested input angles. As illustrated in Fig.3.20, the normalized mutual intensity (NMI), i.e. coupling, not only depends on the input angle, but also on the FWHM. For this matter, the NMI was analyzed as a function of the FWHM for a fix input angle in the same way as the output divergence σ_{out}. For the same fibre configuration, Figure 3.23 shows the results for two different input angles $\phi_1 = 6^o$ and $\phi_2 = 11^o$. For ϕ_1, the coupling is as expected. If the input field diameter is smaller than the fibre, the beam will be coupled with a good efficiency. For ϕ_2, the efficiency of the coupling does depends substantially on the input field diameter.
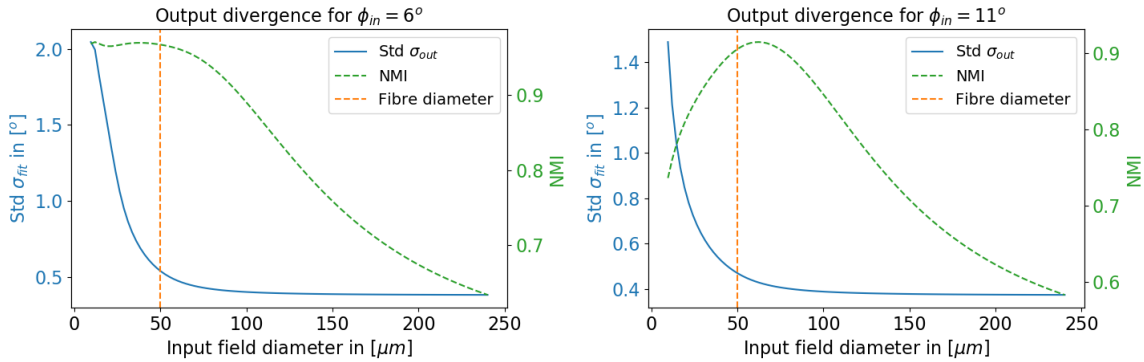
Figure 3.23: Output divergence and normalized mutual intensity as a function of the input field diameter for two different input angles $\phi_{in} = 6^0$ and $\phi_2 = 11^o$.

Coupling loss as a function of the input angle was observed for $\phi_{in} \geq 10^o$, which equals $f\# \leq 2.87$. A higher input angle does helps with the output divergence, since the closer ϕ_{in} to ϕ_{max}, less output divergence is obtained. But if the input angle surpasses a certain threshold, coupling loss will be added to the beam divergence, produced among other factors from the input filed diameter being smaller than the fibre.

Chapter 4

Experimental Setup

Introduction

To test the accuracy of the field propagation model, experimental measurements were conducted on two different test fibres, and the results were compared to simulations with identical parameters as the test fibres. An appropriate experimental setup required FRD measurements with the parallel laser beam method and light cone method. At the time of the measurements, the experimental test-bench developed by Dionne Haynes for prototypes of the science fibres from the 4MOST fibre feed [40] was available, giving the possibility of conducting parallel laser beam measurements, light cone measurements, and scrambling measurements as described in Sec. 2.4. If not stated otherwise, all the measurements and fibre preparation steps were conducted by the author of this thesis.

This chapter is divided into two sections. The first section describes the preparation steps for the measured fibres. Since fibre preparation and termination techniques induce mechanical stress, modal effects are highly sensitive to how these techniques are applied. The second section describes the 4MOST fibre test-bench and the available configuration possibilities.

4.1   Fibre Preparation

Mechanical stress causes perturbations to the refractive index distribution, affecting directly the modal distribution in the fibre. Worst case scenario, fibres could have an enormous amount of losses due to negligence in the preparation techniques. Authors like Avila (1998) [38], Haynes et al. (2011) [53], and Allington-Smith et al. (2012) [39] have demonstrated how imperative termination techniques are for maintaining focal ratio degradation, i.e. loss of throughput in the system, as low as possible.

The preparation techniques for fibres in a lab environment were learned from Dionne Haynes, who worked for the characterization of the 4MOST fibres at the Leibniz Institute for Astrophysics Potsdam (AIP) until the spring of 2019. Two fibres were successfully prepared and measured. Both were purchased as bare fibre rolls. Compared to commercial fibre optic cables, bare fibres do not have a multi-layer protective coating surrounding the cladding. Typically, only a buffer or jacket surrounds the cladding, thus bare fibres are intended for controlled environment usage, e.g. laboratory measurements. In addition, bare fibres have no end-termination (i.e. no connectors).

The first fibre was a circular fibre with a core diameter $d_{core} = 50\mu m$, cladding diameter $d_{clad} = 70\mu m$ and NA $= 0.22 \pm 0.02$. It was an FBP fibre from Polymicro Technologies, which is a type of fibre that is known due to its low loss broad spectrum characteristics in the range from $210nm$ up to $2100nm$. The

core was made of silica and the clad of doped silica. The jacket material was an acrylate buffer. The attenuation coefficient α_λ for the $633nm$ wavelength had a value $\alpha_{633nm} = 3.0dB/km$. It had an original roll length $l = 14m$. The exact batch identification is FBP050070085. This information was given by the manufacturer Polymicro Technologies, Molex$^\circledR$.

The second fibre was an octagonal fibre with a core diameter $d_{core} = 50\mu m$, a cladding diameter $d_{clad} = 90\mu m$, and NA $= 0.22 \pm 0.02$. It was an Optran$^\circledR$ broadband fibre for applications from UV-C to IR-B in the range from $200nm$ to $2000nm$. Information on the attenuation coefficient α_λ for the $633nm$ wavelength was not available. The core was made of silica and the cladding of fluorine-doped silica. The jacket material was polyimide. The original roll length was $l = 10m$. The exact batch identification is OCTWF50/94P. This information was given by the manufacturer Ceram Optec$^\circledR$. Table 4.1 shows the main parameters of both fibres.

Parameter	Circular fibre	Octagonal fibre
Core diameter d_{core}	$50\mu m$	$50\mu m$
Clad diameter d_{clad}	$70\mu m$	$90\mu m$
NA	0.22 ± 0.02	0.22 ± 0.02
Core/clad material	silica/doped silica	silica/doped silica
Low loss bandwidth	$210nm - 2100nm$	$200nm - 2000nm$
α_{633nm}	$3.0dB/km$	-
Buffer	acrylate	polyimde
Manufacture	Polymicro Technologies, Molex$^\circledR$	Ceram Optec$^\circledR$

Table 4.1: Parameters of the circular and octagonal fibres.

A length $l \approx 2m$ was cut from each fibre role. The resulting end-face surface after a fibre cut is highly uneven. Even after a cleaving process, which can be seen as a more controlled fibre cut, the end-face surface could be too uneven for the fibre to be used in laboratory tests. To eliminate any surface damage and reduce the surface roughness, the fibre needs to be polished. Additionally, reducing the surface roughness through polishing diminishes the end-face scattering and the output beam divergence [40].

To be able to polish a bare fibre, the buffer needs to be removed and typically a ferrule or any type of reinforcement mechanism needs to be attached to both ends of the fibre. Both fibres had different types of buffer. Therefore, two different buffer removing techniques were applied. To avoid inducing mechanical stress that could damage the fibre, chemical removal, e.g. with hot sulfuric acid, is recommended for an acrylate buffer [90]. This option was not available at the time the fibres were prepared. The acrylate buffer was removed mechanically with a simple razor blade. Since too much pressure from the blade would have broken or shattered the fibre, the buffer removal was a very delicate process. After the acrylate buffer was removed, the fibre was cleaned to remove any buffer fragment that could have still be attached. Acetone or isopropyl alcohol (IPA) are usually used for the cleaning process.

A polyimide jacket can not be removed mechanically (e.g. with a razor blade). Although chemical removal is suitable, it was not an available option. A laser stripping machine is usually recommended. It uses typically an excimer laser source (308nm) to avoid thermal heating. An advantage of the laser removal method is that no stress is induced to the fibre, eliminating the risk of damaging the fibre due to mechanical stress [90]. An alternative was used for removing the buffer. The 3SAE Technologies Polyimide Fiber Preparation Unit II, FPUII, was used. It provides a non-contact, chemical free removal of the polyimide jacket. It uses the 3SAE's patented Ring of Fire$^\circledR$ technology. The fibre gets surrounded by a low temperature arc plasma that is delivered through 3 electrodes and eliminates the polyimide jacket.

After the buffer was removed, it was possible to attach the ferrules to both ends of the fibres. The adhesive material was the two-component epoxy EPO-TEK$^\circledR$ 301-2 from Epoxy Technology. It is a slow hardening adhesive, quality that is needed to ensure low stress/pressure gradients that could cause mirco ruptures and would increase FRD/throughput losses. Thomas Jahn helped with this process since he had developed an effective and efficient technique for the adhesive to be equally distributed along the fibre and inner part of the ferrule.

After the ferrules were attached, the fibres could be polished. The fibre end needed to be mounted into a polishing jig which was designed and made in house. To manually achieve a smooth fibre end-face finishing, different polishing films were needed. At first, a course film is used. Afterwards, a smoother film is applied in each following step. The polishing films were acquired from ThorLabs, Inc. The fibres were end-polished with a film having a grid size of $1\mu m$. A profilometer was not available. Actual measurements of the surface roughness on the fibre end-faces were not possible. A Buehler$^{\circledR}$ ViewMet$^{\text{TM}}$ inverted laboratory microscope was available and was used to acquire images of the results from the fibre preparation process. Figure 4.1 shows the end results of both fibres.
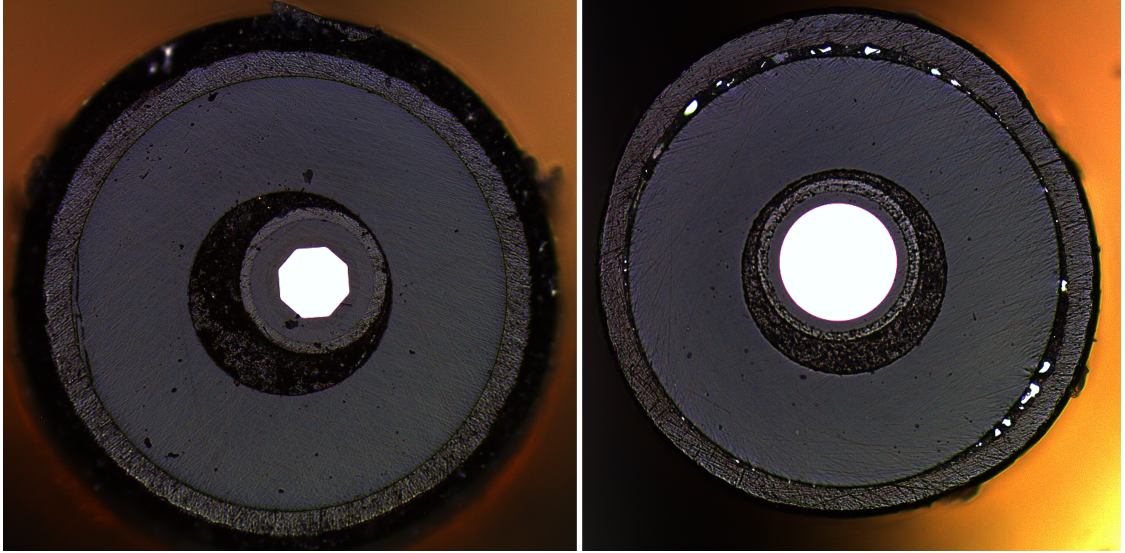

Figure 4.1: Final product of the octagonal and circular fibre after preparation. Around two meters of each fibre were cut from the fibre roll; the buffers were removed with the appropriate and available techniques; the ferrules were attached with slow hardening adhesive to minimize FRD; and finally, the fibres were polished. The fibres were end-polished with a film having a grid size of $1\mu m$. The images were taken with a Buehler$^{\circledR}$ ViewMet$^{\text{TM}}$ inverted laboratory microscope.

4.2 Description of the Test-Bench

The test-bench was developed and used by Dione Haynes to characterize the FRD and throughput properties for prototypes of the science fibres from the 4Most fibre feed [40]. Through it, the simulation of the VISTA telescope pupil was possible. The beam speed could be set to $F/3.32$ and a pupil stop was available that had the entrance aperture with both the central obscuration and secondary mirror support structure of the VISTA telescope [40]. Additionally, a second assembly was available at the input feed that allowed measurements using the parallel laser beam technique.

The test-bench was mounted on a large optical table with thick protective black curtains to prevent light contamination. It was separated via an internal curtain into two parts: 1) the Back-End and 2) the Front-End. This was done to ensure the minimum amount of contamination from the light sources to the measurement devices (e.g. CDDs). Light sources were located in the back-end of the test-bench, while the measurement devices were located at the front-end of the test-bench. Figure 4.2 shows a schematic illustration of the test-bench.
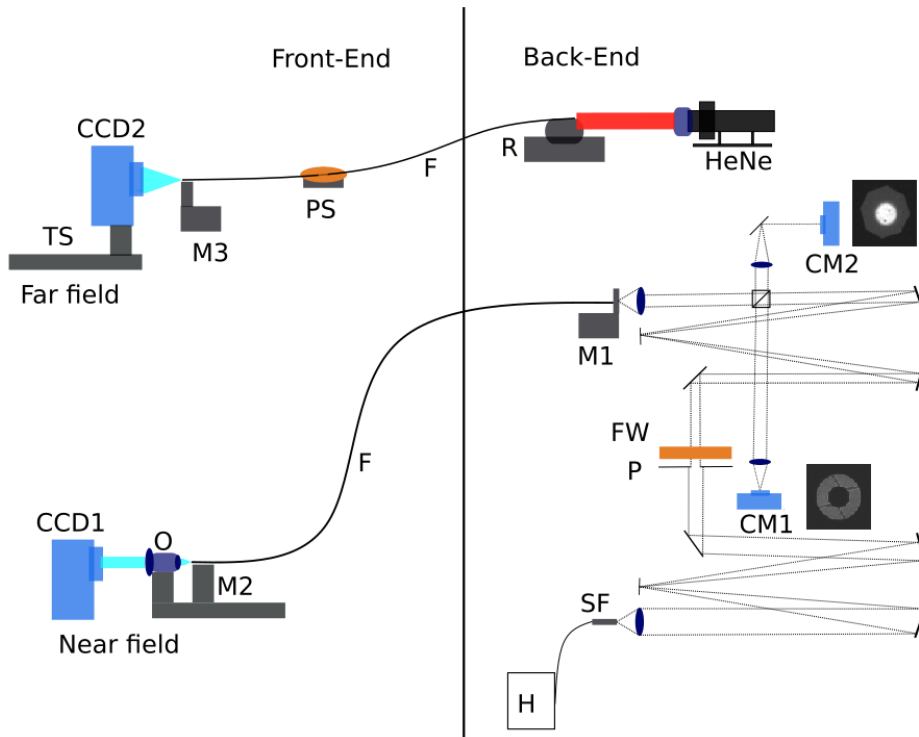
Figure 4.2: Schematic representation of the optical test-bench. [**Back-End**] H: Halogen lamp; SF: seed fibre + 10×LWD objective; P: interchangeable pupil stop; FW: filter wheel; M1: x-y-z stage with pitch and yaw platform + 10×LWD objective; CM1: pupil control CMOS + 10×LWD objective; CM2: injection control CMOS + magnification optics; HeNe: helium-neon laser + beam expander; R: rotation stage. [**Front-End**] F: test fibre; M2: x-y-z stage; O: 50×LWD objective; CCD1: 1kx1k Apogee CCD camera; PS: probe shaker; M3: x-y-z stage; TS: translation stage; CCD2: 2kx2k Apogee CCD camera [40].

4.2.1   Back-End

The back-end of the test-bench contained the light sources and allowed for different light injection methods into the optical fibre. Two light sources were available: the HeNe laser for the parallel laser beam measurements, and the halogen lamp for the light cone and scrambling measurements. The halogen lamp was introduced via a seed fibre into the test-bench. The seed fibre, **SF** in Fig. 4.2, had a core diameter of $20\mu m$. The near field of the seed fibre was expanded with a $10\times$ long working distance (LWD) objective before it entered the optical path. After the optical path, the near field of the seed fibre was re-imaged at the input of the test fibre with another $10\times$LWD objective. The result was a $20\mu m$ input spot.

The optical path allowed to introduce an aperture into the pupil plane. Figure 4.2 describes the interchangeable pupil stop as **P**. Through the available pupil stops, different f-numbers could be introduced into the fibre. Directly after the aperture, a filter wheel, **FW** in Fig. 4.2, was mounted. Filters with the following central wavelengths λ_c were available: $436nm, 546nm, 600nm, 750nm$, and $905nm$. Each filter had a $\Delta\lambda = 10nm$ bandwidth. A re-imaging arm was used for the alignment and focus control of the pupil. The pupil control image was delivered to the CMOS camera **CM1** in Fig. 4.2. The mount stage for the optical fibre, **M** in Fig. 4.2, was an x-y-z stage with pitch and yaw platform and allowed for the adjustment of the input spot across the fibre input face. A secondary re-imaging arm was used for alignment and focus control of the input spot. The input image was delivered to the CMOS camera **CM2**. The helium-neon laser was the second source. For safety reasons, a beam expander was used at the output of the laser for expanding and then collimating the beam to a diameter $d_{beam} = 50mm$. If the HeNe laser was used, then the test fibre was mounted into the rotation stage **R** in Fig. 4.2. The stage had one axis of rotation and was capable to rotate from -2π to 2π.

4.2.2 Front-End

The front-end of the test-bench contained the CCD cameras. Both far-field and near-field measurements were possible. For recording the near-field, the fibre was mounted on an x-y-z stage, **M2** in Fig. 4.2, and brought to the focus of the 50×LWD objective labeled as **O** in Fig. 4.2. The objective projected the fibre end-face into the 1kx1k Apogee CCD camera illustrated as **CCD1** in Fig. 4.2. CCD1 operated with a thermoelectric cooler that could reach a nominal temperature difference of $\Delta T = -40^{o}C$ from the room temperature. Since the lab had a controlled room temperature of $T_o = 20^{o}C$, the CCD1 was operating at $-20^{o}C$.

For the far-field measurements, the fibre was mounted on the x-y-z stage **M3** in Fig. 4.2. The fibre was attached to a probe shaker, **PS** in Fig. 4.2, for agitation and inducing modal scrambling [67]. The probe shaker was also used for the near-field measurements. It was the Vortex-Genie 2 from Scientific Industries, Inc. To prevent too much mechanical stress on the fibres, it was never operated over level 6 of the available power range. The output of the fibre was recorded directly into the 2k×2k Apogee CCD **CCD2** in Fig. 4.2. The temperature of CCD2 was also regulated by a thermoelectric cooler, having the same characteristics and working temperature as CCD1. To map the output cone of the fibre, the CCD2 was mounted on the translation stage **TS** in Fig. 4.2. TS had a range of 150mm. For the light cone measurements, only 10mm were needed. A step size $\Delta x = 1mm$ was used.

4.2.3 Available configurations

Three types of measurements were done for comparing experimental results to the simulations: parallel laser beam measurements, light cone measurements, and scrambling measurements. Each needed a particular part of the back-end or front-end. Each of the three arrangement will be explained.

Parallel laser beam measurements

In the back-end, the HeNe laser was used as the input source for the parallel laser beam measurements. Due to the beam expander, the input beam had a diameter of $50mm$. Since the fibre was mounted on the rotation stage, different input angles ϕ_{in} for the incoming beam were possible. The input angle was changed in steps $\Delta\phi_{in} = 1^{o}$ in both positive and negative directions.

In the front-end, both near-field and far-field were measured. In both cases, measurements were realized with and without induced modal scrambling. By attaching the test fibre to the probe shaker, the fibre was agitated and mode scrambling was induced. Since a highly coherent source was used, measurements without scrambling were dominated with modal interference. These measurements gave the opportunity to analyze the speckle pattern intensity as a function of the input angle $I(\phi_{in})$. When scrambling was induced, it was possible to compare the intensity fields with simulations using incoherent propagation. Furthermore, it was possible to use the Voigt function to analyze the divergence of the far-field ring as a function of the input angle. Figure 4.3 shows the parts of the test-bench used for the parallel laser beam method. In this example, both near- and far-field images are from the circular fibre. The input angle in both images was $\phi_{in} = 9^{o}$. The output fields are dominated by modal interference, producing a uniformly distributed speckle pattern.

Light cone measurements

The halogen lamp was the input source for the light cone measurements. The halogen lamp was connected to the $20\mu m$ seed fibre. The near-field of the seed fibre was re-imaged as the input spot in the test fibre. Different f-numbers and different wavelength filters were available. Measurements were realized with the input spot located at the center of the fibre. The CMOS camera CM2 was used to assure that the input
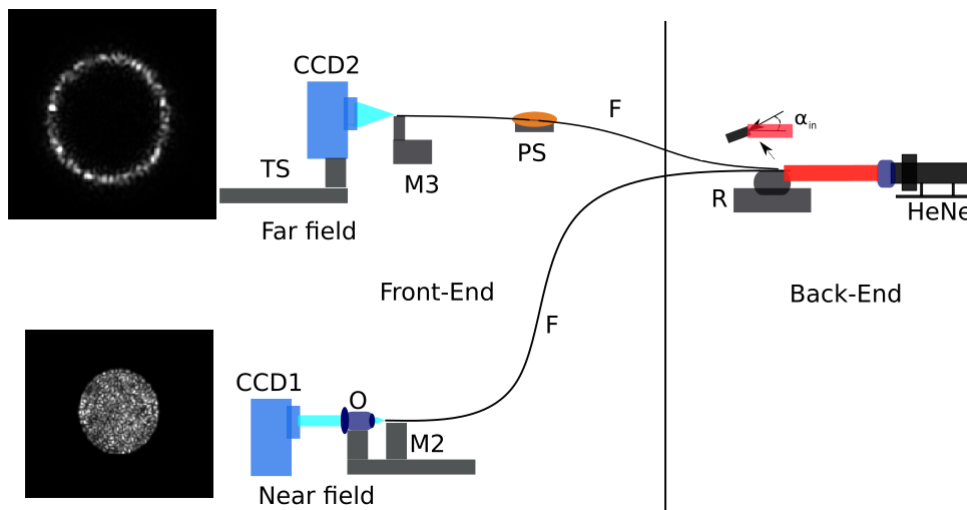
Figure 4.3: Example of the parallel laser beam measurements using the test-bench. Both near-field and far-field are shown. The source is the HeNe laser. The input angle is $\phi_{in} = 9^o$ in both cases. Since the source is highly coherent and no scrambling is induced, measurements are dominated by modal interference. A speckle pattern is visible in both NF and FF images.

spot was in focus. The image delivered to CM2 was additionally used to control and move the input spot across the input face of the test fibre.

The light cone method only needs the recording of the far-field intensity distribution. The far-field distribution was recorded through 10 controlled steps $\Delta x = 1mm$ of the translation stage. Afterwards, a linear fit as a function of the encircled energy determines the output f-number. Since a broadband source was used, no fibre agitation was needed. Figure 4.4 shows the elements in both back- and front-end for the light cone measurements. It shows an example of three images taken in three consecutive Δx steps of the translation stage.
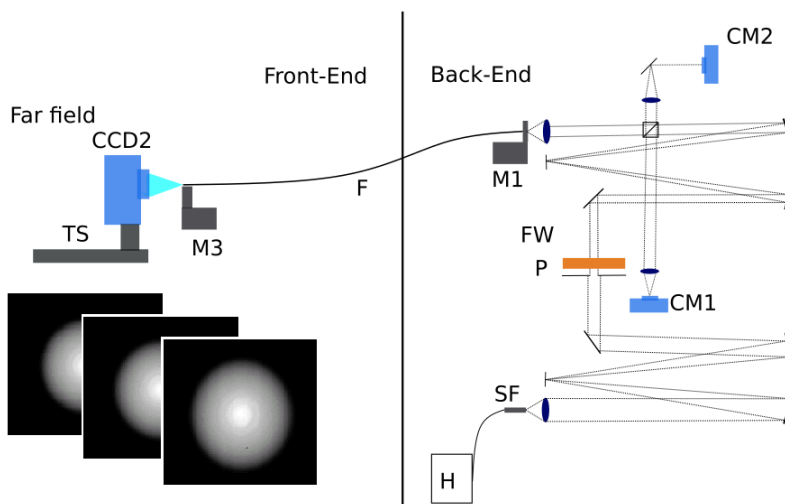

Figure 4.4: Example of the light cone measurement using the test-bench. Three images are taken in three consecutive Δx steps of the translation stage. The source is the halogen lamp connected to the $20\mu m$ seed fibre.

Scrambling measurements

For the scrambling measurements, the input source was once more the halogen lamp connected to the seed fibre. Similar to the light cone measurements, different f-numbers and different wavelength filters were available. The input spot was moved in Δx_{in} steps across the input face of the test fibre. The image delivered to the CMOS camera CM2 was used to control and regulate the movement across the fibre input face. The x-y-z-stage was operated manually for each translation step Δx_{in}. In the front-end, both near- and far-field could be measured. Figure 4.5 shows the elements in the back- and front-end for the scrambling measurements.
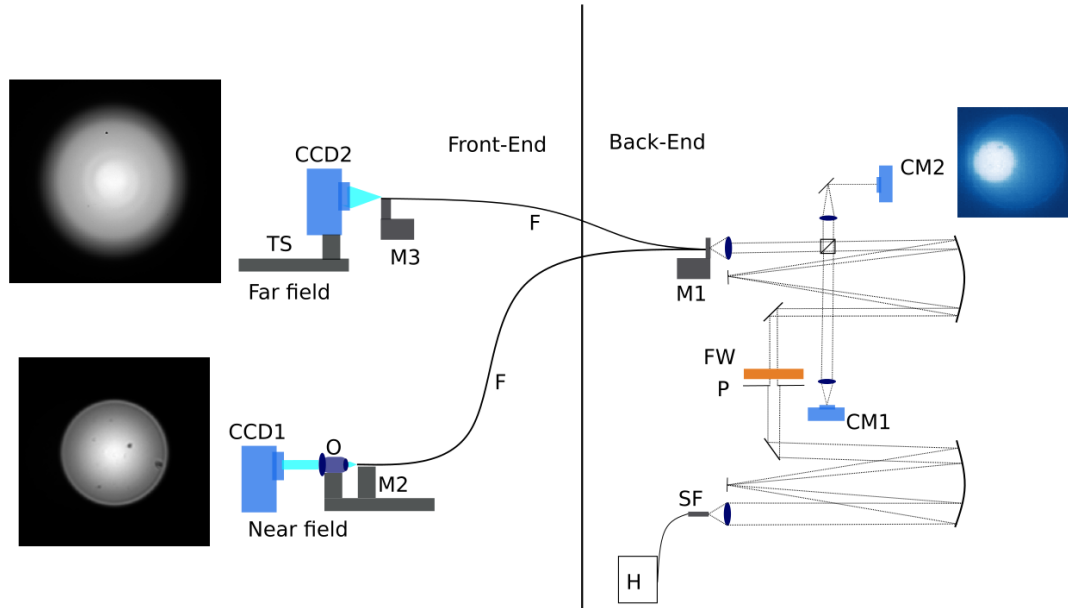

Figure 4.5: Example of the scrambling measurements using the test-bench. The images are from the circular fibre. The source is the halogen lamp connected to the $20\mu m$ seed fibre. An image of CM2 illustrates how the input spot could be located at the edge of the test fibre. In the front-end, both near-field and far-field are displayed.

Chapter 5

Analysis and Results

Introduction

The possibility of obtaining realistic measurements allowed testing the accuracy of the field propagation model developed for astronomical multimode fibres. Since the properties of every measurement were known, similar results were expected when emulating the parameters in the simulation environment.

The simulations work under certain constraints. For example, the loss coefficient α_λ is not taken into account. However, since the distances of the fibres were $\sim 2m$, the lack of the loss coefficient was not noticeable. A suitable approach for partial coherence was not develop in this work, meaning simulations restricted to the coherent or incoherent propagation case were possible. It is still to be investigated, how partial coherence affects the output fields of highly multimode fibres. Only monochromatic propagation can be simulated. This was an issue for both the light cone measurements and scrambling measurements since a halogen lamp was used as the source. However, wavelength filters with a bandwidth $\Delta\lambda = 10nm$ were available. Although the simulations resembled a simplified situation of the field propagation in highly multimode fibres, comparable results were achieved.

The first section of this chapter presents the analysis done on modal interference. Due to the coherence of the HeNe source, it was possible to analyze the near-field speckle pattern resulting from the different injection angles ϕ_{in} into the test fibers. The power spectral distribution was used for the analysis (see Sec. 2.4.3). Section 5.2 deals with induced modal scrambling. First, the monochromatic case is examined. Afterwards, the simulations are compared with measurements in which the halogen lamp was used as the source. The results of near-field enlargement and incoherent intensity fluctuations are illustrated.

The angular far-field analysis of the parallel laser beam measurements is introduced in Sec. 5.3. The divergence of the far-field that originates as a function of the input angle ϕ_{in} is analyzed. Since the simulations are limited to the modal diffusion element of the far-field distribution (see Sec. 2.4.1), the modal diffusion element needed to be extracted from the measurements. This was achieved by means of the Voigt function [53]. The angular divergence between measurements and simulations is compared and shown as a figure of merit. Furthermore, it will be explained, how the angular divergence of the measurements was matched through the mode coupling parameter of the simulations.

Section 4.4 deals with the light cone measurements. Examples of the FRD characteristics from the test fibres are given. Calculations of the loss of radiance as a function of the f-number are presented. How the cone of light can be simulated is explained in this section. Afterwards, the simulations are used to match the FRD characteristics of the measured fibres. The last section provides a summary of all the insights obtained throughout this chapter.

5.1   Analysis of Modal Interference

The test-bench was in the configuration of the parallel laser beam measurements. The optical source was the HeNe laser. Since the field propagation model simulates only monochromatic light, it makes the HeNe laser a suitable source for comparison. The coherence of the laser source causes modal interference in both the near- and far-field. Modal interference is the origin of speckles in the output fields. The corresponding size of the speckles can be expressed as a function ϕ_{in}. As already demonstrated in Sec. 3.6, the increase of the input angle yields the excitation of higher-order modes. Analog to the Fourier analysis, higher-order modes have higher spatial frequencies that account for the finer speckle pattern.

Both the circular and the octagonal fibres were measured. The characteristics of the fibres can be found in Tab. 4.1. As described in Lemke et al. (2011) [73], the number of modes that propagate in the system can be approximated by the number of speckles that can be counted in the near-field distribution. This statement was proved by simulations. In the same manner as the measurements, the near-field distribution was simulated as a function of increasing input angles $\phi_{in} \in \{0^o, 1^o, ..., 12^o\}$. Figure 5.1 shows the example of simulations and measurements with two different input angles, $\phi_{in,1} = 1^o$ and $\phi_{in,2} = 10^o$. The axes of the measurements are in pixels, and the axes of the simulations are in micrometers (μm). For clarity, only the values of the axes are illustrated.

Figure 5.1: Measurement and simulations of the near-field intensity using input angles of $\phi_{in,1} = 1^o$ and $\phi_{in,2} = 10^o$. The axes of the measurements are in pixels, and the axes of the simulations are in micrometers (μm). For clarity, 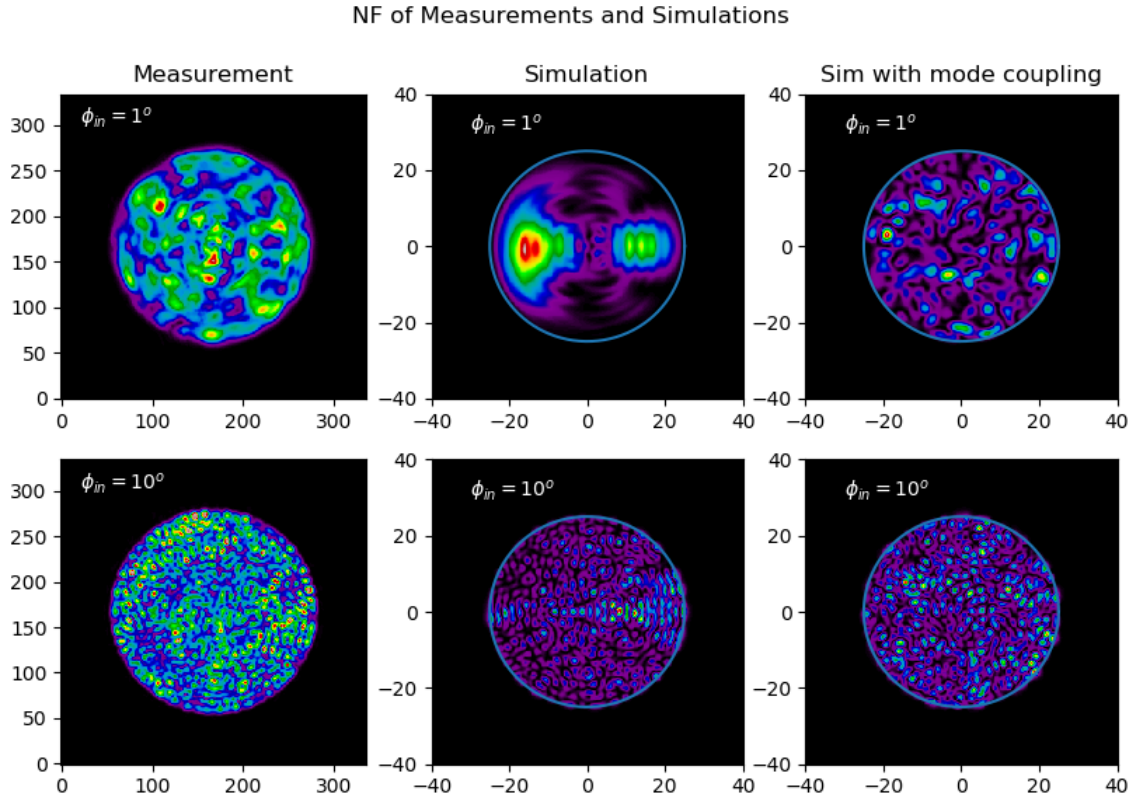only the values of the axes are illustrated. *(left)* Measurements; *(center)* Simulations; *(right)* Simulations with mode coupling.

As stated in Sec. 4.2, the $50\times$LWD objective was used to image the near-field intensity distribution into the $1k \times 1k$ CCD. For better comparison reasons, the original output field was cropped to an appropriate size. For a better resemblance to the $\phi_{in} = 1^o$ measurement, mode coupling needed to be simulated. As can be seen in Fig. 5.1, the simulation without mode coupling do not appear to reproduce a similar

outcome as the measurement for the shallow input angle. This is due to the fact that a higher number of modes than expected are excited. Effects like refractive index defects in the fibre or mechanical stress caused by the input/output interfaces could be the cause of the augmented number of propagation modes. For $\phi_{in} = 10^o$, both simulations have a similar outcome as the measurements. This relies on the fact that the group of modes with the highest order and power (modal amplitudes) accounts for the size and shape of the speckle pattern.

As demonstrated in Gloge (1972) [52] and Allington-Smith et al. (2011) [39], the power interchange between the modes is a critical cause for the beam divergence in the angular far-field distribution. Since mode coupling appears to have an important influence in the outcome of the results, it will be taken into account for the rest of the comparisons. How mode coupling is simulated in the field propagation model, is explained in Sec. 3.5. A fixed value for σ is implemented, if not stated otherwise. As can be seen in Fig. 3.12, a low σ-value results in minor mode coupling.

Equation 3.11 is used to calculate the number of modes as a function of the input angle ϕ_{in}. If solved for M, it equals

$$M(\phi_{in}) = \frac{(2\pi r \sin(\phi_{in}))^2}{2\lambda^2}. \tag{5.1}$$

To get an estimate on the number of speckles in the near-field intensity distribution, the ratio between the area of a speckle and the area of the fibre is calculated. This was performed for the measurements and the simulations. Figure 5.2 shows the results as well as the theoretical calculations of the number of modes using Eq. 5.1.
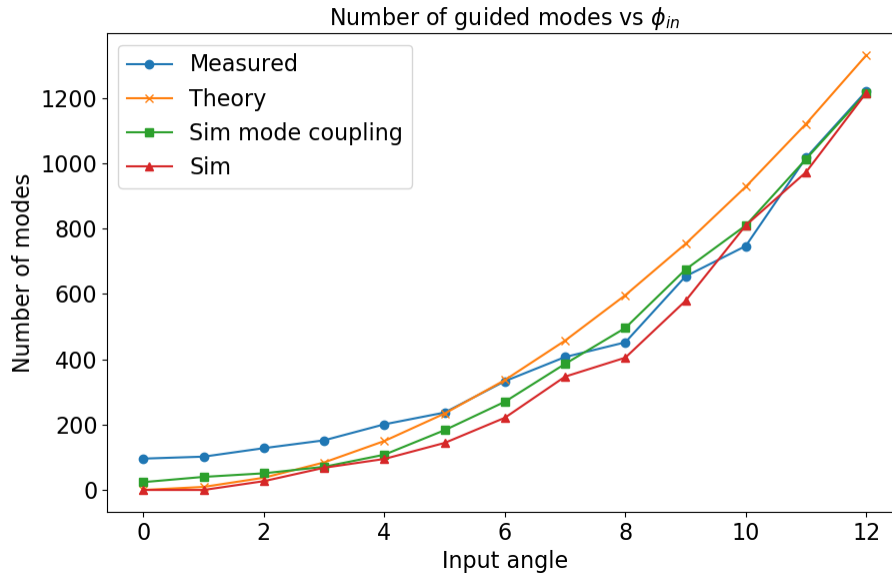

Figure 5.2: Number of modes vs input angle ϕ_{in}. The theoretical calculation using Eq. 5.1 is shown and compared to the estimation of the number of speckles for both measurement and simulations.

Figure 5.2 shows a good agreement between theoretical calculations (Eq. 5.1) and measurements/simulations. The measurements do show a higher number of active modes for shallower input angles. It resembles the results from Lemke et al. (2011) [73], in which the experimental results seem to have an higher number of modes than the theoretical prediction for lower incident angles. In the same manner, fewer number of modes than the theoretical predictions could be observed for steeper incident angles.

The number of speckles increases with the increment of the incident angle, but the actual amount of active modes does not necessarily increases. As already stated, the active group of modes with the highest number and power dictates the speckle pattern. Various examples can be seen in the simulations of the

modal power distributions presented in the Chapter 3. Any input angle ϕ_{in} excites a specific group of modes that accounts for the output fields as a function of the angle. This does not mean that all modes are excited until that specific group.

5.1.1   Power spectral density analysis

Although the visual representation and the counting of modes are helpful tools to assess the resemblance between the simulations and experimental data, spatial frequency analysis provides a better tool for the characterization of the modal variations [71]. This can be achieved through the power spectral density (PSD) analysis. As already explained in Sec. 2.4.3, the PSD is the Fourier transform of the autocorrelation function of the field which contains the power across a range of wave vectors. It decomposes the field's intensity into contributions from different spatial frequencies [72]. The PSD provides a powerful tool for analyzing surface roughness and can be applied to examine speckle pattern variations.

The first step for obtaining the PSD requires the calculation of the 2D Fast Fourier Transform (2D FFT) from the near-field intensity distribution, $I_{NF}(x, y) = |\Psi_{NF}(x, y)|^2$. Afterwards, the power spectral density is given through the square of the absolute value as

$$PSD = |\mathcal{F}\left(I_{NF}(x, y)\right)|^2 = |I(\nu_x, \nu_y)|^2 \,, \tag{5.2}$$

with I_{NF} representing the near-field intensity and $I(\nu_x, \nu_y)$ representing the image after the FFT in the spatial frequency plane (ν_x, ν_y).

To successfully compare spatial frequencies between measurements and simulations, the measurements were cropped to the same area as the simulations. This means an $80\mu m \times 80\mu m$ area. Since the measured fibre is augmented by a $50\times$LWD objective, it means it should project a diameter $50\mu m \times 50\mu m = 2500\mu m$ on the CCD. The pixels of the CCD are of $13\mu m$, which means that the effective diameter of $2500\mu m$ should be sampled by ≈ 192 pixels. The $80\mu m$ frame of the simulations should be mapped by the CCD on $80 * 50/13 \approx 308$ pixels. The actual measurement of the fibre projects on the CCD a diameter of $\approx 2730\mu m$ and diverges from the $2500\mu m$ by 9%. This means the pixel area needs a 9% increment, resulting on ≈ 337 pixels. Figure 5.3 shows the comparison of a near-field measurement cropped to match the simulation area. The simulations extend $80\mu m$ over 280 (sim-)pixels and the measurements extend $80\mu m$ over 337 pixels.
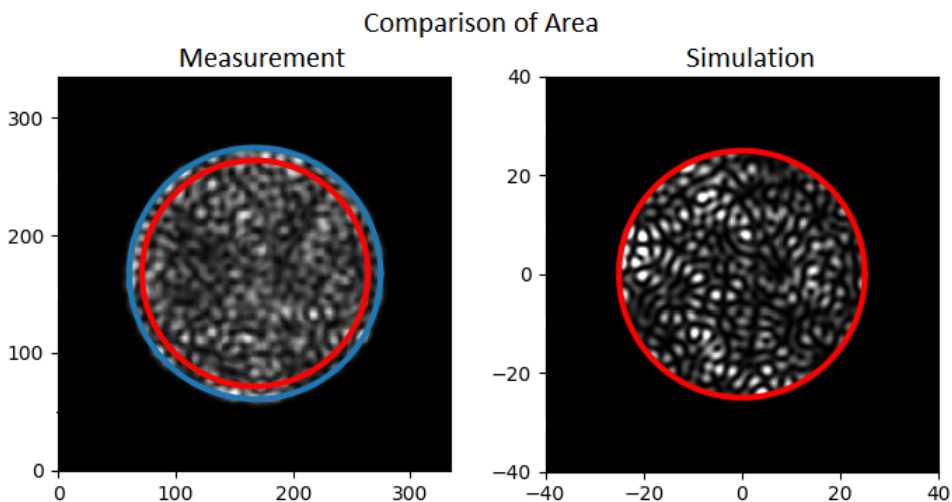

Figure 5.3: Comparison of area to be transformed by the FFT. *(left)* The red circle marks the area that should be mapped by the $50\mu m$ fibre and the blue circle maps the actual size of the $50\mu m$ on the CCD. *(right)* The red circle maps the $50\mu m$ area.

After the 2D-FFT of the intensity field, the spatial frequency image $I(\nu_x, \nu_y)$ is rotationally averaged to produce a normalized power over spatial frequency $\mathcal{I}(\nu)$ 1D-plot. The rotationally averaging of the 2D distribution is explained in Sec. 3.4.3. Figure 5.4 illustrates the process of obtaining the $\mathcal{I}(\nu)$ 1D-PSD for both a measurement and a simulation.
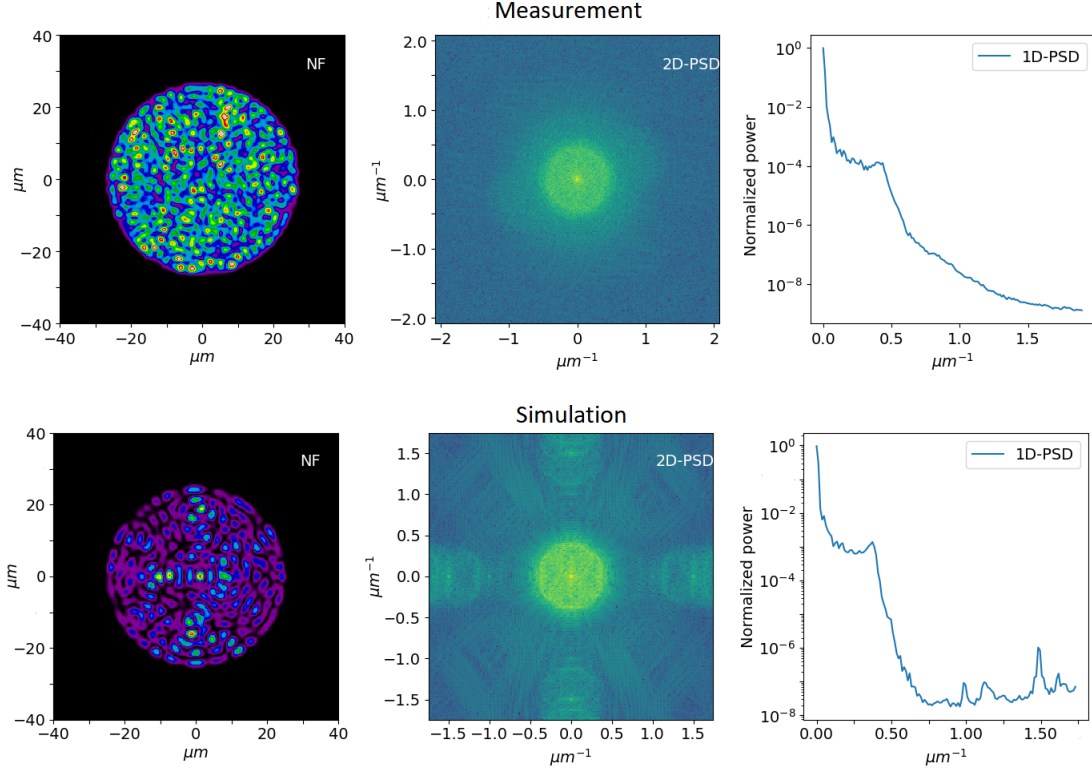

Figure 5.4: Comparison of the power spectral density for a measurement and a simulation. The upper part of the image shows the process for a measurement, and the lower part of the image shows the process for a simulation.

As can be observed in both the 2D- and 1D-PSD, there is high spatial frequency noise in the simulations. It is believed by the author of this thesis that the noise comes from the 2D mesh needed for calculating the propagation modes with the FemSIM module of Rsoft. A non-uniform hybrid triangular/rectangular mesh is used for solving the modes of a 1D and 2D profile. The mesh is calculated automatically based on the required structure, grid size, boundary conditions and other mesh properties. Each triangular and rectangular shaped element has a constant index of refraction that covers the computational domain [81]. The numerical structure of the mesh is saved in every calculated modal distribution and could be the cause of the high spatial frequency noise.

Different ways were tested to get rid of the high spatial frequencies creating noise (e.g. manipulating the grid sizes), but none were successful. For a better comparison of the 1D-PSD, the high spatial frequencies of the simulations was taken as noise and left out. Figure 5.5 shows the comparison between the measurements and the simulations of the 1D-PSD. For the simulations, both the mode coupling case and the case without mode coupling was included. For these examples $\phi_{in} \in \{0^o, 3^o, 5^o, 7^o, 9^o, 11^o\}$.

As can be observed, there is once more a good correlation between measurements and simulations. There is an offset that could come from the difference in the dynamic range. The higher spatial frequencies tend to get more power with increasing ϕ_{in}. This is expected, since higher spatial frequencies imply higher fluctuations in the intensity pattern as a result from the diminished speckle size. The results appear to be in more correlation with higher input angles.
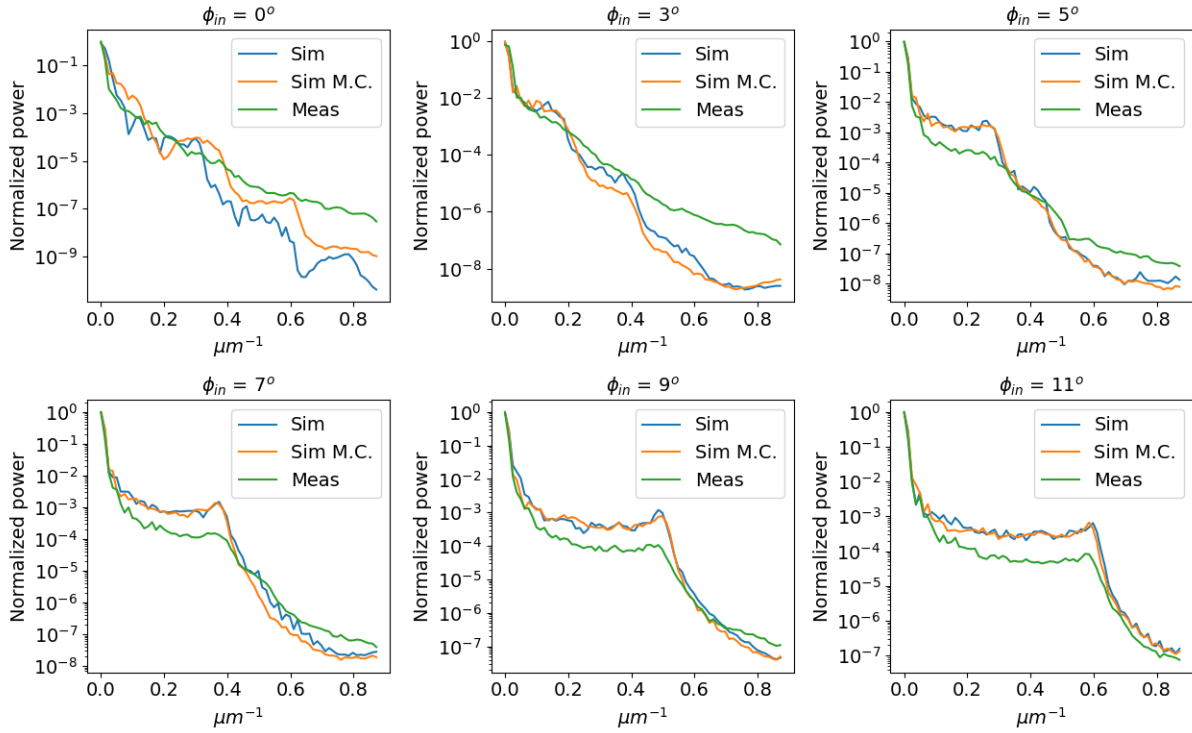
Figure 5.5: Comparison of power spectral density for measurements and simulations with incident angles of $\phi_{in} \in \{0^o, 3^o, 5^o, 7^o, 9^o, 11^o\}$. The x-axis represents the spatial frequency and the y-axis is the normalized power in the logarithmic scale. Simulations with mode coupling are marked as [Sim M.C.], normal simulations as [Sim] and measurements with [Meas].

For all input angles, it appears that mode coupling does not have a substantial change. To verify the actual difference between normal simulations and simulations with mode coupling, the averaged ratio between $\mathcal{I}_{mess}(\nu)$ and $\mathcal{I}_{sim}(\nu)$ was used. It is calculated through

$$\epsilon = \frac{\sum_{\nu}^{N} \left| \log \left(\frac{\mathcal{I}_{mess}(\nu)}{\mathcal{I}_{sim}(\nu)} \right) \right|}{N}. \tag{5.3}$$

Since the 1D power spectral density plot is expressed in the logarithmic scale, it is useful to express the average ratio in dB. This is equivalent to

$$\epsilon_{dB} = 10 \cdot \frac{\sum_{\nu}^{N} \left| \log \left(\mathcal{I}_{mess}(\nu) \right) - \log \left(\mathcal{I}_{sim}(\nu) \right) \right|}{N}. \tag{5.4}$$

If $\rho = \left| \log \left(\mathcal{I}_{mess}(\nu) \right) - \log \left(\mathcal{I}_{sim}(\nu) \right) \right|$ and μ_ρ represents its mean, it is possible to get the standard deviation of the array in dB through

$$\sigma_{\rho,dB} = 10 \cdot \sqrt{\frac{1}{N} \sum_{i=1}^{N} (\rho_i - \mu_\rho)^2}. \tag{5.5}$$

The lower the values ϵ_{dB} and $\sigma_{\rho,dB}$, the better the simulations resemble the measurements. Figure 5.6 shows comparison of the average ratio ϵ_{dB} and the standard deviation $\sigma_{\rho,dB}$ for the simulations with and without mode coupling using the input angles $\phi_{in} \in \{0^o, 1^o, ..., 12^o\}$.

Figure 5.6 illustrates the divergence between simulations and measurements for smaller input angles. Both ϵ_{dB} and $\sigma_{\rho,dB}$ diminish substantially towards higher input angles. Mode coupling reduces ϵ_{dB} throughout the complete range $\phi_{in} \in \{0^o, 1^o, ..., 12^o\}$, with a few exceptions.
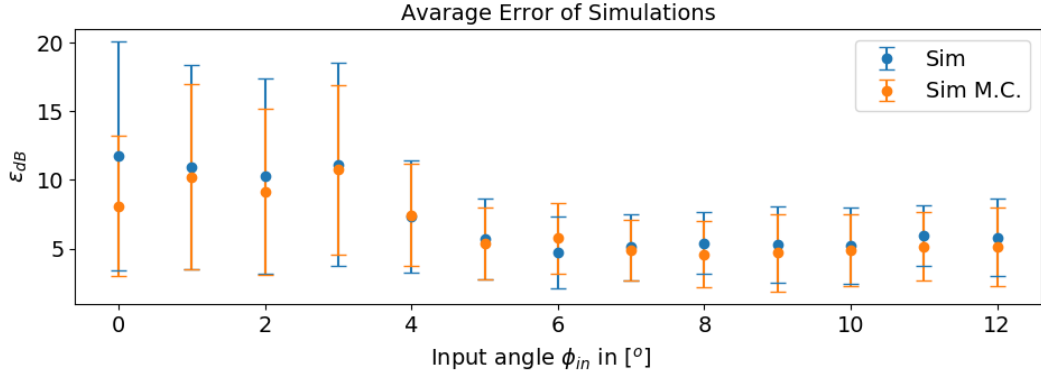
Figure 5.6: Comparison of the average ratio for all input angles $\phi_{in} \in \{0^o, 1^o, ..., 12^o\}$ of the measured/simulated fibre. ϵ_{dB} reduces towards higher input angles. With a few exceptions, the simulations with mode coupling reduce ϵ_{dB} values, and have lower standard deviation values. The x-axis is ϕ_{in} in $[^o]$ and the y-axis represents ϵ_{dB}.

To determine how much does the mode coupling factor affects ϵ_{dB}, the mode coupling factor was changed through different simulations. The higher the value of σ, the stronger the amount of mode coupling that will be induced. Simulations with $\sigma \in \{0.01, 0.05, 0.10, 0.15, 0.25\}$ were conducted. Figure 5.7 shows the results.
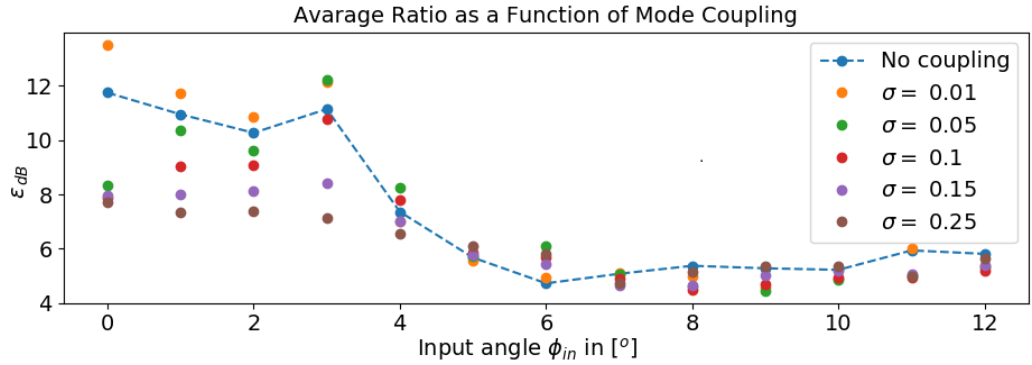

Figure 5.7: Influence of mode coupling in ϵ_{dB}. Values of $\sigma \in \{0.01, 0.05, 0.10, 0.15, 0.25\}$ are compared against the case without mode coupling.

Higher σ values seem to work better for smaller input angles, but there is no actual pattern for the σ-values that can be recognized. In most of the cases, simulations with mode coupling produce a reduced ϵ_{dB}. The standard deviation $\sigma_{\rho,dB}$ showed similar results. Interestingly, there is no prominent change in ϵ_{dB} nor $\sigma_{\rho,dB}$ for higher angles, regardless of how high the value for mode coupling σ is used.

The same analysis was conducted on the octagonal fibre. A larger amount of mode coupling appeared to diminish the average ratio for smaller input angles, but no real improvement could be observed with higher input angles. Although the same increment in spatial frequency values as for the circular fibre could be observed, the simulations could not match as well the spatial frequency increment of the measured octagonal fibre. This led to an increase of ϵ_{dB} for higher input angles when compared to the simulated circular fibre. Figure 5.8 shows the example of three power spectral density measurements of the octagonal fibre for the three higher input angles, $\phi_{in} \in \{7^o, 9^o, 11^o\}$. By $\phi_{in} = 11^o$ is clear that the measured fibre possesses higher spatial frequencies than the simulated fibre. Since only the modal interference of the propagation modes account for the increase of spatial frequency of the speckles, it appears that the measured fibre had more propagation modes than the simulated fibre. Figure 5.9 shows the results for ϵ_{dB} and different values of mode coupling for the octagonal fibre. The results for ϵ_{dB} diverge at some point.
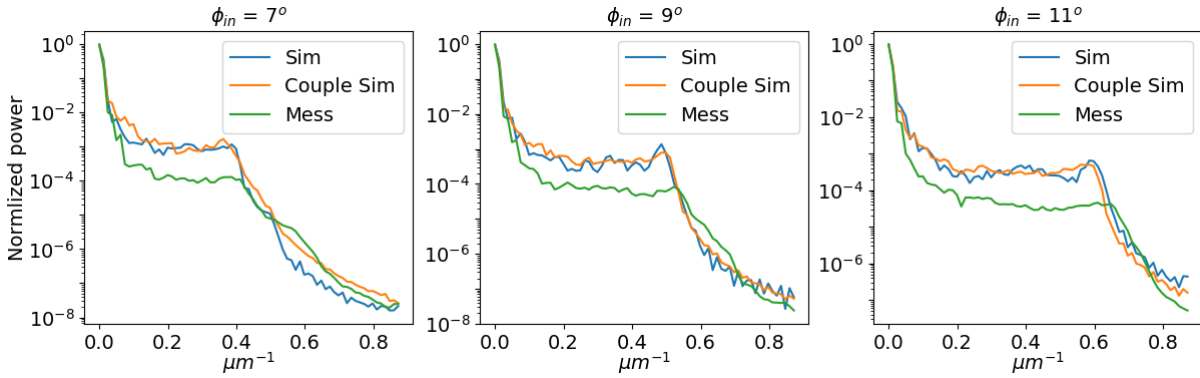
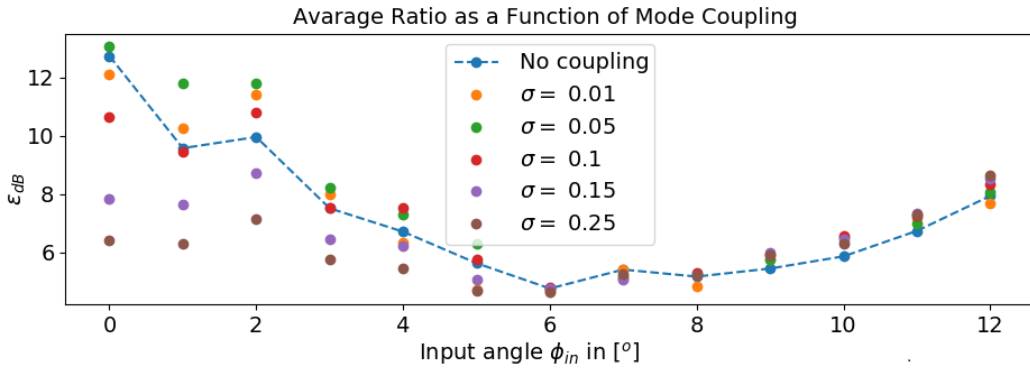Figure 5.8: Example of the power spectral density for three different input angles $\phi_{in} \in \{7^o, 9^o, 11^o\}$.

Figure 5.9: Influence of mode coupling in ϵ. Values of $\sigma \in \{0.01, 0.05, 0.10, 0.15, 0.25\}$ are compared against the case without mode coupling for the octagonal fibre.

Interestingly, this could be attributed to manufacture tolerances of the measured octagonal fibre. If the simulations can not match the speckle pattern, it means that not all propagation modes are being simulated. The individual fields of the group of propagation modes that carry the most power will determine the spatial frequency of the modal interference patterns, i.e. speckles. The measured octagonal fibre was propagating modes with higher spatial frequency fields than the simulated fibre.

A real fibre has tolerances, e.g. the core/cladding size, NA, and shape. Since the information of the NA is given by the manufacture as $NA = 0.22 \pm 0.02$ (see Tab. 4.1), the tolerance in the NA was investigate. For the simulated system with a wavelength of $633nm$, the tolerance in the NA defines that the normalized spatial frequency can be between the values $V_{low} = 49.66$ and $V_{high} = 59.76$. The number of available propagation modes translates into $M_{low} \approx 1250$ and $M_{high} \approx 1800$. This accounts for a substantial range in spatial frequencies that the propagation modes could have. If the NA is beyond the tolerances, even stronger changes could be expected.

To verify the statement that modes of higher order are being excited in the measured fibre, a simulation was made with two octagonal fibres having the parameters match the cases of V_{low} and V_{high}. This would be the limits of the tolerance range from the measured fibres at the $633nm$ propagation wavelength. The same input angle $\phi_{in} = 11^o$ was used for both fibres. This is within the NA of both fibres, since $\phi_{max,low} = 11.54^o$ and $\phi_{max,high} = 13.94^o$. For both simulations, coherent propagation was taken into account and no mode coupling was simulated. The 1D power spectral density was calculated from the near-field distributions of both fibres. Figure 5.10 shows the results. The fibre with V_{max} is marked as "High tolerance", and the fibre with V_{min} is marked with "Low tolerance".
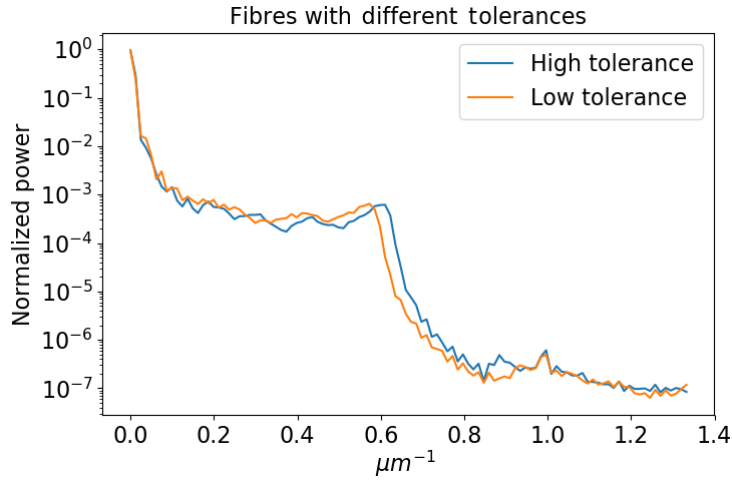
Figure 5.10: Comparison of two octagonal fibres within the N.A. tolerance of the measured octagonal fibre. The fibre with V_{max} is marked as *"High tolerance"*, and the fibre with V_{min} is marked with *"Low tolerance"*.

As can be observed, although the same input angle is being simulated, the fibre with V_{high} possesses higher spatial frequency values than the fibre with V_{low}. Both simulation are within the tolerances of the measured fibre and can change the outcome of the analysis. It can be expected that there is a substantial influences concerning the beam divergence, which translates into the FRD characteristics of a fibre, i.e. loss of throughput in the system. The influence of the manufacture tolerances in the angular divergence was not in the scope of this work, but it is aimed to be analyzed for a future publication.

5.2 Modal Scrambling

Modal interference is the main cause of modal noise and introduces difficulties for both near-field and far-field analyses. To smooth out the speckle pattern, modal scrambling can be induced (see Sec. 2.4.3). Perfect modal scrambling occurs when the phases of all active propagation modes are completely randomized. Because of the arbitrarily phase distribution, incoherent superposition of the propagation fields occurs.

Because of the coherence, the HeNe laser is an excellent source of modal interference. One method to induce mode scrambling is through fibre agitation [71] [73]. As describe in Sec. 4.2, the fibres were attached to a probe shaker and were agitated in order to induce modal scrambling. This was done for both the octagonal and the circular near-field intensity measurements. Interestingly, the fibres reacted to the agitation with different sensibilities. Although the speckles vanished in both cases, intensity patterns of different frequencies appeared as a function of the input angle ϕ_{in}. At first glance, it appeared that the near-field diameter of the octagonal fibre enlarged with higher input angles whilst the near-field diameter of the circular fibre remained nearly unchanged. Figure 5.11 illustrates the results of the input angles $\phi_{in} \in \{1^o, 10^o\}$.

As can be observed in Fig. 5.11, the speckles vanished with agitation, but other type of fluctuations appeared in the intensity distribution. For the $\phi_{in} = 1^o$ case, the octagonal fibre showed a smooth intensity pattern with low spatial frequency fluctuations. The low spatial frequency fluctuations can be attributed to the field distribution of the low order modes. Although the speckles cleared out for the circular fibre, the fluctuations of the intensity distribution appeared to have higher spatial frequency values. For the $\phi_{in} = 10^o$ case, the intensity structures of the excited modes became in the octagonal fibre visible. The circular fibre appeared once again with high spatial frequency fluctuations.
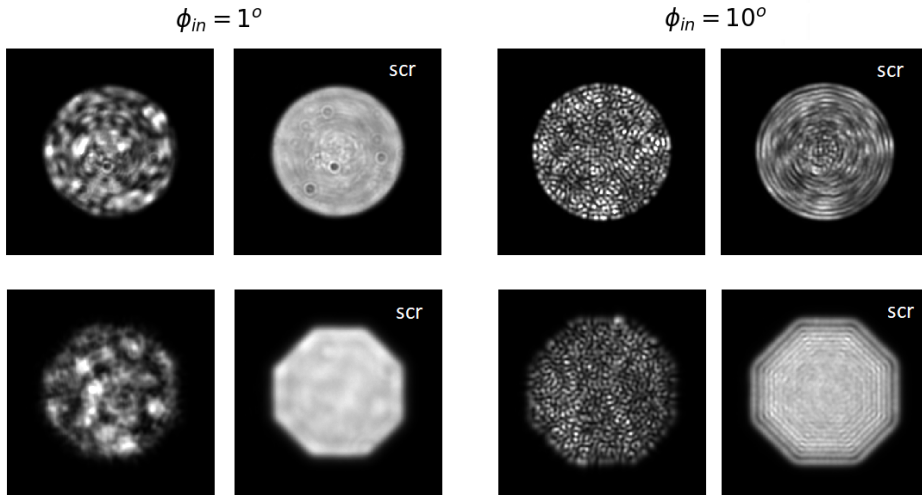
Figure 5.11: Example of induced modal scrambling in both fibres. The upper images are from the circular fibre and the lower images from the octagonal fibre. The input angles $\phi_{in} \in \{1^o, 10^o\}$ are marked above the images. Images with induced scrambling are marked with "*scr*".

The field propagation model uses the cases of complete coherence or complete incoherence (see Sec. 3.4.1). This makes it possible to compare the scrambled measurements with the case of complete incoherence. Once again, the simulations were done with the same characteristics as the measured fibres. The simulated propagation wavelength was the HeNe laser wavelength of $633nm$. Figure 5.12 illustrates the comparison between the input angles $\phi_{in} \in \{1^o, 10^o\}$. The measurements are marked with *"meas"* on the top right corner, and the simulations are marked with *"sim"* on the top right corner. The upper part of the figure shows the circular fibres, whilst the bottom part shows the octagonal fibres.
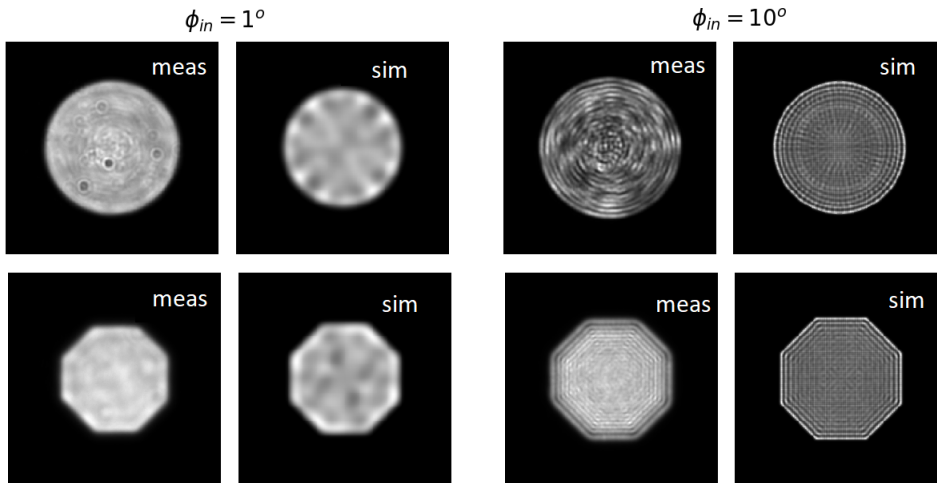

Figure 5.12: Comparison between measurements and simulations for the case of complete incoherent propagation through induced modal scrambling for both fibres.

For the simulated fields to resemble the real measurements, mode coupling needed to be applied. As can be observed, the simulations can reproduce the measurements of the octagonal fibre very accurately. The low spatial frequency fluctuations for the case of $\phi_{in} = 1^o$ are visible for both the measurement and the simulation. The fluctuations are caused by the fields of the excited modes being summed incoherently. The same principle applies for the case of $\phi_{in} = 10^o$. The visible structures are caused by the fields of the higher-order modes being summed incoherently.

In the case of the circular fibre, the simulations slightly differed from the measurements. For the case of $\phi_{in} = 1^o$, low spatial frequency fluctuations can be observed in both results, but also higher frequency fluctuations confined mostly in the center of the fibre are visible in the measurement. It appears that coherent interference could be taking place. The same situation occurs for $\phi_{in} = 10^o$. Fluctuations resembling coherent interference patterns are visible in the center of the fibre. In both cases $\phi_{in} \in \{1^o, 10^o\}$ the interference patterns are confined in the center of the scrambled intensity distribution. This can be attributed to two situations: **A)** Actual modal interference is taking place but somehow confined in the center of the fibre. **B)** Observed is an aberration from the 50×LWD objective. Both cases are analyzed in the following paragraphs.

If situation **A** would be the cause, it would mean that coherent and incoherent propagation is taking place. If coherent and incoherent addition of the modes does occur, the system could be best described with partial coherent propagation. Equation 2.26 in Sec. 2.1.3 describes the normalized mutual intensity of two fields with $g_{1,2} = 1$ for the case of complete coherence and $g_{1,2} = 0$ for complete incoherence. In partial coherence, $g_{1,2}$ can take values between 0 and 1. For the field propagation model, the parameter $g_{n,m}$ for all $n, m \in M$, with M being the total amount of modes, would need to be calculated. An expression to determine $g_{n,m}$ was beyond the scope of this thesis but can be analyzed in future work.

Since the same setup was used for the octagonal fibre, situation **B** should also appear for the octagonal fibre measurements, but it is not the case. It could be attributed to the fact that the octagonal fibre was not in the exact focus position as the circular fibre. The repetition of the measurements would have given insights if the objective aberrations are the cause or part of the cause concerning the confinement of the interference patterns in the center of intensity distribution.

In addition to the intensity fluctuations of the fibres, the enlargement of the near-field intensity distribution was observed. For the simulated and measured fibres, the enlargement is a function of the input angle ϕ_{in}. The next section analyses the near-field enlargement.

5.2.1   Near-field enlargement

In a fibre-fed spectrograph system, the near-field intensity is usually projected on the recording device, e.g. CCD [30]. If the near-field size changes as a function of the input angle, it could create extra fluctuations in the intensity sampling on the finite area of pixels. For stability reasons, it is of interest to know if the fluctuations of the near-field size occur for both the case of monochromatic propagation as well as for the case of chromatic propagation. First, the monochromatic case will be discussed. Afterwards, using the test-bench in the configuration for scrambling measurements, example of near-field measurements will be presented.

In the previous section was observed that the near-field intensity enlarged with higher input angles for both the measurements and the simulations. This can be attributed to the fact that higher-order modes posses larger field diameters, and the modes excited by $\phi_{in} = 10^o$ are of a higher order than for $\phi_{in} = 1^o$. To observe the enlargement, the change in the field diameter as a function of the input angle was recorded. For the analysis, the intensity fields were cut into a 1D distribution and the $1/e^2$ definition of the field diameter was used [45]. The field diameter was normalized as follows. The normalization takes into account the maximum diameter of the fields as a function of ϕ_{in}. The array is normalized as in $d_n = d/d_{max}$. It is expected that d_{max} occurs for $\phi_{in,max}$. For the analysis, $\phi_{in,max} = 12^o$. The illustration of d_n allows to display the rate of normalized increment from d_{min} up to d_{max}. Figure 5.13 shows the results of the normalized increment as a function of ϕ_{in}.

Although the enlargement of the near-field intensity can be seen, the fibres produce different results. The increment in the measured circular fibre was of around 5% from $\phi_o = 0^o$ up to ϕ_{max}. The simulated circular fibre had an increment of $\sim 12\%$. For the measured fibre, it means that the shallow input angles have more active modes than expected. This again can be attributed to changes in the refractive index of the fibre, mechanical stress caused by the connectors/fibre termination, positioning in the test bench,
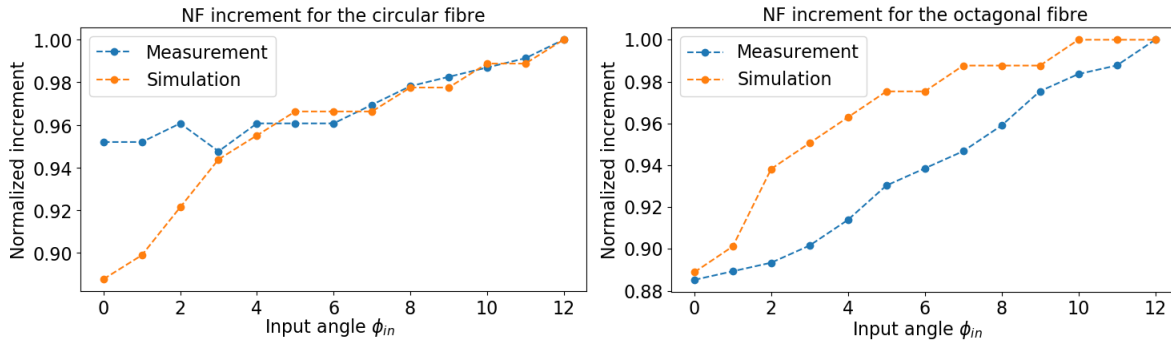
Figure 5.13: Near-field increment for the measurements and simulations of the circular and octagonal fibre. *(left)* Measurements and simulations of the circular fibre. *(right)* Measurements and simulations of the octagonal fibre.

and/or agitation through the probe shaker. The results for the octagonal fibres are more correlated. The enlargement is of $\sim 12\%$ for both the simulations and the measurements. The rate of enlargement does diverge from one another. The simulated octagonal fibre reaches d_{max} already at an input angle of $\phi_{in} = 10^{o}$. Through adjusting the coupling factor in the simulations for each individual position, it should be possible to match the same rate of enlargement.

As already stated at the beginning of this section, it is of interest to know if the fluctuations of the near-field diameter occur for both the case of monochromatic propagation as well as for the case of chromatic propagation. The results shown in Fig. 5.13 were obtained for the monochromatic case using the parallel laser beam method. For the chromatic case, a broadband light source needs to be used. To test the chromatic case, near-field measurements using the halogen lamp in the test-bench were available (see Sec. 4.2). Since the enlargement of the near-field was observed after the experimental tests were concluded, it was possible to work only with the available data. The setup configuration for acquiring the data will be explained in the following paragraph.

The test-bench arrangement was set to record the near-field intensity in scrambling measurements. Once more, the fibre end face was projected via the $50\times$LWD objective to the $1k \times 1k$ CCD. For this type of measurements, the fibre input face is fixed on a x-y-z stage with pitch and yaw platform. Compared to the parallel laser beam measurements, collimated light is not being used. Instead, a cone of light with a specific f-number is injected into the fibre. A different f-number is equivalent to a change in the input angle ϕ_{in}. This was achieved by placing different pupil stops in the pupil plane of the test-bench (see Fig. 4.5). The first near-field measurements were done with the input spot at the center of the fibre. The input spot had a diameter $d_{in} = 20\mu m$ (see Sec. 4.2). Measurements of the circular fibre were available with $f\# \in \{2.5, 3, 5, 8, 12\}$. The fastest f-number, $f\#2.5$, represents an input angle $\phi_{in} = 11.54^{o}$. The slowest f-number recorded, $f\#12$, is equivalent to an input angle $\phi_{in} = 2.38^{o}$. A fewer amount and different set of f-numbers were available for the octagonal fibre, $f\# \in \{2.7, 5, 15\}$. The fastest f-number, $f\#2.7$, represents an input angle $\phi_{in} = 10.67^{o}$. The slowest f-number, $f\#15$, is equivalent to an input angle $\phi_{in} = 1.91^{o}$. The measurements were taken at different periods of time and were meant for practicing the analysis the scrambling parameters of the different fibres. Figure 5.14 shows the measurements of both fibres with the different f-numbers.

It can be clearly observed from Fig. 5.14 that the near-field of the circular fibre increases in diameter with faster f-numbers. Due to the nearly perfect scrambling of the octagonal fibre, the increment in the near-field intensity is not as evident as for the circular fibre. Not only does the octagonal fibre shows a more stable near-field intensity diameter, but also the intensity is uniformly distributed across the fibre transverse plane. This can be attributed to the better scrambling properties that fibres with polygonal cross-sections posses, a characteristic that was demonstrated in the works of Avila (2012) [88] and Allington-Smith et al. (2012) [39]. As can be observed, slower f-numbers result in better scrambling across the circular fibre transverse plane. This is in good agreement with the theory presented in Sec. 2.4.5. It states that slower
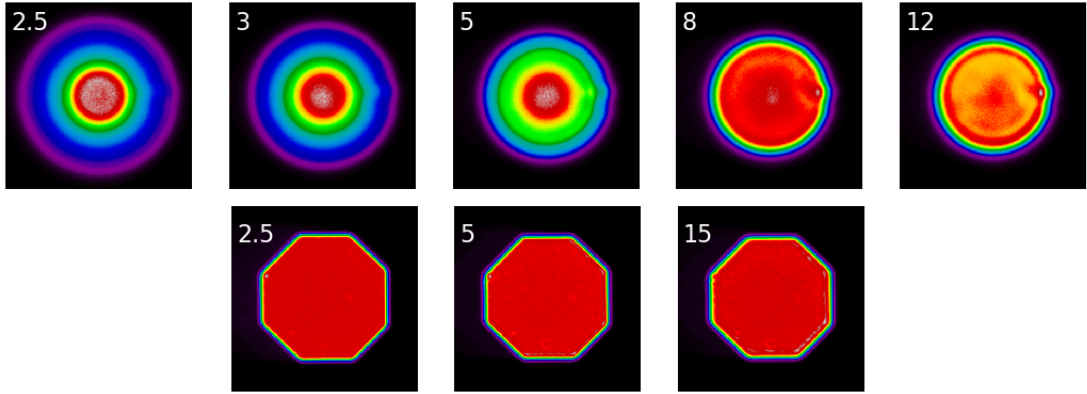
Figure 5.14: Measured near-field using different f-numbers for both fibres. The f-number is marked on each respective corner.

f-numbers help with scrambling but create considerably more FRD. Fig. 5.15 shows the 1D cut of the fastest and slowest f-number for both fibres.
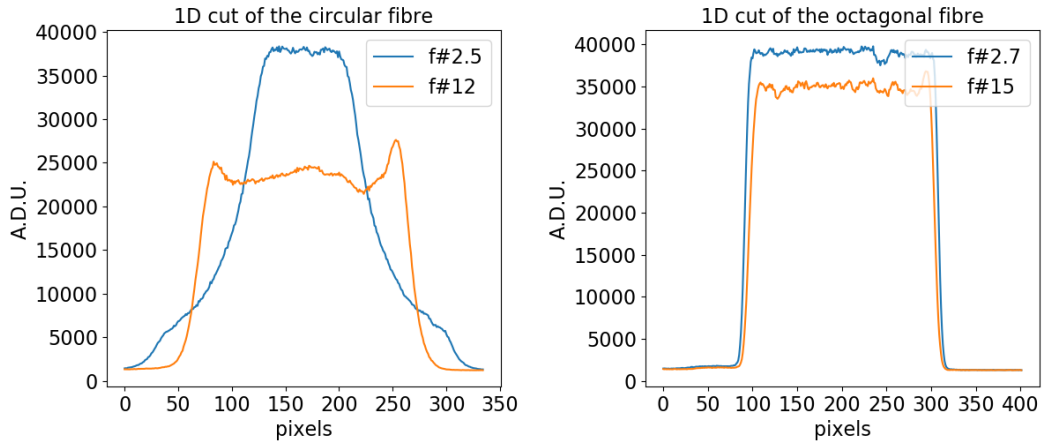

Figure 5.15: One dimensional representation of the fibres near-field intensity for the fastest and slowest f-numbers available.

The near-field intensities were analyzed in the same way as for the parallel laser beam measurements. The enlargement in field diameter is once again plotted as the normalized increment. This way, it is possible to see the rate of change from d_{min} up to $d_{max} = 1$. Figure 5.16 shows the results of d_n as a function of ϕ_{in} for both fibres. The input f-number is traced by a second x-axis on the upper part of the plot. The circular fibre is marked as *"Circ"*, and the octagonal fibre is marked as *"Oct"*.

For the circular fibre, the normalized increment was of $\sim 15\%$, whilst the increment for the octagonal fibre was of $\sim 2.5\%$. A similar behavior to the results of the circular fibre was expected for both fibres. It is unknown, why the results of the octagonal fibre differed considerably from the parallel laser beam method. A new measurement of the octagonal fibre would be necessary to reaffirm that the results are correct.

Since the measurements were conducted for the scrambling analysis of the fibres, it was possible to compare the near-field diameter enlargement for input spots located at the edge of the fibre input face. The input spot was located at the position $x_o \approx 15\mu m$. Figure 5.17 shows the results of the circular fibre for the input spot located at $x_o \approx 15\mu m$. The results with the input spot on $x_o = 0$ are also illustrated in the plot for comparison reasons. Once again, the input f-number is traced by a second x-axis on the upper part of the plot. The circular fibre measurement without offset is marked as *"Circ"*, the octagonal fibre is
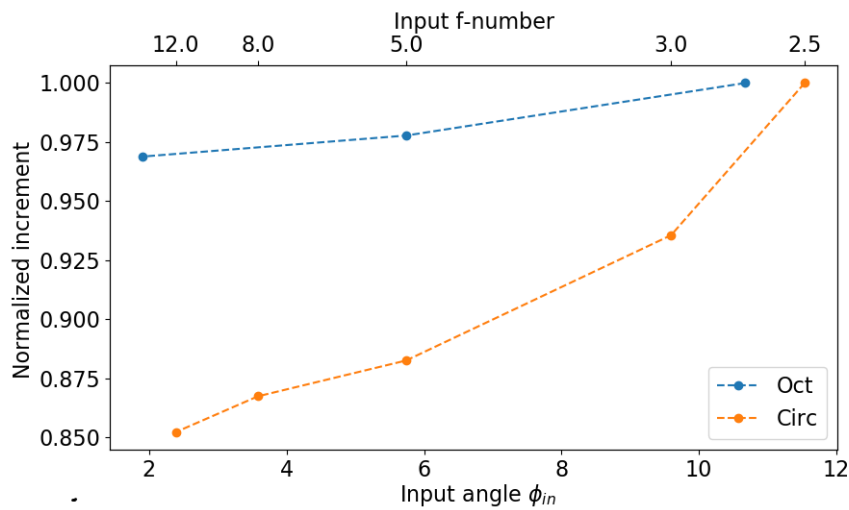
Figure 5.16: Increment of the near-field for the octagonal and circular fibre using different f-numbers. The input f-number is traced by a second x-axis on the upper part of the plot.

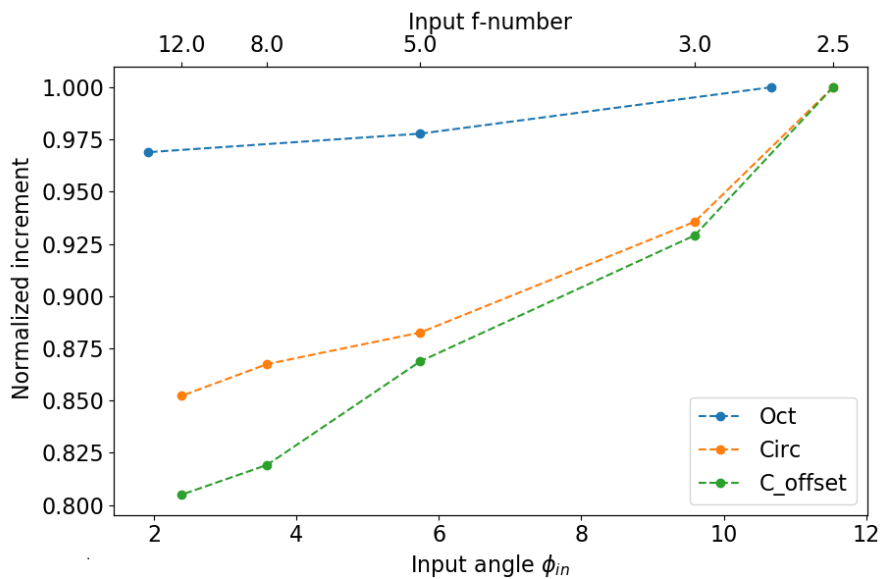marked as *"Oct"*, and the circular fibre measurement with an offset is marked as *"C_offset"*.

Figure 5.17: Increase of the near-field diameter with the input spot having offset of $x_o = 15\mu m$ for both the octagonal and circular fibre and using different f-numbers. The input f-number is traced by a second x-axis on the upper part of the plot.

The measurement of the octagonal fibre with $x_o = 15\mu m$ resulted in exactly the same values as the measurements without an offset $x_o = 0\mu m$. This is another hint that unfortunately the measurements with the octagonal fibre were somehow corrupted. Even if the results could be similar, due to noise in every measurement system, it is highly unlikely that the measurements with $x_o \in \{0\mu m, 15\mu m\}$ for the octagonal fibre produced exactly the same results. Due to the uncertainty of the octagonal fibre scrambling data, only the circular fibre was further analyzed for enlargement of the near-field and additional scrambling properties.

Figure 5.17 shows that the circular fibre measurements with an offset produced a stronger change in the near-field increment. Although the enlargement can be attributed to the difference of the individual mode field diameters, it is unclear why an offset could produce a reduced field diameter for smaller input angles/slower f-numbers. Since the input spot was introduced with a spatial offset $x_o = 15\mu m$, it was possible to calculate the radial and azimuthal scrambling parameters Rs and As with the methods explained in Sec. 2.4.6. Values of Rs and As close to zero translate into good scrambling properties of the fibre. Figure 5.18 shows the results. As expected, measurements with slower f-numbers produced better scrambling results. Both Rs and As are in good agreement with already known work, e.g. Olaya et al. (2011) [48].
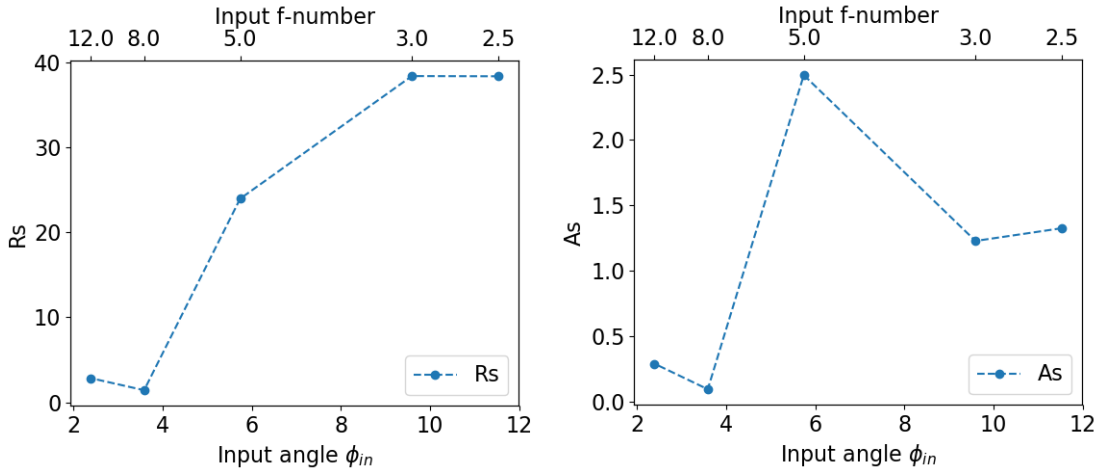

Figure 5.18: Radial and azimuthal scrambling parameters of the circular fibre. The offset measurements allowed for the calculations of Rs and As. *(left)* Radial scrambling parameter as a function of the input angle and f-number. *(right)* Azimuthal scrambling parameter as a function of the input angle and f-number.

Measurements of the circular fibre in combination with the different bandpass filters were available for analyzing the enlargement of the near-field as a function of the wavelength. The bandpass filters had the central wavelengths $\lambda_c \in \{436nm, 546nm, 600nm, 905nm\}$. Each filter had a $\Delta\lambda = 10nm$ bandwidth (see Sec. 4.2.1). Figure 5.19 shows the results. The results of the different bandpass filters are marked on the plot with respect to the wavelength color, $\lambda_c \in \{blue, yellow, red, NIR\}$. An increase in field diameter as a function of the wavelength can be observed. The results are in good agreement with theory, since individual mode field diameters tend to increase with wavelength [45]. The NIR bandpass filter shows stronger fluctuation than the red and the yellow filter. Since the NIR filter was measured on a different date, systematic errors, such as dissimilar placement on the focal plane of the objective lens, could be the cause of the augmented NIR near-field diameter fluctuations. With a difference of d_{min} to d_{max} of $\sim 5\%$ the results of the yellow, red, and NIR bandpass filters are in good agreement with the results of the parallel laser beam measurement of the circular fibre which uses a wavelength $\lambda_c = 633nm$.

Although there is a substantial difference in size for the blue wavelength, the overall fluctuations for the full band are still the strongest. For applications of astronomical spectroscopy even low resolution gratings will produce results with smaller bandpass properties than the used filters. This implies that the diameter fluctuations should not get worse than the results for the shortest wavelength, in this case $\Delta d_{blue} \approx 8\%$. Depending on the spectrograph/detector arrangement, $\Delta d \approx 8\%$ could already imply changes of the detected signal. The field diameter fluctuation together with the fibre tolerances could be causes for the difficulty in calibration between individual fibres for high precision spectrographs.

Although the propagation was done incoherently, intensity fluctuations were observed for both the simulations and the measurements. The fluctuations originate from the individual mode fields adding up incoherently and will be illustrated in the next section.
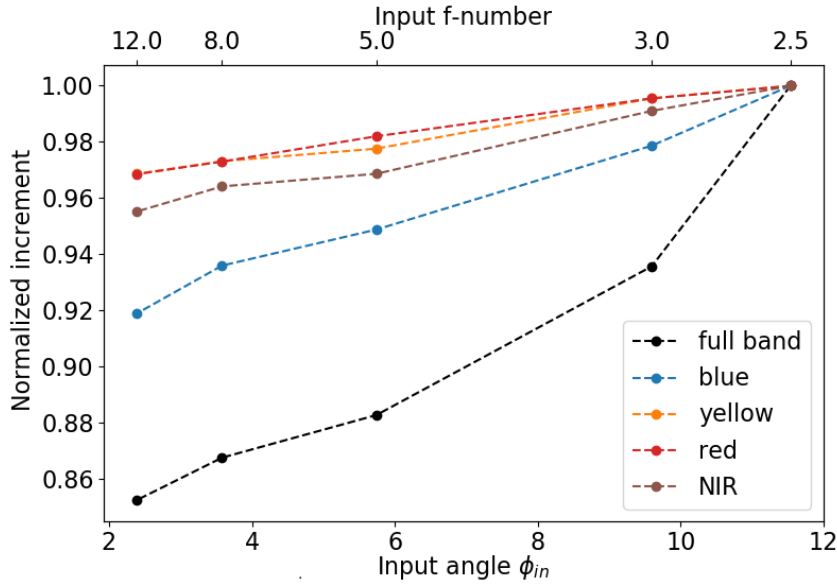
Figure 5.19: Near-field enlargement as a function of the wavelength with the circular fibre. The results of the different bandpass filters are marked on the plot with respect to the central wavelength color λ_c.

5.2.2   Incoherent intensity fluctuations

The monochromatic case demonstrates that the results of incoherent superposition still produce intensity fluctuations in the near-field distribution. This can be best observed for the induced scrambling measurements of the octagonal fibre and the simulation through incoherent superposition of the propagation modes (see Fig. 5.12). Due to the bandwidth $\Delta\lambda = 10nm$ of the filters, a quasi-monochromatic case with incoherent superposition could be measured.

The incoherent intensity fluctuations are attributed to the incoherent superposition of the individual mode fields. Each mode field possesses intensity fluctuations of a specific spatial frequency. As described for Fig. 5.12, higher-order modes will consequently have higher spatial frequency fluctuation. The structures observed in the case of the octagonal fibre are from higher-order modes. Since higher-order modes are excited through faster f-numbers, the measurements of the circular fibres with f-numbers should possess incoherent intensity fluctuations.

Due to the long propagation wavelength of $\lambda_c = 905nm$, it is possible to illustrate best the effect of intensity fluctuations with the NIR filter. The previous statement is explained in the following sentences. Since the measured fibre has a diameter of $d = 50\mu m$ and NA ≈ 0.21, the total number of propagation modes is equivalent to $M_{NIR} \approx 661$ modes and the normalized frequency number equals $V_{NIR} = 36.36$. If compared with the blue central wavelength, $\lambda_{blue} = 436nm$, the total number of propagation modes equals $M_{blue} \approx 2847$ modes, with $V_{blue} = 75.46$. Both systems excite the highest propagation modes for the highest input angle, $\phi_{in} = \phi_{max}$. But in the case of the NIR-wavelength, the highest propagation mode will have the number 661 instead of 2847. Since the spatial frequency of the intensity fluctuations increase with mode number, the NIR system will have substantial lower spatial frequency values than the blue system.

To help illustrate the case, the propagation modes calculated for the HeNe laser will be used to simulate the intensity fluctuations, and are going to be compared to the λ_{NIR} intensity fluctuations. Using Eq. 5.1 it is possible to calculate the number of propagation modes as a function of the input angle (as in $M(\phi_{in})$). For ease of the illustration, two fast f-numbers are taken into account, $f\# \in \{2.5, 5\}$. The equivalent input angles take the values $\phi_{in} \in \{11.54^o, 5.74^o\}$. If ϕ_{in} is used in Eq. 5.1 with $\lambda_{NIR} = 905nm$, the corresponding number of propagation modes as a function of the input angle equals approximately

$M(\phi_{in}) \in \{600, 150\}$. The corresponding input angles $\phi_{in,HeNe}$ for the HeNe system can be calculated using the values obtained for $M(\phi_{in})$. Using Eq. 5.1 and solving for $\phi_{in,HeNe}$ as a function of $M(\phi_{in})$ and λ_{HeNe}, the corresponding angles equal $\phi_{in,HeNe} \in \{8.04^o, 4.01^o\}$. Using $\phi_{in,HeNe}$ with the modes calculated for the HeNe, the resulting near-field distribution are illustrated together with measured field distributions for $\lambda_{NIR} = 905nm$. Figure 5.20 shows the results. The measurements are shown in the upper part of the image and are marked with *"meas"* plus the corresponding f-number. The simulations are displayed in the lower part of the image and are marked with *"sim"*. It is important to note that the simulations do not attempt to reproduce the intensity distribution of the measurements. Only the outer intensity fluctuations are of interest, which is what the simulations can reproduce. The actual cone injection simulation is not realized here.
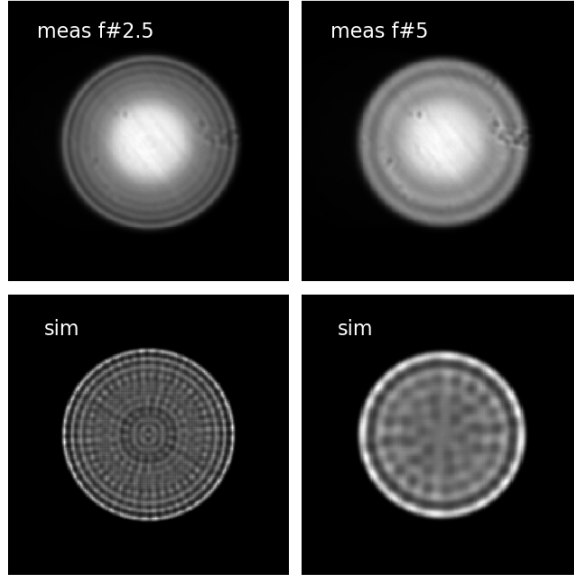

Figure 5.20: Comparison between simulations and measurements for the incoherent superposition of quasi monochromatic light. For ease of clarity only two fast f-numbers are displayed, $f\# \in \{2.5, 5\}$. The measurements are shown in the upper part of the image and are marked with *"meas"* plus the corresponding f-number. The simulations are displayed in the lower part of the image and are marked with *"sim"*. It is important to note that the simulations do not attempt to reproduce the intensity distribution of the measurements. Only the outer intensity fluctuations are of interest, which is what the simulations can reproduce.

The incoherent intensity fluctuations for the measurements can be easily observed in Fig. 5.20. Despite the fact that incoherent propagation is taking place, intensity fluctuations still manifest in the near-field distribution. As opposed to modal noise, the incoherent intensity fluctuations should be of a static matter. If the characteristics of the input field are stable, the output should remain stable. At the moment, the localized maximum in the center of the fibre can not be simulated. But using the corresponding input angles $\phi_{in,HeNe}$ for the HeNe system, the intensity fluctuations in the outer parts of the fibre appear to match the measurements.

To better analyze the intensity fluctuations between measurements with $\lambda_c = 905nm$ and the simulations using the HeNe system, 1D functions of the measurements and simulations with the corresponding f-number are compared to each other. As can be observed from Fig. 5.21, the incoherent intensity fluctuations result from the spatial frequency of the individual intensities of the propagation modes being added incoherently.

The next sections analyze the far-field angular distribution of the measured fibres. The far-field analysis provides information about the FRD characteristics of the individual fibres. First, the parallel laser beam method is used to produce the far-field annular distributions that are matched by the simulations. Afterwards, light cone measurements are used for observation of the actual loss as a function of the input
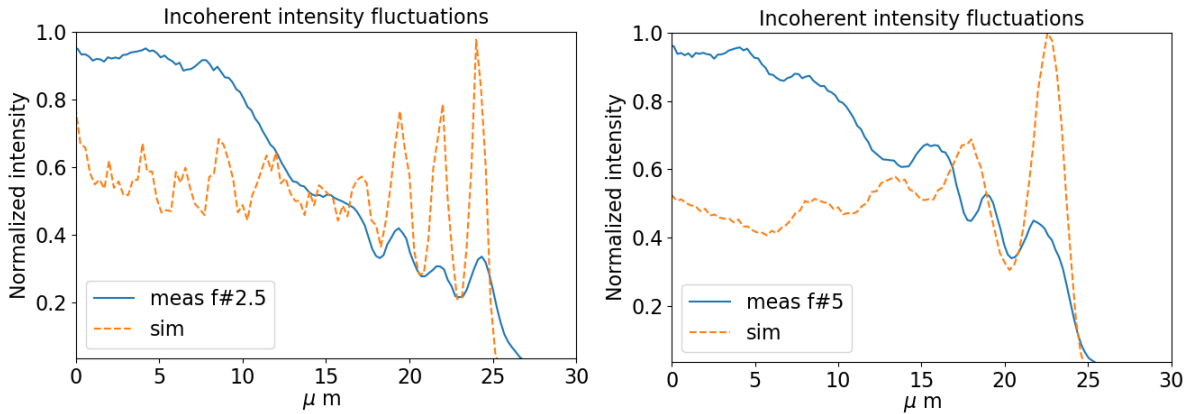
Figure 5.21: Incoherent intensity fluctuations of measurements with the NIR filter $\lambda = 905nm$ compared to simulations using the propagation modes of the HeNe laser.

characteristics.

5.3   Far-Field Analysis of the Parallel Laser Beam Measurements

For a monochromatic configuration and under certain constraints, the simulations can reproduce the results of certain fibre characterization measurements. Since the parallel laser beam measurements work with a monochromatic source, it should be possible to compare the resulting angular far-field distributions with the simulations. As described in Haynes et al. (2011) [53], the measurements of the far-field represent a ring that expands as a function of ϕ_{in}. The characteristics of the ring give insights into the FRD characteristics that the fibre exhibits. One particular factor of interest is the thickness of the far-field ring which can be represented as angular divergence as a function of the input field characteristics and fibre parameters. The less angular divergence, the less FRD is expected in the system.

Since the angular divergence depends on a broad range of parameters, an analytical solution for obtaining the minimal divergence a system can produce results in an arduous procedure. By the means of the field propagation model and knowledge of the basic fibre parameters, numerical calculations for obtaining the minimum output divergence as a function of the input beam diameter and injection angle were demonstrated in Sec. 3.6.2. Actual measurements should provide a guide for adjusting the parameters of the simulations to resemble realistic systems.

Using the test-bench in the configuration for the parallel laser beam measurement (see Sec. 4.2.3), the resulting far-field was measured with the available $2k \times 2k$ CCD. As explained in Sec. 4.2, the fibres were mounted on a stage that provided a distance of $\sim 4cm$ to the CCD. The arrangement allowed recording the angular output intensity without the usage of any additional optical elements. Since the HeNe laser source was being used, the measured angular intensities were dominated by modal interference. To apply analytical functions to the far-field distribution, modal scrambling was needed and was induced once more using the probe shaker (see Sec. 5.2). Figure 5.22 shows examples of far-field measurements for the input angles $\phi_{in} \in \{2^o, 4^o, 6^o, 8^o, 10^o, 12^o\}$ from the circular fibre.

Although scrambling is being applied, intensity fluctuations can be observed in every measurement of the circular fibre. The measurements with shallower input angles seem to have intensity fluctuations of high spatial frequency, situation that can be attribute to modal interference. The images are once more a hint that partial coherence occurs. For comparison purposes, Fig. 5.23 shows a few examples of the octagonal fibre far-field measurements for $\phi_{in} \in \{2^o, 6^o, 8^o\}$.
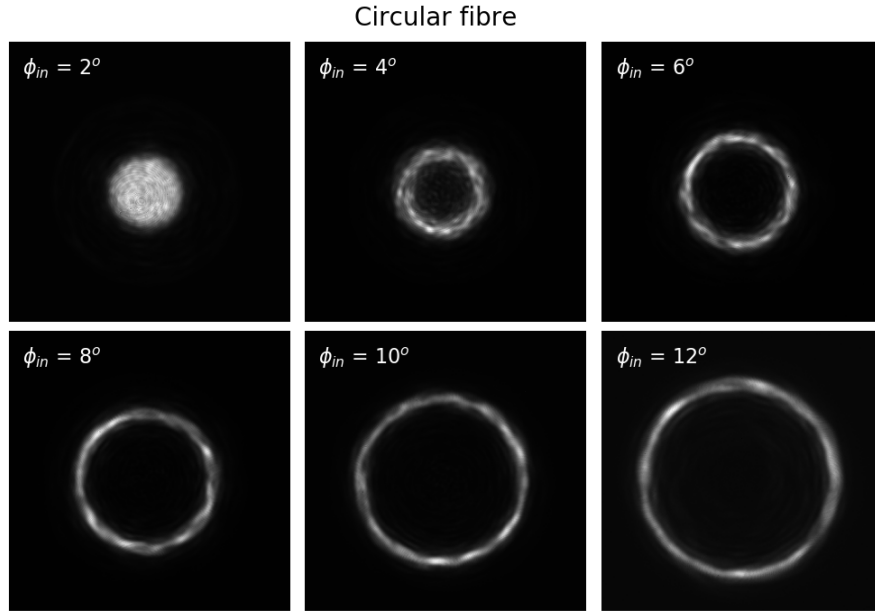
Circular fibre

Figure 5.22: Measurements of the angular far-field distribution as a function of the input angle $\phi_{in} \in \{2^o, 4^o, 6^o, 8^o, 10^o, 12^o\}$ from the circular fibre.
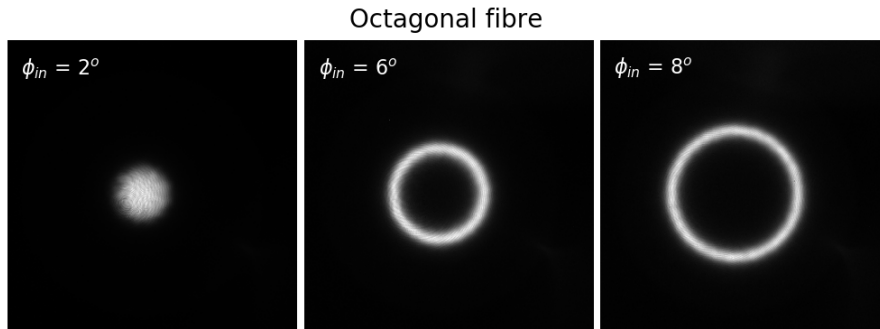
Octagonal fibre

Figure 5.23: Examples of the octagonal fibre far-field measurements for $\phi_{in} \in \{2^o, 6^o, 8^o\}$

The octagonal fibre once more shows better scrambling characteristics than the circular fibre. As can be observed, the intensity is uniformly distributed along the ring formation. To better illustrate the difference in the scrambling properties of the two fibres, raw measurements of each fibre are presented next to each other. The spectral color map is used, and the color bar is showed for the dynamic range of each image to be illustrated. Figure 5.24 shows the comparison images of the two fibres. Each image is marked on the left corner with the appropriate identification.

The intensity distribution of the octagonal fibre appears to be uniformly distributed along the far-field ring. Interestingly, eight localized maxima in a symmetrical position distributed along the azimuthal axis can be observed. The eight symmetrical localized maxima can also be observed for the far-field simulations of the octagonal fibre and arise from the octagonal shape of the fibre. The circular fibre shows an uneven intensity distribution along the azimuthal axis but with a fixed radial component as function of the input angle ϕ_{in}.

For the further assessment of the measurements, each measured intensity needs to be integrated along the azimuthal axis to create a one dimensional averaged distribution. As explained in Sec. 3.4.3, the one dimensional averaged distribution can be interpreted as a function of the radius $F(r)$. Figure 5.25 shows $F(r)$ for four different measurements of the circular fibre with the input angles $\phi_{in} \in \{5^o, 7^o, 9^o, 11^o\}$.
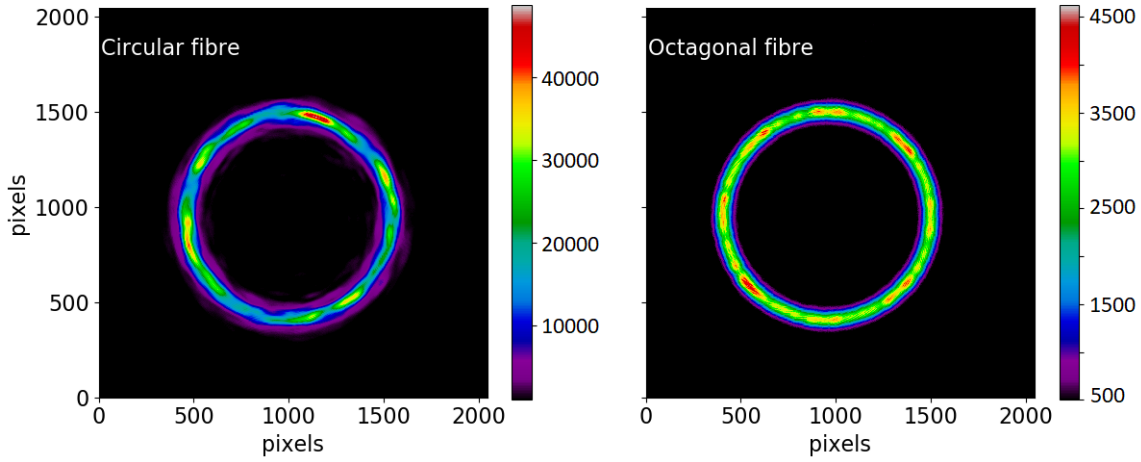
Figure 5.24: Comparison of the far-field distribution for the two fibres. Each image is marked on the left corner with the appropriate identification.
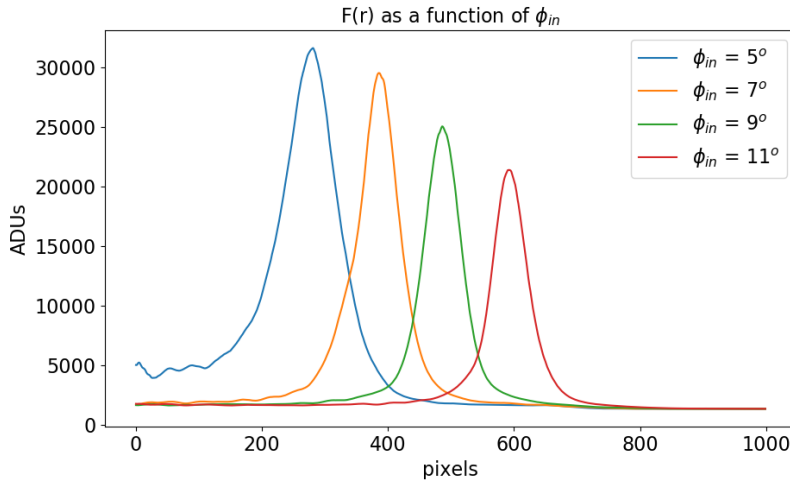

Figure 5.25: Evolution of $F(r)$ as a function of $\phi_{in} \in \{5^o, 7^o, 9^o, 11^o\}$. Only a reduced number of examples is presented for clarity of the plot. The x-axis is in pixels and the y-axis in ADUs.

As can be observed from Fig. 5.25, the maximum of the function $F(r)$ moves linearly along the x-axis with incrementing ϕ_{in}. This is expected, since the increment of the far-field ring distribution is linear to the increment of the input angle ϕ_{in}. To prove the validity of the measurements, the ring was recorded in both positive and negative directions of the rotation stage (see Sec. 4.2, Fig. 4.3). Afterwards, the location of the maximum value from $F_k(r), k \in \{positive, negative\}$, was recorded and plotted as a function of the input angle ϕ_{in}. In order to measure the linearity of both positive and negative directions, a linear fit as a function of the located $F(r)$ maxima was used. Figure 5.26 shows the results. The x-axis marks the input angle ϕ_{in}. The y-axis is in pixels, and marks the location of the maxima (see Fig. 5.25). Since the far-field ring distribution was visible for $\phi_{in} \geq 4^o$, the plot shows the recorded maxima for the range $\phi_{in} \in \{4^o, ..., 12^o\}$. The slope β of the linear fit is marked for both positive and negative rotation directions in the plot, and the value is given in $[pixels/^o]$. Both slopes show an increment of $\beta \approx 51 \frac{pixels}{o}$.

The principles to produce far-field simulations are explained in Sec. 3.4.2. For a better comparison between the measurements and the simulations, the measurements were mapped to an equivalent angular space as the simulations. The angular space is $A_{sim}(\theta_x, \theta_y) = 18.48^o \times 18.48^o$, and was obtained empirically since it results in an appropriate ratio of field to background for systems with an NA $= 0.21$, $\phi_{max} = 12^o$.
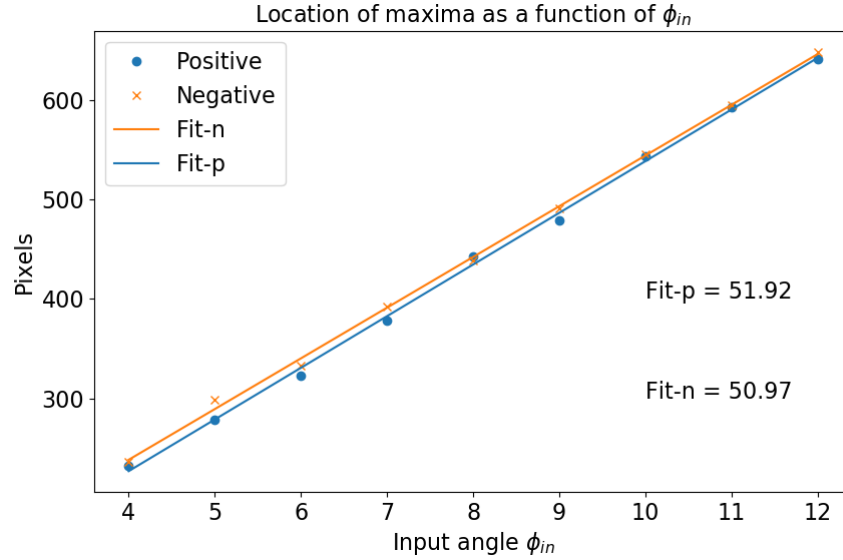
Figure 5.26: Location of the maxima from $F(r)$ as a function of the input angle $\phi_{in} \in \{4^o, ..., 12^o\}$. The x-axis shows the input angle ϕ_{in}. The y-axis is in pixels, and marks the location of the maxima. The slope β of the linear fit is marked for both positive and negative rotation direction in the plot, and the value is given in $[pixels/^o]$.

The following procedure was done to map the measurements into the angular space A_{sim}. First, the center of mass is found as explained in Sec. 3.4.3. The value is given in pixels $[c_x, c_y]$. Afterwards, the radius of the ring is found through a function that looks for the maximum value $\mathrm{M}[m_x, m_y]$ in the 1D cut of the ring. The radius takes the value of distance in pixels from the central coordinate $\mathrm{P}[c_x, c_y]$ up to the maximum value $\mathrm{M}[m_x, m_y]$. This procedure is done for the two horizontal and two vertical directions. Then, the mean of the four values is calculated and given as the end result radius $r_{o,p}$ in pixels. This same principle was applied to obtain the results from Fig. 5.26. Afterwards, the input angle ϕ_{in} for the specific measurement is divided by the radius $r_{o,p}$. This results in pixels representing the angular unit $\phi_{o,p}$ and can be described in $[^o/pixel]$. Since the area of the simulated far-field equals $A_{\theta_x, \theta_y} = 18.48^o \times 18.48^o$, the number of pixels equivalent to that area is calculated through $A_{pixels} = 18.48^o/\phi_{o,p}$.

If one simulation and one measurement are plotted as $F_k(\phi_{o,p}), k \in \{\text{sim,meas}\}$, the full width half maximum (FWHM) of $F_{meas}(\phi_{o,p})$ will be broader than the FWHM of the simulation for any input angle ϕ_{in}. A broader FWHM traduces into augmented divergence for the far-field distribution. In real measurements, there are many factors that will produce augmented divergence in the angular distribution. Some examples are fluctuations in the refractive index of the fibre, fibre positioning in the test rig, fibre termination procedures, agitation procedure of the fibre, among others. Figure 5.27 shows one example of $F_k(\phi_{o,p}), k \in \{\text{sim,meas}\}$, for the circular fibre. The input angle was $\phi_{in} = 8^o$. Both functions are normalized as $F_n = F/F_{max}$ for comparison reasons. The measurement is marked with "Meas", and the simulation is marked with "Sim". The x-axis represents the angular distribution, and the y-axis is the normalized intensity. The unsymmetrical appearance comes from the number of sampling points used in the simulation.

As can be observed in Fig 5.27, the FWHM of the measurement is almost twice as broad as the FWHM of the simulation. By fitting $F(\phi_{o,p})$ with an appropriate function, the FWHM can be precisely calculated. This was already demonstrated using a Gaussian fit for the simulations in Sec. 3.6.2. Gloge (1972) [52] explained that the sum of the propagation modes in the angular far-field can be best approximated with a Gaussian function. Haynes et al. (2011) [53] summarized the effects that cause beam divergence to scattering, diffraction and modal diffusion. The diffraction and modal diffusion components can be modeled by a Gaussian function, whereas the scattering can be modeled by a Lorentz function. If both a Gauss- and a Lorentz function are needed to fit a measurement, a good tool for characterizing $F(\phi_{o,p})$ is
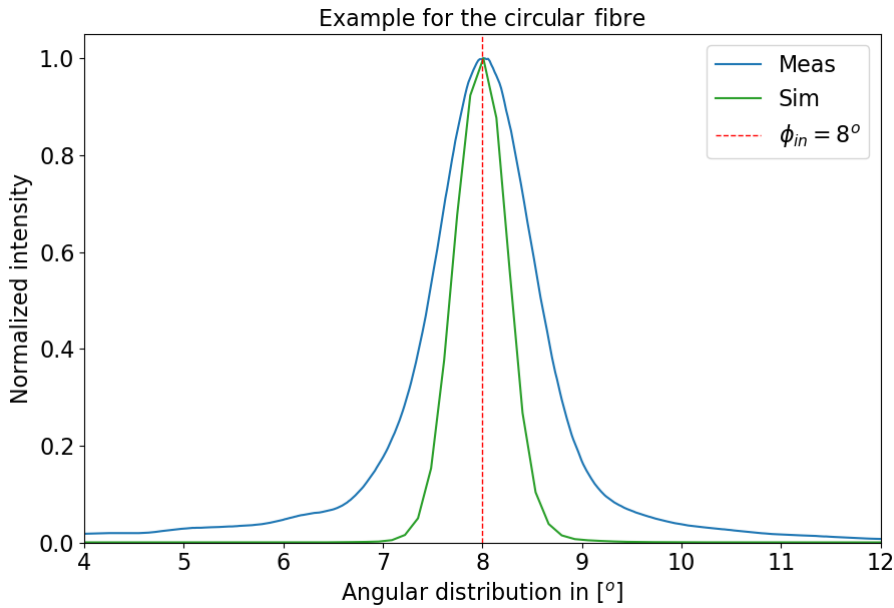
Figure 5.27: Comparison of the angular distribution between measurement and simulation when using a incident angle of $\phi_{in} = 8^o$. The x-axis represents the angular distribution, and the y-axis is the normalized intensity. The unsymmetrical appearance comes from the number of sampling points used in the simulation.

the Voigt profile. The Voigt profile is the convolution of a Gaussian and a Lorentz function. Next section explains the usage of the Voigt fit and demonstrates the results of the analysis from the angular divergence between measurements and simulations.

5.3.1   Analysis through the Voigt function

As already discussed in Sec. 2.4.2, the Voigt function can be used as a tool for characterizing the angular divergence of the far-field obtained from the parallel laser beam measurements. In this work, the pseudo-Voigt function $\mathcal{V}(r)$ is used for ease of calculations. It is explained in Sec. 2.4.2, and represents a linear approximation that provides an analytical integrable combination of Gaussian and Lorentzian functions [53]. The validity of the pseudo-Voigt function has been proven by authors such as Whiting (1968) [57], Peyre and Principi (1972) [58], Kielkopf (1973) [59], Wertheim et al. (1974) [60], Titov and Haus (1997) [61], Ida et al. (2000) [62] and Liu et al. (2001) [63]. Figure 5.28 shows the example of the Voigt profile for $F(r)$ of measurements for both the circular and the octagonal fibre. In both cases the incident angle is of $\phi_{in} = 10$. The x-axis is in pixels, and the y-axes represents the normalized integrated intensity in the log_{10} scale.

The log_{10}-scale is used to illustrate the asymmetry towards the inner part of the far-field distribution. Light is scattered inside the ring distribution into a smaller area (see Sec. 2.4.2). After the averaging over the azimuthal axis, the scattering inside the ring leads to a higher intensity than the outside of the ring. At first glance, it appears that the circular fibre shows increased scattering. The actual cause is the integration time I_t that was used to acquire the images. The integration time for the circular fibre measurements was set to $I_t = 4sec$. For the octagonal fibre, the measurements were done using an integration time of $I_t \sim 1sec$. The difference in I_t comes from the fact that the measurements were acquired in separated periods of time. This involved rebuilding the input of the experimental setup, which means placing the fibre in the correct position for both input and output, setting the laser to an appropriate distance and setting the CCD parameters appropriately for correct data acquisition. As already described by Avila (1998) [38], the positioning between the fibre and detector tends to be the most critical error introduction.
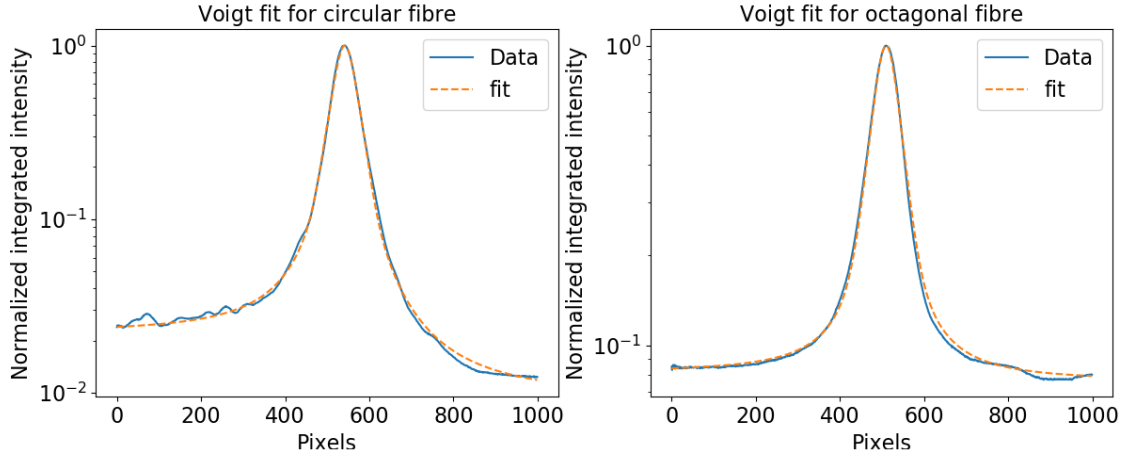
Figure 5.28: Voigt function applied to a circular and an octagonal fibre measurement. In both cases the incident angle is of $\phi_{in} = 10^o$. The x-axis is in pixels, and the y-axes represents the normalized integrated intensity in the log_{10}-scale.

The integration time of the octagonal fibre measurements was set to low for the scattering to be recorded. As described by Haynes et al. (2011) [53] a Gaussian is a good fit for the core region, and the Lorentzian is needed for the wings (scattering) of the profile. Since the core of the profile represents the region of interest, the measurements are still valid for the modal diffusion component obtained from the Gaussian part of the Voigt fit.

Due to the augmented intensity towards the inner part of $F(\phi_{o,p})$, the results of the Voigt analysis as a function of $\phi_{in} \in \{4^o, 5^o\}$ were not appropriate for comparison between measurements and simulations. Although it is not clear, a similar situation as for the near-field could have taken place. For shallower angles, there are substantially more modes active than in the simulations. For $\phi_{in} = 12^o$, the simulations could not be used to match the measurements. It could be that additional modes are needed, or the simulation of cladding modes is necessary to produce accurate results if ϕ_{max} is being used. The results are limited to $\phi_{in} \in \{6^o, ..., 11^o\}$.

The modal diffusion component is compared between simulations and measurements. The first goal of the analysis is to calculate the FWHM of the Gaussian component from the Voigt profile. The FWHM of the Gaussian component can be calculated with $\Gamma_G = 2\sigma_G\sqrt{\ln 2}$, with σ_G representing the standard deviation of the Gaussian function. The FWHM of the Lorentzian function is given by $\Gamma_L = 2\gamma_L$, with γ_L being the parameter that specifies the width of the function. The parameter Γ_G represents both the diffraction and modal diffusion components. To separate the modal diffusion component, it is possible to apply the addition of two Gaussian as in

$$\sigma_G = \sqrt{\sigma_A^2 + \sigma_D^2}, \tag{5.6}$$

with σ_A representing the circular aperture diffraction parameter, and σ_D representing the modal diffusion parameter. The diffraction parameter is the same for both the measurements and the simulations. Circular aperture diffraction can be described with the Airy disk [45]. The angle subtended by the radius of the Airy disk is given by

$$\theta_{Airy} = 1.22\frac{\lambda}{D} \tag{5.7}$$

Since the central part of the Airy disk can be approximated by a Gaussian, the standard deviation of the Airy disk is given through [45]

$$\sigma_{Airy} = \frac{1}{2}\theta_{Airy}. \tag{5.8}$$

The light source is the HeNe laser which has the propagation wavelength $\lambda = 0.633\mu m$. The diameter of the fibre is $d = 50\mu m$. By applying Eq. 5.7 and Eq. 5.8, the FWHM of the Airy disk results in $A_{FWHM} = 0.7368^o$. After acquiring σ_G for both the simulations and the measurements, the standard

deviation of the modal diffusion component is obtained through $\sigma_D = \sqrt{\sigma_G^2 - \sigma_A^2}$. The results of the angular divergence are given as the FWHM of the modal diffusion component. As previously described, the FWHM of a Gaussian distribution is a function of the standard deviation, $\text{FWHM}_x = 2\sigma_x\sqrt{\ln 2}$. Figure 5.29 shows the results for the circular fibre. The field diameter of the simulations was of $d_{in} = 50\mu m$, matching the diameter of the fibre. The x-axis represents the input angle ϕ_{in}, and the y-axis is the angular divergence illustrated as the FWHM of the Gaussian fit. A linear fit is displayed and shows the slope of the measurements. The simulations are marked as G_{sim}, the measurements are marked as G_{meas}, and the linear fit is marked as *"linear fit"*.
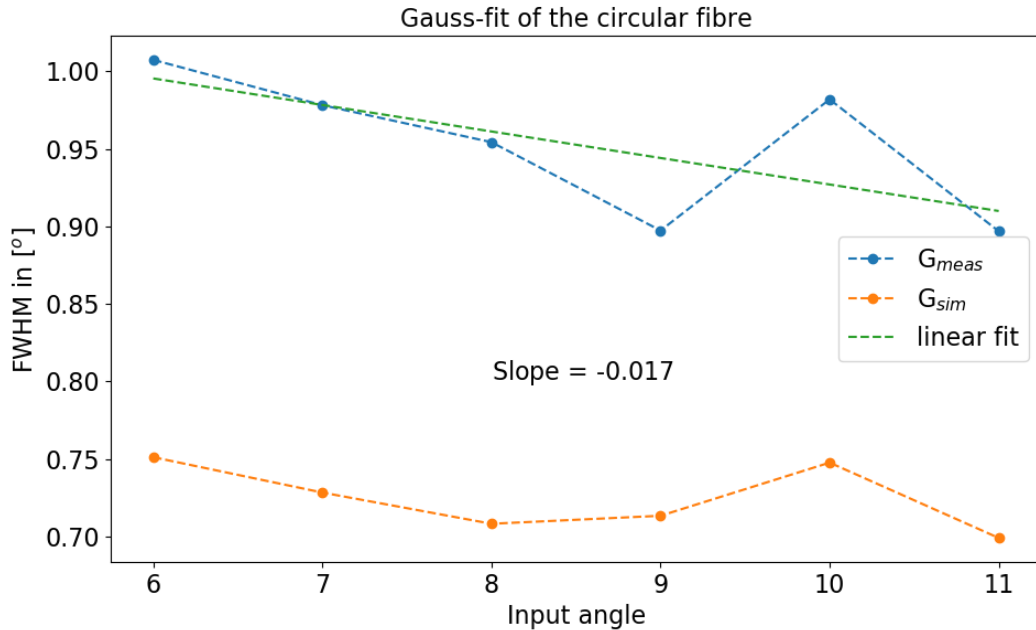
Figure 5.29:   Results of the angular divergence between simulations and measurements for $\phi_{in} \in \{6^o, ..., 11^o\}$ using the circular fibre.   The x-axis represents the input angle ϕ_{in}, and the y-axis is the angular divergence illustrated as the FWHM of the Gaussian fit.

The same analysis was done for the octagonal fibre, and the results are presented in Figure 5.30. Once more, the field diameter of the simulations was of $d_{in} = 50\mu m$. The x-axis represents the input angle ϕ_{in}, and the y-axis is the angular divergence illustrated as the FWHM of the Gaussian fit. A linear fit shows the slope of the measurements. The simulations are marked as G_{sim}, the measurements are marked as G_{meas}, and the linear fit is marked as *"linear fit"*. The meaning of the slope of the linear fit will be explained in the following paragraphs.

As can be seen from Fig. 5.29 and Fig. 5.30, both fibres show similar results. It was expected that the angular divergence reduces with the increment of the input angle ϕ_{in}. This can be explained as follows. As the ring distribution expands with incrementing ϕ_{in}, the intensity is distributed into a larger area. Through the distribution of intensity into a larger area, the thickness of the ring reduces. The reduction of thickness translates into reduction of the FWHM for the fit functions. The reduction of the FWHM means a diminished angular divergence.

Table 5.1 shows the results of the divergence analysis. The parameter "Mean simulations" is the mean of the simulations $\overline{G_{sim}}$. The parameter "**Mean difference**" represents the mean of the difference between measurement and simulations $\overline{G_{meas} - G_{sim}}$. The parameter "Sensibility" represents the absolute value of the slope β from the linear fit with $Sensibility = |\beta|$.

Since there are no disturbances taken into account in the simulations, the results of the simulations can be interpreted as the best case scenario for the angular divergence. The mean of the simulations for both
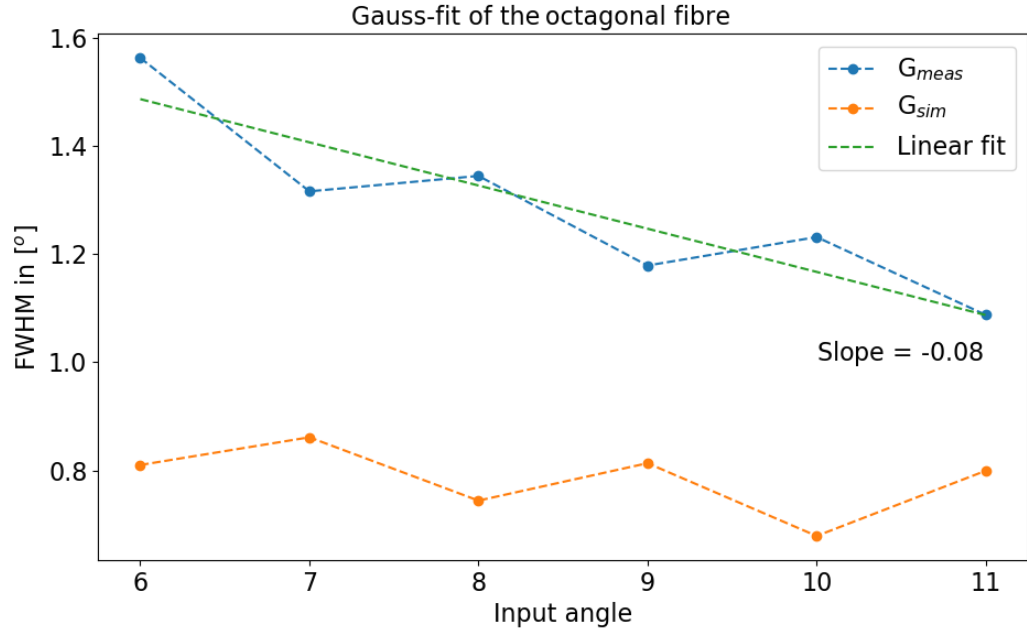
Figure 5.30: Results of the angular divergence comparison between simulations and measurements for $\phi_{in} \in \{6^o, ..., 11^o\}$ using the octagonal fibre. The x-axis represents the input angle ϕ_{in}, and the y-axis is the angular divergence illustrated as the $FWHM$ of the Gaussian fit.

Parameter	Circular fibre	Octagonal fibre
Mean simulations	0.724^o	0.7843^o
Mean difference	0.228^o	0.503^o
Sensibility	0.017	0.08

Table 5.1: Results of the divergence analysis for both fibres.

fibres showed similar results, with the simulated circular fibre having slightly better results. The closer the measured fibre is to the simulated case, the better the performance. As a figure of merit, the mean of the difference for every input angle was calculated. The closer the value is to zero, the better the performance. Interestingly, the circular fibre performed better than the octagonal fibre. The slope of the linear fit represents the change in divergence per input angle and has the unit $[^o/^o]$. A steeper slope means more sensibility to input angular fluctuations. Once again, the circular fibre performed better.

The mode coupling factor σ_c of the simulations accounts for all the beam broadening factors that can occur in a real measurement. Through σ_c, the divergence of G_{meas} can be matched. As explained in Sec. 3.5.1, the modal amplitude array is convolved with a Gaussian array to produce a new modal amplitude array that accounts for the mode coupling. The Gaussian array has the same length as the modal amplitude array. By increasing the σ_c of the Gaussian, the stronger the mode coupling factor works. The values for σ_c are normalized to 1. To match the measurements, σ_c takes values between 0.05 and 0.16. Figure 5.31 shows the example for $\phi_{in} = 8^o$ of the circular fibre. The mode coupling factor σ_c has the value $\sigma_c = 0.10$ to match G_{meas}. For clarity of the plot, only the Gaussian fit of the simulation, and the Gaussian fit of the simulation with mode coupling are shown. Additionally, bar plots showing the difference in modal population are illustrated.

This procedure was done for every $\phi_{in} \in \{6^o, ..., 11^o\}$. Figure 5.32 shows the results for both the circular and the octagonal fibre. A linear fit for both fibres is also displayed and shows the increment in mode coupling per input angle.
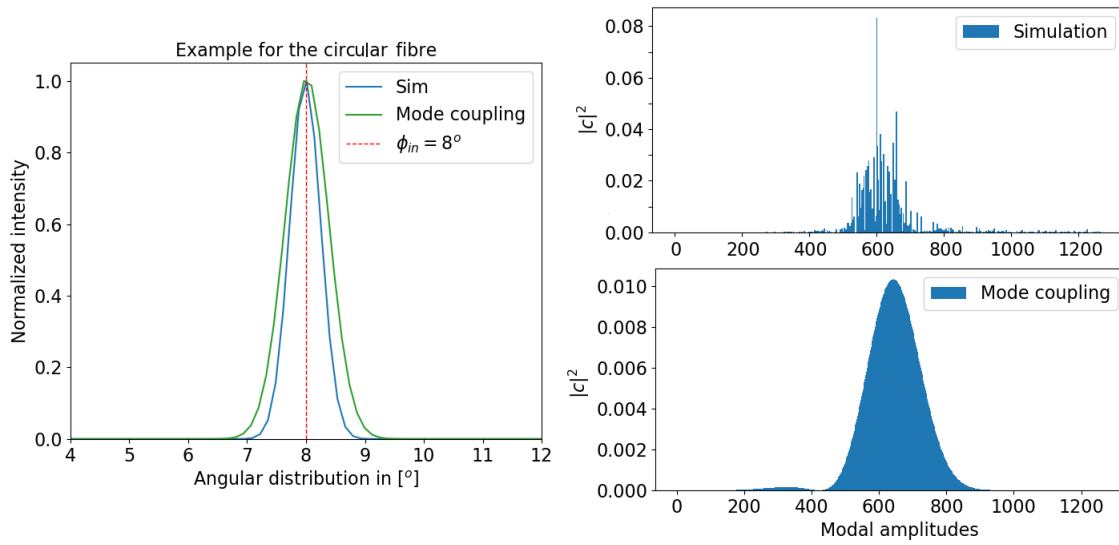
Figure 5.31: Usage of mode coupling in the simulations to match G_{meas}. Bar plots showing the difference in modal population are also illustrated.
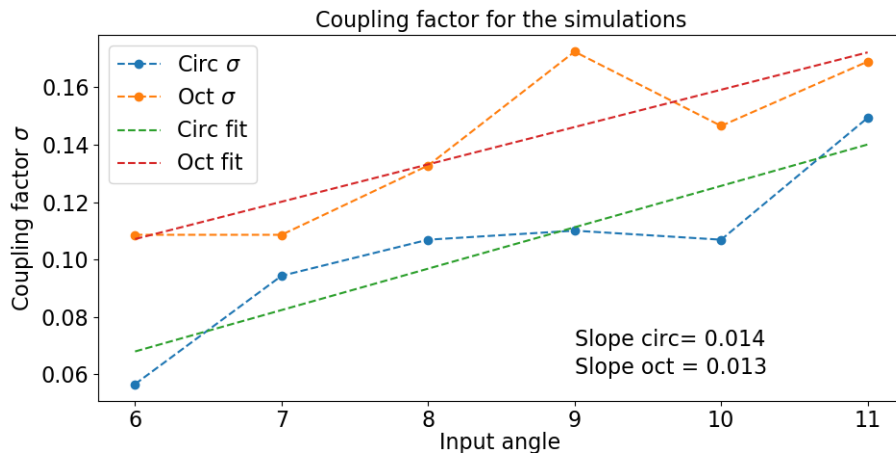

Figure 5.32: Mode coupling factor σ_c needed to match G_{meas} for both the circular and the octagonal fibre.

As can be observed from Fig. 5.32, both fibres show a similar response. There is a tendency that the mode coupling factor increases with input angle. In both cases, which are fairly similar, the increment is described by the slope of the linear fits. Since the real octagonal fibre showed an augmented angular divergence, the σ_c values for the octagonal fibre were expected to be higher. Unfortunately, there is still no answer to why the mode coupling factor increases with the input angle. This should be solved in future work.

For both Fig. 5.29 and Fig. 5.30, a total number of 5 measurement points were available. To check the angular divergence with a finer resolution, simulations were conducted with $\phi_{\in}\{6^o, ..., 11^o\}$ in steps of 0.05^o/simulations, giving a total of 100 simulated points. This was done for both the circular and the octagonal fibre. Figure 5.33 shows the result.

As can be observed from Fig. 5.33, no actual pattern can be recognized. It is to be noticed that the pattern will change with spatial translation or change in the FWHM of the input spot. This leads to the conclusion of a chaotic system. For the best case, the median can be calculated but it is hard to identify any sort of pattern that would lead to a reduction of the angular divergence.
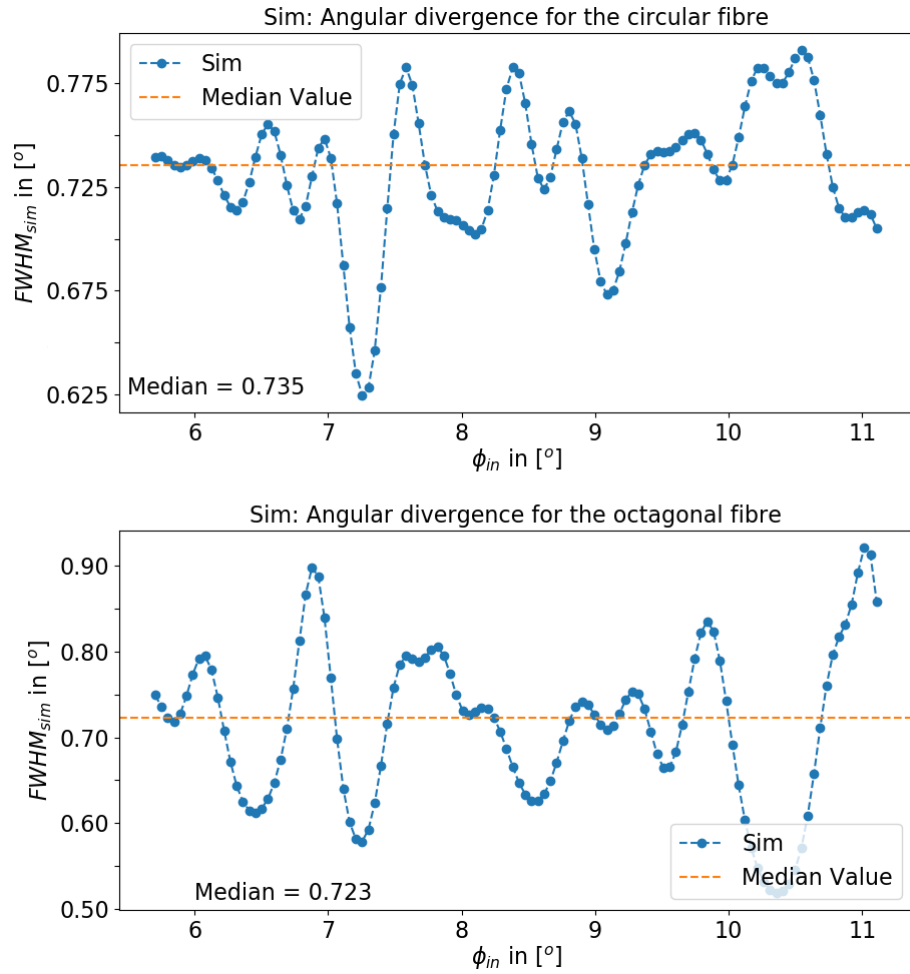
Figure 5.33: Simulations with increased resolution between $\phi_\in \{6^o, ..., 11^o\}$. A total of 100 points were simulated for both the circular and octagonal fibre. The x-axis marks the input angle ϕ_{in}. The y-axis marks the divergence as the FWHM of the fit function.

The parallel laser beam method is a good tool for the characterization of the angular divergence as a function of the input angle ϕ_{in}. To calculate the actual loss of the system, the light cone measurement is a more appropriate method. The next section presents the results acquired using the test bench configuration for the light cone method and how the simulations can be used to resemble the obtained results.

5.4 Light Cone Measurements

The light cone method consist in the injection of an f-number to the test fibre and recording the output cone for the comparison between the input and output f-numbers (see Sec. 2.4.2). For the measurements, the test-bench was set in the appropriate configuration. The light source was the halogen lamp with the $20\mu m$ seed fibre, resulting in an $20\mu m$ input spot reimaged at the input face of the test fibre. Similar to the scrambling measurements presented in Sec. 5.2, the f-number was changed by inserting an appropriate pupil stop in the pupil plane of the optical path. Using the $2k \times 2k$ CCD and the translation stage TS (see Sec. 4.2.3), the recording of the output cone was possible. The translation stage moved the CCD camera in 10 controlled steps of $\Delta x = 1mm$.

The resulting output f-number depends on the encircled energy (EE) the system should have. For this work, the encircled energy was determined as follows. The output intensity was integrated along the azimuthal axis and a 1D distribution $F(r)$ was created. The one dimensional distribution was weighted by the circumference at distance r as in $F_w(r) = F(r) * 2\pi r$ and normalized to the condition $\sum_{r=0}^{R} F_w(r) = 1$. A given encircled energy can be found by adding the distribution until $\sum_{r=0}^{\rho} F_w(r) = EE$. For any given encircled energy, the measurements should deliver a linear increase as a function of the sampling step $\Delta x = 1mm$. The resulting output f-number is a function of the slope from the linear fit. Figure 5.34 shows the result of an FRD cone measurement. The circular fibre was used with an f-number $f\#_{in} = 5$. The x-axis represents the output f-number, and the y-axis displays the amount of EE as a function of $f\#_{out}$. In this example, $EE = 82.4\%$ for the case that $f\#_{out} = f\#_{in}$. A typical value for the encircled energy is $EE = 95\%$ [54]. If the EE is aimed for 95%, the measurement in Fig. 5.34 has a value of $f\#_{out} = 4.39$.
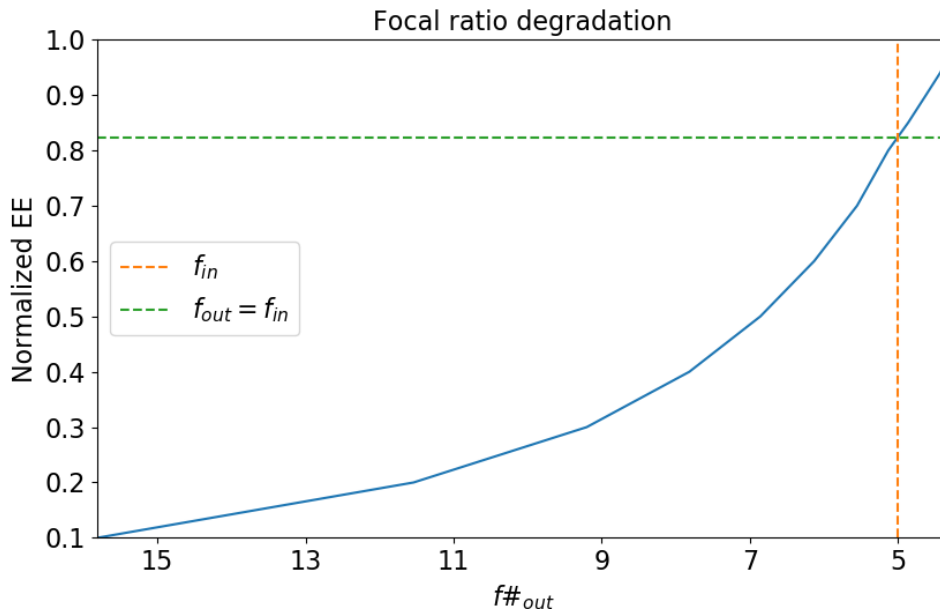

Figure 5.34: Example of an FRD cone measurement. The circular fibre was used with an f-number $f\#_{in} = 5$. The x-axis represents the output f-number, and the y-axis displays the amount of EE as a function of $f\#_{out}$.

Since a vast number of factors can affect the output angular distribution of a fibre, FRD measurements tend to vary in results, even if the same fibre is being measured. As an example, the measurement that produced the results of Fig. 5.34 was realized on the 10th of May, 2017. A second run of FRD measurements was realized on October, 2017, five months later than the first run. The same circular fibre and the octagonal fibre were characterized. Although the same procedure was followed, and the same equipment was used, there was an increase in performance in the measurements of the circular fibre. For the same case of using an input f-number of $f\#_{in} = 5$ and $f\#_{out} = f\#_{in}$, the encircled energy obtained was $EE = 87.16\%$. There was an increment of $\sim 5\%$ in performance. For the case of $EE = 95\%$, the output f-number was measured to $f\#_{out} = 4.48$. The octagonal fibre showed for $f\#_{out} = f\#_{in}$ a value $EE = 84.6\%$. For the case $EE = 95\%$, the output f-number was measured to $f\#_{out} = 4.39$. This shows that the octagonal fibre performed worse than the circular fibre in the second run of measurements but better than the first measurement of the circular fibre. Figure 5.35 shows the results of the second measurement run for both the circular and the octagonal fibre. The x-axis represents the output f-number, and the y-axis displays the amount of EE as a function of $f\#_{out}$.
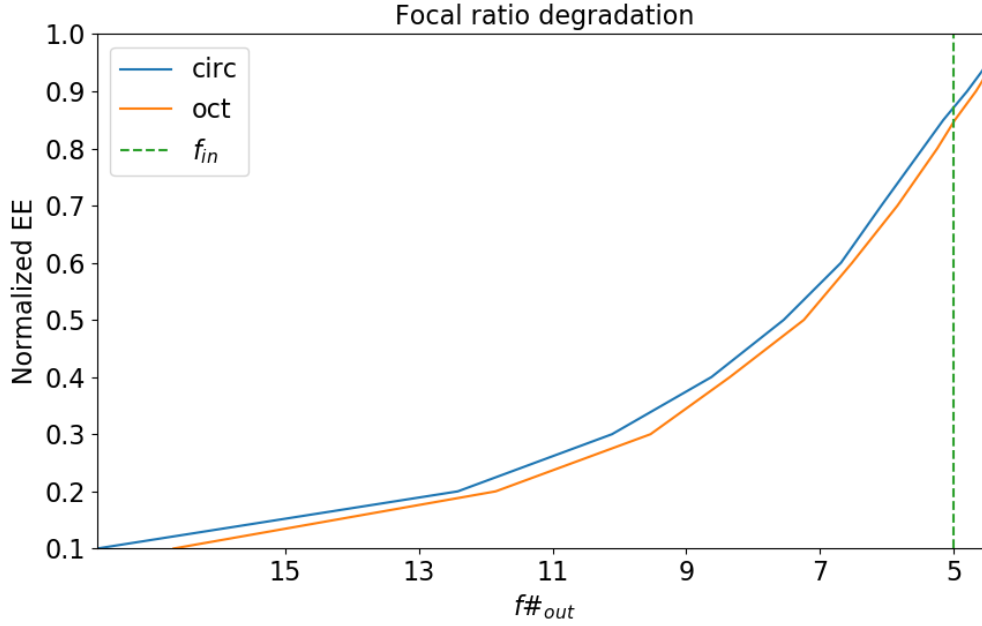
Figure 5.35: Results for both the circular and octagonal fibre. The x-axis represents the output f-number, and the y-axis displays the amount of EE as a function of $f\#_{out}$.

Radiance loss

The radiance gives the amount of power contained in the angular distribution and is in the best case invariant for a lossless optical system. To calculate the loss of radiance in a system, the equations of optical throughput from Sec. 2.2 are used. The radiant flux is described as $\Phi = LS\Omega$, with L representing the radiance in $[W \cdot sr^{-1} \cdot m^{-2}]$, S the surface, and Ω the solid angle. As stated by Eq. 2.29, the optical etendue is described with $E = n^2 S\Omega$. If applied to an optical fibre, S represents the acceptance area of the fibre. If the complete input/output face of the fibre is illuminated, S can be describe with $S = \pi d^2/4$. The solid angle Ω of an optical fibre is calculated through $\Omega = \pi \sin^2 \theta_{max}$ [30]. Using the first principle of thermodynamics (flux conservation, see Eq. 2.31), the input/output radiance of a fibre is described through

$$L_{in} \frac{\pi r_{in}^2}{(2f\#_{in})^2} = L'_{out} \frac{\pi r_{out}^2}{(2f\#_{out})^2}. \tag{5.9}$$

To solve for the radiance loss in the system, Eq. 5.9 translates to

$$\frac{L'_{out}}{L_{in}} = \left(\frac{f_{out}}{f_{in}} \cdot \frac{r_{in}}{r_{out}} \right)^2 \tag{5.10}$$

Equation 5.10 describes the loss of radiance by using the input/output f-number as well as the input/output near-field radius of a given system.

Using the value of $EE = 95\%$, the first measurement of the circular fibre and the measurement of the octagonal fibre had an output value of $f\#_{out} = 4.39$. The second measurement recorded an output value of $f\#_{circ} = 4.48$. For the case that $r_{in} = r_{out}$, Eq. 5.10 delivers a radiance loss of $L'_{out} \approx L_{in} * 0.77$ for $f\#_{out} = 4.39$. If $f\#_{circ} = 4.48$ is used, the radiance loss equals $L'_{out} \approx L_{in} * 0.80$.

Since the seed fibre was reimaged on the input face of the test fibre, the radius r_{in} equals $r_{in} = 10\mu m$. As was illustrated in Sec. 5.2.1, the output near-field radius enlarges with increasing input angle. For $f\#_{in} = 5$, the output near-field distribution of the circular fibre had a radius of $r_{nf} \approx 0.88 r_f$ (see Fig. 5.14), with $r_f = 25\mu m$. The output near-field radius of the octagonal fibre could not be analyzed, since the

scrambling measurements of the octagonal fibre were corrupted. Fortunately, the near-field measurements of the parallel laser beam method delivered appropriate results. Using the values obtained in Fig. 5.13, the value of $r_{nf,oct}$ can be set to $r_{nf} \approx 0.92 r_f$. If the difference between r_{in} and r_{out} is taken into account, Eq. 5.10 delivers a total radiance loss of $L'_{out} \approx L_{in} * 0.159$ for the first measurement of the circular fibre, $L'_{out} \approx L_{in} * 0.165$ for the second measurement of the circular fibre, and $L'_{out} \approx L_{in} * 0.145$ for the octagonal fibre. Equation 5.10 reveals that the input spot radius should match the fibre radius for best results. Table 5.2 summarizes the results of the calculations. The second measurement of the circular fibre showed the best results.

Parameter	Circular fibre 1	Circular fibre 2	Octagonal fibre
$f_{in} = f_{out}$	$EE = 82.4\%$	$EE = 87.16\%$	$EE = 84.6\%$
$EE = 95\%$	$f_{out} = 4.39$	$f_{out} = 4.48$	$f_{out} = 4.39$
$L_{out}/L_{in}, r_{in} = r_{out}$	0.77	0.80	0.77
$L_{out}/L_{in}, r_{in} \neq r_{out}$	0.159	0.165	0.145

Table 5.2: Results of the FRD analysis and radiance loss.

Simulating the input light cone

To date, the simulations are limited to the monochromatic case of light propagation. Furthermore, the injection of a light cone can not be simulated as effectively when compared to the injection of only specific input angles. Two methods were tested for the simulations to resemble a simplified case of the light cone injection. Both will be explained in the following paragraphs.

The first approach consist in using the maximum mode $M(\phi_{in})$ a specific input angle ϕ_{in} excites. The input f-number $f\#_{in}$ can be translated to an input angle $\phi_{in} = \arcsin{(1/(2f\#_{in}))}$. As described in Eq. 5.1, the amount of modes excited by a specific input angle ϕ_{in} is equivalent to $M(\phi_{in}) = (2\pi r \sin(\phi_{in}))^2/(2\lambda^2)$. Afterwards, all modes in the modal power distribution are activated equally up to mode $M(\phi_{in})$. Figure 5.36 shows the example of the resulting output far-field distribution after simulating a cone injection with $f\#_{in} = 5$, which is equivalent to $\phi_{in} = 5.74^o$. The 1D intensity distribution is also illustrated. The x-axis represents the output angle ϕ_{out}, and the y-axis shows the normalized intensity distribution. The mark represents where the encircled energy equals $EE = 95\%$. The encircled energy was calculated utilizing the same method as for the measurements. In this simulation example, the output f-number equals $f\#_{out} \approx 5.1$ for $EE = 95\%$, which is not consistent with the real case.

The second method consist in simulating an input spot using different input angles as in $\phi_{in} \in \{\phi_o, ..., \phi_{max}\}$, and obtaining different field propagations for each ϕ_{in}. In this case, ϕ_{max} is dictated by the input f-number and once again can be calculated through $\phi_{max} = \arcsin{(1/(2f\#_{in}))}$. This method gives the opportunity of simulating an input spot with a smaller diameter than the simulated fibre, simulating spatial translation of the input spot, and allows for the usage of mode coupling. The end result consist in incoherently adding all the output fields $\psi_{out,i}$, with $i \in \{o, ..., max\}$, and takes the form

$$\sum_i \psi_{out,i} = \Psi_{out,cone} \tag{5.11}$$

As an example, the identical system as for the former method was simulated. The input f-number was of $f\#_{in} = 5$, which represents an input angle $\phi_{max} = 5.74^o$. Five steps with an equivalent angular spacing were used for ϕ_{in}, resulting in five different $\psi_{out,i}$. As demonstrated in the previous sections, the mode coupling factor is needed for the output intensity distributions of the simulations to resemble actual output intensity distributions. Based on the results of the Voigt-analysis (see Sec. 5.3.1), a normalized mode coupling factor of $\sigma = 0.08$ was used in every step. The input spot was chosen to resemble the $r_{in} = 10\mu m$ of the measurements and was inserted in the center of the input face of the simulated fibre. Figure 5.37 shows the results.
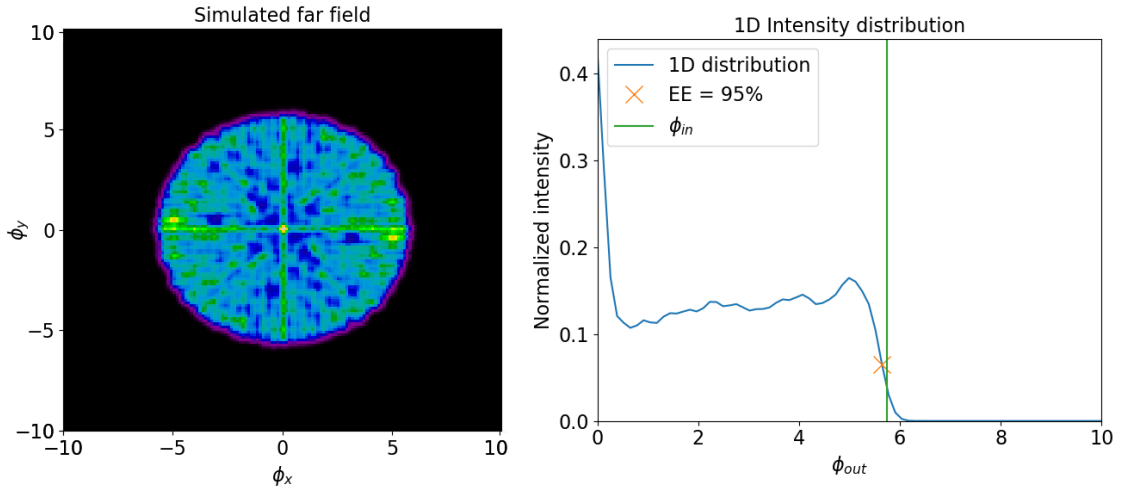
Figure 5.36: *(left)* The resulting output far-field distribution. The x-axis and y-axis represent the angular coordinates ϕ_x and ϕ_y. *(right)* The resulting 1D intensity distribution. The x-axis represents the output angle ϕ_{out}, and the y-axis shows the normalized intensity distribution. The mark represents where the encircled energy equals $EE = 95\%$.
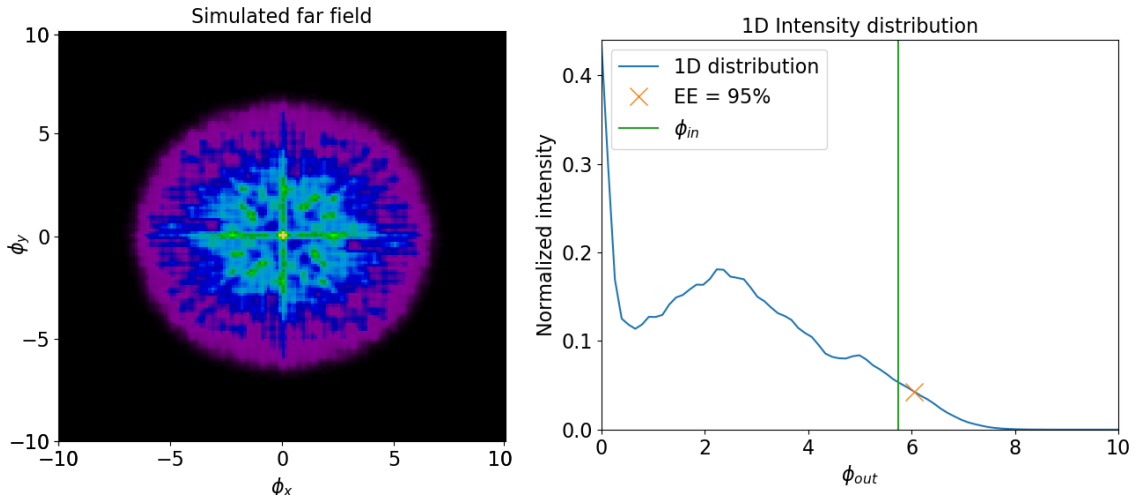

Figure 5.37: *(left)* The resulting output far-field distribution. The x-axis and y-axis represent the angular coordinates ϕ_x and ϕ_y. *(right)* The resulting 1D intensity distribution.

Once again, the resulting output far-field distribution as well as the 1D intensity distribution are illustrated. The x-axis represents the output angle ϕ_{out}, and the y-axis shows the normalized intensity distribution. The mark represents $EE = 95\%$. In this simulation example, the output f-number equals $f\#_{out} \approx 4.37$ for $EE = 95\%$. Through this method, a similar result to the first circular fibre measurement was obtained.

It is possible to obtain the input/output angular information from each simulation that allows for the calculation of the encircled energy plot (see Fig.5.34 and Fig. 5.35). Due to the resemblance in the result $EE = 95\%$ between the simulation and the first measurements of the circular fibre, the FRD plots of both were compared. Figure 5.38 shows the results. The x-axis represents the output f-number, and the y-axis displays the amount of EE as a function of $f\#_{out}$. The input f-number $f\#_{in} = 5$ is illustrated as well as the location in the plot corresponding to $EE = 95\%$. As can be observed, both systems converge towards the same value for $EE = 95\%$, but the simulation shows an overall better performance. For the case $f\#_{in} = f\#_{out}$, the simulated fibre shows an encircled energy $EE_{sim} = 86.2\%$ instead of $EE_{meas} = 82.4\%$.
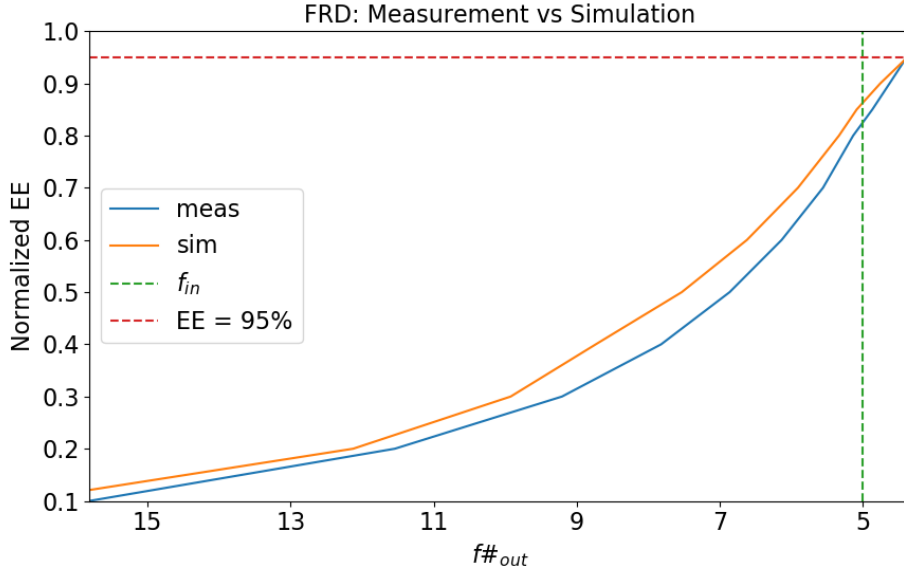
Figure 5.38: Comparison between the first measurement of the circular fibre and the simulation. The input f-number $f\#_{in} = 5$ is illustrated once more, as well as the location in the plot corresponding to $EE = 95\%$.

As can be observed from Fig. 5.38, the FRD characteristics can be approximated well using the second cone simulation method. To make the measurements and simulations match, the mode coupling parameter could be manipulated in every step $\phi_{in} \in \{\phi_o, ..., \phi_{max}\}$. Due to the incoherent addition of every $\psi_{out,i}$, the analysis of the contribution in the overall sum of each individual mode coupling factor results in a complicated task that could be targeted in future work.

To finalize the assessment, the octagonal fibre was simulated and compared to the simulations of the circular fibre. Once again the results of the Voigt-analysis were used to choose an appropriate value of the normalized mode coupling factor σ_{oct}. The coupling factor was set to $\sigma_{oct} = 0.12$. Figure 5.39 shows the results. The results are quite similar for both fibres. The circular fibre does produce better values for the cases of $f\#_{in} = f\#_{out}$ and $EE = 95\%$. Table 5.3 summarizes the results. The outcome of the circular fibre outperforming the octagonal fibre was expected since the results of the angular divergence from the circular fibre were already better than for the octagonal fibre.

Parameter	Circular fibre	Octagonal fibre
$f\#_{in} = f\#_{out}$	$EE = 86\%$	$EE = 79\%$
$EE = 95\%$	$f\#_{out} = 4.37$	$f\#_{out} = 4.12$
$L_{out}/L_{in},\ r_{in} = r_{out}$	0.76	0.67
$L_{out}/L_{in},\ r_{in} \neq r_{out}$	0.16	0.14

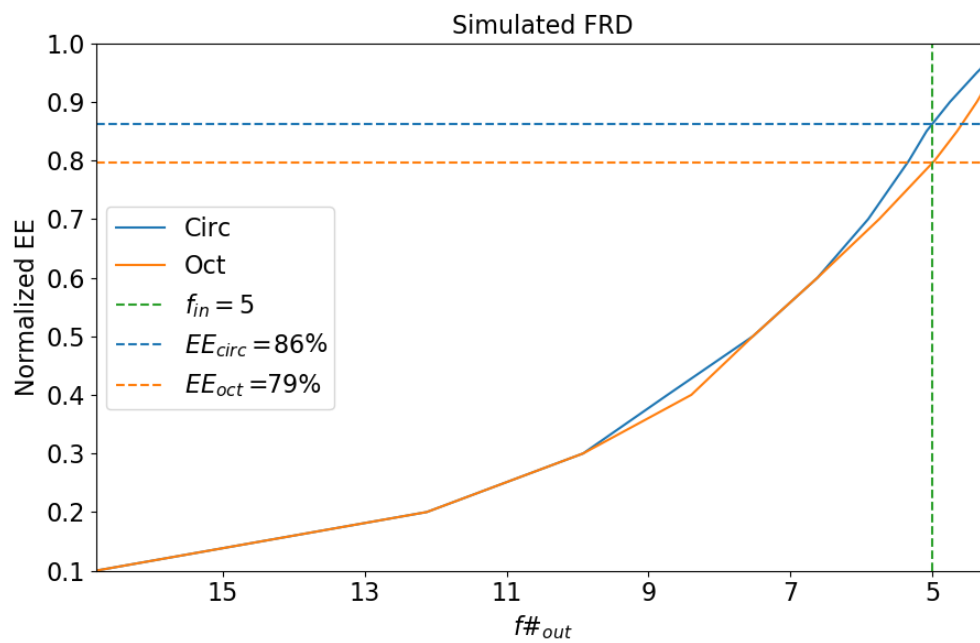Table 5.3: Results of the FRD analysis and radiance loss of the simulations.

Figure 5.39: Comparison between the simulations of the circular fibre and octagonal fibre. The x-axis represents the output f-number, and the y-axis displays the amount of EE as a function of $f\#_{out}$. The input f-number $f\#_{in} = 5$ is once more illustrated as well as both cases for $f\#_{in} = f\#_{out}$.

5.5   Summary

Realistic measurements allowed testing the accuracy of the field propagation model developed for this work. By emulating the properties of the measured fibres, similar results through the simulations were accomplished. There are several constraints for the simulations. For example, the loss coefficient α_λ is not taken into account, the field propagation is only monochromatic, a phenomenological approach is used for simulating mode coupling, and only complete coherence propagation or complete incoherence propagation can be simulated. Nevertheless, equivalent results were obtained for all tests.

Modal interference was analyzed in Sec. 5.1. Having a highly coherent source as the HeNe laser gave the advantage to analyze the near-field speckle pattern as a function of the input angle ϕ_{in}. The speckles are the result of modal interference. For higher-order modes, the spatial frequency of the intensity fluctuations increment and the speckles reduce in size. For shallow input angles, the measurements showed a higher number of propagation modes than expected. This can be attributed to refractive index defects, mechanical stress caused by input/output interfaces, fibre positioning in the test rig and/or the fibre termination procedure. Using the mode coupling factor σ, it was possible to increment the number of propagation modes in the simulations.

For the characterization of the speckle pattern, the power spectral density analysis was applied. It decomposes the intensity of the field into contributions from the different spatial frequencies [72]. There was a good correlation between measurements and simulations. The higher spatial frequencies tend to get more power with increasing ϕ_{in}. This was expected since higher spatial frequencies imply increased fluctuations in the intensity pattern as a result of the diminished speckle size. Figure 5.40 shows examples of the circular fibre PSD analysis for the input angles $\phi_{in} \in \{7^o, 9^o, 11^o\}$.
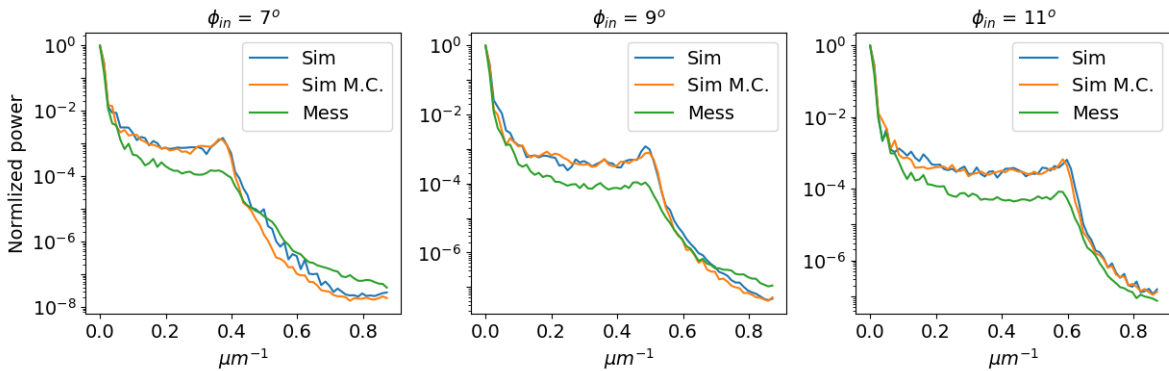

Figure 5.40: Comparison of the PSD between the measurements and simulations of the circular fibre.

An error analysis between the measurements and the simulations was realized for both the circular and the octagonal fibre. Through the error analysis of the octagonal fibre, it was found that the results diverged between the simulations and the measurements. The PSD was recording higher spatial frequencies for the same input angles. Since only modal interference could account for the increase in spatial frequencies, it meant that higher-order modes were propagating in the measured fibre. This was attributed to the tolerances that the real fibres possess. Since the information of the NA is given by the manufacture as $NA = 0.22 \pm 0.02$ (see Tab. 4.1), the tolerance in the NA was investigate. To test the hypothesis, a low tolerance fibre and a high tolerance fibre were simulated. The PSD analysis was done, and the results for an input angle of $\phi_{in} = 11^o$ showed good agreements with the error analysis. Figure 5.41 shows the comparison of the simulations between the fibres with low and high NA tolerances. It is expected that the fibre tolerances also contribute to the beam divergence which translates into the FRD characteristic of the fibre, i.e. loss of throughput. This analysis will be done for a future publication.

Section 5.2 dealt with modal scrambling. To smooth out the speckle pattern, modal scrambling can be induced. Perfect modal scrambling occurs when the phases of all active propagation modes are completely
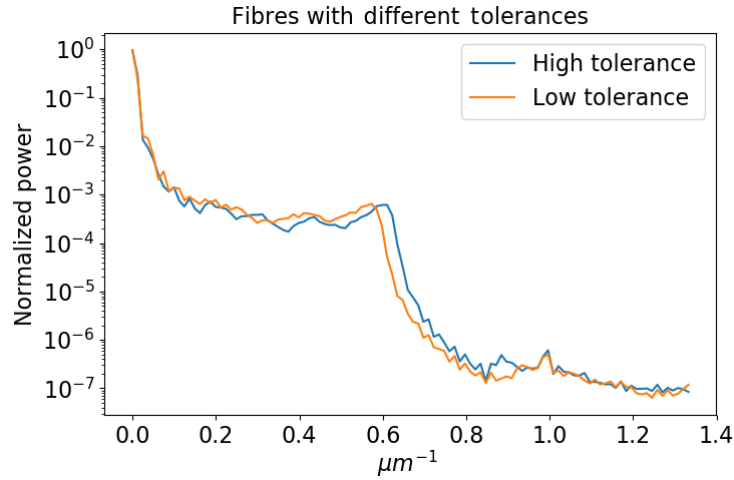
Figure 5.41: Comparison of two octagonal fibres within the NA tolerance of the measured octagonal fibre. The high tolerance fibre is marked as *"High tolerance"*, and the low tolerance fibre is marked with *"Low tolerance"*.

randomized. Both test fibres were agitated with a probe shaker to induce scrambling. Although the speckles vanished, intensity patterns of different frequencies appeared as a function of the input angle ϕ_{in}. The low spatial frequency fluctuations were attributed to the field distribution of the low order modes. For higher input angles, e.g. $\phi = 10^o$, the modal structures of the high order modes became visible, especially in the case of the octagonal fibre. The circular fibre appeared to still have modal interference for both examples presented with $\phi_{in} \in \{1^o, 10^o\}$, giving the hint that partial coherence was taking place. The simulations can only emulate the propagation cases of complete coherence or complete incoherence. The simulations with incoherent propagation were compared with the measurements with induced modal scrambling for both fibres. Figure 5.42 shows the comparison for both fibres. Mode coupling was used for all simulations. It was needed for the fields to resemble real measurements, especially with smaller input angles.

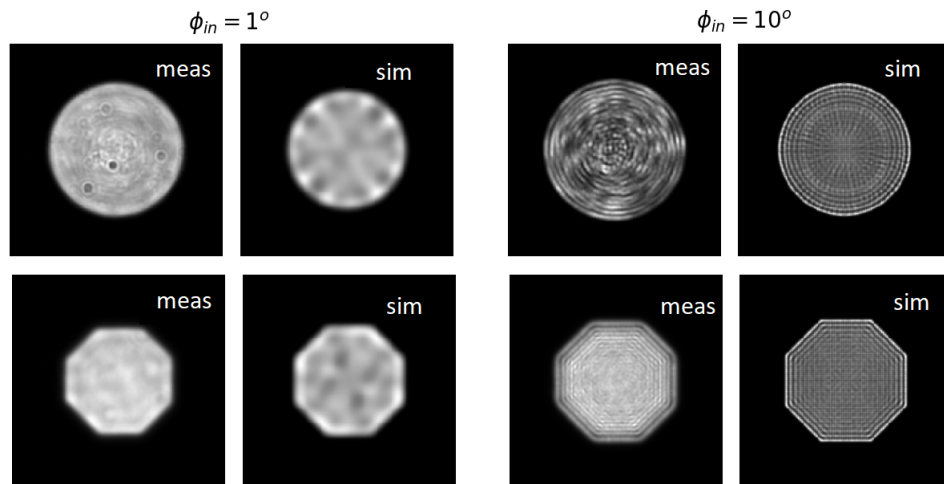Figure 5.42: Comparison between measurements with induced modal scrambling and simulations with incoherent propagation. Both the circular and octagonal fibres are illustrated. The axes are eliminated for displaying purposes.

The simulations of the circular fibre differed more from the respective measurements than the simulations of the octagonal fibre. For both input angles in the circular fibre measurements, high spatial frequency

fluctuations appeared to be confined in the center of the measured near-field intensity distribution. This was attributed to two situations: **A)** Actual modal interference was taking place but somehow confined to the center of the fibre. **B)** An aberration from the 50×LWD objective was observed. The first situation could be analyzed with partial coherence in future work. The second situation could be evaluated by remeasuring with the same objective and once more analyzing the results. It could be that the objective aberrations are the cause or part of the cause concerning the confinement of the high spatial frequency fluctuations mostly in the center of the intensity distribution.

As can be observed from Fig. 5.42, the size of the near-field intensity distribution changed as a function of the input angle ϕ_{in}. In a fibre-fed spectrograph, the near-field intensity is usually projected on the recording device, e.g. CCD [30]. If the near-field intensity distribution changes as a function of the input angle, it will create extra fluctuations in the intensity sampling on the finite area of pixels. For a proper assessment of the near-field enlargement, both the monochromatic case and the chromatic case were analyzed. Figure 5.43 shows the results for the monochromatic case. The increment of both fibres is presented as a function of the input angle ϕ_{in}. In this example, the octagonal fibre appeared to be more sensitive to the near-field enlargement. The simulations were once more in good agreement with the measurements.
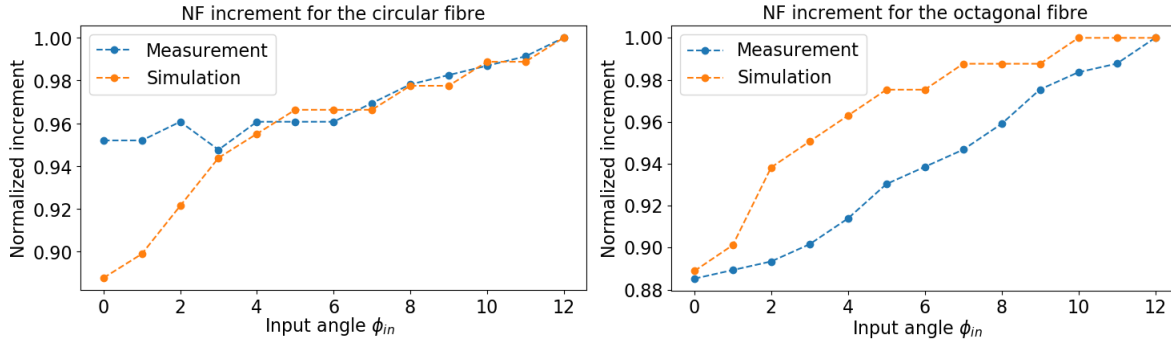

Figure 5.43: Near-field increment for the measurements and simulations of the circular and octagonal fibre. *(left)* Measurements and simulations of the circular fibre. *(right)* Measurements and simulations of the octagonal fibre.

To test the near-field enlargement for the chromatic case, near-field measurements using the halogen lamp in the test-bench were used. Since the enlargement of the near-field was observed after the experimental tests were concluded, it was possible to work only with the available data. After the analysis of the results using this specific test-bench configuration, it was concluded that the measurements with the octagonal fibre were unfortunately corrupted. The measurements of the circular fibre in combination with different bandpass filters were analyzed. The bandpass filters had the central wavelengths $\lambda_c \in \{436nm, 546nm, 600nm, 905nm\}$. Each filter had a $\Delta\lambda = 10nm$ bandwidth. Figure 5.44 shows the results. The results were in good agreement with theory since individual mode field diameters tend to increase with the wavelength [45]. The NIR bandpass filter showed stronger fluctuation than the red and the yellow filter. Since the NIR filter was measured on a different date, systematic errors, such as dissimilar placement on the focal plane of the objective lens, could be the cause of the augmented NIR near-field diameter fluctuations. Although there is a substantial difference in size for the blue wavelength, the overall fluctuations for the full band are still the strongest. For applications of astronomical spectroscopy, even low-resolution gratings will produce results with smaller bandpass properties than the used filters. This implies that the diameter fluctuations should not get worse than the results for the shortest wavelength, in this case, $\Delta d_{blue} \approx 8\%$.

The monochromatic case demonstrated that the results of incoherent superposition still produced intensity fluctuations in the near-field distribution. This can be best observed for the induced modal scrambling measurements of the octagonal fibre and its simulation through the incoherent superposition of the propagation modes. The incoherent intensity fluctuations as a function of the input angle were also observed during the measurements of the circular fibre using the different bandpass filters. Due to the bandwidth
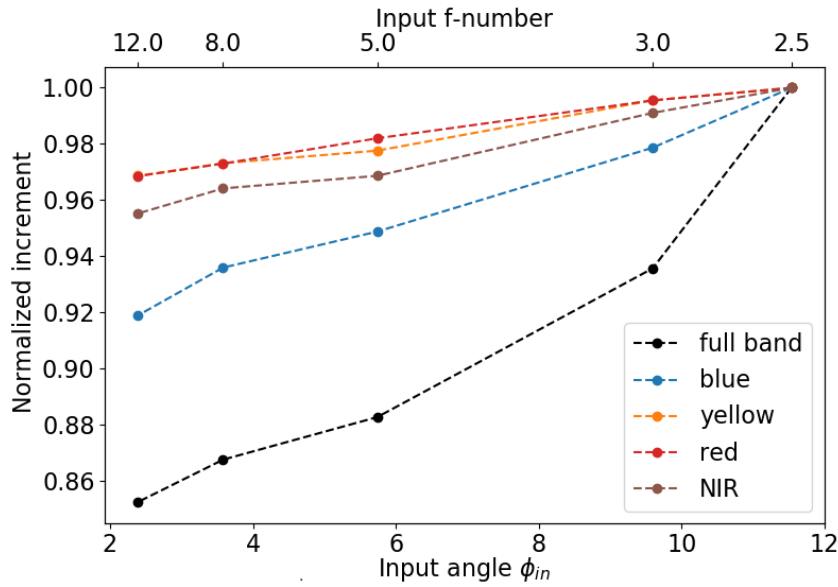
Figure 5.44: Near-field enlargement as a function of the wavelength with the circular fibre. The results of the different bandpass filters are marked on the plot with respect to the central wavelength color λ_c.

of the filters $\Delta\lambda = 10nm$, a quasi-monochromatic case with incoherent superposition was measured. The incoherent intensity fluctuations were attributed to the incoherent superposition of the individual mode fields. Each mode field possesses intensity fluctuations of a specific spatial frequency. High order propagation modes will consequently have higher spatial frequency fluctuation. Due to the long propagation wavelength of $\lambda_c = 905nm$, it was possible to illustrate better the effect of intensity fluctuations with the NIR filter. Using the modes calculated for the HeNe wavelength together with fast f-numbers, the incoherent intensity fluctuations as a function of the input f-number could be demonstrated. Figure 5.45 shows an example for the f-number $f\# = 2.5$.

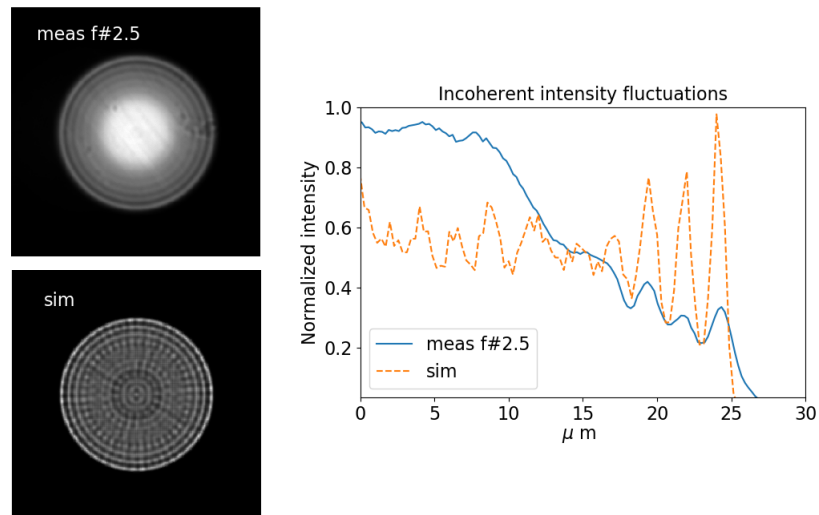Figure 5.45: Comparison between simulations and measurements for the incoherent superposition of quasi-monochromatic light. The example with an input f-number of $f\# = 2.5$ is illustrated.

Section 5.3 dealt with the angular far-field analysis of the parallel laser beam method. The angular distribution was recorded as a function of ϕ_{in} and compared to the simulations using matching parameters.

As described in Haynes et al. (2011) [53], the measurements of the far-field represent a ring that expands
as a function of ϕ_{in}. The thickness of the far-field ring represents the angular divergence as a function
of the input field characteristics and fibre parameters. The less angular divergence, the less FRD can be
expected in the system. By the means of the fibre field propagation model and knowledge of the basic
fibre parameters, numerical calculations were possible that obtain the minimum output divergence as a
function of both the input beam diameter and the input injection angle.

Each measured far-field intensity needed to be integrated along the azimuthal axis to create a one dimen-
sional averaged distribution. The one dimensional averaged distribution can be interpreted as a function
of the radius $F(r)$. Both measurements and simulations were mapped in an equivalent angular space for
better assessment. The one dimensional function becomes $F(\phi_{o,p})$, with $\phi_{o,p}$ describing angular units per
pixel [$^o/pixel$]. If both a simulation and a measurement are plotted as $F_k(\phi_{o,p}), k \in \{\text{sim,meas}\}$, the full
width at half-maximum (FWHM) of $F_{meas}(\phi_{o,p})$ will be broader than the FWHM of a simulation for any
input angle ϕ_{in}. Figure 5.46 shows the example for $\phi_{in} = 8^o$. The unsymmetrical appearance comes from
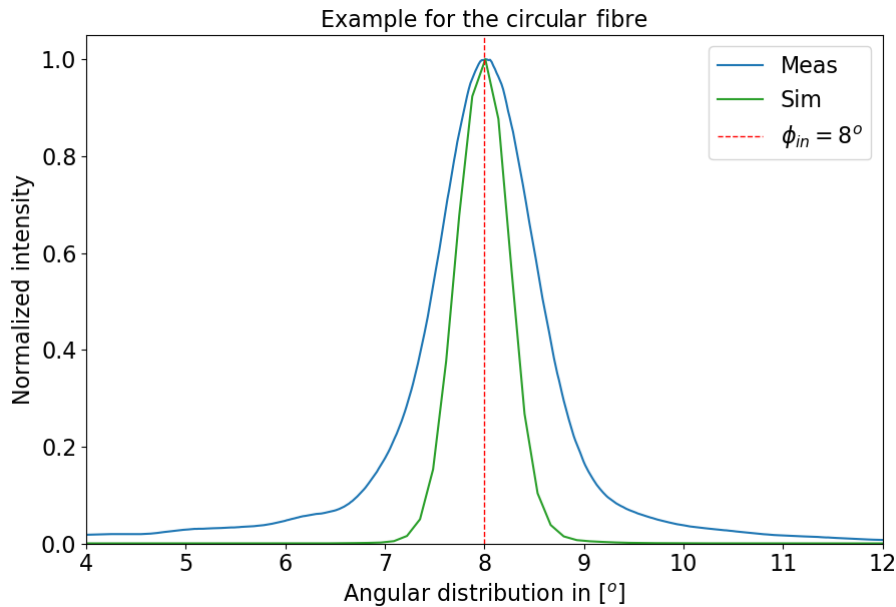the number of sampling points used in the simulation.

Figure 5.46: Comparison of the angular distribution between a measurement and a simulation when using
an incident angle of $\phi_{in} = 8^o$. The x-axis represents the angular distribution, and the y-axis is the
normalized intensity. The unsymmetrical appearance comes from the number of sampling points used in
the simulation.

Haynes et al. (2011) [53] summarized the effects that cause beam divergence in the far-field to scattering,
diffraction, and modal diffusion. The diffraction and modal diffusion components can be modeled by a
Gaussian function, whereas the scattering can be modeled by a Lorentz function. If both a Gauss- and a
Lorentz function are needed to fit a real measurement, a good tool for characterizing $F(\phi_{o,p})$ is the Voigt
profile. Through the Voigt analysis, it was possible to separate the modal diffusion component from the
measurements. The modal diffusion component was used to give an appropriate assessment in the analysis
of the angular divergence of the measured fibres. The results of the angular divergence were given as the
FWHM of the modal diffusion component. Figure 5.47 shows the results for the circular fibre.

The same procedure was realized for the octagonal fibre. As no disturbances are taken into account in
the simulations, the results are interpreted as the best case scenario for the angular divergence. The mean
of the simulations for both fibres showed similar results, with the simulated circular fibre having slightly
better results. The closer the measured fibre is to the simulated case, the better the performance. As a
figure of merit, the mean of the difference for every input angle was calculated. The closer the value is
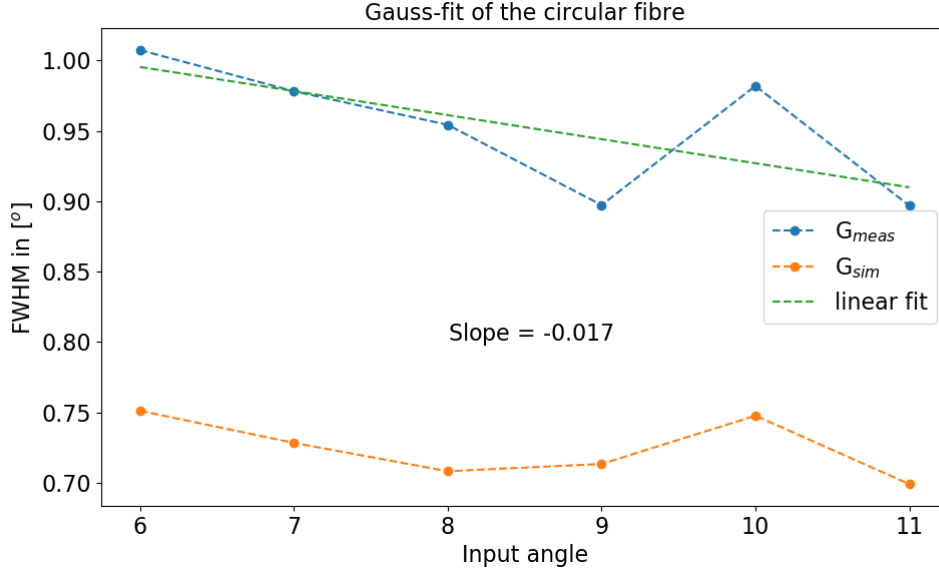
Figure 5.47: Results of the angular divergence comparison between simulations and measurements for $\phi_{in} \in \{6^o, ..., 11^o\}$ using the circular fibre. The x-axis represents the input angle ϕ_{in}, and the y-axis is the angular divergence illustrated as the FWHM of the Gaussian fit.

to zero, the better the performance. Interestingly, the circular fibre performed better than the octagonal fibre. The slope of the linear fit represents the change in divergence per input angle and has the unit $[^o/^o]$. A steeper slope means more sensibility to input angular fluctuations. Once again, the circular fibre performed better. Table 5.4 presents the results.

Parameter	Circular fibre	Octagonal fibre
Mean simulations	0.724^o	0.7843^o
Mean difference	0.228^o	0.503^o
Sensibility	0.017	0.08

Table 5.4: Results of the divergence analysis for both fibres.

The mode coupling factor σ_c of the simulations accounts for all the beam broadening factors that can occur in a real measurement. Through σ_c, the divergence of G_{meas} can be matched. A specific σ_c was used for every $\phi_{in} \in \{6^o, ..., 11^o\}$. Figure 5.48 shows the results of σ_c for both the circular and the octagonal fibre. A linear fit for both fibres is also displayed and shows the increment in mode coupling per input angle. Both fibres show a similar response. There is a tendency that the mode coupling factor increases with input angle. The increment is described by the slope of the linear fits. For both cases, it is fairly similar. Since the real octagonal fibre showed an augmented angular divergence, the σ_c values for the octagonal fibre were expected to be higher. Unfortunately, there is still no answer as to why the mode coupling factor increases with the input angle, this should be solved in future work.

The light cone measurements were analyzed in Sec. 5.4. The resulting output f-number depends on the encircled energy (EE) the system should have. To determine the encircled energy, the output intensity was averaged along the azimuthal axis and a 1D distribution $F(r)$ was created. The one dimensional distribution was weighted by the circumference at distance r as in $F_w(r) = F(r) * 2\pi r$ and normalized to the condition $\sum_{r=0}^{R} F_w(r) = 1$. A given encircled energy can be found by adding the distribution until $\sum_{r=0}^{\rho} F_w(r) = EE$. The slope of the linear fit as a function of sampling steps gives the output f-number. A typical value for the encircled energy is $EE = 95\%$ [54].
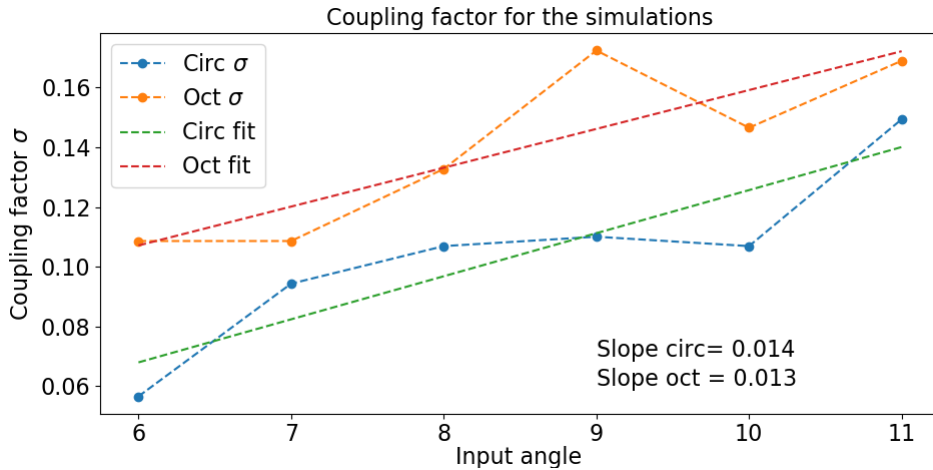
Figure 5.48: Mode coupling factor σ_c needed to match G_{meas} for both the circular and the octagonal fibre.

Since a vast number of factors can affect the output angular distribution of a fibre, FRD measurements tend to vary in results, even if the same fibre is being measured. With a time difference of 5 months, two light cone measurement runs of the same fibre were realized during the period of this thesis. The circular fibre produced better results the second time around. The octagonal fibre was only measured in the second run. The throughput equations presented in Sec. 2.2 were used to calculate the radiance loss of the displayed FRD plots. The radiance loss can be described by using the input/output f-number as well as the input/output near-field radius of a given system and is in its best case invariant for a lossless optical system. Table 5.5 summarizes the results of the calculations and FRD assessment realized for an input f-number $f\# = 5$ on both measurements of the circular fibre and the measurement of the octagonal fibre.

Parameter	Circular fibre 1	Circular fibre 2	Octagonal fibre
$f_{in} = f_{out}$	$EE = 82.4\%$	$EE = 87.16\%$	$EE = 84.6\%$
$EE = 95\%$	$f_{out} = 4.39$	$f_{out} = 4.48$	$f_{out} = 4.39$
L_{out}/L_{in}, $r_{in} = r_{out}$	0.77	0.80	0.77
L_{out}/L_{in}, $r_{in} \neq r_{out}$	0.159	0.165	0.145

Table 5.5: Results of the FRD analysis and radiance loss.

To date, the simulations are limited to the monochromatic case of light propagation. Furthermore, the injection of a light cone cannot be simulated as well as the injection of only specific input angles. Two methods were tested for the simulations to resemble a simplified case of the light cone injection but only one was successful. The successful method consisted in simulating input spots with different input angles as in $\phi_{in} \in \{\phi_o, ..., \phi_{max}\}$ and incoherently adding each resulting propagation field. Furthermore, the values of the mode coupling factor obtained from the Voigt analysis were applied for the simulations. Figure 5.49 shows the comparison between the simulation and the measurement with an input f-number $f\# = 5$. The octagonal fibre was simulated and compared to the simulations of the circular fibre. Figure 5.50 shows the results of the simulated octagonal and circular fibres. Table 5.6 summarizes the results.

Parameter	Circular fibre	Octagonal fibre
$f\#_{in} = f\#_{out}$	$EE = 86\%$	$EE = 79\%$
$EE = 95\%$	$f\#_{out} = 4.37$	$f\#_{out} = 4.12$
L_{out}/L_{in}, $r_{in} = r_{out}$	0.76	0.67
L_{out}/L_{in}, $r_{in} \neq r_{out}$	0.16	0.14

Table 5.6: Results of the FRD analysis and radiance loss of the simulations.
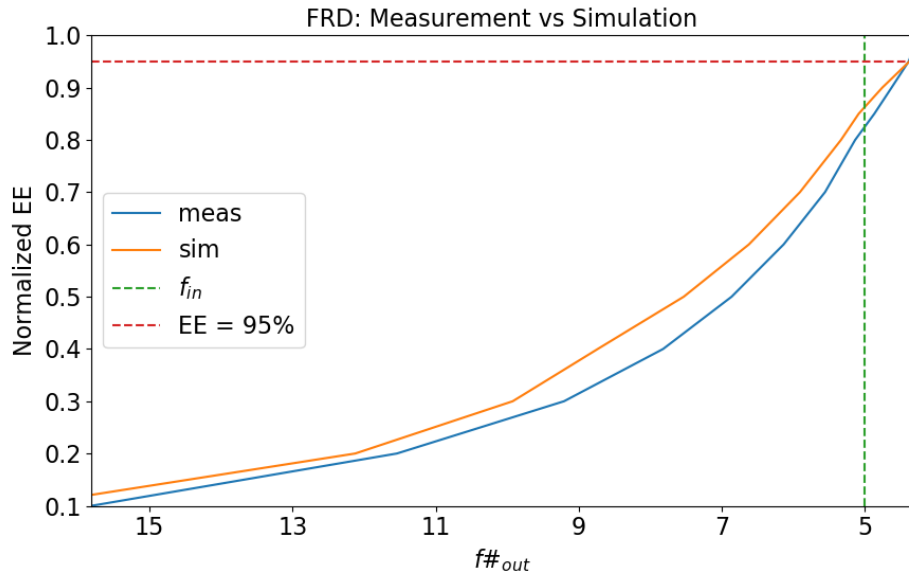
Figure 5.49: Comparison between the first measurement of the circular fibre and the simulation. The input f-number $f\#_{in} = 5$ is illustrated once more, as well as the location in the plot corresponding to $EE = 95\%$.
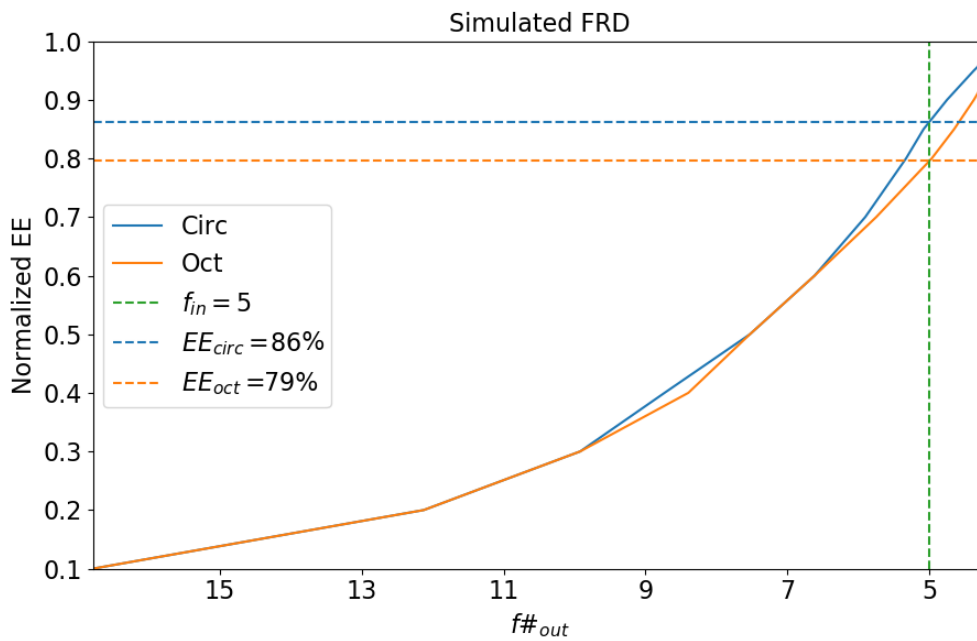
Figure 5.50: Comparison between the simulations of the circular fibre and octagonal fibre. The x-axis represents the output f-number, and the y-axis displays the amount of EE as a function of $f\#_{out}$. The input f-number $f\#_{in} = 5$ is once more illustrated as well as both cases for $f\#_{in} = f\#_{out}$.

Chapter 6

Conclusion and Outlook

Optical fibres are used for astronomical instrumentation mainly to provide more stability for the spectrograph and detector systems. Through decoupling the spectrograph from the telescope, issues such as temperature and humidity controlling, optical alignment sensibility, movement and vibration, detector functionality, maintenance, and operation become less complex to handle. Although there are many benefits of fibre-fed systems, fibres do incorporate unwanted effects to the optical train that diminish throughput and in some cases the signal to noise ratio of the spectrographic measurements. Changes in the focal ratio, the modal distribution of the light or non-perfect scrambling limits the accuracy of the measurements, e.g. the flux determination of the astronomical object, the sky-background subtraction and detection limit for faint galaxies, or the spectral line position accuracy used for the detection of extra-solar planets.

Focal ratio degradation is the broadening of the output angular distribution with respect to the input angular distribution and translates directly into the loss of throughput for fibre-based systems. Modal noise arises from modal interference. If the beam is coherent enough, interference patterns appear that can reduce the signal-to-noise ratio in a high-resolution spectrograph. Scrambling is a property that fibres possess. It decouples the input distribution from the output distribution. It is a helpful characteristic since spatial translations at the input of the fibre will not affect the output distribution, leading to a more stable spectrograph response. All of these effects can be explained through the wave properties of the propagation of light in fibre waveguides. The solution of the Helmholtz equation gives a discrete set of modes that can propagate through the optical fibre. The propagation modes can be used as a basis for linear expansion to create the Eigenmode Expansion Method which can describe the field at any distance z in the fibre as a summation of all the propagation modes with the respective phase and modal amplitude.

This thesis presents a model that is based on the Eigenmode Expansion Method. It provides the opportunity of simulating input spatial fluctuations, input angular fluctuations and focus variations with any kind of fibre cross-section, propagation wavelength, diameter, and numerical aperture. Through the use of the Fraunhofer approximation, the angular far-field output distributions can be simulated as a function of any of the mentioned parameters. The model allows for the analysis of both the near-field and far-field distribution of the simulated optical fibre. To test the accuracy of the results, real fibres were measured with an appropriate test-bench that allowed for different configurations of typical fibre characterization measurements.

The resemblance between simulations and measurements in the fully coherent case was demonstrated via the power spectral density analysis of the modal interference patterns. The increase in spatial fluctuations and speckles was attributed to the field interference of higher-order modes. Through an error assessment, the manufacture tolerances of the measured octagonal fibre were found to be the cause of increased spatial frequency fluctuations. Since the optical fibres have high tolerances, e.g. the NA tolerance equals almost 10%, it is an issue that can affect not only the near-field distribution, but also manifest in augmented

angular divergence.

Due to the observed interferences in both the near-field and far-field measurements of the circular fibre that appeared after induced modal scrambling, there is a high probability that partial coherence propagation occurs. An appropriate assessment on the influences of partial coherence in the field propagation of optical fibres was not conducted during the time of this work. This can be realized in future work.

The scrambling analysis demonstrated that the near-field intensity of the fibres increases in size with different input angles. Higher input angles translated into larger near-field intensities, a characteristic that was perfectly predicted by the simulations. The enlargement not only appeared in the coherent monochromatic case but could also be observed for incoherent chromatic measurements. Wavelengths towards the blue-end of the spectrum appeared to be more affected, matching the theory that longer wavelengths have larger mode field diameters. Incoherent intensity fluctuations could also be demonstrated with the simulations. Measurements with the bandpass filters exhibited intensity fluctuations and are not to be compared with modal interference. Due to the incoherence, the intensity fluctuations should be stable compared to normal modal interference. The higher the order of the excited modes, the higher the spatial fluctuations will be.

The simulations were used as a tool to asses angular divergence using the parallel laser beam measurements. The two fibres were measured and analyzed via the Voigt function to extract the modal diffusion part that accounts for the angular divergence. Once more, the simulations were able to match the results. A baseline for the minimal angular divergence was provided through the simulations. Through the mean of the difference from each measured point, a figure of merit was given that provides a value for the optimal angular divergence a system can reach.

As a final assessment on the validity of the simulations, measurements using the light cone method were compared to the simulations. Although the measurements were realized using an incoherent broadband light source, it was possible to recreate the FRD characteristics of the measured fibres through an appropriate method. To obtain a perfect agreement between the measurements and simulations, the mode coupling parameter could be manipulated in every angle employed for the simulation of the input cone. Due to the incoherent addition of every angle, the analysis of the contribution in the overall sum of each individual mode coupling factor leads to a complicated task that will be targeted in future work. The overall results give different opportunities of incorporating the simulations as a valid tool for testing the FRD characteristics of fibres which will be properly evaluated in future work.

Through the different analyses, it became clear that the input spot size will have a substantial influence on the angular divergence characteristics of the fibres. For real systems, fluctuations on the input spot size could manifest due to seeing variations or mechanical tolerances in fibre positioning systems. The simulations showed that for fluctuations of input spot diameter of the size of the fibre, strong fluctuations of the angular divergence can be expected. This particular issue could be one of the sources for discrepancies on the calibration in fibre-based systems. Fibre systems with smaller normalized frequency numbers are expected to be more sensitive to this issue, meaning that it could affect NIR systems more than VIS systems. A proper assessment on the influence of the input spot size as a function of the V-number as well as the effect of the manufacture tolerances on the angular divergence will be prepared for a future publication.

An end-to-end simulation environment is planned that should incorporate the outcome of the simulated near- and far-field results to Zemax. The Zemax environment applies ray tracing to successfully simulate the PSF from a given spectrograph design. If the outcome of the simulations is used as the input feed for the Zemax environment, it should be possible to simulate the radiant flux from the input end of the fibre to the sampling of the pixels on the detector. At the end of the year 2017, a demonstration was done in order to see how simulated output fields would influence the PSF based on the input position on the slit of the spectrograph and the propagation wavelength. A mask designed by Dr. Benito Moralejo in the programming language C allows for the incorporation of the simulated output fields into the Zemax environment. Figure 6.1 shows a preliminary version of the end-to-end simulations. A simulated intensity distribution can be seen at the input end of the simulated spectrograph. The intensity field is propagated

via ray tracing through the spectrograph, and the resulting distribution is delivered at the output end. In this example, the area of the input intensity field is reduced by the spectrograph. Afterwards, the resulting distribution is sampled by an NxN pixel area on the CCD. Through proper evaluation, the end-to-end simulations can be a powerful supplementary tool for characterizing the effects fibres introduce to fibre-fed spectrographs.
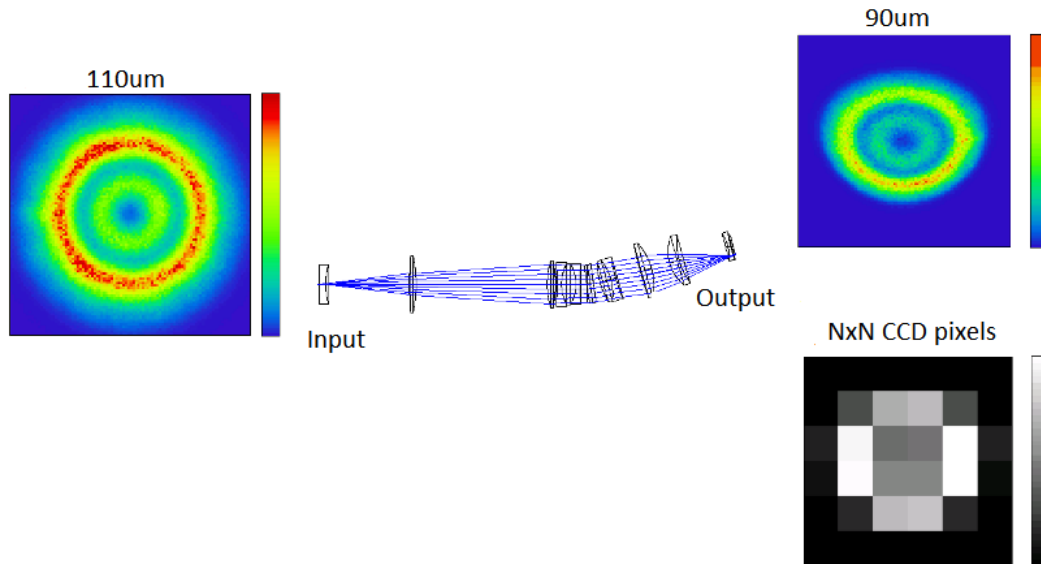

Figure 6.1: Illustration of an end-to-end simulation. An intensity distribution is used at the input end of the spectrograph. The output end shows the resulting distribution after ray tracing through Zemax. Afterwards, the resulting distribution is sampled by an NxN pixel area on the CCD.

Bibliography

[1] J. R. P. Angel, M. T. Adams, T. A. Boroson, and R. L. Moore. A very large optical telescope array linked with fused silica fibers. *The American Astronomical Society Journal*, 218:776–782, Dec 1977.

[2] J. M. Hill, J. R. P. Angel, J. S. Scott, D. Lindley, and P. Hintzen. Multiple object spectroscopy: the medusa spectrograph. *The Astrophysical Journal Letters*, 242:L69–L72, Dec 1980.

[3] T. Wilken, C. Lovis, A. Manescau, T. Steinmetz, L. Pasquini, G. Lo Curto, T. W. Hänsch, R. Holzwarth, and T. Udem. High-precision calibration of spectrographs. *Monthly Notices of the Royal Astronomical Society*, 405:L16–L20, Jun 2010.

[4] Donald G. York, J. Adelman, Jr. Anderson, John E., Scott F. Anderson, James Annis, Neta A. Bahcall, J. A. Bakken, Robert Barkhouser, Steven Bastian, Eileen Berman, William N. Boroski, Steve Bracker, Charlie Briegel, John W. Briggs, J. Brinkmann, Robert Brunner, Scott Burles, Larry Carey, Michael A. Carr, Francisco J. Castander, Bing Chen, Patrick L. Colestock, A. J. Connolly, J. H. Crocker, István Csabai, Paul C. Czarapata, and the SDSS Consortium. The Sloan Digital Sky Survey: Technical Summary. *The Astrophysical Journal*, 120:1579–1587, Sep 2000.

[5] Chris Stoughton, Robert H. Lupton, Mariangela Bernardi, Michael R. Blanton, Scott Burles, Francisco J. Castander, A. J. Connolly, Daniel J. Eisenstein, and the SDSS Data Release Consortium. Sloan digital sky survey: Early data release. *The Astronomical Journal*, 123:485–548, Jan 2002.

[6] Nathan M. De Lee, J. Ge, B. Lee, S. Mahadevan, S. W. Fleming, T. Sivarani, X. Wan, and the SDSS-III MARVELS Consortium. The SDSS-III MARVELS Survey: The First Year. In *American Astronomical Society Meeting Abstracts #215*, volume 215, page 472.05, Jan 2010.

[7] Nicholas Ross, E. S. Sheldon, A. D. Myers, C. Yeche, G. T. Richards, R. G. McMahon, J. F. Hennawi, K. Lee, W. M. Wood-Vasey, A. Weyant, P. Petitjean, D. J. Eisenstein, R. C. Nichol, N. Padmanabhan, D. J. Schlegel, D. P. Schneider, M. A. Strauss, D. H. Weinberg, and M. White. The SDSS-III Baryon Oscillation Spectroscopic Survey (BOSS): Quasar Target Selection and Initial Results from the Commissioning Run. In *American Astronomical Society Meeting Abstracts*, volume 215, page 471.04, Jan 2010.

[8] C. Allende Prieto, S. R. Majewski, R. Schiavon, K. Cunha, P. Frinchaboy, J. Holtzman, K. Johnston, M. Shetrone, M. Skrutskie, V. Smith, and J. Wilson. APOGEE: The Apache Point Observatory Galactic Evolution Experiment. *Astronomische Nachrichten*, 329:1018, Dec 2008.

[9] David R. Law and MaNGA Team. Mapping Nearby Galaxies at APO: The MaNGA IFU Galaxy Survey. In *American Astronomical Society Meeting Abstracts*, volume 223, page 254.31, Jan 2014.

[10] M. Colless. First results from the 2dF Galaxy Redshift Survey. *Philosophical Transactions of the Royal Society of London Series A*, 357:105, Jan 1999.

[11] F. Hammer, S. Morris, L. Kaper, B. Barbuy, J. G. Cuby, M. Roth, P. Jagourel, C. J. Evans, M. Puech, E. Fitzsimons, G. Dalton, and M. Rodrigues. The E-ELT multi-object spectrograph: latest news from MOSAIC. In *SPIE Proceedings*, volume 9908, page 990824, Aug 2016.

[12] A. Marconi, C. Allende Prieto, P. J. Amado, M. Amate, S. R. Augusto, S. Becerril, N. Bezawada, I. Boisse, F. Bouchy, and the HiReS consortium. ELT-HIRES, the high resolution spectrograph for the ELT: results from the Phase A study. In *SPIE Proceedings*, volume 10702, page 107021Y, Jul 2018.

[13] C. J. Evans, M. Puech, B. Barbuy, P. Bonifacio, J. G. Cuby, E. Guenther, F. Hammer, P. Jagourel, L. Kaper, S. L. Morris, J. Afonso, P. Amram, H. Aussel, A. Basden, N. Bastian, G. Battaglia, B. Biller, N. Bouché, E. Caffau, S. Charlot, Y. Clénet, F. Combes, C. Conselice, T. Contini, G. Dalton, B. Davies, K. Disseau, J. Dunlop, F. Fiore, H. Flores, T. Fusco, D. Gadotti, A. Gallazzi, E. Giallongo, T. Gonçalves, D. Gratadour, V. Hill, M. Huertas-Company, R. Ibata, S. Larsen, O. Le Fèvre, B. Lemasle, C. Maraston, S. Mei, Y. Mellier, G. Östlin, T. Paumard, R. Pello, L. Pentericci, P. Petitjean, M. Roth, D. Rouan, D. Schaerer, E. Telles, S. Trager, N. Welikala, S. Zibetti, and B. Ziegler. Science case and requirements for the MOSAIC concept for a multi-object spectrograph for the European Extremely Large Telescope. In *SPIE Proceedings*, volume 9147, page 914796, Jul 2014.

[14] P. Jagourel, E. Fitzsimons, F. Hammer, F. De Frondat, M. Puech, C. J. Evans, R. Sanchez, I. Guinouard, F. Chemla, M. Frotin, Y. Yang, P. Parr-Burman, T. Morris, M. Dubbeldam, M. Close, K. Middleton, G. Rousset, É. Gendron, A. Kelz, A. Janssen, J. Pragt, R. Navarro, M. Larrieu, K. El Hadi, K. Dohlen, G. Dalton, I. Lewis, M. Rodrigues, S. Morris, L. Kaper, B. Barbuy, J.-G. Cuby, and O. Le Fèvre. MOSAIC: the ELT multi-object spectrograph. In *Society of Photo-Optical Instrumentation Engineers (SPIE) Conference Series*, volume 10702, page 10702A4, July 2018.

[15] K. G. Strassmeier, T. Granzer, M. Weber, M. Woche, J. Hildebrandt, K. Arlt, A. Washuettl, S. M. Bauer, J. Paschke, M. Roth, J. H. M. M. Schmitt, A. Hempelmann, and A. Hagen. The STELLA Project: a 1.2m Robotic Telescope for High-resolution Echelle Spectroscopy. In *Astronomische Gesellschaft Meeting Abstracts*, volume 18, page P232, Jan 2001.

[16] Klaus G. Strassmeier, Axel Hofmann, Manfred F. Woche, John B. Rice, Christoph U. Keller, N. E. Piskunov, and Roberto Pallavicini. PEPSI spectro-polarimeter for the LBT. In Silvano Fineschi, editor, *SPIE Proceedings*, volume 4843, pages 180–189, Feb 2003.

[17] D. P. Sablowski, M. Weber, M. Woche, I. Ilyin, A. Järvinen, K. G. Strassmeier, and P. Gabor. PEPSI-feed: linking PEPSI to the Vatican Advanced Technology Telescope using a 450m long fibre. In *SPIE Proceedings*, volume 9912, page 99125H, Jul 2016.

[18] G. Dalton. WEAVE: The Next Generation Spectroscopy Facility for the WHT. In I. Skillen, M. Balcells, and S. Trager, editors, *Multi-Object Spectroscopy in the Next Decade: Big Questions, Large Surveys, and Wide Fields*, volume 507, page 97, Oct 2016.

[19] Jeremy Allington-Smith, Claire Poppett, David Bramall, Jerry Edelstein, Robin Lafever, Jürgen Schmoll, Colin Dunlop, Graham Murray, Robert Besuner, and Gordon Talbot. Fibre system of DESI. In *SPIE Proceedings*, volume 9147, page 91475M, Jul 2014.

[20] Hajime Sugai, Naoyuki Tamura, Hiroshi Karoji, Atsushi Shimono, Naruhisa Takato, Masahiko Kimura, Youichi Ohyama, Akitoshi Ueda, and the Subaru PFS consortium. Prime Focus Spectrograph for the Subaru telescope: massively multiplexed optical and near-infrared fiber spectrograph. *Journal of Astronomical Telescopes, Instruments, and Systems*, 1:035001, Jul 2015.

[21] Yongtian Zhu and Gerard R. Lemaitre. LAMOST multi-object spectrographs with asperized gratings. In Masanori Iye and Alan F. M. Moorwood, editors, *SPIE Proceedings*, volume 4841, pages 1127–1133, Mar 2003.

[22] M. Cirasuolo, J. Afonso, R. Bender, P. Bonifacio, C. Evans, L. Kaper, E. Oliva, and L. Vanzi. MOONS: The Multi-Object Optical and Near-infrared Spectrograph. *The Messenger*, 145:11–13, Sep 2011.

[23] R. S. de Jong, S. C. Barden, O. Bellido-Tirado, J. G. Brynnel, S. Frey, D. Giannone, R. Haynes, D. Johl, D. Phillips, O. Schnurr, J. C. Walcher, R. Winkler, W. R. Ansorge, S. Feltzing, R. G. McMahon, G. Baker, P. Caillier, T. Dwelly, W. Gaessler, O. Iwert, H. G. Mandel, N. A. Piskunov, J. H.

Pragt, N. A. Walton, T. Bensby, M. Bergemann, C. Chiappini, N. Christlieb, M.-R. L. Cioni, S. Driver, A. Finoguenov, A. Helmi, M. J. Irwin, F.-S. Kitaura, J.-P. Kneib, J. Liske, A. Merloni, I. Minchev, J. Richard, and E. Starkenburg. 4MOST: the 4-metre Multi-Object Spectroscopic Telescope project at preliminary design review. In *Ground-based and Airborne Instrumentation for Astronomy VI*, volume 9908, page 99081O, Aug 2016.

[24] A. Saviauk, P. Buschkamp, P. Caillier, C. Feiz, D. Haynes, R. Haynes, T. Jahn, A. Kelz, J.E. Migniau, J. Piotrowski, D. Plueschke, S. Rahurkar, and W. Seifert. Final design of optical fibre routing for 4MOST. In *Society of Photo-Optical Instrumentation Engineers (SPIE) Conference Series*, volume 10706, page 10706, Jul 2018.

[25] G. J. Hill, K. Gebhardt, E. Komatsu, N. Drory, P. J. MacQueen, J. Adams, G. A. Blanc, R. Koehler, M. Rafal, M. M. Roth, A. Kelz, C. Gronwall, R. Ciardullo, and D. P. Schneider. The Hobby-Eberly Telescope Dark Energy Experiment (HETDEX): Description and Early Pilot Survey Results. In T. Kodama, T. Yamada, and K. Aoki, editors, *Panoramic Views of Galaxy Formation and Evolution*, volume 399, page 115, Oct 2008.

[26] Andreas Kelz, Thomas Jahn, D. Haynes, G. J. Hill, H. Lee, J. D. Murphy, Justus Neumann, Harald Nicklas, M. Rutowska, C. Sandin, O. Streicher, S. Tuttle, M. Fabricius, S. M. Bauer, B. Vattiat, H. Anwand, and R. Savage. VIRUS: assembly, testing and performance of 33,000 fibres for HETDEX. In *Ground-based and Airborne Instrumentation for Astronomy V*, volume 9147, page 914775, Jul 2014.

[27] M. M. Roth, A. Kelz, T. Fechner, Thomas Hahn, S.M. Bauer, T. Becker, P. Boehm, L. Christensen, F. Dionies, J. Paschke, E. Popow, D. Wolter, J. Schmoll, U. Laux, and W. Altmann. PMAS: The Potsdam Multi-Aperture Spectrophotometer. I. Design, Manufacture and Performance. *Astronomical Society of the Pacific*, 117:620–642, Jun 2005.

[28] A. Kelz, M. A. W. Verheijen, M. M. Roth, S. M. Bauer, T. Becker, J. Paschke, E. Popow, S. F. Sánchez, and U. Laux. PMAS: The Potsdam Multi-Aperture Spectrophotometer. II. The Wide Integral Field Unit PPak. *Publications of the Astronomical Society of the Pacific*, 118:129–145, Jan 2006.

[29] S. F. Sánchez, R. C. Kennicutt, A. Gil de Paz, G. van de Ven, J. M. Vílchez, L. Wisotzki, C. J. Walcher, D. Mast, J. A. L. Aguerri, S. Albiol-Pérez, A. Alonso-Herrero, J. Alves, J. Bakos, T. Bartáková, J. Bland-Hawthorn, A. Boselli, D. J. Bomans, A. Castillo-Morales, C. Cortijo-Ferrero, A. de Lorenzo-Cáceres, A. Del Olmo, R.-J. Dettmar, A. Díaz, S. Ellis, J. Falcón-Barroso, H. Flores, A. Gallazzi, B. García-Lorenzo, R. González Delgado, N. Gruel, T. Haines, C. Hao, B. Husemann, J. Iglésias-Páramo, K. Jahnke, B. Johnson, B. Jungwiert, V. Kalinova, C. Kehrig, D. Kupko, Á. R. López-Sánchez, M. Lyubenova, R. A. Marino, E. Mármol-Queraltó, I. Márquez, J. Masegosa, S. Meidt, J. Mendez-Abreu, A. Monreal-Ibero, C. Montijo, A. M. Mourão, G. Palacios-Navarro, P. Papaderos, A. Pasquali, R. Peletier, E. Pérez, I. Pérez, A. Quirrenbach, M. Relaño, F. F. Rosales-Ortega, M. M. Roth, T. Ruiz-Lara, P. Sánchez-Blázquez, C. Sengupta, R. Singh, V. Stanishev, S. C. Trager, A. Vazdekis, K. Viironen, V. Wild, S. Zibetti, and B. Ziegler. CALIFA, the Calar Alto Legacy Integral Field Area survey. I. Survey presentation. *The Astronomy and Astrophysics Review*, 538:A8, Feb 2012.

[30] Roland Bacon and Guy Monnet. *Optical 3D-Spectroscopy for Astronomy*. Wiley-VCH, 2017.

[31] R. E. Epworth. Phenomenon of modal noise in fiber systems. In *Optical Fiber Communication*, page ThD1. Optical Society of America, 1979.

[32] J. Baudrand, I. Guinouard, L. Jocou, and M. Casse. Use and Development of Fiber Optics on the VLT. In S. Arribas, E. Mediavilla, and F. Watson, editors, *Fiber Optics in Astronomy III*, volume 152, pages 32–43, Jan 1998.

[33] Ian S. McLean. *Electronic Imaging in Astronomy*. Springer, 2008.

[34] William D. Heacox and Pierre Connes. Optical fibers in astronomical instruments. *The Astronomy and Astrophysics Review*, 3:169–199, Apr 1992.

[35] Lawrence W. Ramsey. Focal ratio degradation in optical fibers of astronomical interest. *Astronomical Society of the Pacific*, 3:26–39, Jan 1988.

[36] Sam Barden. *Implementation of an Optical Fiber Coupled Spectrograph for Astonomical Spectroscopy.* PhD thesis, The Pennsylvania State University, 1983.

[37] William D. Heacox. On the application of optical-fiber image scramblers to astronomical spectroscopy. *The Astronomical Journal*, 92:219–229, Jul 1986.

[38] G. Avila. Results on Fiber Characterization at ESO. In S. Arribas, E. Mediavilla, and F. Watson, editors, *Fiber Optics in Astronomy III*, volume 152, page 44, Jan 1998.

[39] J. Allington-Smith, G. Murray, and U. Lemke. Simulation of complex phenomena in optical fibres. *Monthly Notices of the Royal Astronomical Society*, 427:919–933, Dec 2012.

[40] D. M. Haynes, A. Saviauk, A. Kelz, R. Haynes, T. Jahn, D. Plüschke, S. Rahurkar, F. Zscheyge, J. Piotrowski, and R. Brown. 4MOST fibre feed: performance and final design. In *Society of Photo-Optical Instrumentation Engineers (SPIE) Conference Series*, volume 10702, page 1070289, July 2018.

[41] David W. Coutts. A diagnostic tool for microbends in fibre termination as a source of FRD. In *Proceedings SPIE*, volume 10706, page 107066E, Jul 2018.

[42] G. Avila, P. Singh, and B. Chazelas. Results on fibre scrambling for high accuracy radial velocity measurements. In *Ground-based and Airborne Instrumentation for Astronomy III*, volume 7735, page 773588, Jul 2010.

[43] Dennis Derickson. *Fiber Optic Test and Measurement.* Prentice Hall, 1997.

[44] Fedor Mitschke. *Fiber Optics Physics and Technology.* Springer, 2009.

[45] B.E.A. Saleh and M.C. Teich. *Fundamentals of Photonics.* Wiley Series, 2007.

[46] S. C. Ellis and J. Bland-Hawthorn. The case for OH suppression at near-infrared wavelengths. *Monthly Notices of the Royal Astronomical Society*, 386:47–64, May 2008.

[47] S. C. Ellis, S. Bauer, C. Bacigalupo, J. Bland-Hawthorn, J. J. Bryant, S. Case, R. Content, T. Fechner, D. Giannone, R. Haynes, E. Hernandez, A. J. Horton, U. Klauser, J. S. Lawrence, S. G. Leon-Saval, E. Lindley, H.-G. Löhmannsröben, S.-S. Min, N. Pai, M. Roth, K. Shortridge, L. Waller, P. Xavier, and R. Zhelem. PRAXIS: an OH suppression optimised near infrared spectrograph. In *Society of Photo-Optical Instrumentation Engineers (SPIE) Conference Series*, volume 10702, page 107020P, Jul 2018.

[48] J.-C. Olaya, S. G. Leon-Saval, D. Schirdewahn, K. Ehrlich, D. M. Haynes, and R. Haynes. 1:61 photonic lanterns for astrophotometry: a performance study. *Monthly Notices of the Royal Astronomical Society*, 427:1194–1208, Dec 2012.

[49] H. Hodara and C. Slemon. Throughput and coupling in optical fibers. *Applied Scientific Research 41*, 41:203–221, Sep 1984.

[50] James Harrington. Infrared Fiber Optics. *OSA Handbook 3*, 2001.

[51] Alexis Mendez and T.F. Morse. *Specialty Optical Fibers Handbook.* Academic Press Inc, 2007.

[52] D. Gloge. Optical power flow in multimode fibers. *Bell System Technical Journal*, 51:1767 – 1783, Oct 1972.

[53] D. M. Haynes, M. J. Withford, J. M. Dawes, J. S. Lawrence, and R. Haynes. Relative contributions of scattering, diffraction and modal diffusion to focal ratio degradation in optical fibres. *Monthly Notices of the Royal Astronomical Society*, 414:253–263, June 2011.

[54] J. Schmoll, M. M. Roth, and U. Laux. Statistical Test of Optical Fibers for Use in PMAS, the Potsdam Multi-Aperture Spectrophotometer. *Publications of the Astronomical Society of the Pacific*, 115:854–868, Jul 2003.

[55] L. Crause, M. Bershady, and D. Buckley. Investigation of focal ratio degradation in optical fibres for astronomical instrumentation. In *Ground-based and Airborne Instrumentation for Astronomy II*, volume 7014, page 70146C, Jul 2008.

[56] Sam Barden, editor. *Fiber Optics in Astronomy*, volume 3. Astronomical Society of the Pacific Conference Series, 1988.

[57] E.E. Whiting. An empirical approximation to the Voigt profile. *Journal of Quantitative Spectroscopy and Radiative Transfer*, 8:1379–1384, June 1968.

[58] J.J. Peyre and G. Principi. Linear combination of lorentzian and gaussian profiles to fit resonance spectra. *Nuclear Instruments and Metdhos*, 101:605–606, June 1972.

[59] John F. Kielkopf. New approximation to the voigt function with applications to spectral-line profile analysis. *J. Opt. Soc. Am.*, 63:987–995, Aug 1973.

[60] G.K. Wertheim, M.A. Butler, K.W. West, and D.N.E. Buchanan. Determination of the gaussian and lorentzian content of experimental line shapes. *Review of Scientific Instruments*, 45:1369–1371, Nov 1974.

[61] D.V. Titov and Rainer Haus. A fast and accurate method of calculation of gaseous transmission functions in planetary atmospheres. *Planetary and Space Science*, 45:369–377, Mar 1997.

[62] T. Ida, M. Ando, and H. Toraya. Extended pseudo-voigt function for approximating the voigt profile. *Journal of Applied Crystallography*, 33:1311–1316, Dec 2000.

[63] Yuyan Liu, Jieli Lin, Guangming Huang, Yuanqing Guo, and Chuanxi Duan. Simple empirical analytical approximation to the Voigt profile. *Journal of the Optical Society of America B*, 18:666–672, May 2001.

[64] Eric G. Rawson and Joseph W. Goodman. Modal noise in multimode optical fibers. In *Proceedings of SPIE*, volume 355, pages 37–42, Mar 1983.

[65] Klaus Petermann. Nonlinear distortions and noise in optical communication systems due to fiber connectors. *IEEE Journal of Quantum Electronics*, 16:761 – 770, Jul 1980.

[66] Thomas H. Wood. Actual modal power distributions in multimode optical fibers and their effect on modal noise. *Opt. Lett.*, 9:102–104, Mar 1984.

[67] Jacques Baudrand and Gordon A.H. Walker. Modal noise in high-resolution, fibre-fed spectra: A study and simple cure. *The Astronomical Society of the Pacific*, 113:851–858, Jul 2001.

[68] J. C. W. Corbett and J. Allington-Smith. Fibre modal noise issues in astronomical spectrophotometry. In *Society of Photo-Optical Instrumentation Engineers (SPIE) Conference Series*, volume 6269, page 62693N, Jun 2006.

[69] U. Lemke, J. Corbett, J. Allington-Smith, and G. Murray. Characterising modal noise in fibre-coupled spectrographs for astronomy. In *Modern Technologies in Space- and Ground-based Telescopes and Instrumentation*, volume 7739, page 773924, Jul 2010.

[70] Tetsuya Kanada and Koh ichi Aoyama. Modal-noise evaluation in multimode-fiber transmission. *Opt. Lett.*, 8:339–341, Jun 1983.

[71] Keegan S. McCoy, Lawrence Ramsey, Suvrath Mahadevan, Samuel Halverson, and Stephen L. Redman. Optical fiber modal noise in the 0.8 to 1.5 micron region and implications for near infrared precision radial velocity measurements. *SPIE Proceedings*, 8446:84468J, Sep 2012.

[72] Tevis D B Jacobs, Till Junge, and Lars Pastewka. Quantitative characterization of surface topography using spectral analysis. *Surface Topography: Metrology and Properties*, 5:013001, Jan 2017.

[73] U. Lemke, J. Corbett, J. Allington-Smith, and G. Murray. Modal noise prediction in fibre spectroscopy - I. Visibility and the coherent model. *Monthly Notices of the Royal Astronomical Society*, 417:689–697, Oct 2011.

[74] Todd R. Hunter and Lawrence W. Ramsey. Scrambling Properties of Optical Fibers and the Performance of a Double Scrambler. *Publications of the Astronomical Society of the Pacific*, 104:1244, Dec 1992.

[75] Samuel Charles Barden, Richard Joseph Elston, Taft Emerson Armandroff, and Carlton Tad Pryor. Observational performance of fiber optics - high precision sky subtraction and radial velocities. In *Fiber Optics in Astronomy II*, volume 37, page 223. Astronomical Society of the Pacific Conference Series, Jan 1993.

[76] F.G. Watson and P. Terry. Fibre characterization at fast focal ratios. In *Society of Photo-Optical Instrumentation Engineers (SPIE) Conference Series*, volume 2476, pages 10–19, Jun 1995.

[77] Samuel Charles Barden. Review of fiber optic properties for astronomical spectroscopy. In *Fiber Optics in Astronomy III*, volume 152, page 14, Jan 1995.

[78] G. Avila and P. Singh. Optical fiber scrambling and light pipes for high accuracy radial velocities measurements. In *Proceedings of SPIE*, volume 7018, page 70184W, Jul 2008.

[79] Beamprop manual. Rsoft Design Group. Accessed since: 2014 - 09 - 20.

[80] Eloy Hernandez, Daniel Bodenmüller, Martin M. Roth, and Andreas Kelz. Model-based calculations of fiber output fields for fiber-based spectroscopy. In *Society of Photo-Optical Instrumentation Engineers (SPIE) Conference Series*, volume 9907, page 990734, Aug 2016.

[81] Femsim manual. Rsoft Design Group. Accessed since: 2014 - 09 - 20.

[82] RSoft Design Group. *FemSIM User Guide*. RSoft Design Group, Inc, Version 9.

[83] E. Hernandez, M.M. Roth, and A. Kelz. Analysis of mode excitation on different geometries of optical fibres for astronomical spectroscopy. In *Society of Photo-Optical Instrumentation Engineers (SPIE) Conference Series*, volume 10705, page 107051K, Jul 2018.

[84] J. Corbett, T. Butterley, and J. R. Allington-Smith. Fibre modal power distributions in astronomy and their application to OH-suppression fibres. *Monthly Notices of the Royal Astronomical Society*, 378:482–492, Jun 2007.

[85] C. Lang, J. Ohser, and R. Hilfer. On the analysis of spatial binary images. *Journal of Microscopy*, 203:303–313, Dec 2000.

[86] Wei-Ping Huang. Couple-mode theory for optical waveguides: an overview. *Journal of the Optical Society of America A*, 11:963–983, Mar 1994.

[87] J. F. P. Spronck, Z. A. Kaplan, D. A. Fischer, C. Schwab, and A. E. Szymkowiak. Extreme Doppler precision with octagonal fiber scramblers. In *Proc. SPIE*, volume 8446, page 84468T, Sep 2012.

[88] G. Avila. FRD and scrambling properties of recent non-circular fibres. In *Ground-based and Airborne Instrumentation for Astronomy IV*, volume 8446, page 84469L, Sep 2012.

[89] Julian Stürmer, Christian Schwab, Stephan Grimm, André Kalide, Adam P. Sutherland, Andreas Seifahrt, Kay Schuster, Jacob L. Bean, and Andreas Quirrenbach. Optimal non-circular fiber geometries for image scrambling in high-resolution spectrographs. In *Proceedings of SPIE*, volume 9912, Jul 2016.

[90] Fiberguide Industries. Technical Data Reference Summary - Buffer Removal. Accessed since: 2019 - 07 - 09.